Sheffield Hallam University

Characterisation and development of a new multi-purpose surface analytical instrument.

RIGNALL, Michael.

Available from the Sheffield Hallam University Research Archive (SHURA) at:

http://shura.shu.ac.uk/20280/

A Sheffield Hallam University thesis

This thesis is protected by copyright which belongs to the author.

The content must not be changed in any way or sold commercially in any format or medium without the formal permission of the author.

When referring to this work, full bibliographic details including the author, title, awarding institution and date of the thesis must be given.

Please visit http://shura.shu.ac.uk/20280/ and http://shura.shu.ac.uk/information.html for further details about copyright and re-use permissions.

LEARNING CENTRE
CITY CAMPUS, POND STREET,
SHEFFIELD S1 1WB.

101 667 488 0

REFERENCE

ProQuest Number: 10700925

All rights reserved

INFORMATION TO ALL USERS
The quality of this reproduction is dependent upon the quality of the copy submitted.

In the unlikely event that the author did not send a complete manuscript
and there are missing pages, these will be noted. Also, if material had to be removed,
a note will indicate the deletion.

ProQuest 10700925

Published by ProQuest LLC (2017). Copyright of the Dissertation is held by the Author.

All rights reserved.
This work is protected against unauthorized copying under Title 17, United States Code
Microform Edition © ProQuest LLC.

ProQuest LLC.
789 East Eisenhower Parkway
P.O. Box 1346
Ann Arbor, MI 48106 – 1346

'Characterisation and development of a new multi-purpose surface analytical instrument'

Michael Rignall

A thesis submitted in partial fulfilment of the requirements of Sheffield Hallam University for the degree of Doctor of Philosophy.

In collaboration with Kratos Analytical and Oxford Instruments Micro-Analytical Group.

October 2000.

SHEFFIELD HALLAM UNIVERSITY
TH
ADSETTS CENTRE

Abstract

A new multi-purpose surface analytical instrument (the 'Hallam' instrument) is described, which combines the surface specific information obtained using x-ray photoelectron spectroscopy (XPS), with bulk information obtained using Energy Dispersive X-ray (EDX) detection. A 15kV electron gun and an ultra high vacuum EDX detector give the instrument an EDX mapping capability. To exploit this to its full potential, spatial alignment of EDX maps acquired at various electron beam energies, E_o, was required. The misalignment of images acquired at various E_o values was investigated, and a means of describing the misalignment as a function of E_o was presented. An algorithm was developed which would allow the alignment of offline images acquired at different E_o values. This was demonstrated on images acquired on both the Hallam instrument and on a Phillips XL40 electron microscope.

The small area XPS system developed by Kratos analytical gave a spatial resolution of 30μm at the centre of the field of view, although this deteriorated away from the centre. The reasons for this deterioration in spatial resolution were investigated, and two methods of improving the system were presented. The improvements were implemented on the Hallam instrument and demonstrated using a standard silver grid sample. The small area XPS was applied to a TiAlNi coated stainless steel sample to demonstrate its application to real samples, and to display the spatial alignment between the XPS and EDX maps.

Finally, the instrument was calibrated for quantitative XPS studies. This involves determining the response of the instrument as a function of the photoelectron kinetic energy. From several methods presented in the literature, the most appropriate was chosen for calibration of the 'Hallam' instrument. The effectiveness of the method used was assessed by recording spectrum intensity from pure elemental standards, and comparing the results with intensity values calculated using the calibration curves.

Preface

This thesis, no part of which has been submitted elsewhere, describes the work performed in the Materials Research institute, Sheffield Hallam University, Sheffield, during the period 1995-1998. The work is original and was performed under the supervision of Dr A. Wirth (1995-1997) and Prof. J. Titchmarsh (1997-1998). Where the work of others have aided the investigation, acknowledgements are given. At the request of the industrial partners, no part of this work was published, although a poster titled 'Calibration and Improvement of an XPS and Small Area XPS system.' was presented at the 10 the International Conference on Quantitative Surface Analysis (QSA-10).

I would like to thank the following people. Dr A. Wirth who initiated this project, made available the facilities and funding necessary, and supervised the first part of the project. Dr A.R. Walker (formerly Kratos Analytical), who provided much advice, technical support, and hardware. Dr P. Statham (Oxford Micro-Analysis Group) who gave significant input to the project in terms of ideas and actual hardware and software. Dr V. Vishnyakov (Sheffield Hallam University), Dr S. Clarke (Sheffield Hallam University) and Dr. T. English (British Steel's Swindon Technology Centre.) for their help and co-operation. Prof. J. Titchmarsh, who supervised the final year of the PhD, and provided much help and guidance during the writing of this thesis. Finally, my parents, for their continued support and encouragement over the years.

Contents

Chapter 1 Introduction. 1

Chapter 2 Theory and Literature Review.

2.0 Introduction 3
2.1 Basic introduction to analytical techniques
2.1.1 X-ray Photoelectron spectroscopy. 3
2.1.2. Basic Instrumentation of XPS. 5
2.1.3 Electron probe analysis. 6
2.2 Quantification of XPS data
2.2.1 Introduction 8
2.2.2 Factors affecting quantification 8
2.2.3 Determination of Energy analyser transmission function. 13
2.2.4 Determination of the instrumental transmission function using the bias method. 16
2.2.5 Development of the metrology spectrometer. 18
2.2.6 Discussion 20
2.3 The Development of Small Area XPS.
2.3.1 Introduction. 22
2.3.2 X-ray Probe Methods 22
2.3.3. Electro-Optical Methods. 24
2.3.4 Single pole piece magnetic lens. 28
2.3.5. Alternative methods. 31
2.3.6 Discussion of various techniques. 33
2.4 Thickness Determination By Electron Probe X-ray Analysis.
2.4.1 Introduction. 35
2.4.2 The Depth Distribution Function $\phi(\rho z)$. 35
2.4.3. Application to thickness determination. 37
2.4.4. Alternative methods. 39
2.4.4. Techniques for specialist applications. 40
2.4.5. Discussion. 41

Chapter 3 Instrumentation.
3.1 Introduction 45
3.2 Overview 45
3.3 UHV pumping system. 47
3.4 Energy Analyser. 49
3.5 Excitation sources. 51
3.6 Energy Dispersive X-ray Detector. 51

3.7 Ion gun. 53
3.8 Sample stage. 53
3.9 Secondary Electron Detector. 53
3.10 System Control. 54
3.11 25kV Field Emission Gun 55
3.12 Thickness Mapping capability. 56
3.13 Comments on thickness mapping. 58

Chapter 4 Alignment of Electron Induced Images Acquired at Different Primary Beam Energies.
4.0 Introduction 61
4.1.0 Image shift measurement 61
4.1.1 Shift compensation 66
4.2.0 Image Distortion Assessment. 69
4.2.1 Image Geometrical Transformations. 70
4.2.2 Singular Value Decomposition. 72
4.2.3 Implementation of SVD using C code. 73
4.2.4 Application of Distcof.exe. 75
4.2.5 Results of Image Distortion Assessment. 78
4.2.6. Discussion of transformations. 83
4.3.0 Application of transformation coefficients to acquired images. 84
4.3.1. Application of nearest neighbourhood approximation 86
4.3.2 Implementation of transkV.exe and results. 86
4.3.3. Discussion. 96
4.3.4 Conclusion 97

Chapter 5 Characterisation and improvement of Scanning Small Area XPS System.
5.0 Introduction 99
5.1 Assessment of scanning system.
5.1.0 Alignment of magnetic field 99
5.1.1 Experimental Edge Measurement 100
5.1.2 Spatial resolution as a function of position 102
5.1.3 Spatial resolution as a function of photoelectron energy. 105
5.1.4 Spatial resolution as a function of iris setting. 105
5.1.5 Spatial resolution as a function of coil current and sample height 107
5.1.6 Possible improvements to the SAXPS system 108
5.2 Improvements to scanning system.
5.2.0 Simulation of deflection system 109
5.2.1 Modification to an Octopole Scanning System 113
5.2.2 Effect of improvements to scanning system. 121
5.3 Application of improved Scanning Small Area XPS and alignment

with electron beam techniques. 125
5.4. Conclusion 128

Chapter 6 Calibration of instrument transmission as a function of energy.
6.0 Introduction 131
6.1.0. Application of method proposed by Carrazza and Leon (1991) using peak area measurements. 131
6.1.1 Results of peak area measurements. 132
6.1.2. Application of method proposed by Carrazza and Leon (1991) using Background Measurements. 133
6.1.3. Results of background measurements. 134
6.1.4 Extension of this technique for regular calibration. 145
6.1.5. Comparison of transmission function with elemental measurements. 147
6.2.0. Application of bias method proposed by Zommer (1995). 159
6.2.1 Results 160
6.2.2 Further investigation of method. 161
6.3 Discussion. 163
6.4 Conclusion. 164

Chapter 7 Conclusion. 166

Appendix 1 168

Chapter 1 Introduction.

The purpose of this thesis is to explain the development of a multi-technique instrument for the analysis of surfaces, surface coatings and interfaces. The 'Hallam' instrument was built as a test bed for a Department of Trade and Industry funded project, as part of the Link Nanotechnology Program. The project, titled 'Simultaneous Quantitative Thickness Mapping and Chemical Analysis of Thin Films', was a collaboration between Kratos Analytical, Oxford Instruments Microanalysis Group and Sheffield Hallam University. The project aim was to develop an instrument capable of non-destructive acquisition of quantifiable thickness data, in the range 1nm to 5μm.

The 'Hallam' instrument is equipped for both surface and bulk analysis techniques. The surface analytical techniques available on the instrument are X-ray Photoelectron Spectroscopy (XPS) and Auger Electron Spectroscopy (AES). Both techniques must be performed within an Ultra High Vacuum (UHV) environment and require high resolution electron spectroscopy. For these reasons it has been common practice among commercial manufacturers to build instruments configured to accommodate both methods. The Kratos Axis-165 is such an instrument and is the foundation of the 'Hallam' instrument that is to be described in this thesis.

X-ray analysis on the scanning electron microscope is a much more widely used analytical tool than surface analysis. While surface analysis was developed to inspect the outermost monolayers of a surface, x-ray analysis is used for the general characterisation and inspection of materials. X-ray analysis is based around the Scanning Electron Microscope (SEM) and thus requires less complicated instrumentation than that used for surface analysis. In order to integrate the components required for x-ray analysis onto the Axis-165, the instrument was reconfigured to accommodate an Energy Dispersive X-ray (EDX)detector and a Backscattered electron detector, which were supplied by Oxford Instruments. This equipment was specially engineered by Oxford Instruments to be compatible with a UHV environment. A full description of the instrumentation is given in Chapter 3.

The benefits of the project to Oxford Instruments was that thickness mapping by electron probe methods would be developed, and this technique could be directed at the SEM market. The benefits to Kratos were the instrumental improvements which were to be made as part of the project. These included a sample chamber to accommodate an EDX detector, a 25kV field emission electron gun, and a long working distance lens for XPS analysis of thick samples. These features would then be available as options on the Axis-165.

Analysis of EDX data can yield information of the thickness and composition of surface films and coatings. The EDX control system on the Hallam instrument is provided with software to calculate film thickness and composition from x-ray signals and back scattered electron signals. It was envisaged

that during the diagnostic stage, depth profiling XPS (eroding the sample by ion bombardment between XPS analysis) could be used as verification of the non-destructive depth profiling techniques. Oxford Instruments were committing resources to research into thickness mapping, so it was considered that an up to date review of the subject was carried out. This task was undertaken by the author, and a literature review of thickness mapping by electron probe methods is presented in Chapter 2.

Additional information of film thickness/composition can be obtained by taking EDX measurements at different values of electron beam energy, E_0. Oxford Instruments wished to extend their software so this multi kV analysis could be realised. If this data is to be used in the context of mapping then we would wish to obtain spatially resolved information from the same point of a sample at different values of E_0. Practically, this requires the registration of SEM images acquired at different values of E_0, and Oxford Instruments requested that this should be investigated by the author. Chapter 4 deals with determining the degree of misalignment between images acquired at different beam energies, and methods of rectifying this misalignment.

An objective of the project was to configure the instrument or create offline procedures to align images acquired from the various techniques. This was necessary to allow verification of non-destructive thickness and compositional mapping, by depth profiling XPS. For these reasons it was decided that scanning small area XPS should align spatially with the other techniques available. The acquisition of spatially resolved XPS data can be achieved using various methods, but that used on the Axis-165 is the sequential pixel by pixel method which shall be described in further detail later. The instrumentation present on the Axis-165 offers a minimum spatial resolution of 30μm. It is known, however, that this was limited to the centre of the field of view and the image generated by small area XPS was distorted as the distance from the centre of the field of view is increased. It was considered an important part of the project to improve this, and Chapter 5 of this thesis describes this. As this work was carried out by the author, it was considered important that a comprehensive knowledge of spatially resolved XPS was obtained. A review of the literature relevant to this was carried out and is presented in Chapter 2.

It was intended that compositional XPS depth profiles could be compared with non-destructive depth profiling thickness and compositional data. It was also envisaged that a knowledge of the outermost surface of a sample, which could be determined by XPS, would help to develop the non-destructive depth profiling techniques. In order to determine elemental composition by XPS, the data must be quantified, which requires the characterisation of the instrument in terms of electron transmission. The quantification of XPS data is the subject of numerous publications, which are reviewed in Chapter 2. The 'Hallam' instrument was characterised for quantification, and the methodology and result of this are presented in Chapter 6.

Chapter 2 Theory and Literature Review.

2.0 Introduction

A brief introduction to the two main techniques for which the Hallam instrument is equipped shall be given. The following sections will discuss, in detail, the subjects of specific interest to this project. These are quantitative x-ray photoelectron spectroscopy , small area x-ray photoelectron spectroscopy and film thickness determination by electron probe x-ray analysis.

2.1 Basic introduction to analytical techniques

2.1.1 X-ray Photoelectron Spectroscopy.

When an x-ray photon interacts with a sample, a photoelectron is ejected. The energy of the photoelectron depends primarily on the shell from which the electron is ejected. A schematic of the emission process is shown in Figure 2.1.1 (Watts 1994) for an electron ejected from the k-shell.

Figure 2.1.1.Shematic of the photo-emission process. (Watts 1994)

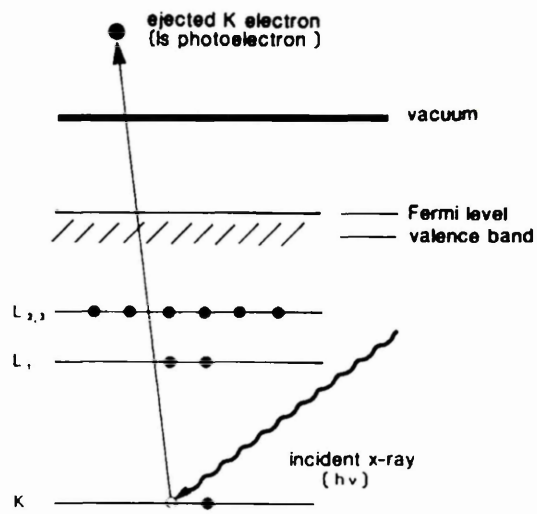

The diagram shows the x-ray photon interacting with an electron in the K-shell, causing the emission of a 1s photo-electron. The resulting K shell vacancy is filled by an electron from a higher level which can lead to X-ray fluorescence, or by the radiationless de-excitation process of Auger emission.

X-ray Photoelectron Spectroscopy (XPS) involves irradiating a sample with x-rays so photo-emission occurs, and determining the kinetic energy of the ejected photoelectron. The kinetic energy (E_k) of the ejected photo-electron is related to the electron binding energy (E_b) by the expression (Seah 1990a)

$$E_k = h\nu - E_b - \phi$$

Equation 2.1

There are further terms that may be included in Equation 2.1 but these are small when compared to the uncertainties in the terms shown (Woodruff and Delchar 1994). As the x-ray photon energy (hv) and the work function ϕ are known and E_k are determined experimentally, calculation of the electron binding energy is possible. It is the binding energy which defines the element and atomic level from which the photoelectron originated.

Figure 2.1.2 shows a typical XPS spectrum from SiO_2 (Drummond 1996). The characteristic XPS core level peaks are super imposed on a background of inelastically scattered electrons. The technique is surface sensitive because only the electrons from the top few nanometers of a surface contribute to these peaks, as those from within the sample would lose kinetic energy by inelastic collisions before leaving the surface of the sample.

Figure 2.1.2 XPS spectrum from SiO_2. (Drummond 1996)

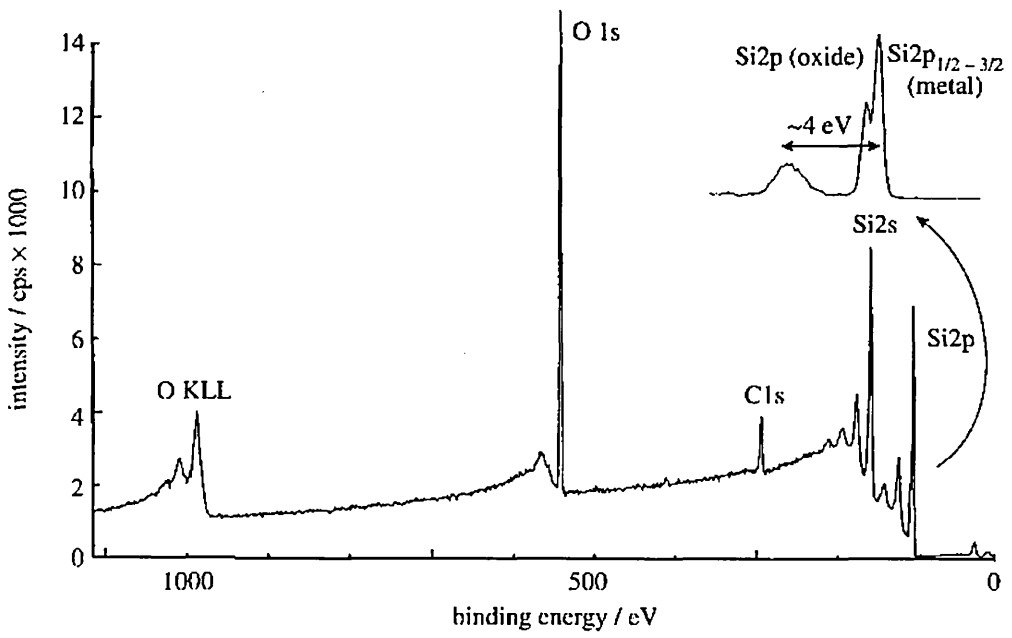

Also shown in the spectrum is the peak shift of the Si peak due to its chemical state. This shift may be used to determine the chemistry of the sample surface, which is an advantage XPS has over other surface analytical techniques.

2.1.2. Basic Instrumentation of XPS.

XPS may be considered in simple terms as a primary source of x-rays, a sample, an electron analyser and a detector, all contained within an ultra high vacuum (UHV) enclosure and controlled by a dedicated computer. The need for a UHV environment arises from the surface sensitive nature of the analytical technique. If the sample was not held in UHV conditions then the surface which was being examined would rapidly become contaminated. UHV conditions are usually obtained using ion or diffusion pumps. A simplified schematic of an XPS instrument is shown as Figure 2.1.3.

The x-ray source consists of a filament held at ground potential, and an anode held at high potential (15kV-20kV). The anode material determines the energy of the x-ray radiation, and also the linewidth of the energy. The linewidth of the radiation must not be excessively large so as to widen the resultant XPS peaks. In practice Al and Mg anodes are used as the x-ray energy (1486.6eV and 1253.6eV, respectively) is high enough to excite most peaks of interest from the elements of the periodic table. If an x-ray source of narrow energy linewidth is required for a high resolution study of XPS peak position and shape, then a monochromator may be employed between the source and the sample.

Figure 2.1.3 Simplified schematic of XPS instrument.

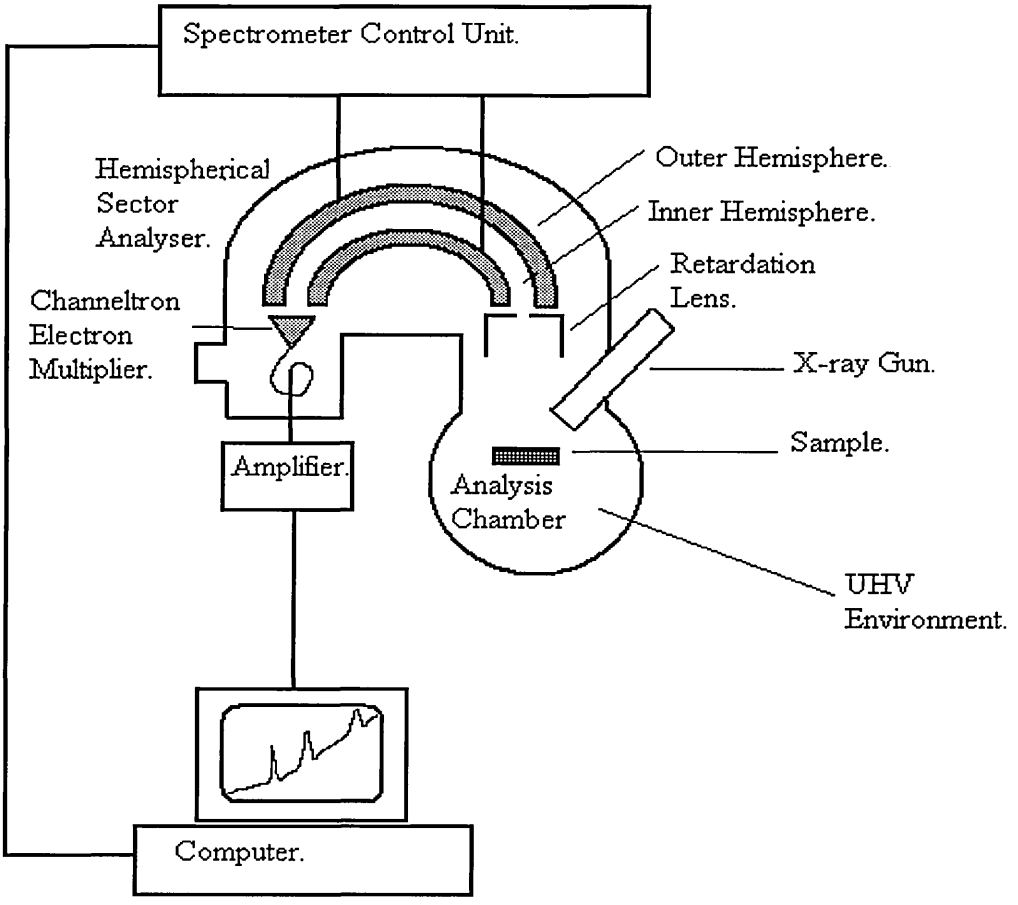

Two types of analyser have been used in commercial XPS systems, the concentric hemispherical sector analyser (HSA) and the double pass cylindrical mirror analyser (CMA). The HSA has the higher resolution and is most commonly used in dedicated XPS instruments (Seah 1990b). The electrons pass between inner and outer electrodes which are held at different potentials to disperse the electrons according to energy. To obtain high energy resolution the electrons are retarded to a constant pass energy at which they enter the analyser, the retardation stage consisting of a lens before the analyser entrance slit. The mode of operation is known as fixed analyser transmission mode (FAT). The value of pass energy used may be chosen on the basis of energy resolution and count rate. A channel electron multiplier is usually employed at the exit to the analyser as the electron detector.

2.1.3 Electron probe analysis.

When an electron beam is focused onto a sample surface interactions between the incident electrons and the sample take place, and variety of signals are generated which can be used for analysis. Figure 2.1.4 shows electron beam impinging onto a surface. The signals used in electron probe microanalysis are shown.

Figure 2.1.4. An electron beam impinging on a sample.

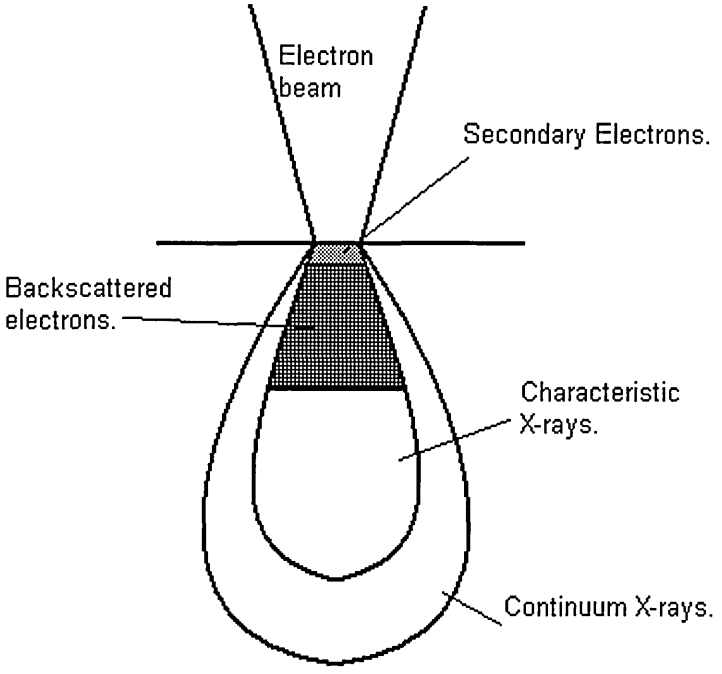

Secondary electrons result from the Coulomb interaction between incoming electrons and those present in the sample (Blackmore 1985), while backscattered electrons are elastically and inelastically scattered electrons (Lorreto 1984).The characteristic x-rays are the result of transitions between inner atomic electron energy levels. Electron bombardment causes ionisation

of the inner energy levels and the vacancy is filled by the transition of an electron from a higher energy level. The wavelength of the characteristic x-ray line is equal to the difference between the energy of the atom in its initial and final states. The x-ray lines are referred to as 'characteristic' because the energy of the lines is specific to the emitting element. For each element a number of characteristic x-ray lines exist depending on the possible transitions, and the energy of the incident electron beam. A full explanation of the characteristic x-ray generation is given by Reed (1993a). Electron bombardment also generates continuum or Bremsstrahlung (Reed 1993b). This is generated by electrons decelerating due to collisions with atoms.

If an x-ray spectrometer is used to detect the x-ray emission from a sample then an x-ray spectrum may be recorded consisting of both characteristic and continuum radiation. This spectrum can be used for qualitative analysis as the characteristic peaks identify the elements present in the sample. Quantitative analysis can also be performed as the spectrum may be used to obtain the x-ray intensity for a particular characteristic x-ray line. The concentration of a given element may be determined with an accuracy of 1% if suitable standards are available (Feldman & Mayer 1986).

The x-ray spectrum may be recorded with either a 'wavelength dispersive'(w.d.) or 'energy dispersive'(e.d.) spectrometer. The former uses a diffracting crystal which acts as a monochromator, so the x-ray detector sequentially scans through the wavelengths. An e.d. spectrometer records the whole spectrum simultaneously using a solid state x-ray detector. Electronic pulse height analysis is used to sort the pulses produced in the detector according to x-ray energy. Wave dispersive spectrometers produce a much better spectral resolution and peak to background ratio than e.d. spectrometers, but take longer to record a spectrum. As the w.d. spectrometer is an optical system, complicated mechanical arrangements are necessary, which coupled with the need for high quality optics, makes the spectrometer expensive and awkward to fit onto instruments. Energy dispersive spectrometers are commonly used on scanning electron microscopes as little modification to the instrument is necessary. This is the type of spectrometer which was fitted to the Hallam instrument.

The spatial resolution of EDX and WDX is limited since the volume from which characteristic x-rays are emitted is larger compared to the electron beam spot size (Goldstein et al 1981), as shown in Figure 2.1.4. Although the spot size of the electron beam may be, for example, 100nm, the spatial resolution obtained using EDX would still be in excess of 1μm.

2.2 Quantification of XPS data

2.2.1 Introduction

XPS provides an effective tool for surface analysis of materials, detecting elements which are present and providing information about the chemical state of these elements. Quantitative studies are also possible using XPS as a means of compositional analysis. As surface compositional quantification by XPS is to be used for the project, the theory of quantification was studied. Further attention was then focussed on the various methods of characterising the instrument for XPS quantification. As this would have to be done for the Hallam instrument before quantitative studies could be performed, it was necessary to choose which methods should be applied to the Hallam instrument.

2.2.2 Factors affecting quantification

In order to interpret the intensity of an XPS photoelectron peak we must understand the factors which affect the detection of the photoelectrons.When irradiated by x-rays, ionisation occurs at the core levels over the depth of x-ray penetration. The excited electrons are ejected from the surface of the sample after passing through the solid. The electrons lose energy as they traverse to the surface, so only those from a depth ~3λ adjacent to the surface escape to provide the line intensity in the XPS spectrum. Seah (1990c) expressed the intensity of electrons produced per second from a level X of an element A as,

$$I_A = \sigma_A(h\nu)D(E_A)\int_{\gamma=0}^{\pi}\int_{\Phi=0}^{2\pi} L_A(\gamma)\int_{y=-\infty}^{\infty}\int_{x=-\infty}^{\infty} J_0(xy)\sec\delta \cdot T(xy\gamma\Phi E_A) \times \int_{z=0}^{\infty} N_A(xyz)\exp\left[-z/\lambda(E_A)\cos\theta\right]dzdydxd\Phi d\gamma$$

Equation 2.2.1

where $\sigma_A(h\nu)$ is the cross-section for emission of a photoelectron from the relevant inner shell per atom of A by a photon of energy $h\nu$, $D(E_A)$ is the detection efficiency for each electron transmitted by the electron spectrometer. The geometrical terms which are present in Equation 2.2.1 are shown in Figure 2.2.1. $L_A(\gamma)$ is the angular asymmetry of the intensity of the photoemission from each atom, $J_0(xy)$ is the flux of the X-ray characteristic line per unit area at a point (x,y) on the sample, $T(xy\gamma\Phi E_A)$ is the analyser transmission and $N_A(xyz)$ is the atom density of the A atoms at xyz. This general equation takes account of all possible variables which could affect the intensity. Although this equation as written above is not useful for actual quantification of data, as it would be impractical to determine each term, it does demonstrate the

factors which could determine the detected intensity. The integral over z can be reduced to $N_A\lambda(E_A)\cos\theta$ for a homogeneous solid. If reference spectra I_{RA} and I_{RB} are taken on the same instrument, then for a homogeneous binary alloy of elements A and B the intensities can be written as

$$\frac{I_A / I_A^{\infty}}{I_B / I_B^{\infty}} = \left[\frac{\lambda_{AB}(E_A)\lambda_B(E_B)}{\lambda_{AB}(E_B)\lambda_A(E_A)}\right]\left(\frac{R_{RB}}{R_{RA}}\right)\left(\frac{N_A N_{RB}}{N_B N_{RA}}\right)$$

Equation 2.2.2

where λ_{AB} is the attenuation length in the alloy, R_{RB} and R_{RA} are roughness's of the pure elemental standards, and N_{RB} and N_{RA} are the atom densities in the pure reference materials.

Figure 2.2.1. The geometry of XPS analysis configuration (Seah 1990c).

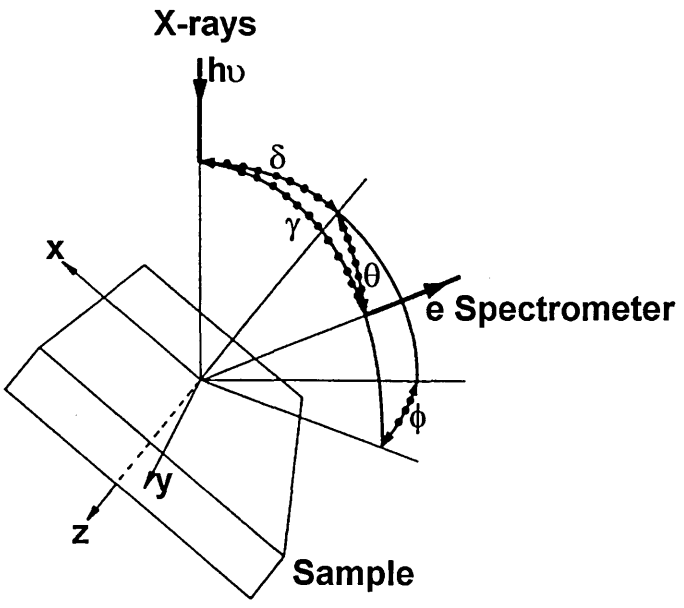

If we ignore the roughness terms and express the matrix term F_{AB} as (Seah 1986)

$$F_{AB} = \left[\frac{\lambda_{AB}(E_A)\lambda_B(E_B)}{\lambda_{AB}(E_B)\lambda_A(E_A)}\right]\left(\frac{a_B}{a_A}\right)^3$$

Equation 2.2.3

and use the expression (Seah 1986)

$$\frac{N_A N_{RB}}{N_B N_{RA}} = \frac{X_A}{X_B}\left(\frac{a_A}{a_B}\right)^3$$

Equation 2.2.4

where a_A and a_B are the atomic sizes of elements A and B, respectively, the molar concentration of the elements A and B can then be described by the formula

$$\frac{X_A}{X_B} = F_{AB} \frac{I_A / I_A^{\infty}}{I_B / I_B^{\infty}}$$

Equation 2.2.5

Assuming the matrix term F_{AB} to be unity would lead to the case where the signal is assumed to be proportional to molar fractional content. This leads to the general equation

$$\frac{X_A}{X_B} = \frac{I_A / I_A^{\infty}}{\sum_{i=A,B} I_i / I_i^{\infty}}$$

Equation 2.2.6

Variations on the above equation are generally quoted as a suitable starting point for quantification. Studies have shown, however, that the value of F_{AB} may scatter around unity considerably for different alloys (Seah 1980).

Wagner et al (1981) quoted a variation on Equation 2.2.1

$$I = nf\sigma\phi yAT\lambda$$

Equation 2.2.7

where n is the number of atoms per cubic centimetre of the element of interest, f is the flux of X-ray photons impinging on the sample, in units of photon $cm^{-2}s^{-1}$, σ is the photo-electric cross section for the particular transition in cm^2, ϕ is the angular efficiency factor for the instrumental arrangement (angle between photon path and emitted photoelectron), y is the efficiency of production in the photoelectric process to give photoelectrons of normal energy, A is the area of the sample from which photoelectrons can be detected, T is the efficiency of detection of the photo electrons emerging from the sample and λ is the mean free path of the photoelectrons in the sample. Although simpler that the equation quoted by Seah, the terms(e.g. y) are less well defined.

Wagner goes on to define the atomic sensitivity factor S as

$$S = \sigma\phi yAT\lambda$$

$$S = \sigma\phi yAT\lambda$$

Equation 2.2.8

so for elements A and B of a single binary homogeneous sample

$$\frac{n_A}{n_B} = \frac{I_A / S_A}{I_B / S_B}$$

Equation 2.2.9

This approach contradicts Seah's claim that matrix effects are of significance although Wagner et al (1980) claims that λ_A/λ_B is only slightly matrix dependent. Wagner states that if S is evaluated for each photoelectron line present in the spectra, quantification can be carried out. Wagner's experimental work concentrated on the evaluation of S for various compounds, each containing either fluorine or potassium. This enabled the sensitivity factor for the other element present in the compound to be expressed relative to the F1s or K2p line. This study was carried out on two instruments producing a set of empirical sensitivity factors still commonly used today. It must be noted that the instruments used both had double cylindrical mirror analysers, as opposed to semi hemispherical analysers. The intensities used in the study were taken from peak area measurements with straight line background subtraction. This approach is criticised by Seah et al (1984) as much intensity is neglected after background subtraction, which could otherwise be used in quantitative calculations. Figure 2.2.2 shows this.

Figure 2.2.2. The shaded area of the peak is the area contributing to the intensiy after background subtraction.

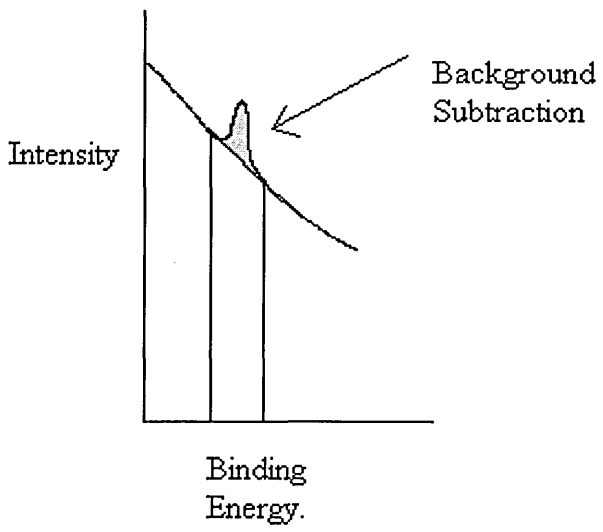

We shall consider the approach of Wagner as the most convenient, as pure standards are not required for each analysis, but use Seah's terminology, as it is complete and each term precisely defined. From Equation 2.2.1,if the electron spectrometer has a small entrance aperture and the sample is uniformly illuminated, we get

$$I_A = \sigma_A(h\nu)D(E_A)L_A(\gamma)J_0 \sec(\delta)N_A\lambda(E_A)\cos\theta$$
$$\times \int_{y=-\infty}^{\infty}\int_{x=-\infty}^{\infty} T(xyE_A)dydx$$

Equation 2.2.10

We shall consider the case where we need to compare data recorded on the same instrument but from different photoelectron lines. As we shall compare intensities using Equation 2.2.9, many of the terms cancel out. Only those terms with a dependency on photoelectron kinetic energy or atomic number will remain variables. Although the transmission function term, T, is shown as a function of x and y, this is not significant as we assume that the area of analysis remains constant with changes in photoelectron kinetic energy (true for the Axis-165). So for elements A and B of a single binary homogeneous sample

$$\frac{I_A}{I_B} = \frac{n_A\sigma_A(h\nu)D(E_A)L_A(\gamma)T(E_A)\lambda(E_A)}{n_B\sigma_B(h\nu)D(E_B)L_B(\gamma)T(E_B)\lambda(E_B)}$$

Equation 2.2.11

The asymmetry terms L is given by (Reilman 1976)

$$L_A(\gamma) = 1 + \tfrac{1}{2}\beta_A(\tfrac{3}{2}\sin^2\gamma - 1)$$

Equation 2.2.12

The term β_A is atomic number dependent, but from Equation 2.2.12, we see that no asymmetry correction is needed for values of γ close to 54.7° where $L(\gamma)=1$. We shall assume this to be the case (true for Axis-165) and incorporate the detection efficiency into the term $T(E_A)$ which becomes the transmission function of the whole instrument when operating in wide area XPS mode. In this case Equation 2.2.11 becomes

$$\frac{I_A}{I_B} = \frac{n_A\sigma_A(h\nu)T(E_A)\lambda(E_A)}{n_B\sigma_B(h\nu)T(E_B)\lambda(E_B)}$$

Equation 2.2.13

So, for the purpose of quantification, we have a sensitivity factor S, expressed as

$$S = \sigma_A(h\nu)T(E_A)\lambda(E_A)$$

Equation 2.2.14

λ is known to vary with E but a consensus has not been reached on the nature of the relationship. Seah and Dench (1979) used differing forms of the relation

$$\lambda = cE^{-2} + k(aE)^{0.5}$$

Equation 2.2.15

where a is the atomic spacing and c and k are constants. Different values of c and k were given for pure elements, organic and inorganic compounds. A simpler approach is to assume the relation

$$\lambda = E^{m}$$

Equation 2.2.16

Wagner et al (1980) used experimental data from nine materials to provide a least squares fit, with m in the range 0.54 to 0.81 averaging at 0.66.

The ionisation cross section, σ, is defined as the transition probability per unit time for excitation of a single photoelectron from the core level of interest under an incident photon flux of $1cm^{-2}s^{-1}$. Values of σ were calculated by Schofield (1976) for x-ray excitation from magnesium Kα lines at 1254eV and aluminium Kα lines at 1487eV. The calculations were carried out relativistically using the single potential Hartree-Slater atomic model. The values are published in tabulated form relative to the C 1s line. Inaccuracies will arise from using the Hartree-Slater model due to the approximate manner of treating electron–electron interactions, but an accuracy of 5% is reported for all except high Z elements.

The term T_A is harder to determine as it will vary for individual instruments. It is clear that this must be evaluated experimentally.

2.2.3 Determination of Energy analyser transmission function.

In order to determine the energy analyser transmission function $T(E_k)$ it is obvious that we must express the intensity of XPS peaks in terms of kinetic energy alone. Evaluation of this is non trivial as the true shape of XPS spectra (free from instrumental contribution) are difficult to obtain, thus ruling out direct measurement of intensity as a function of E_k, the kinetic energy of the photoelectrons.

The dependence $T \propto E^m$ is the simplest relationship and theoretical values of m were first calculated by Seah (1980) for several instruments. It was stated that at high photoelectron energies the transmission, $T \propto E_k^{-1}$, and at lower energies $T \propto E_k^{-0.5}$. The energy at which the crossover between the two modes occurs is dependent on the input aperture size, pass energy and sample size. Seah and Anthony (1984) used peak area measurements from Cu, Ag and Au to determine the intensity ratios between two different instruments. For example, they showed that

the ratio of the transmission functions for a Perkin Elmer PHI 550 and a VG Scientific ESCA 3 Mk II was proportional to $E^{-0.244}$ to an accuracy of 2%. The experiment was extended, and 15 different instruments were calibtated in terms of transmission function, relative to a VG Scientific ESCA 3 Mk II (Seah et al, 1984). The relative transmission fuction for each instrument was expressed as $T \alpha E^n$, where n was published for each instrument. Although this this not produce absolute transmission functions, it allowed data from the instruments involved to be compared quantitavely.

The intensity can also be expressed as a function of the analyser pass energy E_p, the energy at which the photoelectrons pass through the analyser after retardation from E_k. Hemminger (1990) proposed the relationship

$$I \ \alpha \ E_p \left(\frac{E_p}{E_k} \right)^{n(E_p/E_k)}$$

Equation 2.2.17

Peak intensities were taken from a variety of samples with peak positions representing the whole of the 0-1100eV energy range. The spectra were obtained at pass energies 5, 10, 20, 50, 100 and 200eV.

For any given peak the ratio of the peak intensity to the pass energy (I/E_p) was plotted against the pass energy to kinetic energy ratio (E_p/E_k) on log scales. From these plots a relationship of the form

$$\log(I/E_p) = c - 0.21 \log^2 (E_p/E_k)$$

Equation 2.2.18

was found for the VG ESCALAB MkII. This was derived from data taken on three different models of the ESCALAB located in different laboratories, so a large assumption is made by neglecting differences between individual instruments. Strong emphasis is placed on the fact that pass energy and kinetic energy are inseparable. Hemminger claims this enables quantitative comparison of data collected at different pass energies. The primary use of a transmission function is to compare peak intensities acquired with the same conditions. The justification for needing to compare data with different pass energies is that one may be required to use high pass energies when using small area XPS (due to large reduction in intensity) or when measuring minor components of low intensity. Data acquired under these conditions may then require comparison with data acquired under normal conditions at lower pass energy. One would,

however, avoid this practice as in both cases (small area XPS or minor component measurement) other factors apart from pass energy change would affect quantification.

A simpler method of determining the transmission function of the energy analyser was proposed by Carrazza and Leon (1991). The transmission function was obtained from the dependence of signal intensity on the instrumental pass energy E_p, at a given kinetic energy of the incident electrons E_k. The values E_p and E_k are related by

$$E_k = R \cdot E_p$$

Equation 2.2.19

where R is the retarding ratio by which the retarding electrode deccelerates the incident electrons to the pass energy E_p before entrance to the dispersive element. In the case of the Hallam instrument the dispersive element is the semi-hemispherical analyser. For XPS analysis the pass energy remains constant while R is varied (Constant Absolute Resolution). As discussed earlier several experimental variables apart from the kinetic energy of the electrons used (E_k) and the pass energy (E_p) influence the transmission function of the instrument. As these experimental variables can be kept constant for XPS measurements, the dependence of the transmission function,T, can be described by

$$T = k(R)^{-n(E_k)} \cdot E_p$$

Equation 2.2.20

If we substitute R from Equation 2.2.19 into Equation 2.2.20, the transmission can be represented by

$$T = kE_k^{-n(E_k)} E_p^{n(E_k)+1}$$

Equation 2.2.21

Evidently, the value n can be determined at a given E_k by measuring the intensity I at various values of E_p. If a plot of the values Log I versus Log E_p is generated then the gradient of the straight line fit is equal to $n(E_k)+1$. This procedure may be repeated for values of E_k across the relevant kinetic energy range, so the value of n as a function of E_k may be established and described by a polynomial such as

$$n(E_k) = a + bE_k + cE_k^2 + dE_k^3 \ldots$$

Equation 2.2.22

The difference between this method and that proposed by Hemminger is that n is a function of E_k only and not E_P/E_k. The function $n(E_k)$ may be determined for several different modes of operation such as magnetic or electrostatic magnification and for different entrance aperture settings.

Carrazza used both peak area measurements and background measurements to evaluate the function $n(E_k)$ for a LHS-11 Leybold-Haraeus analyser. From the reported data, the better polynomial fit appears to come from background measurements. XPS Peak intensities are influenced by many parameters (Equation 2.1.1), so will consequently be subject to many uncetainties. Background signal is the result of many interaction within the sample, so uncertainties will be averaged out. Another advantage of background measurement is that there is no background subtraction method to consider.

The function $n(E_k)$ was applied to quantification using sensitivity factors derived by Equation 2.2.21. Comparison of elemental composition of a catalyst sample was performed, between results when Mg and Al-X-ray sources were used. The results from this showed good agreement which indicated that the validity of Equations 2.2.14 and 2.2.20 is reasonable.

2.2.4 Determination of the instrumental transmission function using the bias method.

This method of determining the instrumental transmission function involves applying a bias voltage to the sample stage relative to ground and was first used by Ebel et al (1983). The mathematical proof of how the transmission function may be derived from measurements taken while the sample is at a bias voltage is presented below (Zommer, 1995).

The measured photoelectron signal intensity at a kinetic energy E may be written as

$$I(E) = I_o \cdot T(E) \cdot N(E)$$

Equation 2.2.23

where I_o is the x-ray photon current incident on the sample, T(E) is the instrumental transmission function and N(E) is the energy distribution of electrons from the sample. If a bias voltage E_{bias} is applied to the sample then the kinetic energy of the electrons entering the analyser will be $E_k=E+E_{bias}$. I_o is assumed to be a constant value, so can be taken as unity. Equation 2.2.23 can now be written as

$$I(E_k, E_{bias}) = T(E_k, E_{bias}) \cdot N(E)$$

Equation 2.2.24

which becomes

$$I(E+E_{bias},E_{bias})=T(E+E_{bias},E_{bias})\cdot N(E)$$

Equation 2.2.25

If we differentiate with respect to E_b we then obtain

$$\frac{dI}{dE_{bias}}=\left(\frac{\partial T}{\partial E_k}\frac{dE_k}{dE_{bias}}+\frac{\partial T}{\partial E_{bias}}\right)N(E)$$

Equation 2.2.26

and, since $dE_k/dE_{bias}=1$,

$$\frac{dI}{dE_{bias}}=\left(\frac{\partial T}{\partial E_k}+\frac{\partial T}{\partial E_{bias}}\right)N(E)$$

Equation 2.2.27

Dividing Equation 2.2.27 by Equation 2.2.23 eventually gives the differential equation:

$$\frac{d\ln I}{dE_{bias}}=\frac{d\ln T}{dE_k}+\frac{d\ln T}{dE_{bias}}$$

Equation 2.2.28

If we assume that the bias voltage has a negligible effect on the instrumental transmission function, the term $d(\ln T)/dE_b$ can be neglected. In this case we obtain the differential equation

$$\frac{1}{I}\frac{dI}{dE_{bias}}=\frac{1}{T}\frac{dT}{dE_k}$$

Equation 2.2.29

the left hand side of Equation 2.2.29 may be established experimentally at different values of kinetic energy E. The relationship between $(1/I)dI/dE_b$ and E may be determined and expressed by the polynomial p(E). The solution of Equation 2.2.29 is given by:

$$T=T_0\exp\left(\int p(E)dE\right)$$

Equation 2.2.30

If the polynomial p(E) is described by $a+bE+cE^2\ldots$ then the final expression for the transmission function will be given by

$$T = T_o \exp(aE + bE^2/2 + cE^3/3)$$

Equation 2.2.31

Ebel et al (1983) applied this method to a Kratos XSM 800 instrument and commented on the range of bias voltages to be used. It is stated that ±100V is suitable but from observation of analyser transmission functions (Carrazza and Leon 1991, Hemminger 1990) it is clear that the change in intensity across that range would not be linear. Zommer used –10 to+40V bias voltage and claimed successful transmission function determination despite reporting problems with background intensity change.

2.2.5 Development of the metrology spectrometer.

Seah and Smith (1990) approached the problem differently to the methods discussed so far. Their objective was to produce true electron emission spectra for reference samples, which could be used to calculate the transmission function and detector sensitivities of all instruments. Previous work had shown that the scatter in the ratio of the XPS intensity of the Cu $2p_{1/2}$ and $Cu3p_{1/2}$ peaks, from different instruments was ±19% (Seah et al 1984). This value was reduced to ±8% when the transmission function of the analyser was taken into account. This showed that, with simple procedures, reproducible data from the same sample could be obtained in different laboratories. It was envisaged that the reference true electron emission spectra could further increase reproducibility when applied to all instruments.

To obtain the true electron emission spectra a metrology spectrometer was developed. The instrument was based on a modified VG ESCALAB electron spectrometer. The channel electron multiplier (CEM) detection assembly was adapted to accommodate a Faraday cup, which was interchangeable with the CEM.

The measured intensity was expressed by

$$I(E) = I_o Q(E) n(E)$$

Equation 2.2.32

where n(E) is the absolute spectral intensity (the true electron emission spectra) from the sample per incident photon as a result of the basic physical process of the excitation, transport and emission of x-ray photoelectrons for the sample, I_o is the x-ray flux and Q(E) represents the effects of the measurement system. Q(E) is expressed by

$$Q(E) = H(E)T(E)D(E)F(E)$$

Equation 2.2.33

where H(E) is the efficiency term representing the effects of the electron detection system, T(E) is the electron optical transmission for the area irradiated, D(E) is the efficiency of the electron detection system and F(E) is the efficiency of the electronics up until the point that the data is recorded.

The instrument could be operated in two modes, constant retard ratio where the energy resolution ΔE varies with the kinetic energy E but $\Delta E/E$ is constant, or constant pass energy mode where ΔE is constant. The theory of the transmission function T(E) is covered by Seah and Smith (1990) for each mode of operation, and states that for the constant retard ratio mode the transmission T(E) of photo electrons is proportional to the energy E. In constant pass energy mode the transmission is a more complicated function of energy.

The term H(E) is said to consist of stray magnetic field effects and analyser scattering effects, and it is stated that under certain conditions, such as low retard ratio and small analyser input slit , these effects are negligible. The term F(E) is discussed and is said to be unity as long as the detector discriminators are set correctly and the count rate of the recorded spectra does exceed a value at which pile up would occur. Using these conditions a spectrum is acquired from a sample of copper irradiated by a 5kV electron beam in the constant retard ratio mode. The spectrum is acquired using both the Faraday cup and the CEM detector. As the Faraday cup is assumed to have a detector efficiency D(E)=1 this procedure allows the term for the CEM to be evaluated. Since it is assumed that in constant retard resolution mode T(E) α E, then

$$n(E) \propto \frac{I(E)}{E}$$

Equation 2.2.34

for the spectra as long as the precautions listed above are taken.

The instrument is then considered in constant pass energy mode. In this case the terms D(E), H(E) and F(E) are constants as the energy E of the electrons passing through the analyser is constant. The transmission function in this mode is subsequently given by

$$T(E) \propto \frac{I(E)}{n(E)}$$

Equation 2.2.35

Spectra are then acquired in constant pass energy mode for a variety of pass energies and analyser input slit settings, so T(E) can be evaluated for these conditions. Conventional XPS is then carried out on Cu, Ag and Au reference samples. The evaluated terms of Equation 2.2.33 are applied to the spectra to produce the true electron emission spectra n(E) for that element.

For the true electron emission spectra to be accurate, the transmission function must be accurate. Two factors could influence this. Firstly, if there is any deviation in the theoretical assumption that $T(E) \alpha E$ for the constant retard ratio mode, errors will arise. Secondly, the assumption is that, in constant pass energy mode the term H(E) is constant. This is assumed because of the constant pass energy through the analyser. The factors included in the H(E) term such as stray magnetic field could influence the electrons before they are retarded to the pass energy and enter the analyser.

As a conclusion to this work a so called round robin study was launched to compare the true electron emission spectra of Cu, Ag and Au to spectra acquired on different instruments. The results of this study were subsequently published (Seah 1993). The study involved 25 different instruments from 9 manufacturers. Each participant was instructed to acquire XPS spectra from the Cu, Ag and Au reference samples they were supplied with, under normal operating conditions. Spectra were acquired from 200 to 1600eV kinetic energy with a 1eV increment. For each instrument used, calibration was accomplished, as the ratio of measured to reference spectra provides the Q(E) function for that instrument.

The study found a large variation in Q(E) for instruments from different laboratories, including variations between the same model operated under identical conditions. This highlights the need for separate and regular calibrations of instruments used for quantitative XPS. The true electron emission spectra were later provided in a standard digital format in a National Physical Laboratory (NPL) software package, which is described by Seah (1995). The software will compare measured spectra to the reference spectra and also diagnose any problems such as errors in quantification.

2.2.6 Discussion

The study of the factors which effect quantification was useful to the characterisation of the Hallam instrument, as it will enable us to apply quantification to pure samples and compare results for different elements. The study told us which factors were relevant and how these should be derived. In the case where published values should be used, as for the ionisation cross section, σ, the necessary publications were obtained.

The spectra derived from measurements on the metrology spectrometer will be used extensively by the surface analysis community. Although the spectra may not truly represent the electron emission spectra, they allow XPS data from different laboratories to be compared. To compare the true emission spectra to spectra taken on the instrument which requires quantification, the digitised spectra must be purchased from the NPL. At the time that the instrument characterisation work took place this was not available to the author.

A comparison of methods of determining the transmission function was carried out by Weng et al (1993). They used the methods of Hemminger et al (1990), Carrazza and Leon (1991) and a method based on evaluating the terms of Equation 2.2.14. The latter method was unsuccessful as it is difficult to obtain many data points in the E_k range, since each point must be obtained from a measurement of a pure element. It was, however, considered useful for checking the validity of other methods. Weng considered Hemminger's method as the most versatile, as the value of n in Equations 2.2.17 and 2.2.21 is dependent on both E_p and E_k. Weng applied the methods to two instruments, a VG ESCA 3 MkII and A Scienta X-probe, and concluded that n was constant for the VG instrument and dependent on E_p/E_K for the Scienta instrument.

It would seem appropriate for an analyst to determine whether n is constant or dependent on E_k or E_p/E_K before choosing which method to use (Hemminger's or Carrazza's method). It would be desirable to use the method proposed by Carrazza as this is the simpler and the parameter n can be related to a physical parameter, R, the retard ratio.

The bias method, proposed by Zommer, is different to the forementioned methods as it does not presume the form of the relationship between the intensity I, and E_p and E_k. This method would produce a useful comparison with which to validate the other methods. On this basis it was decided to apply the methods proposed by Carrazza and Leon (1991) and Zommer (1995) to the Hallam instrument.

2.3 The Development of Small Area XPS.

2.3.1 Introduction.

XPS was largely assumed to be an area averaging technique. With techniques such as Auger electron spectroscopy and SIMS, where the primary excitation beam consists of charged particles, focussing of the beam to submicron dimensions and rastering of the beam is easily achievable using electron optics. As this is not possible with the X-rays used for photoelectron spectroscopy, it was not until the early eighties that techniques for area restricted XPS were developed. A number of review papers have been written on this subject, in particular Seah and Smith (1988), Drummond (1992) and Drummond (1996). These papers all cover the topic comprehensively and give a detailed account of the various methodologies, but can obviously only comment on the technology developed at the time of writing.

There are two approaches to achieving spatially resolved XPS. One is to reduce the size of the X-ray beam, thus using a microprobe to define the area of analysis. The second is to modify the collection electron optics to obtain spatially resolved data. As small area XPS is important to the project we shall examine both cases, so we may be aware of the instrumental options available when constructing a multi-technique instrument. A comprehensive knowledge of the small area XPS may also help us to improve the system on the Hallam instrument.

2.3.2 X-ray Probe Methods

Several methods of generating an X-ray microprobe have been suggested (Seah and Smith 1988). Single or double aperture collomation of the X-ray source is possible but inefficient when applied to XPS. The application of reflecting optics by use of total internal reflection has been applied in x-ray microscopy, but again could not produce the required intensity at the desired spatial resolution.

One method of focussing an X-ray beam is to use the reflecting and diffracting properties of the crystal monochromator (Chaney 1987). The crystal monchromator is primarily used as a means of generating an X-ray beam of characteristic line width <0.4eV, which is free from satellite peaks and Bremsstrahlung radiation. A crystal monochromator uses a quartz crystal to disperse the X-ray energies by diffraction as predicted by the Bragg equation.

$$n\lambda = 2d \cdot \sin\theta$$

Equation 2.3.1

The anode, crystal and specimen are all arranged to lie on the circumference of the Rowland circle. Al-kα characteristic radiation conveniently diffracts from the 1010 plane of α-quartz crystal. This type of crystal can be grown to large sizes and machined into the required geometry. The size of the footprint is

about 0.05% the diameter of the circle, so it is obvious that the monochromator can provide a route to small area XPS.

Chaney (1987) demonstrated that with careful design a probe size of 100μm could be attained. Figure 2.3.1 shows the type of arrangement used, which has been commercially exploited by Fisons in the form of the S-Probe. An x-y stepper motor is used to scan the sample across the beam to provide imaging capability.

The diameter of the x-ray beam on the sample is dependent on the size of the x-ray source spot, which will be the same size of the electron beam incident on the x-ray source material. The electron beam can be focused to a sub-micron diameter, but must be of sufficient beam current to provide a useful x-ray flux. Furthermore, the thermal loading produced by the electron beam on the material must not be excessive. Larson and Palmberg (1994) claim anode thermal loadings of $80kWmm^{-2}$ and $1.2kWmm^{-2}$ in spot diameters of 4μm and 250μm respectfully.

The small x-ray spot will be magnified by the crystal and be subject to chromatic, aperture and diffraction aberration. Larson and Palmberg (1994) used a quartz crystal cut parallel to the 1010 plane and bent elliptically to cause non linear spacing of the lattice planes. This was to compensate for the aperture aberration, and an x-ray beam diameter of 10μm on the sample was achieved. Although the monochromated small spot produced by the aforementioned methods is of low intensity, the resultant spectra are of higher energy resolution and have a higher signal to noise ratio.

Figure 2.3.1 Small x-ray probe generation using a monchromator (Watts 1994b).

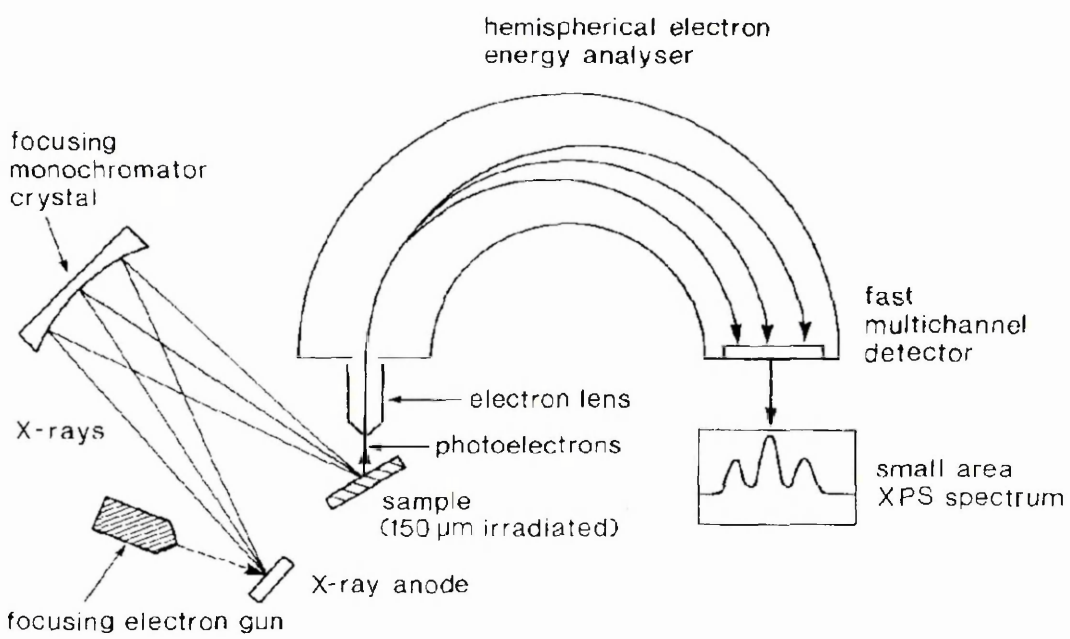

A number of researchers have used Fresnel zone plates to produce a small diameter x-ray beam, utilising synchrotron radiation sources to provide the intense x-rays need for this technique. The first of this type of instrument (Ade et al 1990) used a spherical monochromator followed by a focussing zone plate to produce a spot diameter of 0.3μm. The sample is mechanically scanned across the beam allowing the formation of images from photoelectrons detected by a single pass cylindrical mirror analyser, or a more complete spectroscopic examination of a selected area of the sample. It is stated that x-rays between 400 and 800eV may be focussed by the zone plate system, with 670eV radiation used for the example given in the paper, which we presume is the condition for optimum resolution. The problem presented by this is that electrons with binding energy higher than 670eV (plus the work function) will not be ionised, ruling out a significant part of the XPS spectrum. The obvious disadvantage of this type of system is the need for a synchrotron radiation source, which would be prohibitively expensive and impractical for the purpose of XPS alone.

2.3.3. Electro-Optical Methods.

The simplest method of modifying the collection optics to obtain spatially resolved XPS data is to utilise an area restricting aperture (Yates and West 1983). By selecting a small analyser entrance aperture and configuring the transfer lens to magnify the area of analysis on the sample onto the analyser entrance aperture, small area XPS in the range 10^2-10^3μm analysis spot diameter was achieved. The system is shown in Figure 2.3.2.

Figure 2.3.2. Small area XPS using a Limiting Area Aperture (Yates and West 1983).

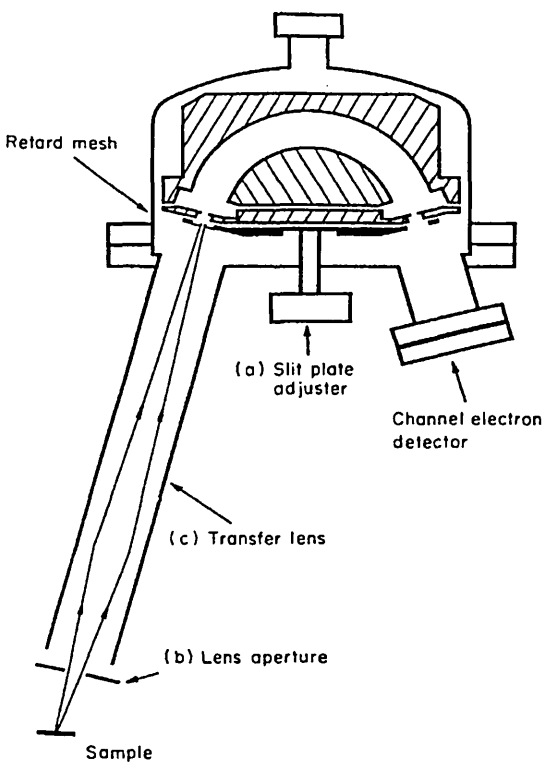

The procedure was carried out on a multi-technique instrument equipped with a scanning electron gun for Auger analysis. The XPS small spot was spatially aligned using the scanning electron gun as an internal reference. The sample was moved manually to locate the sample area of interest at the small area XPS position.

Figure 2.3.3. Imaging XPS using a pre-lens scanning system. Known as the sequential pixel by pixel method of generating an image (Watts 1994b).

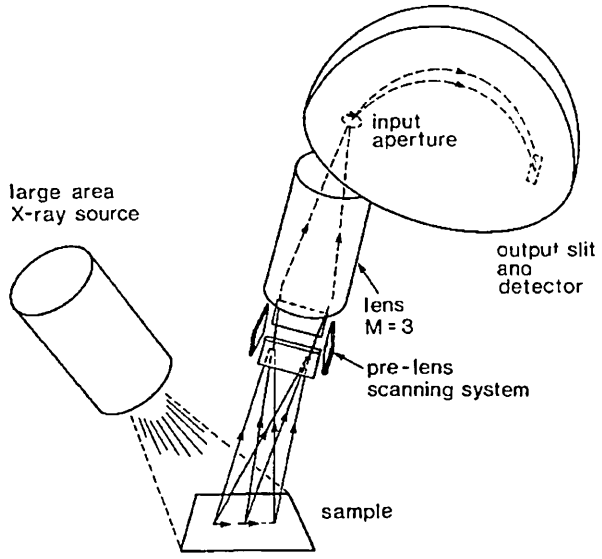

To adapt this system to an imaging system deflection plates were placed between the sample and the lens. By applying voltages to these plates the area selected by the entrance aperture can be scanned across the surface of the sample, and has been implemented on the VG Escalab 2 (Seah and Smith 1988). This type of system may be thought of as an electron microscope in reverse and is commonly known as a virtual microprobe. Figure 2.3.3 shows the pre-lens scanning system. The virtual microprobe can be scanned across the sample surface and the intensity at the detector synchronously monitored to form an image of the distribution of an element or of a particular chemical state. It is also possible to apply point spectroscopy to an area of interest after an image has been acquired.

To further understand how this type of system may be improved upon we must consider the optics. If we examine the system illustrated in Figure 2.3.3, we have a situation where the limiting field aperture is the analyser entrance aperture. If the lens has a magnification M, and the analyser entrance aperture is of width D, then the width of the area of the sample s which can be seen by the analyser is given by

$$s = \frac{D}{M}$$

Equation 2.3.2

Equation 2.3.2 gives the impression that increasing the magnification and thus reducing the analysis area will reduce the detected intensity, but the transmission of the instrument is further limited by the angular acceptance of the analyser. This shall be expressed by the semi-angle of the beam accepted in the dispersive and non dispersive direction as α_s and β_s respectively by the expressions

$$\alpha_s = \frac{M\alpha_o}{R^{1/2}}$$

Equation 2.3.3

and

$$\beta_s = \frac{M\beta_o}{R^{1/2}}$$

Equation 2.3.4

where α_0 and β_0 are the limiting half angles and R is the retarding ratio of the lenses.

The intensity of the transmitted photo electrons is given by the proportionality (Seah and Smith 1988)

$$I \propto \frac{\pi}{4}\left(\frac{D}{M}\right)^2 \alpha_s \beta_s$$

Equation 2.3.5

so if we substitute Equations 2.3.3 and 2.3.4 into Equation 2.3.5 we obtain

$$I \propto \frac{\pi}{4}\frac{D^2}{R}\alpha_0 \beta_0$$

Equation 2.3.6

Hence, the intensity is independent of the magnification, which must be increased if the spatial resolution of the system is to be increased.

Two factors can restrict the implementation of this. Firstly, for XPS it is necessary for the input lens to retard the photoelectrons to the analyser pass energy. If we inspect Equation 2.3.5 it is clear that the need for a sensible retardation ratio will limit the magnification achievable using the input lens. This may be overcome by decoupling the input lens from the probe forming lens.

Secondly, electrostatic lenses suffer from large spherical aberrations (Harting and Reed 1976) which will limit the spatial resolution. These aberrations will increase as the magnification of the probe forming lens is increased.

In order to increase the magnification of the input lens without introducing large aberrations a radical new design was required. This was provided by Walker (1991) in the form of a single pole piece magnetic lens (Mulvey 1982). Although there was initial hesitancy in introducing a magnetic lens into an XPS instrument, the fact that the lens structure is well clear of the sample (≈15mm) gave the idea practical credibility, as the lens could reside outside the vacuum. Figure 2.3.4 shows how the lens is incorporated into the instrument. The system shown in Figure 2.3.4 is the system which is used on the Hallam instrument.

Figure 2.3.4. Incorporation of the magnetic lens in the Axis-165 (Drummond 1996).

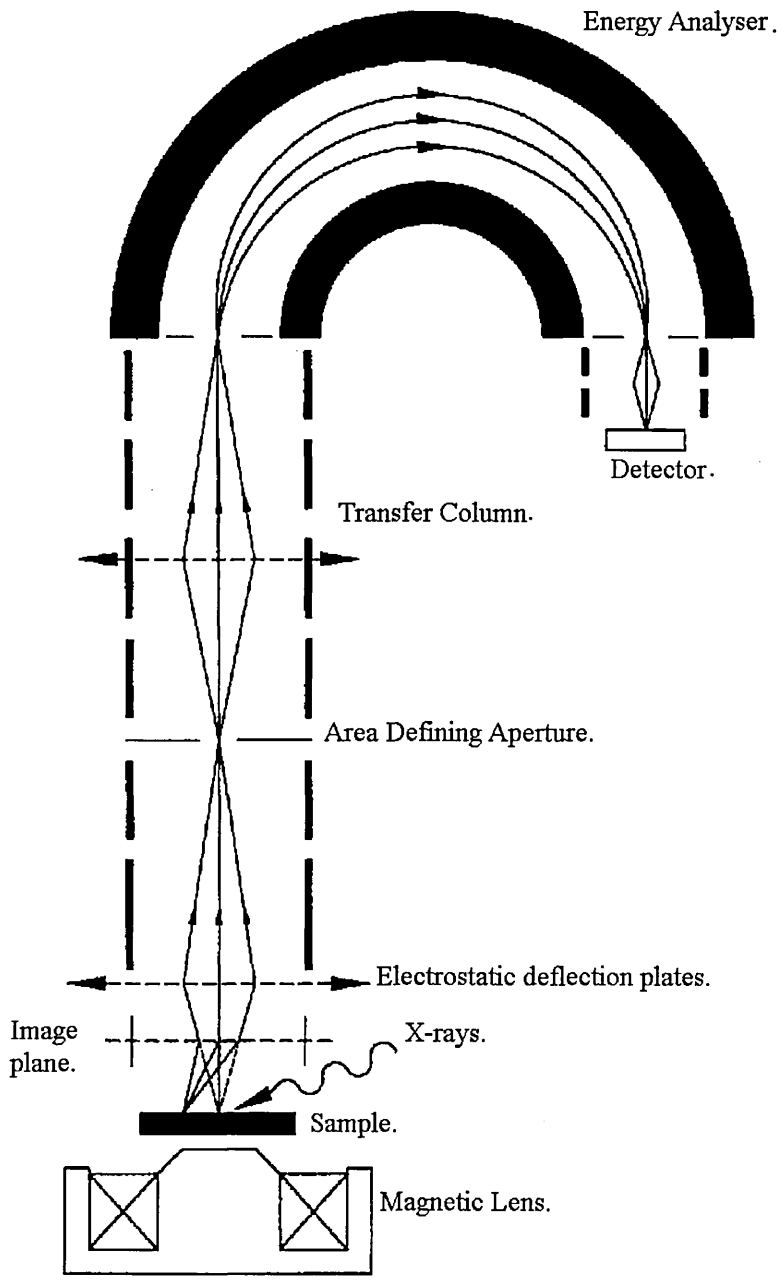

As the magnetic lens is central to part of the work carried out in this thesis, we shall consider the magnetic lens imaging system in more detail.

2.3.4 Single pole piece magnetic lens.

In general, the smallest aberrations are obtained when lenses are operated in an objective mode where the specimen is immersed in the imaging field. This is the case with the single pole piece lens, otherwise known as the magnetic immersion or "Snorkel" lens. Compared with other (electrostatic) lens systems in use in other (imaging) XPS instruments, its spherical aberration is at least two orders of magnitude smaller. The schematic of Figure 2.3.5 shows the lens operating in standard mode, projecting its imaging field remote from its mechanical structure. This is not the case for conventional magnetic lenses, and so the snorkel lens exhibits a clear advantage for surface analysis because the sample may be supported some distance away from the lens, thus providing a clear line of sight for excitation sources. This is particularly important for high performance sources which in general must be placed close to a specimen for optimum specifications.

Figure 2.3.5 Focussing of the magnetic lens.

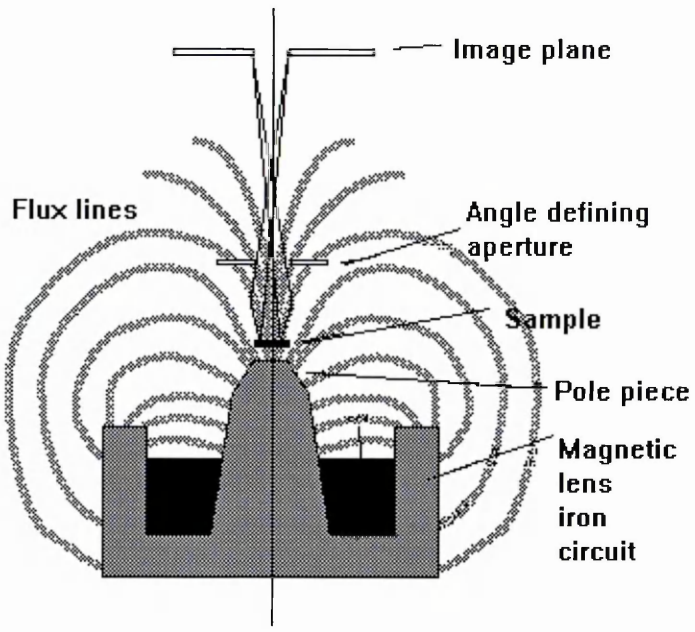

In detail the snorkel lens consists of an iron circuit with a gap through which extends an iron snout (pole piece). A water cooled solenoid energises the iron circuit to produce an intense magnetic field between the pole face and the outer body of the lens.

The properties of the snorkel immersion lens may be expressed in terms of the excitation parameter

$$\frac{(NI)}{\sqrt{V}} \qquad \text{Equation 2.3.7}$$

where N is the number of turns in the lens solenoid, I is the current through the solenoid and V is the kinetic energy of the focused electrons. For a given lens pole piece geometry the coil excitation cannot be substantially increased beyond that at which saturation of the lens iron circuit becomes apparent. When iron saturation occurs, the lens iron circuit becomes less efficient at containing the magnetic flux resulting in a loss of the desired optical properties of the lens. However, for optimum optical performance the flux density at the snout must be a maximum, usually limited by the iron saturation value. In practice this is achieved by shaping the pole piece to a specially tapered geometry which ensures that the field in the iron circuit is less than that at the pole face.

All electron optical lenses have aberrations which limit the minimum area which can be clearly defined in the lens object plane (Grivet 1972, Zworykin 1945). The effects of these lens aberrations may be controlled to an acceptable degree by limiting the collection angle of the lens. Reducing the collection angle will also reduce the sensitivity of the detection system introducing signal to noise ratio as another practical limit on minimum area. A selected area diameter may be defined as:

$$D_{sa}^2 = d_g^2 + d_s^2 + d_c^2 + d_a^2 + d_d^2$$

Equation 2.3.8

Term d_g is the Gaussian selected area diameter and is given by:

$$d_g = \frac{D}{M}$$

Equation 2.3.9

Where M is the magnification, and D is the diameter of the selected area aperture diameter. The second term, d_s, is the diameter of the disc of least confusion caused by spherical aberration of the lens. This is expressed as:

$$d_s = C_s f \alpha^3$$

Equation 2.3.10

where C_s is a constant characteristic of lens, and α is the semi collection angle of the lens controlled by an iris in the lens back focal plane, and f is the focal length. The third term d_c is the contribution from the chromatic aberration of the lens. This may be expressed as:

$$d_c = C_c \frac{\partial E}{E} f \alpha$$

Equation 2.3.11

where C_c is a constant characteristic of the lens, dE is the analyser energy resolution and E is the kinetic energy of the detected photoelectron. Ripple on the lens power supplies can also increase the d_c term.

The fourth term d_a is due to the lens astigmatism and its magnitude depends on the choice of materials, the quality of manufacture of the lens and the alignment of the lens components with respect to the electron optical axis of the instrument (Haine 1961). Contamination of lens components by insulating films and the influence of stray magnetic fields can also cause astigmatism. The final term d_d , is the effect of diffraction caused by the finite aperture of the lens and may be expressed as:

$$d_d = 0.61\left(\frac{\lambda}{\alpha}\right)$$

Equation 2.3.12

where λ is the effective wavelength of the detected photoelectron. Of the above terms, chromatic aberration is less significant than spherical aberration. Lens astigmatism can be reduced to negligible proportions by good design and manufacture, and the effect of diffraction is negligible for the spatial resolutions achievable by XPS. Hence the expression for a selected area diameter becomes

$$D_{sa}^2 = d_g^2 + d_s^2 + d_c^2$$

Equation 2.3.13

The selected area diameter can be characterised further by

$$I = 2.5\beta dE \times d_g^2\alpha^2$$

Equation 2.3.14

where I is the detected intensity in counts per second and βdE is the brightness of the emitted photoelectrons from a particular transition with energies between E and $E+\delta E$ illuminated by a certain x-ray flux. Clearly the value of brightness will depend upon the instrument design and the manner in which it is operated. A typical value for the silver 3d photoelectron peak using MgKα excitation at 450W would be

$$\beta dE = 10 \text{ cps/cm}^2\text{/rad}^2\text{/volt}$$

The value to which d_g can be set (by setting the value of the area selecting aperture) is limited by Equation 2.3.2. If the detected intensity, I, becomes prohibitively low, the signal becomes buried by the noise. This is the factor which limits the spatial resolution of the Kratos Axis-165 to 30μm.

2.3.5. Alternative methods.

The previously mentioned methods of using electron optics to obtain spatial sensitivity have all used an aperture to limit the area of analysis. Gurker et al (1983) proposed a different method, taking advantage of the dispersive characteristics of the hemispherical analyser. Instead of using an aperture to define the area of analysis they used a narrow slit which is geometrically fixed to lie parallel to the energy dispersive plane of the analyser. A pre analyser magnification of one is used, and post analyser detection is accomplished by microchannel plates followed by a phosphor screen and a TV camera. Figure 2.3.6 shows the analyser arrangement and Figure 2.3.7 shows the image recorded by the TV camera.

Figure 2.3.6 Dispersion within the analyser (Gurker et al 1983).

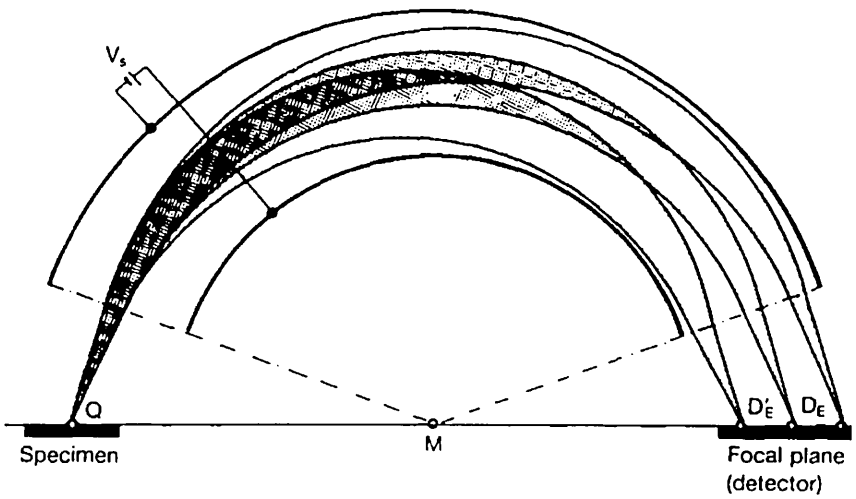

Figure 2.3.7 Detector image where the information along y_D relates to y_s (Gurker et al 1983).

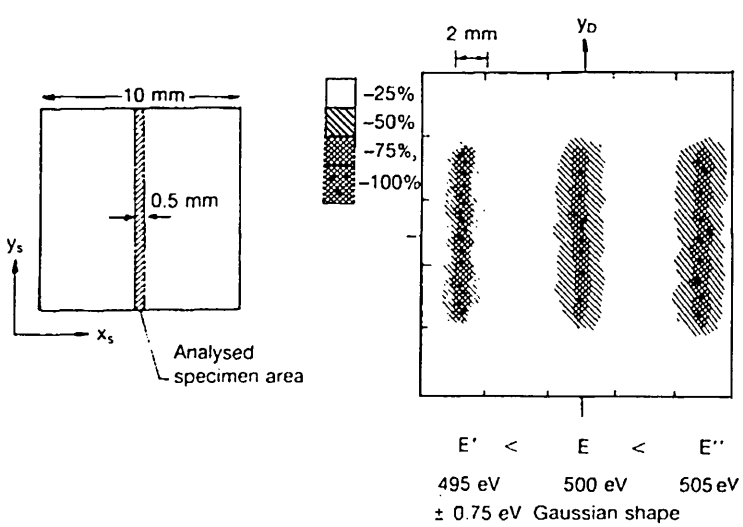

In one plane of the recorded image we have energy specific information along the direction parallel to the entry slit. The spatial resolution in this direction was 100μm. If one is interested in a given photoelectron species and wants to know its intensity distribution along the analysed line shaped specimen area, the sphere voltage V_s has to be adjusted so that the selected energy band lies within the detector area width x_D. Gurker suggested this method could be extended to produce X-Y images with intensity variations of photoelectrons of specific energy. By mechanically scanning the sample along the energy dispersive plane and recording the E-x image at each scan increment the collected information may be decoded to produce an X-Y image at an energy chosen from those in the recorded energy band.

Gurker's method of obtaining spatial sensitivity has been commercially exploited on the Scienta Esca 300 spectrometer. On this instrument the photoelectron image of the sample is magnified by an Einzel lens (Gelius et al 1990), producing a final resolution of 23μm along the slit direction. The excitation source on this instrument is a highly efficient monochromator, producing an elliptical spot. It is subsequently necessary to include deflection plates above the magnifying lens to align the illuminated sample area with the analyser electron-optical axis. The early models of this instrument did not incorporate imaging, but the equivalent instrument now has this capability, probably due to the falling cost and rising performance of the computation required.

The final method to be reviewed approached the problem in a completely different manner, producing an X-Y image at a specific photoelectron energy in real time. The principle of operation is described by Coxon et al (1990) and relies on the fact that although much positional information present when the photoelectrons arrive at the hemispherical analyser entrance aperture, it is lost during energy dispersion, the angular information is retained during electron transmission through the analyser. A diagram of this type of instrument is shown in Figure 2.3.8.

Figure 2.3.8 Parallel imaging XPS system (Coxon et al 1990).

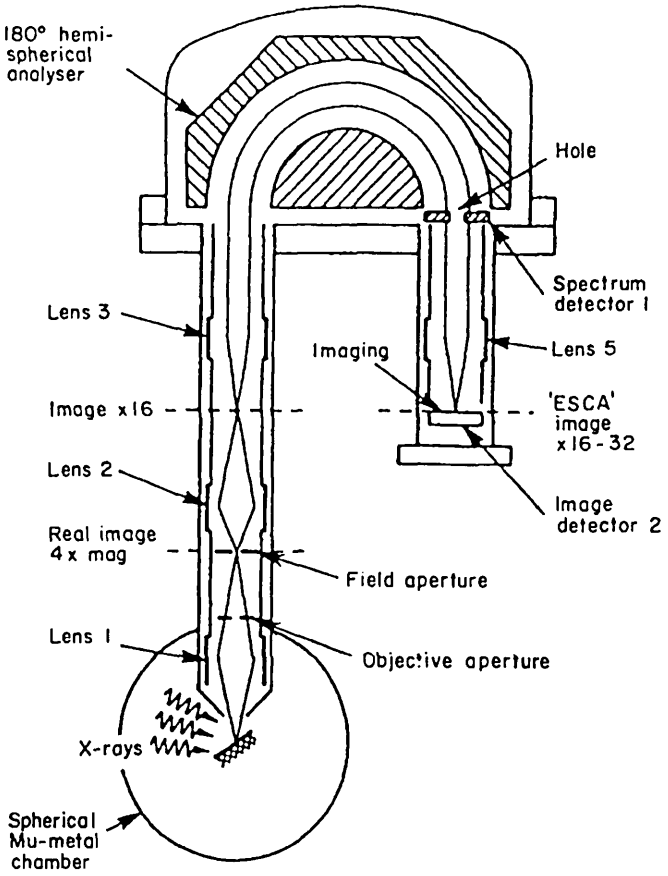

A lens is inserted just before the analyser to convert X-Y information to angular information. and a complementary device at the output stage which re-assembles the energy filtered X-Y image from the angular information. An image resolution of 5μm is attainable using this technique (Coxon et al 1990).

The lenses shown as 3 and 5 use quasi-Fourier transform optics to carry out the conversions. For spectroscopy the area of interest must be mechanically aligned with the electron optical axis and a limiting area aperture introduced. Spectroscopy is then carried out conventionally, as described earlier.

2.3.6 Discussion of various techniques.

The methods which utilise a small x-ray probe, excluding those requiring synchrotron radiation, are limited in spatial resolution by x-ray optics. The methods using post sample electron optics all have specific advantages. The sequential pixel by pixel method using the magnetic immersion lens (the method used on the Hallam instrument) has the advantage of simplicity of the virtual probe. From an image generated by scanning the probe, small area XPS may be carried out with the same electro-optical conditions used for the reference image generation. Also the use of deflection plates for scanning eliminates the need for in vacuum mechanical scanning devices. This method does, however, have the disadvantage of inefficiency, as much information is lost due to the insertion of the aperture. As this is

the method used on the Hallam instrument it is clear that the XPS spatial resolution cannot be improved beyond 30μm.

The E-x method using the entrance slit is less wasteful. The problems here are due to difficulties in generating spectra and images from the E-x maps, although with the increasing speed and capacity of digital hardware, the problem is becoming less significant. Indeed, the combination of this technique with the magnetic lens for initial magnification would, in the authors view, produce the optimum small area XPS system.

The real time imaging system which is implemented on the Scienta Escascope produces images rapidly and with high spatial resolution. Unfortunately XPS images alone do not necessarily provide meaningful surface information, as they are influenced by secondary scattered electrons. To utilise these images small area XPS must be performed on the area of interest. On the ESCASCOPE this requires the use of the electron optics in a conventional manner, so the spectrum is recorded under a different regime to that of the reference image. In this case careful calibration between the two modes of operation must be performed.

2.4 Thickness Determination By Electron Probe X-ray Analysis.

2.4.1 Introduction

In the following section we shall study the development of thickness determination techniques by x-ray analysis in the electron microscope. The techniques are applicable to both wave dispersive and energy dispersive analysis (WDA and EDA), but greater accuracy is expected with WDA. The use of electron probe microanalysis to determine the thickness of a thin surface layer on a solid substrate has been exploited since the establishment of a linear relationship between layer thickness and the k-ratio parameter. The k-ratio is defined as the x-ray intensity from the film to that from a solid sample of the same element. Early procedures for surface film measurements used empirical calibration of intensity versus thickness (Sweeny et al 1960, Cocket and Davis 1963). To appreciate the development of successive methods we must first understand the generation of characteristic x-rays in a sample irradiated by an electron beam.

2.4.2 The Depth Distribution Function $\phi(\rho z)$

X-rays are produced from the surface of the sample down to the maximum depth penetrated by incident electrons before their energy falls below the critical excitation energy E_c of the of the characteristic x-ray line under investigation. Quantitative EPMA analysis requires the calculation of the absorption factor (as part of the ZAF procedure). For that purpose the production of x-rays as a function of depth must be established. The depth distribution function $\phi(\rho z)$ represents the x-ray intensity per unit mass depth (ρz) relative to that produced in an isolated thin layer. A typical graph of the function $\phi(\rho z)$ is shown in Figure 2.4.1.

Figure 2.4.1. The $\phi(\rho z)$ curve showing the x-ray intensity from surface layer of thickness Δz given by shaded area.

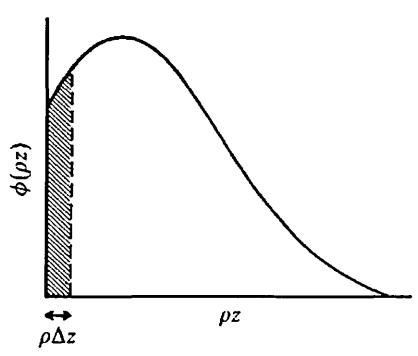

At the surface of the sample, x-ray emission is enhanced by electrons back-scattered from the bulk of the sample. Hence, the value at the surface, ϕ_0, known as the surface ionisation, is greater than 1. Initially, an increase in x-ray production is observed, as the mean path length of the incident electrons is increased in this region due to scattering. After passing through a maximum, $\phi(\rho z)$ decreases due to scattering and the deceleration of electrons, finally falling to zero.

For the purpose of EPMA quantification, much work has been focused on the determination of the $\phi(\rho z)$ function. The function will vary with the electron beam operating voltage, the material under irradiation, the characteristic x-ray line and the geometry of the electron beam/ detection system used. $\phi(\rho z)$ models have been developed which contain expressions which are fitted to available data from 'Monte-Carlo' models and experimental intensity measurements on specimens of known composition. Philibert (1963) formulated the first model using exponential expressions to represent the curve. This model contained many assumptions, mainly that the value of ϕ_0 is equal to zero. Additional work was carried out using rectilinear models (Bishop(1974), Love et al (1984)) and Gaussian models (Packwood and Brown (1981)),but the model which is of particular relevance to thin film analysis is the parabolic (PAP) model of Pouchou and Pichoir (1986, 1987). The $\phi(\rho z)$ curve is represented by two parabolic functions $\phi_1(\rho z)$ and $\phi_2(\rho z)$ as shown in Figure 2.4.2.

Figure 2.4.2. Parabolic model for $\phi(\rho z)$. (Pouchou and Pichoir 1991)

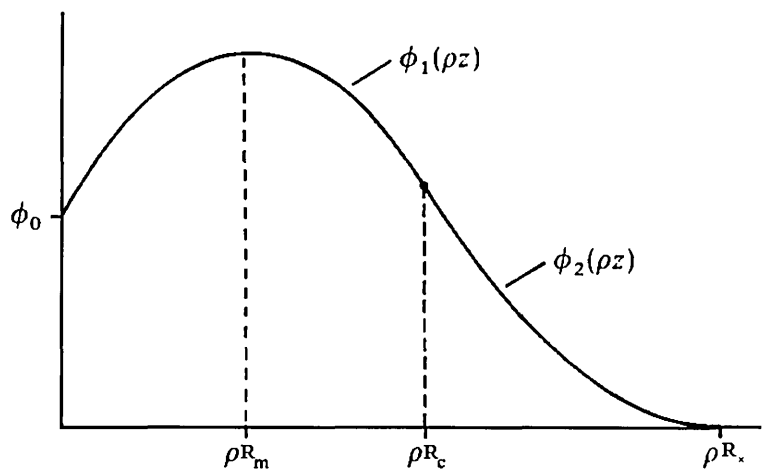

The parabolics $\phi_1(\rho z)$ and $\phi_2(\rho z)$ must be equal in value and slope at a certain mass depth level R_c. The primary condition imposed on the curve is that the area under the curve must be equal to the value F. The value F is defined by the equation $I=Q(E_0)F$ where I is the calculated generated x-ray intensity

(including backscatter corrections) and $Q(E_0)$ is the ionisation cross-section for the primary beam energy E_0.

The constraints which dictate the shape of the curve are :-

- a certain value of ϕ_0 must be obtained at the surface.
- the maximum must appear at a certain value R_m.
- the function must fall to zero with a horizontal tangent at the range of ionisation R_x.

Given these conditions the $\phi(\rho z)$ curve may be expressed by:

-from $\rho z = 0$ to $\rho z = R$ $\quad \phi_1(\rho z)=A_1.(\rho z-R_m)^2+B_1$

-from $\rho z = R$ to $\rho z = R_c$ $\quad \phi_2(\rho z)=A_2.(\rho z-R_x)^2$

where A_1, A_2, and B_1 are coefficients.

Recalling the condition imposed at R_c eventually leads to the coefficients of the parabolic branches:

$A_1=\phi_0/\{R_m.[R_c-R_x.(R_c/R_m-1)]\}$

$B_1=\phi_0-A_1.R_m^2$

$A_2=A_1.(R_c-R_m)/(R_c-R_x)$

A full description of the model, its origins, and its application to quantification is given by Pouchou and Pichoir (1991).

2.4.3. Application to thickness determination.

If we assume that a thin film is composed of a pure element on a solid substrate, then the x-ray intensity generated within the film is given by the integrated area of $\phi(\rho z)$ from the surface to a depth equal to the film thickness. The ratio of the intensity from the film to that from a solid sample of the same element (after correcting for absorption) is equal to the ratio of the area just defined to that of the whole $\phi(\rho z)$ curve. This can be expressed by

$$\frac{\int_t^0 \phi(\rho z)}{\int_{R_x}^0 \phi(\rho z)} = \frac{I_{Film}}{I_{Ref}}$$

Equation 2.4.1.

where t is the thickness of the film, I_{Film} is the corrected intensity from the film, and I_{Ref} is the corrected intensity from the bulk reference standard. Thus, if $\phi(\rho z)$ is of an easily integral form, then this may be evaluated and the thickness term t eventually determined. Obviously the units of t would be mass thickness (conventionally $\mu g/cm^2$), so division by an assumed value of density is necessary to get a true value of thickness. Clearly, this would present a problem for films of more than one element which were inhomogeneous with depth.

Early attempts using this principle relied on the Philibert models (Philibert and Pernot (1966), Reuter (1972)), which carried the inherent disadvantages of the Philbert model. Consequently Pouchou and Pouchoir (1985) applied the parabolic model to the measurement of thin films. A problem encountered is the fact that the distribution $\phi(\rho z)$ in a film would be different to the distribution $*\phi(\rho z)$ in a bulk standard, especially if the surface film is that of a light element and the substrate is that of a heavy element. As described earlier the parameters affecting $\phi(\rho z)$ are R_m, R_x, ϕ_0 and the area under the curve F, which will all differ due to substrate effects. To calculate the modified values of these parameters, initial estimates are varied according to weighting laws, and an iterative procedure followed until a converging solution is obtained.

Pouchou and Pichoir (1991) also claim that the PAP model is applicable to problems where both composition of a multi-element film and its thickness are unknown. It is argued that, as the model can be used to calculate the concentration of a film of N elements alone, analysis of N-1 elements is sufficient to derive the concentration, as the final elemental concentration can be deduced by subtraction. It is then claimed that analysis of all N elements would provide both thickness and concentration, as the Nth element can be used to provide the thickness information. Although no examples are given of results obtained using this procedure, examples are provided of analysis of multi-element coatings at various values of incident electron beam energy. This approach has been applied to a double layer of Al/Cu on aluminium before and after diffusion (Pouchou and Pichoir, 1984) and for layers of Ga-As on glass. If we consider a simple case of elements A/B on substrate C, then determination of both film thickness and concentration of A can be achieved by the measurement of X-ray intensity at two different beam energies. A measurement is required at high beam energy such that R_x will be larger than the mass thickness, which will provide information regarding the thickness, and a measurement at low tension where R_x is approximately equal to the mass thickness, which will give an indication of composition. In a more complex system characterisation is then possible by measuring at several beam energies and trying to reproduce the results by forming reasonable hypotheses about the structure of the sample. Graphical comparison of the relative intensities and the $\phi(\rho z)$ distribution curves at various energies allow various hypotheses to be evaluated.

The use of measurements taken at several beam energies can also be used to increase the accuracy of thickness measurements alone. This has been implemented in the LayerF computer program produced by Pouchou and Pichoir (1991), although it is not clear how the algorithm does this. Work carried out

by Moller et al (1995) , in which thickness determination of copper films on silicon was carried out by Rutherford Back Scattering and by EPMA demonstrates this. Thicknesses in the range of 100-450nm were measured at 6, 8, 10, 15, 20, 25, 29,and 30KV. EPMA thickness estimates from single measurement had a typical accuracy of 5%, whereas a thickness estimate which used all the measurements had an accuracy in the range of 0.5-2%.

2.4.4. Alternative methods.

The methods previously described for obtaining thickness and compositional information of thin films have all been based on generating an accurate model of the $\phi(\rho z)$ distribution curve for the sample from the data available. Another technique has, however, been developed and was first described by Cazaux et al (1988). Cazaux stated the three requirements when analysing surface layers as :-

- The determination of the surface layer composition.
- To determine the composition in terms of stratification.
- To evaluate the thickness and the lateral thickness change.

It was proposed that the determination of composition could be achieved conventionally at a fixed beam energy E_0 using ZAF corrections. To obtain the composition in terms of stratification the characteristic signal intensity change as a function of E_0 was monitored. This uses the threshold energy (the beam energy at which the characteristic line signal intensity becomes apparent) to give an indication of stratification and thickness of overlayers. Although the paper claims that thickness determination is possible using the technique, its most appropriate application is to determine whether a sample is a compound AB or a stratified material A/B or B/A.

To address the third requirement, that of lateral thickness variation, Cazaux proposed an expression similar to that used in Auger analysis. When the range of incident electrons, R, is far greater than the thickness of the overlayer, t, the corresponding signal intensity is given by

$$I_X^A = I_0 \cdot \sigma(1 + R_X)t$$

Equation 2.4.2.

where I_0 is the incident beam current, σ is the ionisation cross section and R_X is the backscatter factor.

Essentially, Equation 2.4.2, which neglects many relevant terms, indicates that for appropriate values of E_0, where the penetration deprth r>>t, the intensity of the signal from the film is proportional to the thickness. Using this relation, EDX maps may be used to represent thickness laterally. The absolute thickness value may be evaluated either by referring to a specimen of calibrated thickness, or by

determining the values of σ and R_X of Equation 2.4.2. As no application of this proposed technique is given, the potential accuracy is unknown.

This approach was later refined by Cazaux et al (1990). Equation 2.4.2 was expanded to include all the relevant parameters, so the characteristic intensity from a film containing element A was given by

$$I_X^A = I_0 N^0 \sigma_A r \omega_{ij} T C_A t$$

Equation 2.4.3.

where N^0 is the atomic density, ω_{ij} is the fluorescence yield, T is the efficiency of the x-ray detector, C_A is the atomic concentration of A and r is a combined correction factor due to backscattering and fluorescence from the substrate. The justification behind using procedures similar to Auger is that both Auger and X-ray emission are the results of complementary de-excitation processes following the core ionisation of an atom.

The linear relationship $I \propto t$ was experimentally investigated by studying various thicknesses of Al on Si, and concluded that the linearity was valid while $t<R/6$. Within this range thickness measurements of Al films on Si substrates were performed, using a reference sample of 42nm and applying the relationship

$$\frac{I_s}{I_r} = \frac{t_s}{t_r}$$

Equation 2.4.4.

where I_s is the intensity from the sample, I_r is the intensity from the reference sample, t_s is the thickness of the sample and t_r is the thickness of the reference. The accuracy was found to be 5%. The technique was applied to mapping and scatter diagrams suggested as an effective image processing tool for stratified materials as this had been applied to scanning Auger images with success (El Gomati 1987).

A limitation of the thickness mapping technique is that local changes in substrate composition which will affect the backscatter coefficient, will be interpreted as thickness changes. This deficiency was later addressed by Benhayoune et al (1995). By biasing the sample at +50V and measuring the sample current, attempts were made to evaluate the backscatter coefficient. A correction was made for this and applied to each pixel in acquired images. Examples are shown of analysis on purpose-made samples of aluminium on a substrate which varied laterally between Cu and Au. The procedure reduced the error caused by substrate variation from 20% to 9%, which indicates that the formulas used in correction were of only partial success.

2.4.4. Techniques for specialist applications.

So far we have concentrated on studying a film by measuring characteristic x-rays from the film. In some cases this is not practical, for example, the energy of the carbon Kα line is 0.274keV, rendering measurement difficult. In such cases thickness determination may be performed by measuring the intensity from the substrate. This has been applied to diamond like coatings on silicon (Lemoine et al 1997).

Where the thickness measurement of an ultra thin metal is required (0-15nm) an alternative to x-ray analysis is to use backscattered electron detection. For ultra thin films it has been noted that the detected backscatter intensity is proportional to the film thickness (Sheng et al 1985). This technique may be applied to thickness mapping by use of a suitable reference.

2.4.5. Discussion.

It is clear that the various methods are applicable to different circumstances. Where absolute thickness is required one would prefer to use the method developed by Pouchou and Pichoir. Where spatial variations are to be studied the Cazaux approach may be more suitable, as the application of the Pouchou and Pichoir procedure at each pixel of a map would be time consuming. It was pointed out by Cazaux (1990) that absolute thickness calculation may be possible by determination of each term in Equation 2.4.3, but it is clear that this approach would not work for multilayered films where the Pouchou and Pichoir approach must be used. The Hallam instrument software may be used to generate thickness maps using the Pouchou and Pichoir method, which would be used where absolute thickness measurement was necessary. Where a rapid indication of film thickness was required, then the method proposed by Cazuax would be more appropriate.

To put the subject of thickness determination by energy dispersive analysis into perspective we may observe the work of Gaarenstroom (1997). The thickness of oxide films on Aluminium was measured using transmission electron microscopy, spectroscopic ellipsometry, WDA and EDA, infrared spectroscopy, x-ray photoelectron spectroscopy and x-ray fluorescence. The electron beam techniques WDA and EDA (using Pouchou and Pichoir procedures) produced the most accurate results (±2% and ±2.2% respectively). This indicates that thickness measurement by EDA may become increasingly important as the use of thin films becomes more widespread.

References for Chapter 2:

Ade H.W., Kirz J., Hulbert S.L., Johnson E.D., Anderson E., Kern, D. (1990) Applied Physics Letters Vol. 56, 1841-1843.

Benhayoune H., Jbara O., Thomas X. (1995) X-ray Spectrometry, Vol 24, 3, 147.

Benzton M.D. , Nielsen P.S. , Eskildsen S.S. (1993) Diamond and Related Materials, Vol. 2, 893.

Bishop H.E. (1974) Journal of Physic D 7,2009.

Blackmore J.S.(1985) In Solid State Physics 2nd Ed, Cambridge University Press, pg 196.

Carrazza J., Leon V., (1991) Surface and Interface Analysis, Vol. 17, 225-229.

Cazaux J. , Jbara O. , Mouze D. , Thomas X. (1988) Inst. Phys. Conf. Ser. No. 93, Vol. 2, 149.

Cazaux J. , Jbara O. , Thomas X. (1989) Inst. Phys. Conf. Ser. No. 98, Chapter 7, 323.

Cazaux J. , Jbara O. , Thomas X. (1990) Surface and Interface Analysis, Vol.15,567-581.

Chaney, R.L. (1987) Surface and Interface Analysis Vol. 10, 36-47.

Cockett G.H. , Davis C.D. (1963) British Journal of Applied Physics, Vol. 13, 813.

Coxon P., Krizek J., Humpherson M., Wardell I.R.M. (1990) J. Electron Spectrosc. Rel. Phenom. Vol. 52, 821-836.

Drummond I.W. (1992) Microscopy and Microanalysis Vol. 28, 29-32.

Drummond I.W. (1996) Phil. Trans. R. Soc. Lond. A Vol. 354, 2667-2682.

Ebel H., G.Zuba, Ebel M.F., (1983) Journal of Electron Spectroscopy and Related Phenomena, Vol. 31, 123-130.

El Gomati M.M., D.C. Peacock, M.Prutton, C.G. Walker, (1987) Journal of Microscopy, Vol 147, 149. Microanalysis ed. R.Castaing, P.Deschamps & J.Philibert (Paris:Hermann) p365.

Feldman L.C. and Mayer J.W. (1986) In Fundamentals of Surface and Thin Film Analysis, North-Holland, pg 243.

Gaarenstroom, S.S. (1997) Journal of Vacuum Science and Technology A, Vol. 15, 3, 470.

Gelius U., Wannberg B., Baltzer P., Fellner-Felegg H., Carlsson G., Larson J., Munger P., Vegefors G. (1990) J. Electron Spectrosc. Rel. Phenom. Vol. 52, 747-784.

Goldstein J.I., Newbury D.E., Echlin P., Joy D.C., Fiori C.E., Lifshin E., (1981) In Scanning Microscopy and X-ray Microanalysis, Newyork, Penum.

Grivet P., (1972) Electron Optics Part 2, Pergamon Press pg 583.

Gurker N., Ebel M.F., Ebel H., (1983) Surface and Interface Analysis Vol. 5, 13-19.

Haine M.E., (1961) The Electron Microscope, E. & F.N. Spon Ltd., pg 51.

Harting E. & Read F.H. (1976) Electrostatic lenses, Elsevier, Oxford.

Hemminger C.S., Land T.A, Christie A., Hemminger J.C., (1990) Surface and Interface Analysis, Vol. 15, g 323-327.

Larson P.E. & Palmberg, P.W. (1994) European Patent Application. Publication No. 0 590 308 A2, European Patent Office.

Lemoine P. , McLaughlin J. (1997) Inst. Phys. Conf. Ser. No. 153, Vol. 11, 585.

Loretto M.H. (1984) In Electron Beam Analysis of Materials, Chapman and Hall Ltd, pg 24.

Love G., Sewell D.A. & Scott V.D. (1984) Journal Physique Vol 45, coll.C2, 21.

Moller A. , Weinbruch S. , Stadermann F.J. , Ortner H.M. , Neubeck K. , Balogh A.G. , Hahn H. (1995) Mikrochimica Acta 119, 41-47.

Mulvey T. (1982) Magnetic Electron Lenses ed. P.W.Hawkes, (Berlin:Springer), 359-415.

Packwood R.H. & Brown J.D. (1981) X-ray Spectrometer. Vol 10,138.

Philibert J. & Penot D. (1966) Proceedings of the 4th International Congress on X-ray Optics

Philibert J. (1963) Proceedings of the 3rd International Congress on X-ray Optics & Microanalysis ed. H.H.Pattee, V.E.Cosslett & A. Engstrom (New York : Academic Press), p.379

Pouchou J.L. & Pichoir F. (1984) La Recherche Aerospatiale Vol 5, 47.

Pouchou J.L. & Pichoir F. (1985) J. Microsc. Spectrosc. Electr. Vol 10, 279.

Pouchou J.L. & Pichoir F. (1986) J. Microsc. Spectrosc. Electr. Vol 11, 229.

Pouchou J.L. & Pichoir F. (1987) Proceedings of the 11th International Congress on X-ray Optics & Microanalysis ed. J.D.Brown & R.H.Packwood (Ontario) p 249.

Pouchou J.L. & Pichoir F. (1991) In Electron Probe Quantitation, ed. K.F.J. Heinrich & D.E.Newbury (New York :Plenum) , p 31.

Reed S.J.B., (1993a) In Electron Probe Microanalysis 2nd Ed., Cambridge University Press, pg 292.

Reed S.J.B., (1993b) In Electron Probe Microanalysis 2nd Ed., Cambridge University Press, pg 169.

Reilman R.F., Msezane A., Manson S.T., (1976) Journal of Electron Spectroscopy and Related Phenomena, Vol. 8, 389.

Reuter W. (1972) Proceedings of the 6th International Congress on X-ray Optics & Microanalysis ed. G. Shinoda, K. Kohra, & T. Ichinikowa. (Tokyo: Tokyo Univ. Press) p 121.

Schofield J.H., (1976) Journal of Electron Spectroscopy and Related Phenomena , Vol. 8, 129-137.

Seah M.P. & Smith G.C. (1988) Surface and Interface Analysis Vol. 11, 69-79.

Seah M.P. , (1980) Surface And Interface Analysis, Vol.2, 222.

Seah M.P. , (1990a) In Practical Surface Analysis 2nd Ed. Vol.1 Auger and X-ray Photoelectron Spectroscopy, Edited by Briggs D., Seah M.P.John Wiley and Sons, pg 112.

Seah M.P. , (1990b) In Practical Surface Analysis 2nd Ed. Vol.1 Auger and X-ray Photoelectron Spectroscopy, Edited by Briggs D., Seah M.P.John Wiley and Sons, pg 75

Seah M.P. , (1990c) In Practical Surface Analysis 2nd Ed. Vol.1 Auger and X-ray Photoelectron Spectroscopy, Edited by Briggs D., Seah M.P., 222-255.

Seah M.P. and Anthony M.T, (1984)., Surface And Interface Analysis, Vol.6, 230.

Seah M.P.,Jones M.E., Anthony M.T, (1984)., Surface And Interface Analysis, Vol.6, 242.

Seah M.P., (1986) Vacuum,Vol. 36, 399.

Seah M.P., (1993) Surface and Interface Analysis, Vol. 20, 243-266.

Seah M.P., (1995) Journal of Electron Spectroscopy and Related Phenomena , Vol. 71, 191-204.

Seah M.P., Jones M.E., Anthony M.T., (1984) Surface and Interface Analysis, Vol. 6, 242.

Seah M.P., Smith G.C., (1990) Surface and Interface Analysis, Vol.15,751-766.

Sheng Q.A. , Munz P. , Schultheiss R. (1985) Phys. Stat. Sol. (a), Vol 92, 121

Sweeny W.E. , Seebold R.E. , Birks L.S. (1960) J. Appl. Phys., Vol. 31, 1061.

Wagner C.D., Davis L.E., Riggs W.M., (1980) Surface and Interface Analysis, Vol. 2, 53.

Wagner C.D., Davis L.E., Zeller M.V., Taylor J.A., Raymond R.H., Gale L.H., (1981) Surface and Interface Analysis, Vol. 3, 211-225.

Walker A.R. (1991) European Patent Application. Publication No. 0 243 060 B1, European Patent Office.

Watts J.F. (1994) In Surface Science Techniques Edited by Wall J.M. and Smith R., Pergomon Press, pg 5.

Watts J.F. (1994b) In Surface Science Techniques Edited by Wall J.M. and Smith R., Pergomon Press, pg 16.

Weng L.T., Vereecke G., Genet M.J., Bertrand P., Stone W.E.E., (1993) Surface and Interface Analysis, Vol. 20, 179-192.

Woodruff D.P. and Delchar T.A., (1994) In Modern Techniques of Surface Science, Cambridge University Press, pg 134.

Yates K. & West R.H. (1983) Surface and Interface Analysis Vol. 5, 217-221.

Zommer L., (1995) Vacuum, Vol. 46, 617-620.

Zworykin V.K., Morton G.A., Ramberg E.G., Hillier J., Vance A.W., (1945) Electron Optics and the Electron Microscope, John Wiley and Sons, pg 206.

Chapter 3 Instrumentation.

3.1 Introduction

Throughout this thesis it will be necessary to refer to the instrumentation used to carry out the experiments, for both surface analysis and electron microscopy. Because the system, which we shall refer to as the Hallam instrument, is of a unique configuration, it is necessary to explain how the system is configured, how it operates, and describe the components used. Since the thickness mapping by x-ray analysis is the unique part of the instrument, thickness measurements and maps shall be presented.

3.2 Overview

The Hallam instrument consists of the tools required for XPS, Small Area XPS, Scanning Small Area XPS, AES and Scanning AES, Secondary Electron Detection and Back Scattered Electron Detection. Figure 3.2.1 is a diagram of the basic components of the system.

Figure 3.2.1. The basic components of the Hallam instruments.

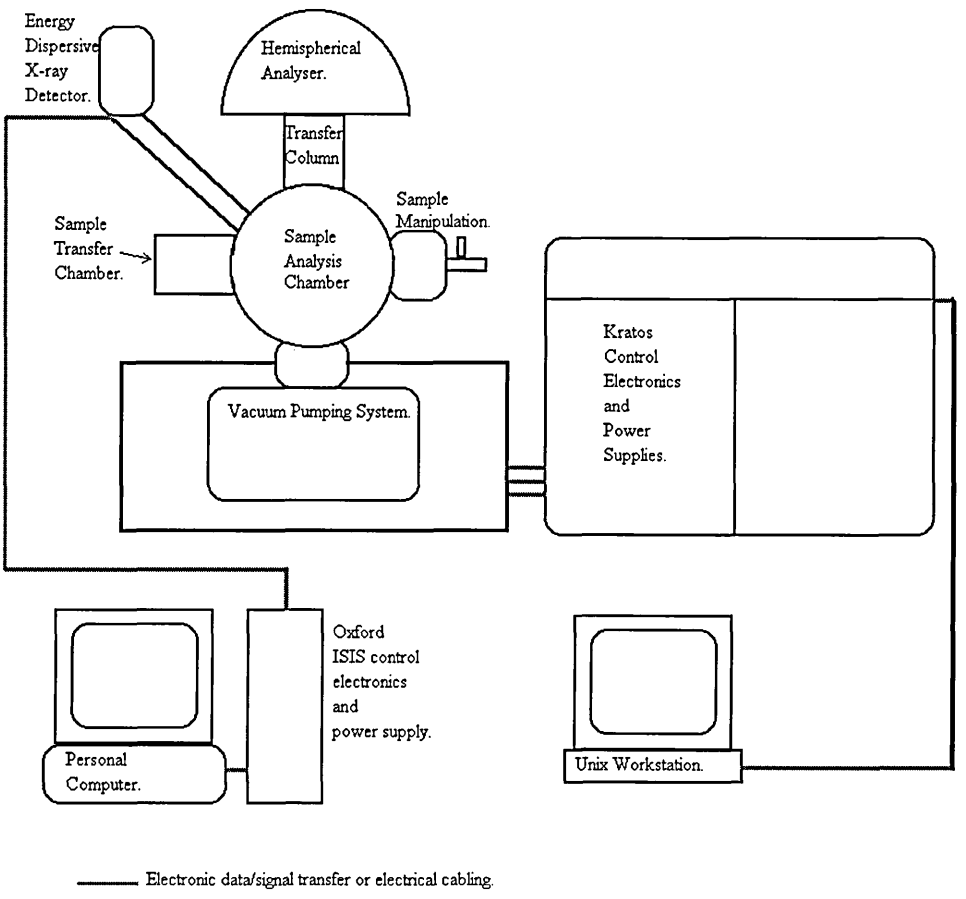

The Unix workstation is the interface through which the user controls the Kratos components of the system. This includes the vacuum pumping system and the power supplies for the excitation sources, detection devices and gauges. The Personal Computer is the user interface for the Oxford instruments components. Through the PC, the energy dispersive detector and the backscatter detector are operated. In Figure 3.2.1. the majority of the analysis tools which are present on the sample analysis chamber have been omitted for clarity. The sample analysis is the central part of the instrument and all tools which are attached to it are focused towards the centre of the chamber where the sample is placed during analysis. The UHV chamber is constructed from type 316 stainless steel and comprises of copper gasket sealed flanges. Figure 3.2.2 shows the chamber stripped of all attachments. The flanges are labelled so the geometry and location of the components may be described.

Figure 3.2.2. Diagrams of Sample Analysis Chamber.

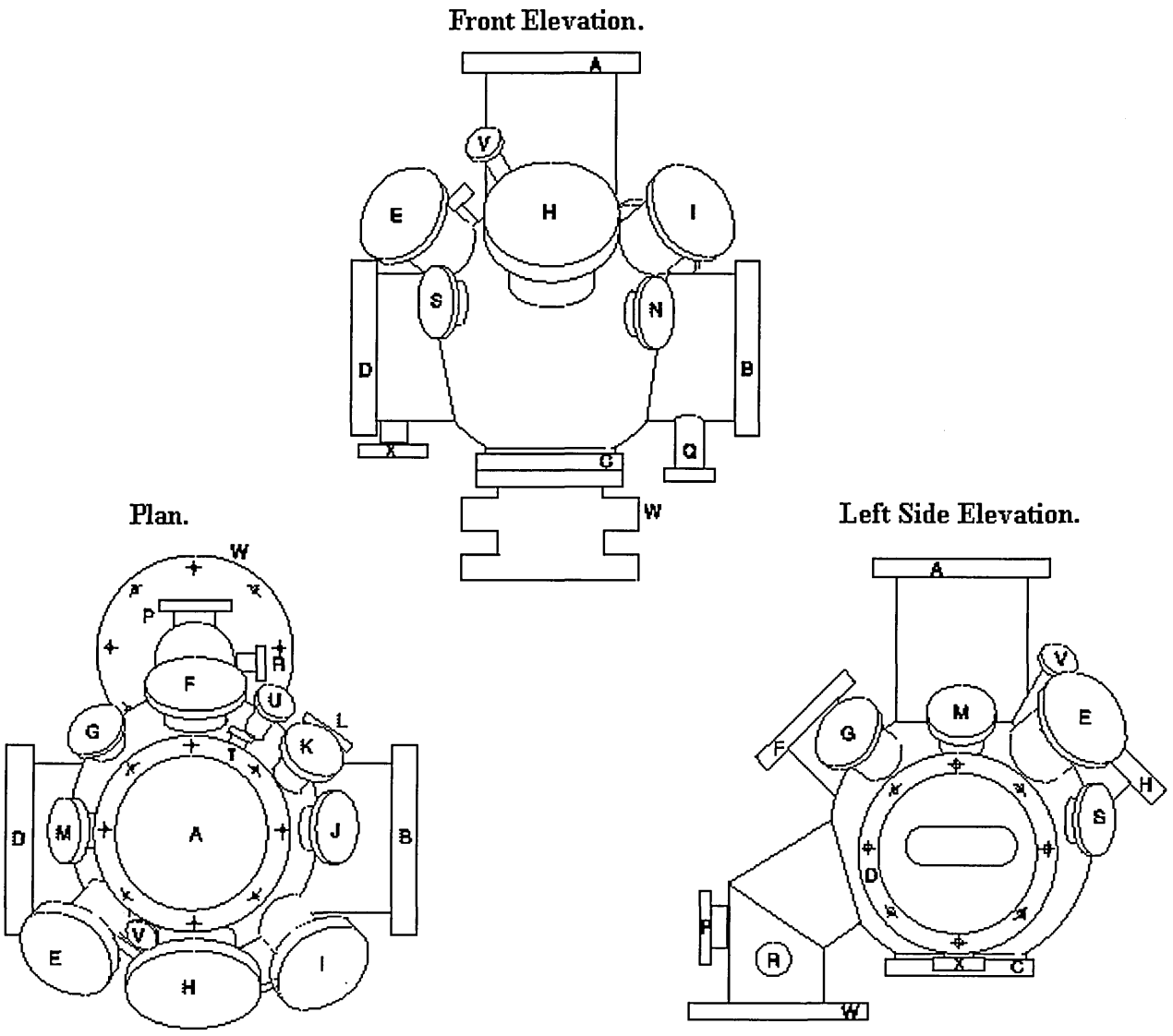

Table 3.2.1 List of components present on the SAC.

Port	Flange outer diameter (mm)	Elevation angle (Degrees)	Component type.
A	200	90	Transfer Column and Analyser.
B	200	0	Sample holder and X, Y, Z, θ manipulator.
C	150	-90	Magnetic lens housing.
D	200	0	Sample Transfer Chamber.
E	115	30	Energy Dispersive X-ray Detector.
F	115	25	Dual Anode X-ray source.
G	70	35	Viewport.
H	150	30	Electron gun.
I	115	35	Viewport.
J	70	40	Iris linear drive.
K	70	35	Viewport.
L	70	0	Blank.
M	70	40	Minibeam I ion gun.
N	70	0	Viewport.
P	70	0	Ion gauge.
Q	70	0	Blank.
R	35	0	Blank.
S	70	0	Secondary Electron Detector.
T	35	0	Aperture linear drive.
U	35	20	Chamber illumination window.
V	35	50	Blank.
W	200	-90	Ion pump.
X	70	-90	Gate valve liner drive.

3.3 UHV pumping system.

The vacuum system on the Hallam instrument provides an Ultra High Vacuum environment within the Sample Analysis Chamber (SAC). All components are supplied by Kratos as it is the same system used on the Axis –165. Figure 3.3.1 is a diagram of the pumping system. The first pumping stage of the system is an Edward's E2M5 rotary pump (Roughing pump). This can pump the whole system from atmosphere to approximately 10^{-3}Torr (Chambers et al 1989a). The gauge labelled P1 is a Pirani gauge and measures the rough pumping pressure. The rotary pump may be isolated using the backing valve labelled V3. The next pumping stage is the Balzers 240 turbomolecular pump. For this system the

ultimate pressure achievable using the turbo pump is approximately 10^{-8} Torr (Chambers et al 1989b). The Pirani gauge P2 measures the backing pressure on the turbomolecular pump.

Figure 3.3.1 The Hallam instrument UHV pumping system.

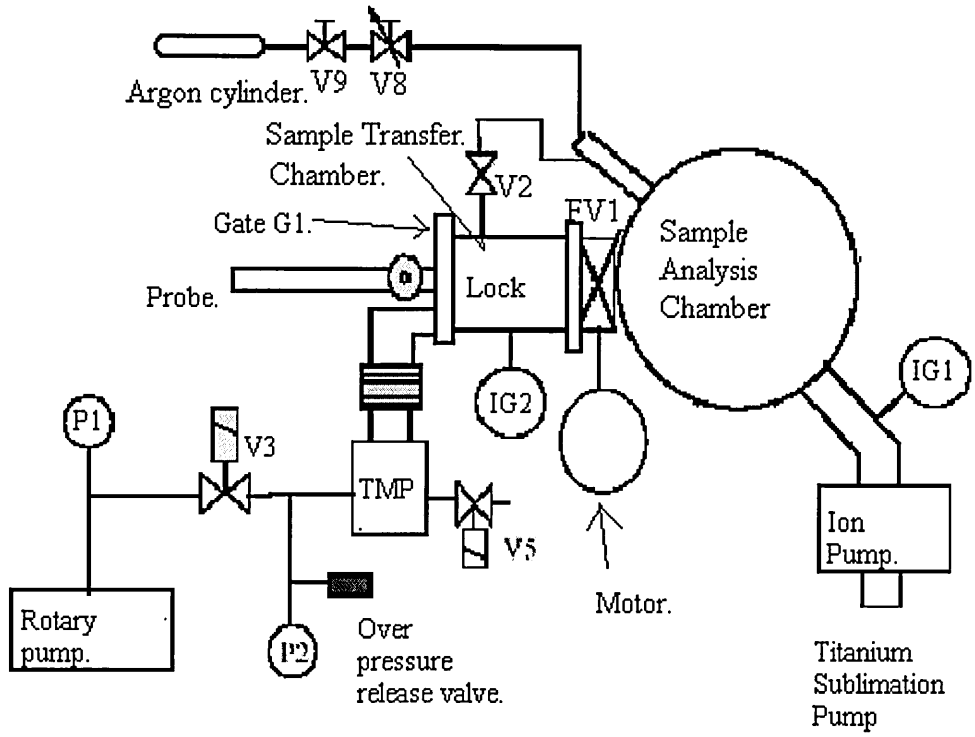

When pumping the chamber pressure down from atmosphere the flap valve FV1 is open allowing the Sample Transfer Chamber (STC) and the SAC to be pumped down. To obtain lower pressures in the SAC an ion pump is used, which should only be used when a pressure below 10^{-5} Torr has been achieved. This is a Perkin-Elmer 220 L/S differential ion pump capable of pumping down to 10^{-11} Torr (Perkin-Elmer 220 Operating Manual). Further reductions to the chamber pressure may be achieved using the four filament Titanium sublimation pump when required (Chamber et al 1989d). To obtain minimum pressures in the SAC the gate valve FV1 is closed to reduce the volume pumped by the ion pump by isolating the SAC from the rest of the instrument.

In order to load a sample into the SAC the STC is exposed to atmosphere by venting to nitrogen gas generated directly from liquid nitrogen through valve V5, with the backing valve V3 shut and the SAC isolated. The sample is inserted onto the probe and the viton sealed gate G1 is shut. The sample is introduced to the SAC by the probe once the STC has been pumped down to approximately 10^{-7} Torr. The vacuum in the STC and SAC is monitored using the ion gauges IG1 and IG2, respectively. The ion gauges are UHV devices covering the range 10^{-4} to 10^{-11}Torr (Roberts and Vanderslice 1963a).

The remaining parts of the vacuum system shown are concerned with introducing argon into the ion gun and preventing it from dispersing to the rest of the system. Valve V9 is used to isolate the argon

cylinder while valve V8 provides fine control of argon gas pressure to the ion gun. Valve V2 is a computer controlled valve and is used to open and close the differential pumping line for the ion gun.

To obtain UHV conditions a regular bakeout is performed which removes absorbed gases from the chambers walls and system components (Roberts and Vanderslice 1963b). The baking system is incorporated into the instrument with the heating elements located around the chamber outer walls. The bakeout temperature is 150°C with a thermal blanket draped over the instrument, and the bakeout period may be set over several days with a 7 day timer. The necessity to vent the STC every time a sample change is required is time consuming and leads to increased working pressure in the STC ($3x10^{-7}$ Torr). Adequate pressure was, however, maintained in the SAC and a working pressure of $3x10^{-9}$ Torr was routinely observed.

3.4 Energy Analyser.

This section covers the parts of the instrument referred to as the transfer column and analyser in Table 3.2.1. The transportation, energy filtering, and detection of the electrons takes place within this section which is under the same vacuum pumping conditions as the SAC. The transfer column and analyser was supplied by Kratos and is the same as those used on the Axis-165. Figure 3.4.1 shows the Hallam instrument transfer column and analyser.

Figure 3.4.1. Cross section of the energy analyser. (Kratos Axis-165)

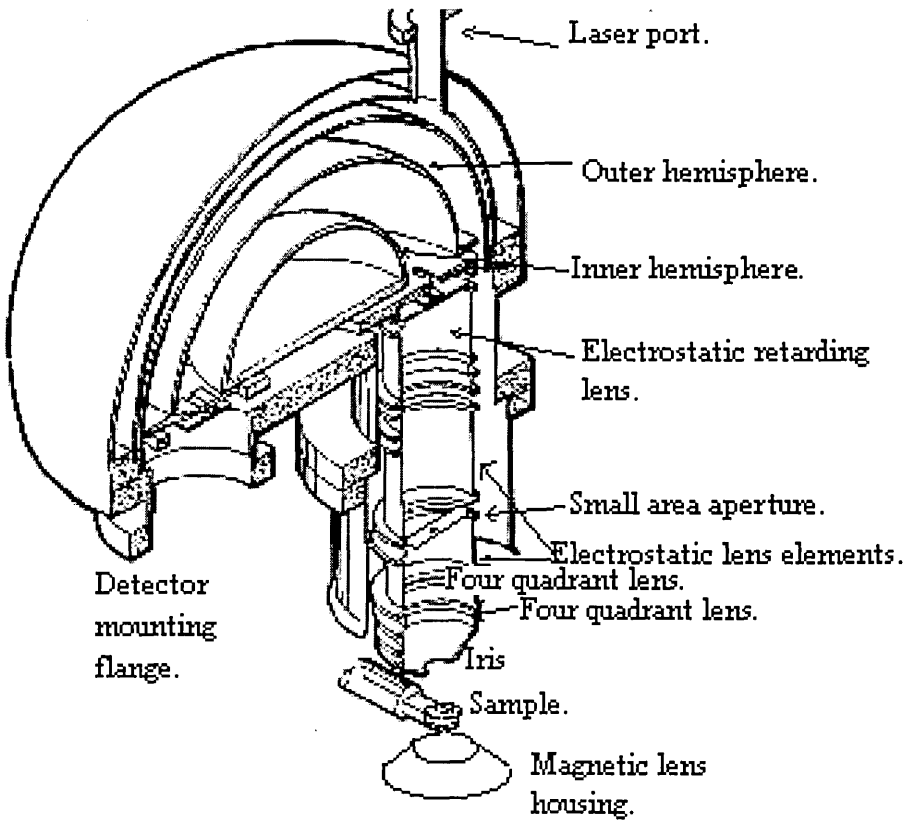

Figure 3.4.1 is a cross section of the electron optics shown in Figure 2.3.4. The magnetic lens shown here is classed as part of the transfer column although as it is an immersion lens it is located below the sample. The actual magnet resides in atmosphere in an inverted housing which makes up part of the chamber wall. Exact alignment of the magnetic lens is achieved using four screws integrated into the lens housing. The magnet coil has about 2200 turns and a maximum current of about 2.5A supplied by a 3A power supply. This translates to a scan energy range of 10-1500eV photoelectron kinetic energy when operating in magnetic magnification mode. The magnet is water- cooled in order to dissipate heat generated within the coils. The iris shown is of adjustable diameter and can vary the solid angle acceptance from ±2° to ±15° when operating in magnetic mode. The electrostatic lens system consists of four elements providing magnification for XPS and AES with a solid angle acceptance of ±2°. The electronics provide a scan range of 50-3200eV in electrostatic mode. The quadropole lens are the deflectors used for scanning small area XPS. There are actually eight elements to the deflector but adjacent plates are interconnected, so a quadropole system is formed. In Chapter 5 the effect of the quadropole system scanning system shall be assessed, and a description of the modifications necessary to upgrade to an octopole system shall be presented.

The small area aperture is a plate with three interchangeable apertures of diameters 2mm, 1mm, and 0.4mm, and a wide slot of dimensions 10x3.7mm. When the apertures are in place they limit the area of analysis to an area dependent on the magnification and can be used in electrostatic and magnetic XPS modes. The input slit to the analyser is of dimensions 3mmx15mm. The three apertures give actual analysis spot sizes of 120μm, 60μm, and 30μm when the instrument is operated in magnetic magnification mode (giving a magnification of approximately 16). The spot sizes are quoted by Kratos in the Axis-165 Operating Manual, and are measured at the centre of the field of view, which is along the axis of the analyser. In Chapter 5 the spot sizes across the field of view shall be measured, and a method of compensation for loss of resolution away from the analyser axis shall be presented.

The energy analyser itself is a concentric hemispherical analyser (CHA) of diameter 330mm. Using this system it can be operated in either Fixed Analyser Transmission (FAT) mode or Fixed Retard Ratio (FRR) mode (Seah 1990a). The electronics provide pass energies of 5, 10, 20, 40, 80, 160 and 320eV in FAT mode with a resolution of 25meV, and retard ratios of 2, 5, 10 and 20 with a resolution of 0.1%-0.8% $\Delta E/E$, in FRR mode. The detection system consists of eight channeltron multipliers. Each channeltron has an individual power supply and the multiplier voltage may be set from 0-3500V, with the channeltrons operating with a maximum gain of about 10^8. The pulses generated by electrons are converted from charge to voltage, then converted to optical pulses at the preamplifier stage. The preamplifier is linked fibre optically to the main electronics where the pulses are counted. In section 2.2, the effect of this instrumentation on the electron as a function of kinetic energy (transmission function) was discussed. In Chapter 6 the results of applying the methods of determining the transmission function shall be presented.

The port labelled 'laser port' is a clear window to the vacuum chamber which accommodates a laser on the exterior. The laser shines down the transfer column onto the sample. With the small area aperture in place the laser diameter is reduced to a fine spot. This enables accurate positioning of the sample area of interest to within the analysis area as defined by the spectrometer. Geometrical adjustment of the laser is possible and it can be tilted to initially align the laser with the area of analysis.

3.5 Excitation sources.

The x-rays required to excite photoelectrons are produced by a dual anode x-ray source, which was supplied by Kratos. The energy range is variable from 0-15kV and the target materials are Mg on one side and Al on the other. Mg produces x-rays of 1253.6eV and Al at 1486.6eV (Seah 1990b). The maximum power is 450W (15kV and 30mA emission from source), but this is at the expense of gun lifetime, so a working power of 300W is recommended (15kV at 20mA emission). The gun is positioned to point directly at the sample, but tilt is incorporated for fine adjustment. The source is water cooled, and this must be flowing before the gun can be operated.

The electron gun provides excitation for SEM, AES and EDX, and was originally fitted with a lanthanum hexaboride (LaB_6) cathode source. An LaB_6 souce was used as higher emission is obtained compared to that from a tungsten hairpin source (Hawkes and Kasper 1989), so a high sample current can be used for x-ray analysis. This is a Kratos product which enables the AES capability to be added to the Axis-165. The accelerating voltage was specified as 500V to 15KV although flashover problems were encountered above 12kV. Focussing is achieved using an objective/condenser electrostatic lens system. Source alignment could be adjusted mechanically using external screws, or by electrostatic deflection and stigmatism could be compensated using an octopole electrostatic lens. Quadropole deflection plates at the end of the gun provided the scanning facility. The gun may be mechanically aligned using four external bolts to give fine control of overlap of the electron beam with the area of analysis. The gun nose is at a working distance of 25mm from the sample. The gun control and power supplies give automatic tracking of condenser and objective lens voltages with the beam energy E_0, hence these voltages can be expressed as fractions of E_0. In Chapter 4 the electron beam spatial drift as a function of E_0 shall be investigated, and a procedure for correcting this shall be proposed.

3.6 Energy Dispersive X-ray Detector.

The energy dispersive x-ray detector on the system is part of the Oxford Instruments ISIS system. The detector assembly is shown in Figure 3.6.1.

The detector is housed within the bellows so when required for use it may be automatically lowered into the analysis chamber, at which point it will be at a working distance of 100mm from the sample. The gate valve is used to isolate the detector from the main chamber. This is necessary when venting the main chamber while the detector is cooled to 100K, as contact with atmosphere at this temperature would damage the detector window. Although the detector will not degrade a UHV environment when

cooled, it is not strictly UHV compatible as it cannot be baked. While the rest of the instrument is being baked the EDX assembly has no heating elements around it, and is not covered by the thermal blanket. As the detector is withdrawn during baking it is remote from the analysis chamber and will not reach high temperatures.

Figure 3.6.1 Detector Assembly.

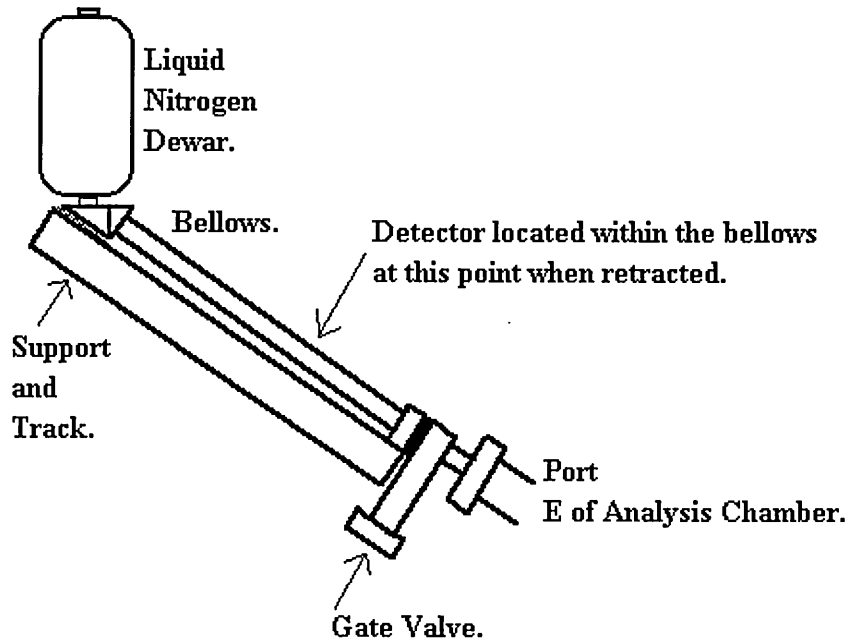

Although specific details of the detector assembly are not available, we shall take a brief look at a typical detector, as shown in Figure 3.6.2 (Reed 1993).

Figure 3.6.2. Typical energy dispersive detector.

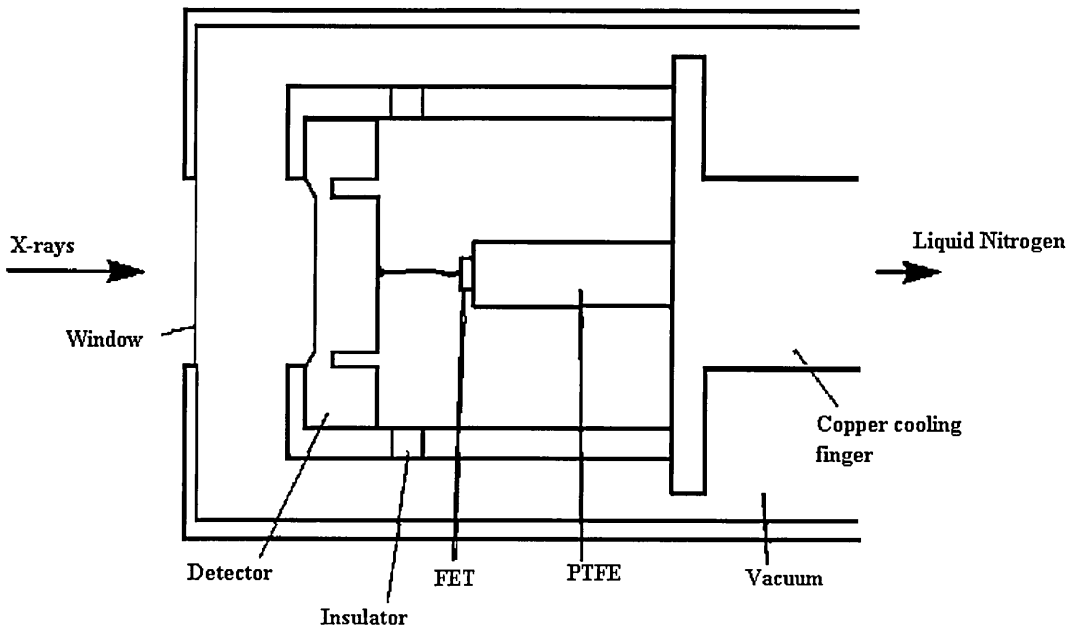

X-rays enter through the thin beryllium window and produce electron-hole pairs in the lithium doped silicon. Generation of each electron hole pair requires 3.8eV at the operating temperature of the detector so the number of pairs produced by a photon of energy E_k is $E_k/3.8$. The charge produced by a x-ray photon is of the order 10^{-16}C, which is amplified by the field effect transistor (FET). The assembly is cooled to 100K by liquid nitrogen in order to minimise noise caused by thermal excitations of electrons. Further amplification is provided by a main amplifier and the resultant shaped pulse is a measure of the x-ray energy. The data is stored in an electronic array of channels, each pulse assigned a channel address on the basis of the pulse height measurement. The time taken for a pulse to be amplified, shaped and recorded at a channel address is referred to as the dead time. During this period no x-ray photons are detected, and the duration of this is typically 50μs. This type of system gives an energy resolution of 160eV at the Mn-K_α peak (~5.9kV).

In the case of the ISIS system the main amplifier and pulse shaping electronics are located in the Oxford Instruments control box. As a spectrum is recorded, a real time display of counts versus energy is shown on the computer screen.

3.7 Ion gun.

The Minibeam I ion source uses argon ions created by electron impact of Argon atoms (Seah 1990c). The accelerating voltage is variable from 0.5 to 5kV and an objective/condenser electrostatic lens system is employed for focus and spot size control. Argon is leaked into the gun as described previously. A minimum beam diameter of about 200μm is achievable, and a maximum beam current of about 5μA. The beam is scanned across the sample using four deflection plates. Mechanical adjustment of gun tilt is available to align the beam with the analysis posistion. The working distance of the gun nose from the sample is 65mm.

3.8 Sample stage.

The sample manipulation stage consists of the sample mount which houses a 15mm sample stub. The manipulator has four-axis movement (X,Y,Z and θ) with a movement range +15-10mm X, ±10mm Y and Z and ±180° θ, with a movement resolution of ±2.5μm X, Y ,Z and 1° tilt. The stub is electrically insulated with a connection for measurement of sample current or external earthing of the sample.

3.9 Secondary Electron Detector.

The secondary electron detector contains a scintillator/photomultiplier assembly and pre-amplifier. The collector grid mounted in front of the scintillator can be biased with a positive, zero or negative voltage, to differentiate between low-energy secondary electrons and high energy reflected electrons. The pulses of light generated by the electrons striking the scintillator are converted to electronic pulses

and amplified within the pre-amplifier before the signal is sent to the main electronics for counting. The counts are used to modulate the SEM image which is displayed in real time.

3.10 System Control.

The hardware used for analysis is controlled by the Unix workstation, via the Vision control software (developed by Kratos), and by the PC, via the Oxford Instruments ISIS software. Figure 3.10.1 is a schematic diagram of the control system. The vacuum control components have been omitted as these are controlled solely by the Kratos system. What is of interest here is the identification of which scans are controlled by which system, and where the detected signals are displayed and recorded.

The Unix workstation communicates with the VME bus through an ethernet link. The VME rack houses the low voltage electronics concerned with the surface analytical functions of the instruments. The basic components are shown in the diagram. The unit labelled H.T. bus interface (1c) communicates with the High Tension (H.T.) bus, specifying the voltages to be applied to the lens and the analysers. The H.T. bus has an individual power supply, so in the event of vacuum failure the power to the H.T. electronics is disabled, ensuring that vacuum components powered by the H.T. electronics cannot be damaged at pressures above UHV.

The VME unit referred to as 'Power Supply Interface' (1e) optically communicates with the X-ray gun and electron gun power supply units. The optical serial link electronically isolates these units, which have voltages of up to 25kV present, from the main electronics. The channeltron detector interface unit counts the optical pulses from the channeltron pre-amp, and consists of eight channels, so counts from all eight channeltrons can be simultaneously detected.

The scan waveform generating unit provides the reference signal scan waveform 1 for the electron gun scan. This is one of two inputs available for the scan H.T. amplification unit. This H.T. unit amplifies the low voltage reference signal from, for example, ±10V to ±500V RMS. The input to this unit can be manually switched to the reference signal, scan waveform 2, provided by the Oxford Instruments electronics. The Oxford Instruments main electronics are linked in parallel communication to the PC.

The output from the secondary electron detector is connected to both the VME secondary electron imaging unit, and the Oxford Instruments main electronics. This arrangement allows the user to display real time SEM images on the Kratos VGA monitor, and acquire Auger maps over the imaged region (using scan waveform 1), then to manually switch to scan waveform 2 so SEM images and EDX maps can be acquired using the Oxford ISIS acquisition system. The images acquired by the ISIS system are displayed on the PC monitor, and are refreshed on a frame by frame basis. The PC and the workstation are linked by an ethernet connection. This allows data transfer and enables the PC to be used as a Unix terminal.

Figure 3.10.1 The control system for the Hallam instrument.

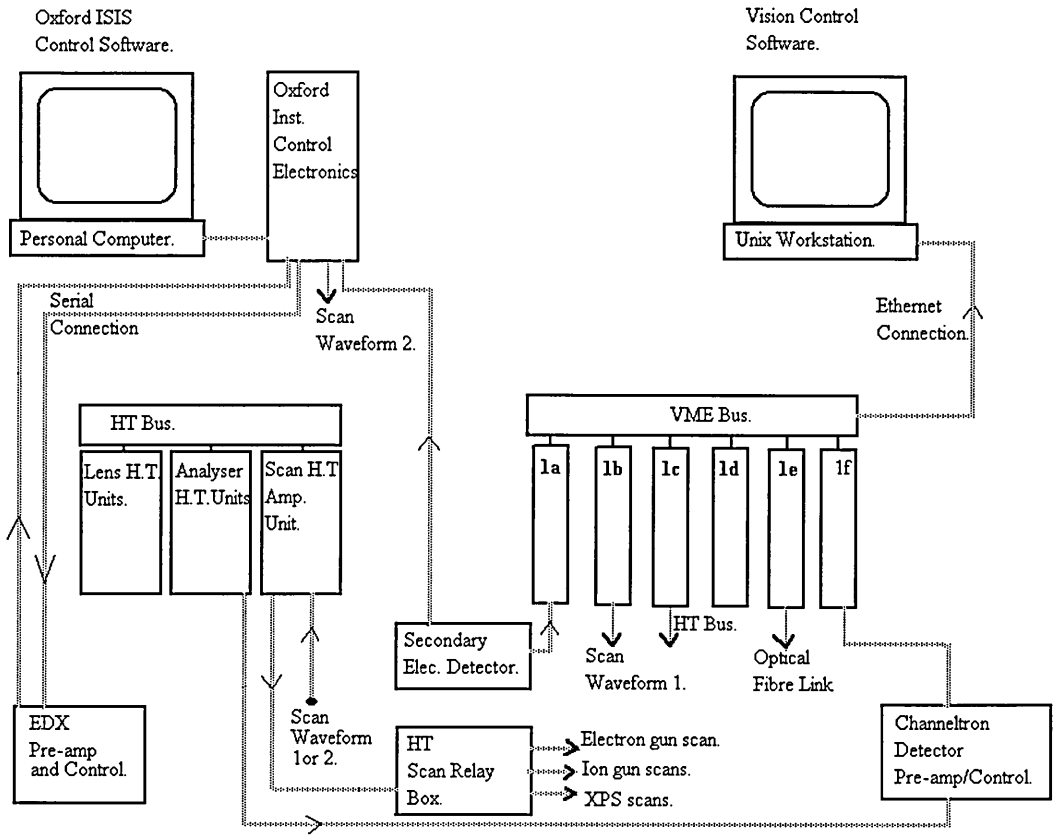

1a-Secondary Electron Counter/Imaging Unit.
1b-Scan Waveform Generating Unit.
1c-H.T. Bus InterfaceUnit.
1d-VME Processor Unit.
1e-Power Supply Interface Unit.
1f-Channeltron Detector InterfaceUnit.

3.11 25kV Field Emission Gun

Towards the completion of the project the LaB_6 thermionic emission gun was stripped down and the LaB_6 filament assembly replaced by a thermal field emission gun. The new assembly was supplied by in co-operation with Kratos. The performance of the gun was of interest to Kratos as it would improve the scanning Auger capability. The brighness of a Schottky field emission source is two orders of magnitude higher than an LaB_6 source (Linsmeier 1994). The gun is designed to operate at beam energies of 25kV, providing increased depth penetration for film thickness/composition studies. Figure 3.11.1 is a schematic of the emitter assembly. This information is taken from the York Electron Optics Schottky Source Operating Manual.

An electric field is established by a 3-4kV potential difference (extractor voltage), between the emitter at the filament potential and the extractor aperture. The field gradient is greatly enhanced at the emitter

owing to its very small radius of less than ~1μm. Electrons will be emitted from the tip if the thermal energy of electrons arriving at the surface is sufficient (1700K-1800K) to overcome the surface potential barrier. A voltage of –300V is applied to the suppressor, whose function is to suppress most of the thermionic emission from the hairpin filament and the shank of the tungsten single crystal. The emitter assembly was mounted onto the column of the existing electron gun. The lens shown in Figure 3.11.1 effectively controls the spot size of the beam, while the objective lens of the column provides the focus. Mechanical alignment of the source is available, and the source can be electrically aligned as with the previous LaB_6 source.

Figure 3.11.1. Field Emission Gun Source Assembly.

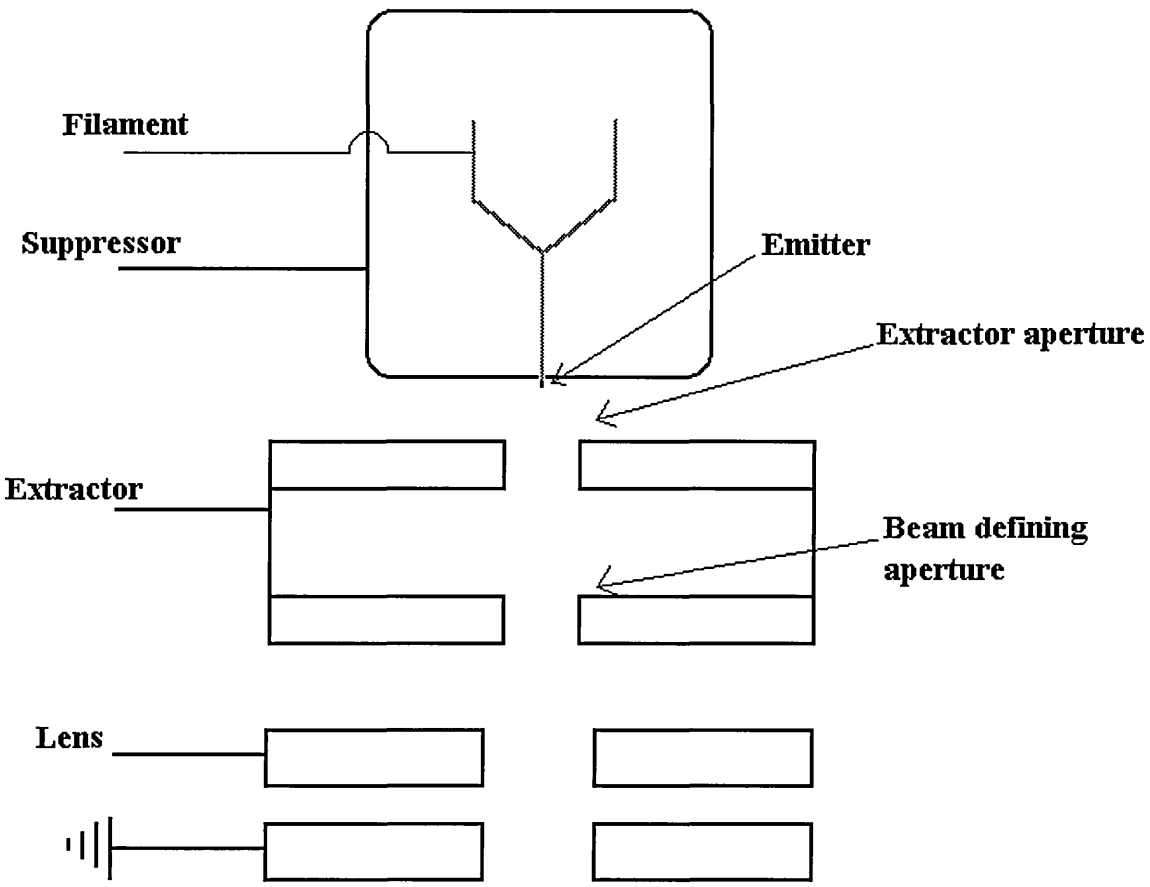

3.12 Thickness Mapping capability.

Although the thickness mapping is derived from EDX data by software, it is appropriate to mention it here. EDX detectors are not usually attached to a UHV instrument, and the software has not yet been released commercially, so both must be tested. The other parts of the instrument were checked routinely as part of the Axis-165 testing procedure. The first sample to be used to test the thickness measurement facility was a silver film on a silicon substrate which had been grown by evaporation

whilst the silver thickness was monitored with a quartz monitor. The thickness of the film was measured as 200nm in this manner. The sample was loaded into the analysis chamber along with pure silver and silicon standards. The EDX spectra of the silicon and silver standards were acquired to calibrate the measurements. Five EDX spectra were taken from the silver film, and the first of these is shown as Figure 3.12.1. Each spectrum was used to obtain a thickness value using the algorithm provided by Oxford Instruments, which also required the experimental parameters such as primary beam energy (10kV in this case), beam incident angle onto the sample, and detector orientation relative to the sample. Five thickness values were obtained which produced an average value of 201.3nm and a standard deviation of 2.7nm. From this we can conclude that the thickness measurement system worked for simple binary systems.

Figure 3.12.1 EDX spectra of silicon standard.

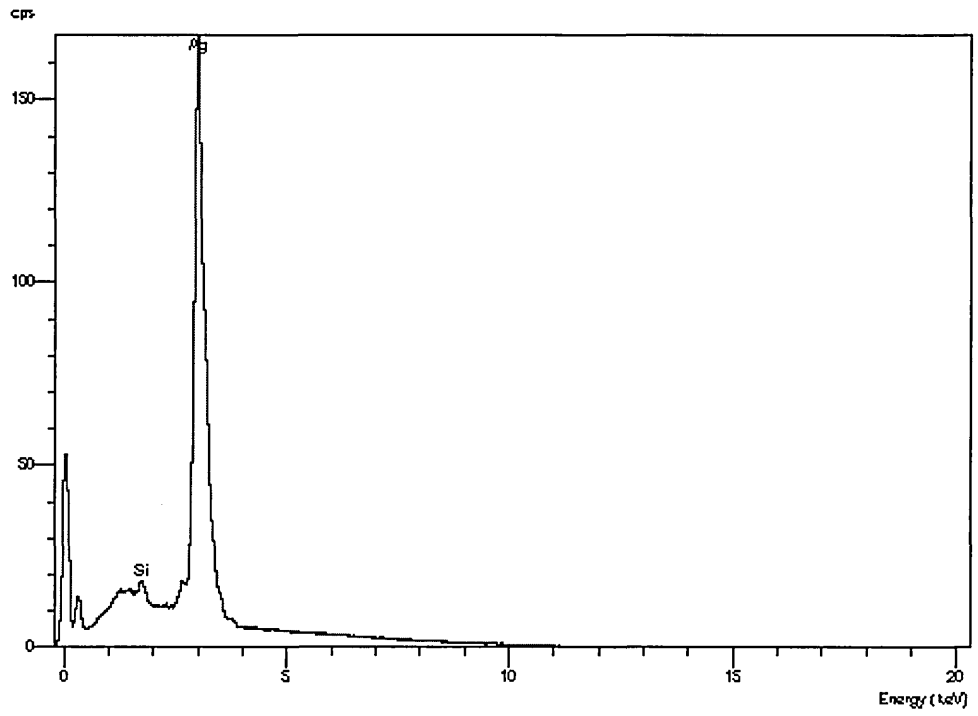

To test the thickness mapping capability of the system a sample consisting of four inverted p shaped gold film deposits was used. The sample was manufactured by evaporation onto a masked substrate. A secondary electron image of the sample is shown as Figure 3.12.2. The sample was argon ion etched from the direction of the top left hand corner of the sample with a 5kV beam. The beam was static and unfocused so had a large spot size on the sample, so the distribution of the beam would produce varying sputtering rates across the sample. This produced spatial variations in the gold thickness across the pattern.

Figure 3.12.2 Secondary electron image of p's.

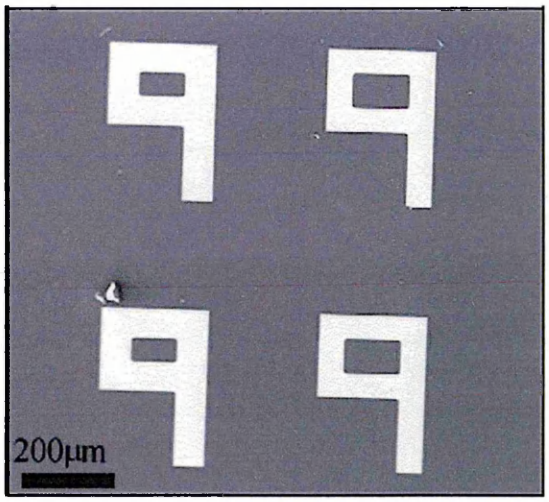

Prior to a thickness map being acquired, spectra of gold and silicon were acquired to calibrate the thickness maps. A thickness map of the sample was acquired over a four hour period and is shown as Figure 3.12.3. A colour key is used to give a better indication of thickness at different regions. Thickness measurements were taken at selected points and found to agree with the values indicated by the map, so we could conclude that the mapping program worked.

Figure 3.12.3 Thickness map of the gold. Acquired with a 12kV beam over a 6 hour period.

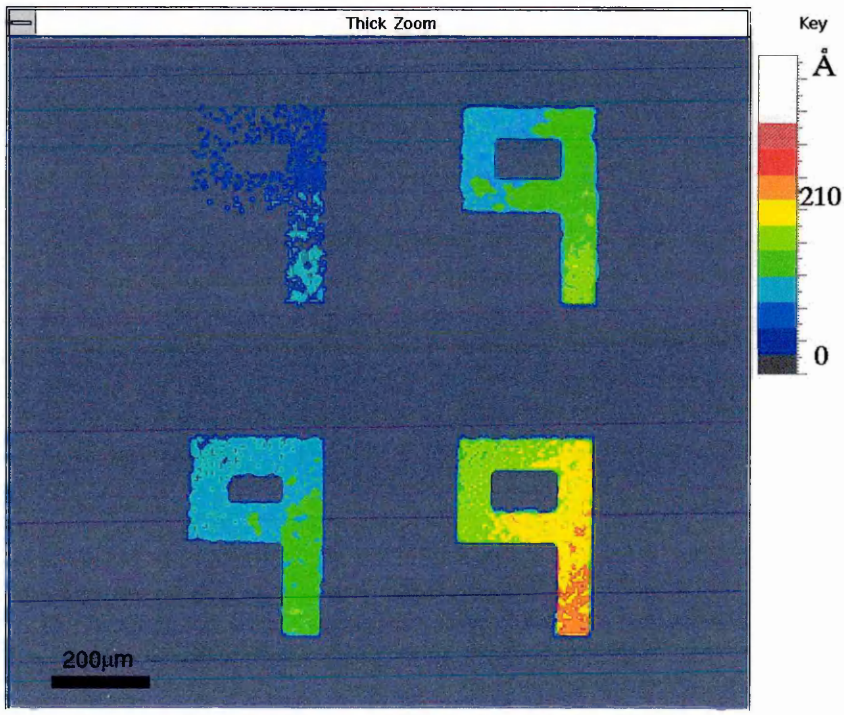

3.13 Comments on thickness mapping.

The thickness map in Figure 3.12.3 took a prohibitively long time to acquire, as the software calculates the thickness at each point of the map, from two EDX spectra acquired at different x-ray energies. In many cases it may be more appropriate to calculate the thickness of a film at just a few points. These measurements could then be used to calibrate EDX maps in terms of thickness. As stated in Section 2.4.4, in many instances the image intensity of an EDX map will be proportional to the film thickness. If this is assumed to be the case, then calibrated EDX maps, acquired relatively quickly, could be converted into thickness maps.

References to Chapter 3:-

Chambers A., Fitch R.K., Halliday B.S. (1989a) In Basic Vacuum Technology, IOP Publishing Ltd, pg51.

Chambers A., Fitch R.K., Halliday B.S. (1989b) In Basic Vacuum Technology, IOP Publishing Ltd, pg60.

Chambers A., Fitch R.K., Halliday B.S. (1989c) In Basic Vacuum Technology, IOP Publishing Ltd, pg67.

Chambers A., Fitch R.K., Halliday B.S. (1989d) In Basic Vacuum Technology, IOP Publishing Ltd, pg63.

Hawkes P.W.. Kasper E. (1989) In Principles of Electron Optics Volume 2, Academic Press, pg 913.

Linsmeier C. (1994) In Surface Science Techniques Edited by Wall J.M. and Smith R., Pergomon Press, pg 25.

Reed S.J.B., (1993a) In Electron Probe Microanalysis 2nd Ed., Cambridge University Press, pg 107.

Roberts R.W., Vanderslice T.A., (1963a) In Ultra High Vacuum and its Applications, Prentice-Hall, pg 31.

Roberts R.W., Vanderslice T.A., (1963b) In Ultra High Vacuum and its Applications, Prentice-Hall, pg 123

Seah M.P. , (1990a) In Practical Surface Analysis 2nd Ed. Vol.1 Auger and X-ray Photoelectron Spectroscopy, Edited by Briggs D., Seah M.P.John Wiley and Sons, pg 75.

Seah M.P. , (1990b) In Practical Surface Analysis 2nd Ed. Vol.1 Auger and X-ray Photoelectron Spectroscopy, Edited by Briggs D., Seah M.P.John Wiley and Sons, pg 52.

Seah M.P. , (1990c) In Practical Surface Analysis 2nd Ed. Vol.1 Auger and X-ray Photoelectron Spectroscopy, Edited by Briggs D., Seah M.P.John Wiley and Sons, pg 66.

Chapter 4 Alignment of Electron Induced Images Acquired at Different Primary Beam Energies.

4.0.0 Introduction

The measurement of thickness and composition of surface layers by Energy Dispersive X-ray Analysis (EDX) was discussed in section 2.2.4, where the advantage of using measurements taken at various primary beam energies was highlighted. The use of measurements taken at a range of E_0 values can give a qualitative understanding of the lateral structure of surface layers, and can improve the accuracy of quantitative calculations. Oxford Instruments envisaged exploiting this in their thin film analysis software. As the software they were developing was applicable to the mapping of surface features, it was desirable to acquire EDX data from the same physical point on the surface at different E_0 values. Essentially this required the spatial registration of EDX maps taken at different E_0 values. If we acquire x-ray and secondary electron images simultaneously using the Oxford Link ISIS scan generator and acquisition unit, they will be perfectly registered, so we may study this problem using secondary electron images as they can be acquired rapidly.

It was intended that the problem be studied on the Hallam Instrument test bed, but the solution must be applicable to conventional electron microscopes fitted with an ISIS system. The electron gun on the Hallam instrument uses electrostatic plates to deflect the electron beam, whereas conventional SEM's use magnetic scan coils. It is clear that both cases must be studied

4.1.0 Image shift measurement

From observation of SEM images when using the LaB_6 gun one could see that at relatively high magnification (x1000) the features of the image would shift as the beam energy was altered. The shift was the most obvious sign of distortion with beam energy, so investigation of this was first undertaken. To determine the degree of shift a sample was chosen which would provide a reference point. The sample, which is shown in Figure 3.12.2, was gold evaporated on silicon, which had been masked so the gold formed four P shaped patterns on the silicon. The corners of the shapes were well defined as no interface region between the gold and the silicon could be detected with the spatial resolution of the imaging system used.

The corner of the bottom left hand P was chosen as the reference point. The gun was operated with the following parameters:-

Filament current = 2.8A

Electron gun emission current=60μA

Gun lens=$0.85E_0$

Gun focus=$0.58E_0$

Image size = 200μm

where E_0 is primary beam energy.

The beam energy was originally set to 4kV and increased in increments of 1kV up to 14kV. At each increment all other settings were left constant . All ten images were saved with a pixel resolution of 256 by 256, to a dataset titled "align.dset". Offline inspection of these images was carried out and the position of the reference point which had been originally positioned at the centre of the field of view was noted at each beam energy. The shift of the reference point from the original position is shown as Figure 4.1.1.

Figure 4.1.1. Co-ordinate graph of reference point shift.

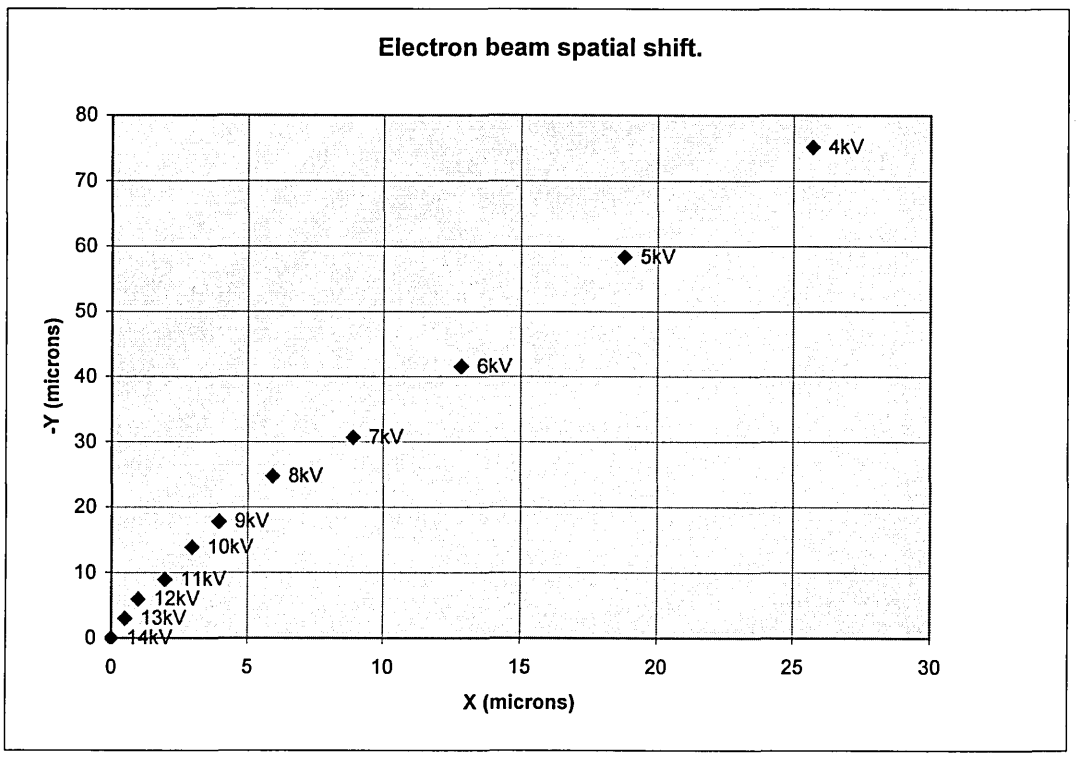

It is obvious that beam shift is occurring along a directional line. In order to see how the shift corresponded to beam energy the magnitude of the shift ($\sqrt{(x^2+y^2)}$) along the direction of shift was plotted against beam energy. This is shown as Figure 4.1.2. Inspection of this graph indicates a relationship $S \propto 1/E_0$ (where S is shift). This is verified by Figure 4.1.3., where S is plotted against the reciprocal of beam energy.

Figure 4.1.2 Magnitude of shift against beam energy.

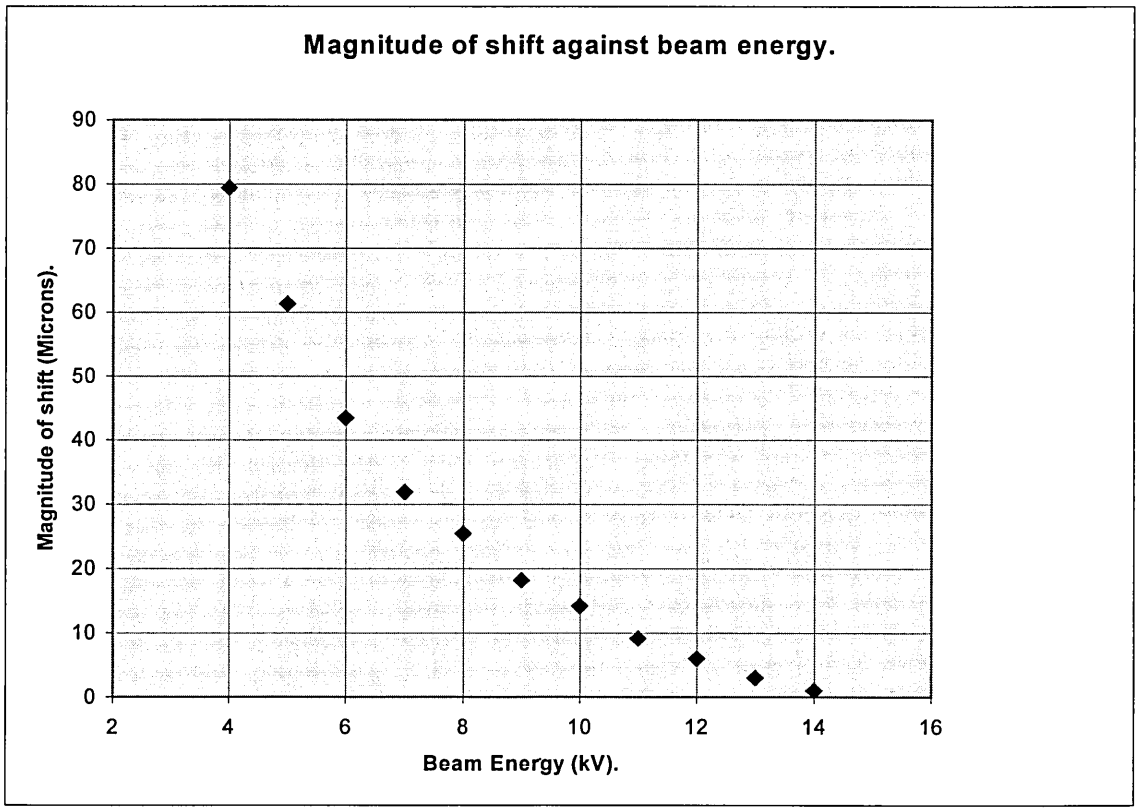

Figure 4.1.3 Magnitude of shift against reciprocal of beam energy.

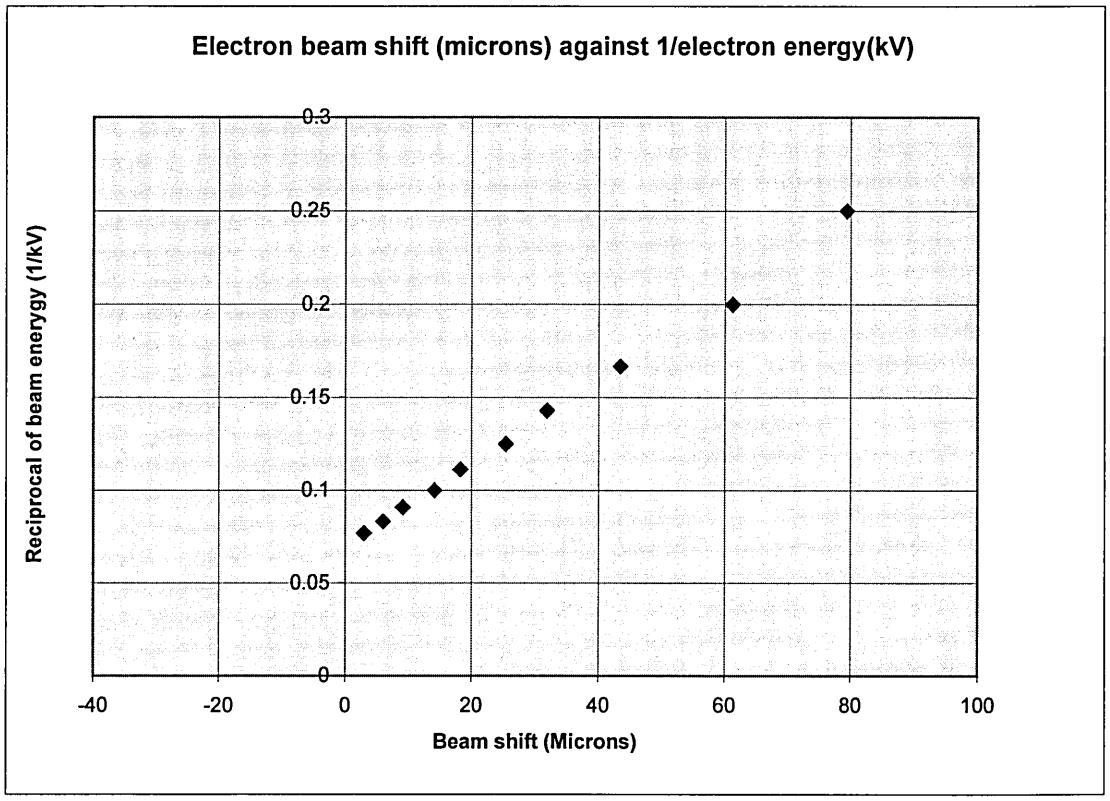

In order to understand this relationship it is necessary to consider the motion of an electron in an electrostatic field. If the acceleration voltage is given by E_0 and q is the charge of the electron then qE_0 is equal to the kinetic energy of the electron, hence

$$qE_0 = \tfrac{1}{2} mv^2$$

Equation 4.1.1.

where m is the mass of the electron and v is the velocity. Now if we consider the lateral force, F, on the electron caused by the external field, E, then

$$F = qE = ma$$

Equation 4.1.2.

where 'a' is the the lateral acceleration of the electron. The time, t, for which the electron is subject to this force is given by

$$t = d/v$$

Equation 4.1.3.

where d is the distance over which the external field effects the electron, as shown in Figure 4.1.4.

Figure 4.1.4 Path of electron.

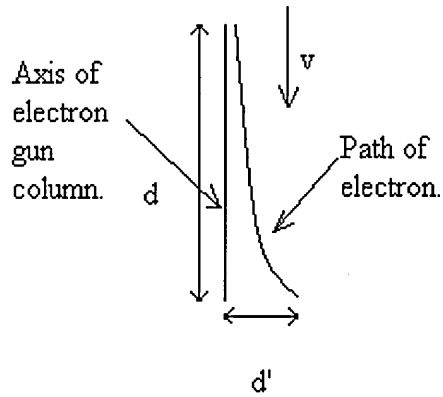

The lateral distance travelled by the electron is given by

$$d' = 1/2at^2$$

Equation 4.1.4.

If we rearrange Equation 4.1.2. and substitute for a, and rearrange Equation 4.1.3. and substitute for t we get

$$d' = \frac{1}{2} q \frac{E}{m} \frac{d^2}{v^2}$$

Equation 4.1.5.

Now if we rearrange Equation 4.1.1. and substitute for v we get

$$d' = 1/4 \frac{d^2 E}{E_0}$$

Euqation 4.1.6.

hence

$$d' \propto \frac{1}{E_0}$$

This simple calculation shows where the relationship $d' \alpha 1/E_0$ originates and confirms that the shift is caused by a parasitic electrostatic field. The mu-metal around the chamber is apparently successful in shielding against magnetic fields, as a parasitic magnetic field would cause more complex effects. These effects may be compensated for by applying offset voltages to the scan plates, which will create another electrostatic field to counteract the parasitic field. At present we shall assume that the parasitic external field is constant with time.

4.1.1 Shift compensation

The circuit which drives the scan plates may be simplified and drawn as in Figure 4.1.5.

Figure 4.1.5. Circuit used to power the deflection plates.

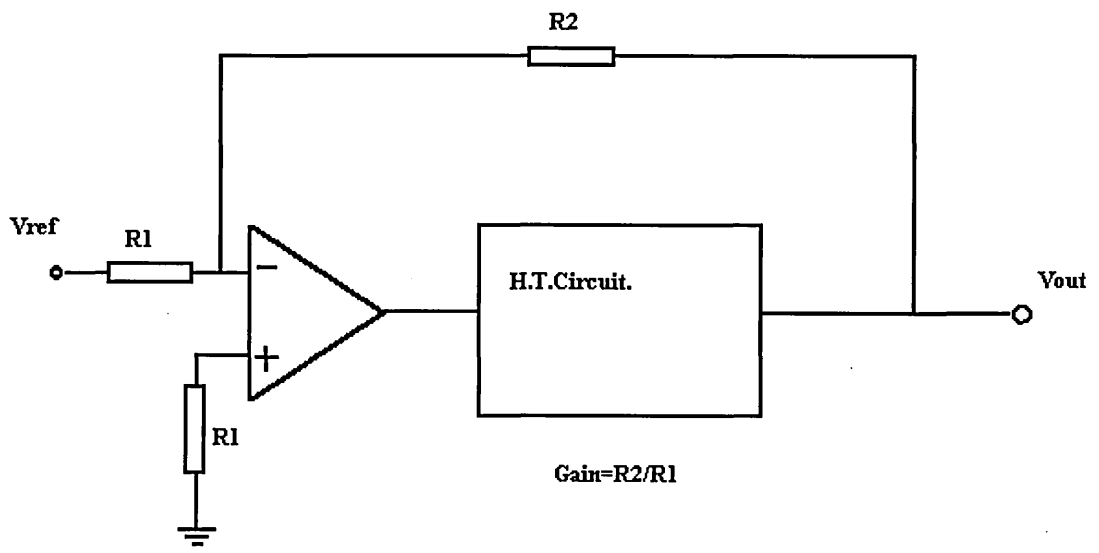

The reference voltage is 0 to ±10V and the gain of the H.T. amplifier is 49. When the beam is placed in the centre of the field of view, the scan plate voltages should be zero. It was found, however, that the H.T. rack circuit produced an offset voltage. As there were four H.T. amps, (one for each scan plate) each scan plate was held at the offset voltage of the circuit which drove it. The offsets were 4.1V, 2.3V, 3.2V and 1.9V on the x, -x, y and -y deflection plates respectively.

The scan circuit was modified to include an extra input voltage. This could be added to V_{ref} to nullify the offset voltage at the output, and could potentially supply the compensating electrostatic field. The modification was implemented on Vero board and attached to the side of the scan unit casing, all connections to the existing scan circuit board were hard wired. The circuit modification is shown as Figure 4.1.6. The output offset voltage was removed for each channel by varying the potentiometer and monitoring the output.

Figure 4.1.6 Modified circuit used to power the deflection plates.

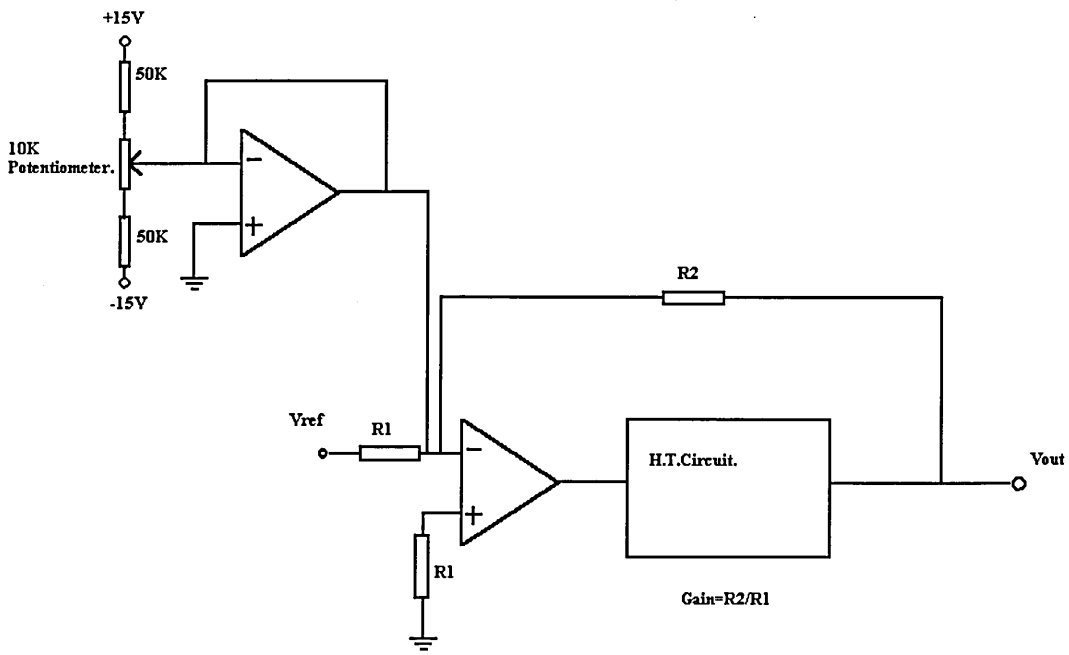

In order to examine the shift further, a copper grid of 1000 lines/inch was attached to a sample stub and inserted into the analysis chamber. On the real-time display system the scan area could be reduced, while the video monitor continued to display the last acquired image around the border, but the smaller area displayed would still be refreshed in real time. Using this, an iterative process could be carried out as follows.

1) Acquire an image at 4kV.
2) Reduce the scan area size to 20%.
3) Increase the beam energy to 14kV.
4) Observe the misalignment of the grid lines and use the voltage input adjustment on the scan plates to re- align the grid lines.
5) Repeat step 1.

This procedure was carried out until adequate alignment was achieved. Figure 4.1.7 shows the grid line alignment with zero offsets on the scan plates and Figure 4.1.8 shows the grid line alignment after the application of a compensating electrostatic field. The middle 20% of the images which shows obvious contrast to the rest of the image is part of an image acquired at 14kV, while the rest of the image was acquired at 4kV.

Figure 4.1.7. Grid line alignment before compensation.

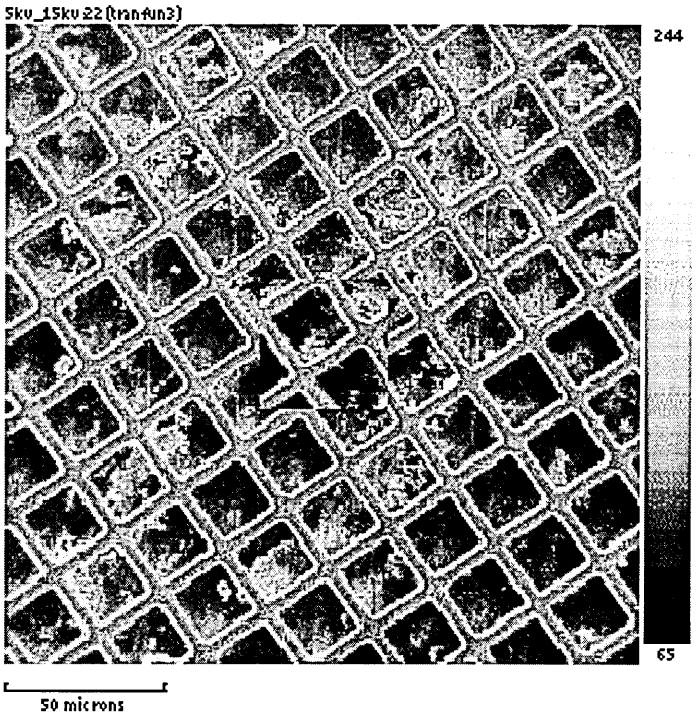

Figure 4.1.8. Grid line alignment after compensation.

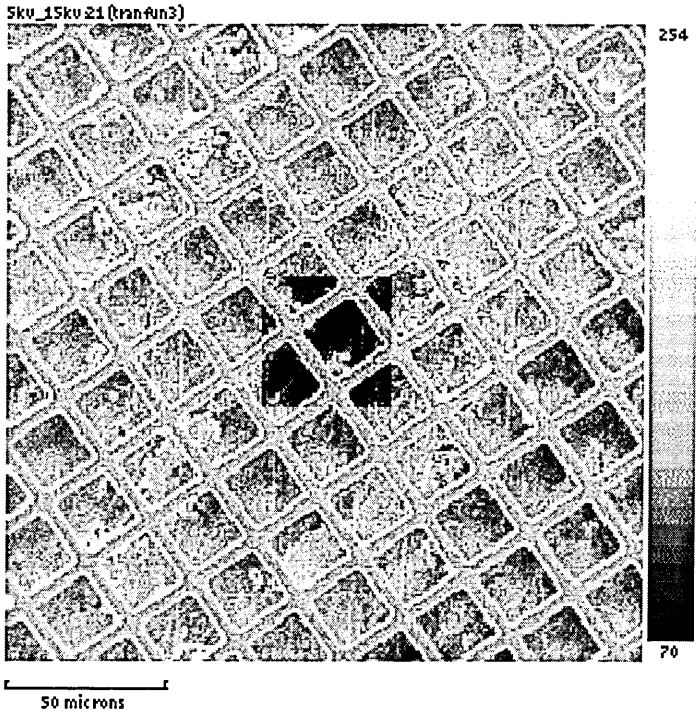

4.2.0 Image Distortion Assessment.

The shift was the dominant factor on the Hallam instrument, so now this had been minimised attention could be focussed on the image distortion across the field of view. In order to assess this, a sample was required which could provide regular reference points over a wide area, and with the physical dimensions of the reference points accurately defined. The copper grid used previously was fabricated from thin foil, so prone to slight bending, which could distort the dimensions, especially over a wide field of view. A silicon test specimen was acquired for use as a reference sample. The sample was made of single crystal silicon of overall dimensions 5mm by 5mm, and is marked with clearly visible squares of periodicity 10μm. The dividing lines are 1.9μm in width and formed by electron beam lithography. A broader marking is made every 500μm. Documentation is received with the sample showing the results of a linescan from a calibrated SEM, which confirms the uniformity of the grid.

To establish the degree of the distortion the sample was first used to establish changes in magnification and shift (still present despite minimisation at the centre of the field of view). The sample was inserted into the chamber and positioned at the standard analysis position. An image of the sample was acquired using the standard gun settings at a beam energy of 5kV. The magnification was set so that a square formed by the large border markings was within the field of view. Images at 10kV and 15kV were also acquired and recorded with a pixel resolution of 512 by 512 for subsequent analysis. The image acquired at 10kV is shown as Figure 4.2.1. The defocusing towards the edge of the image shows the limitation of the LaB_6 electron gun column over a wide field of view.

Figure 4.2.1. Image of silicon grid at 10kV.

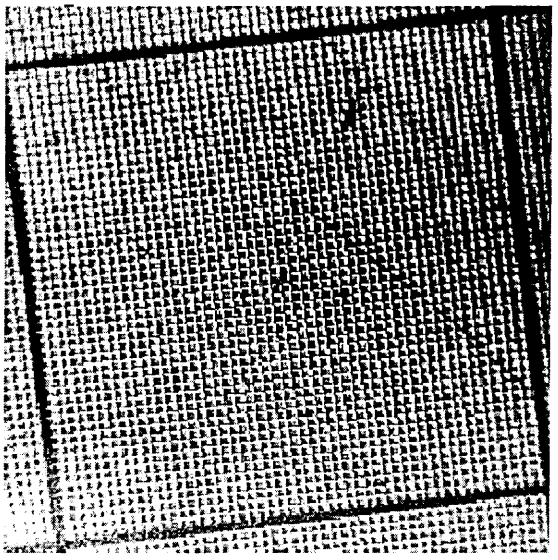

Initial inspection of the images revealed that between 5 and 15kV a shift of approximately 2μm in the x and y directions, and a change in the field of view from 544.7 to 555.1μm in the x direction (1.9%) and

from 563.1 to 575.5μm in the y direction (2.3%). These distances were calculated by counting the squares in the x and y direction of the lines, and taking the component of that distance in the x and y direction. It was obvious that a function needed to be developed which could describe the distortion across the whole field of view, and so we must consider geometrical transformations between images.

4.2.1 Image Geometrical Transformations.

A linear geometrical transformation may be described in terms of translation, scaling and rotations. From the electrostatic scanning system we can expect translation and scaling between images. Although the system compensates for changes in beam energy, slight imperfections in the software and scan generation hardware will lead to the aforementioned effects. If we consider magnetic lenses, as are standard on conventional SEM's, then rotation must also be considered.

Any geometrical distortion caused by translational, scaling, and rotational transformations between images is known as an Affine Transformation (Jain 1989) and can be represented as :

$$x' = a_0 + a_1 x + a_2 y$$

Equation 4.2.1

$$y' = b_0 + b_1 x + b_2 y$$

Equation 4.2.2

where x', y' are the transformed co-ordinates of the distorted image, x and y are the original image co-ordinates and a_0-a_2 and b_0-b_2 are constant values. For an affine transformation the constants may be determined using 3 co-ordinate values from each image. For example, we may have two SEM images of an object, one acquired at E_o=5kV and one acquired at E_o=20kV. If the transformation between the images is known to be affine, the constants a_0-a_2, and b_0-b_2, can be determined by choosing three distinct points on the object, which can be resolved to the nearest pixel position in both images. Using these points equations 4.2.1 and 4.2.2 can be solved manually as simultaneous equations. Using these constants the 5kV image can be geometrically corrected computationally at each pixel position to match the 20kV image.

The danger of this approach is that affinity between the images is assumed so any unexpected non-linear effects present would render the correction inaccurate. In order to allow for non-linear effects it is necessary to use a second order equation to model the transformations (Pratt 1991). These are written as

$$x' = a_0 + a_1 x + a_2 y + a_3 x^2 + a_4 y^2 + a_5 xy$$

Equation 4.2.3

$$y' = b_0 + b_1 x + b_2 y + b_3 x^2 + b_4 y^2 + b_5 xy$$

Equation 4.2.4

We are now dealing with six unknowns for each equation, thus requiring 6 co-ordinates to find the solution. It now becomes impractical to find the solution manually, and computational methods must be used. It is now convenient to express equations 4.2.3 and 4.2.4 in vector notation i.e.

$$\begin{bmatrix} x' \\ y' \end{bmatrix} = \begin{bmatrix} a_0 & a_1 & a_2 & a_3 & a_4 & a_5 \\ b_0 & b_1 & b_2 & b_3 & b_4 & b_5 \end{bmatrix} \begin{bmatrix} 1 \\ x \\ y \\ x^2 \\ y^2 \\ xy \end{bmatrix}$$

Equation 4.2.5

There are several computational techniques for solving a set of linear equations, which is what equations 4.2.3 and 4.2.4 become once the co-ordinates have been substituted into the equations. All the methods require the data to be passed in to the algorithm as a set of matrices as in equation 4.2.5. A full description of techniques such as 'gaussian elimination' (Press et al 1992a) or 'LU decomposition' (Press et al 1992b) is beyond the scope of this report; suffice to say that for an equation with n unknowns, n co-ordinates are required. These algorithms will provide a solution, but this will be specific to the six points chosen. Any measurement error or round-off error encountered when assigning the point pixel positions would be exaggerated. Clearly an algorithm is required that will allow more co-ordinate values to be entered than there are unknowns, allowing measurement errors to be 'averaged' out.

Such an algorithm exists and is referred to as Singular Value Decomposition (SVD) (Press et al 1992c). Although more complicated than previously mentioned algorithms, it will provide the least squares solution to an over determined set of linear equations. This algorithm thus provides a good test of affinity, as the significance of second order coefficients a3-a5 and b3-b5 can be determined.

4.2.2 Singular Value Decomposition.

If we a have a set of simultaneous equations

$$\mathbf{A}\cdot\mathbf{x}=\mathbf{b}$$

Equation 4.2.6.

where A is a matrix of size MxN (M≥N), and **b** and **x** are vectors then **A** can be written as

$$\mathbf{A}=\mathbf{U}\cdot[\mathrm{diag}(\omega_j)]\cdot\mathbf{V}^{\mathbf{T}}$$

Equation 4.2.7

where **U** is a column-orthogonal matrix of size MxN, **W** is a diagonal matrix of size NxN with positive or zero elements ω_j and $\mathbf{V}^{\mathbf{T}}$ is the transpose of an NxN orthogonal matrix **V**. The SVD algorithm calculates the values on the right hand side of equation. The algorithm we used is based on a routine by Forsythe el al (1977).

Once the values have been established we may use the relation

$$\mathbf{x}=\mathbf{V}\cdot[\mathrm{diag}(1/\omega_j)]\cdot\mathbf{U}^{\mathbf{T}}$$

Equation 4.2.8

to evaluate the vector **x**.

4.2.3 Implementation of SVD using C code.

The code to carry out the operation of equations 4.2.8 and 4.2.7, the functions svdcmp() and svdbks(), were taken from a disk supplied with the publication by Press et al (1992), and is licensed for academic use. These functions were integrated into a main program shown below, which was written specifically for this project by the author. The code of the function svdcmp() was altered slightly in order to integrate the function into the main program and the code of svdbksb() was inserted into the function svdcmp() to minimise the number of variables to be declared. The source code for the program coeff.exe is shown in Appendix 1. The diagram Figure 4.2.2. explains the functionality of the program.

Figure 4.2.2. Functionality of program coeff.exe.

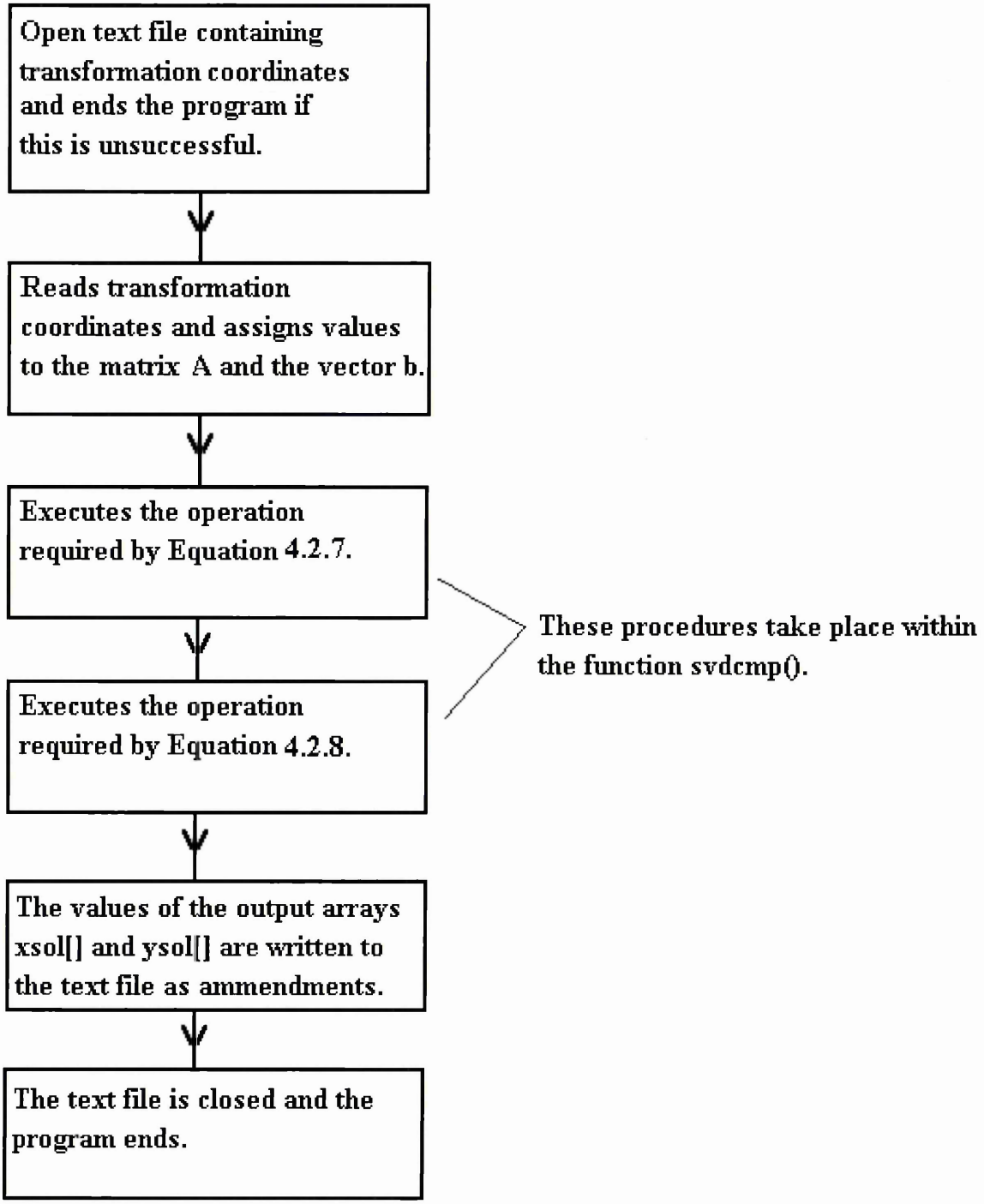

4.2.4 Application of Distcof.exe.

In order to describe the geometrical transformation between two images, both images must contain common physical features. These features are used to give the co-ordinates which are components of the simultaneous equations used to calculate the distortion function. For the application of EDX maps (or any analytical image) it is important that the features are spread across the whole field of view. The silicon test sample is ideal for this purpose as it has regular features which may be identified in two different images, for example one acquired at 5kV beam energy and one acquired at 15kV beam energy.

An image of the grid was acquired in which the one of the squares created by the broad lines was encompassed. The image was recorded with beam energies of 5, 10 and 15kV. Figure 4.2.3 shows numbered points on the 5kV image which were used to identify co-ordinate points.

Figure 4.2.3 Image at beam energy 5kV showing points which were used to take co-ordinate values.

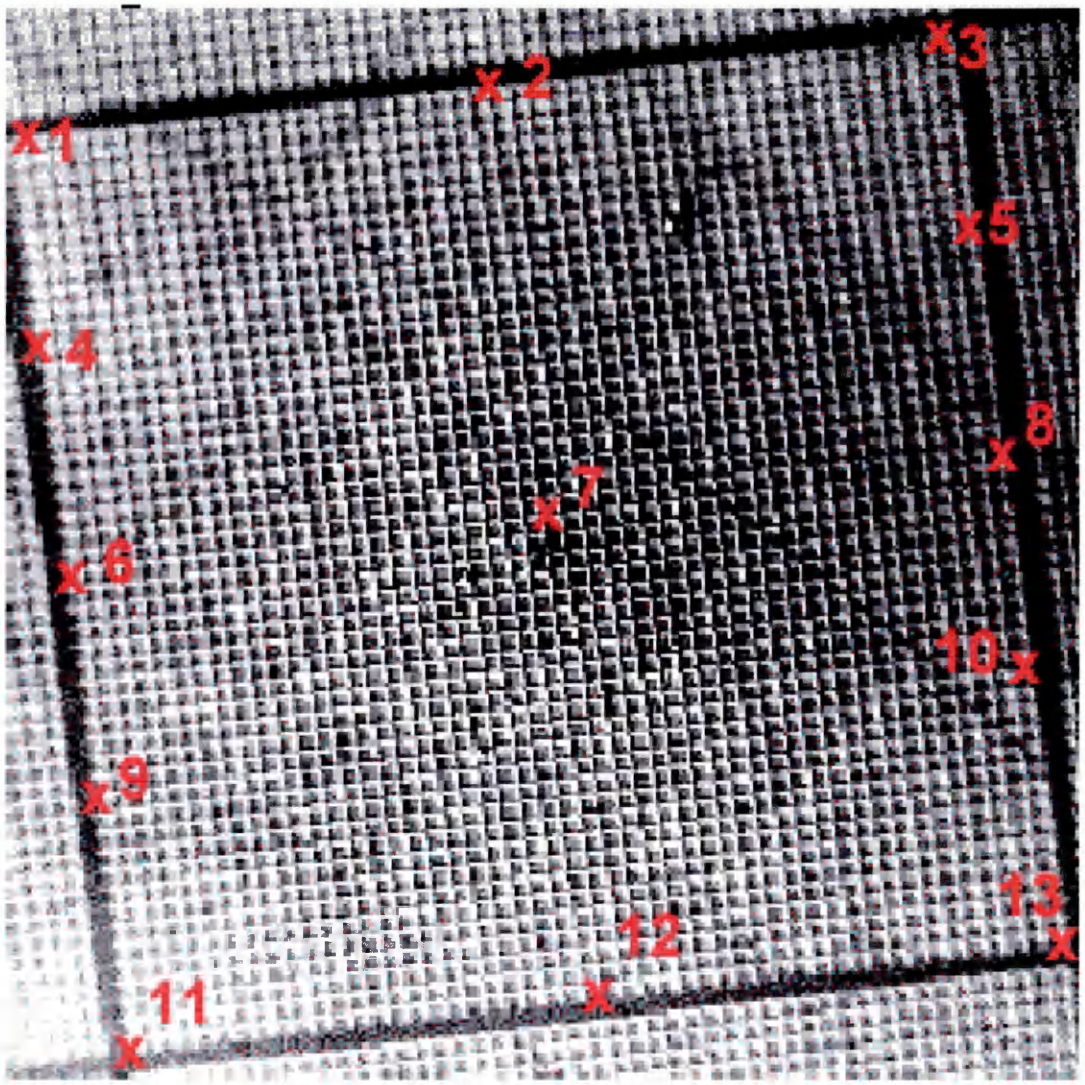

When choosing these points the main concern was to preserve symmetry about the centre of the field of view, and to cover a large section of the field of view. These measures are to prevent a solution which is localised to a part of the image. Obviously, to meet these criteria the more points used the better. The limiting factor is that the point co-ordinate values must be determined manually by the user, using a graphics viewing package, for each image. An excessive number of points would render the distortion determination procedure impractical. On this basis the thirteen points shown in Figure 4.2.3 were chosen. The markers indicate where one broad line crosses another broad line in the case of the outer perimeter points. The inner points are the intersection of the 20th small square in the particular direction with the broad line. The users themselves may decide which side of the line the pixel should lie, as long as consistency is maintained within the set of images.

The points were recorded manually and written into a text file in the form.

x_1,y_1,x_1',y_1'
x_2,y_2,x_2',y_2'
x_3,y_3,x_3',y_3'
.....
$x_{13},y_{13},x_{13}',y_{13}'$

This was done for the image transformation from 5kV to 10kV, and from 5kV to 15kV. The program distcof.exe was executed using the text files containing the co-ordinates, thus generating the coefficients of Equations 4.2.3. and 4.2.4 for the aforementioned transformations.

As mentioned in section 4.1 it was also necessary to investigate the image transformations on a conventional SEM. For this purpose a Philips XL40 microscope was used. This is a modern instrument in which we can assume all current design features to compensate for beam energy change have been implemented. In this instrument the sample could be rotated within the analysis chamber to align the square with the x and y axes of the image. Due to the higher spatial resolution attainable with the XL40 and the wider field of view, four squares were imaged. This meant that the chosen reference points were easier to define. Images of the sample were acquired and digitally recorded with a resolution of 1424 x 968 pixels at beam energies of 5, 10,15 and 20kV. Figure 4.2.4 shows the micrograph at 20kV and the chosen reference points. The co-ordinates of these points for all images were taken and written into text files. The program distcof.exe was executed and the coefficients for the transformations 5kV to 20kV, 10kV to 20kV and 15kV to 20kV were obtained.

Figure 4.2.4. Image with beam energy 20kV acquired on the XL40.

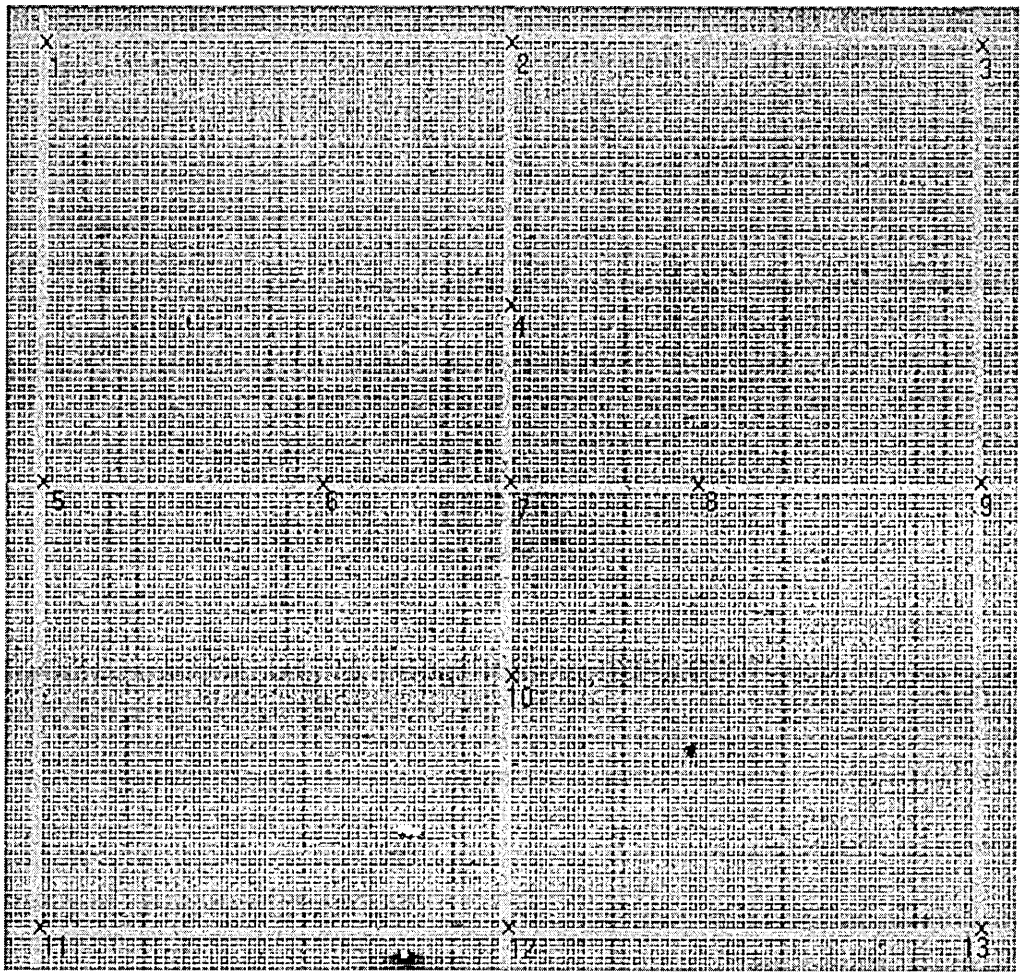

The procedure was also applied to images of the Cu grid which had previously been acquired. These images were x-ray images acquired with the EDX detector using the Cu Lα line (0.9297keV) as this line could be excited by primary beam energies from 5kV to 15kV. Images were recorded at beam energies from 5kV to 15kV at increments of 1kV. The image acquired at beam energy 15kV is shown as Figure 4.2.5 with the points used to take the co-ordinate values. The points were taken by noting the co-ordinates of the pixel at the middle of the square formed by the intersecting lines. The points were chosen to form a square of five small squares, as this covered a large area of the image. As the procedure for defining the points was less precise, more points were used. This example is one in which the images were not acquired specifically with the determination of transformation coefficients in mind, and where the image is of a smaller field of view. The co-ordinates were written into text files for all images and the transformation coefficients for 5kV to 6kV, 5kV to 7kV ..... up to 5kV to 15kV were calculated by the execution of the program distcof.exe.

Figure 4.2.5 Image of Cu grid acquired at beam energy 15kV.

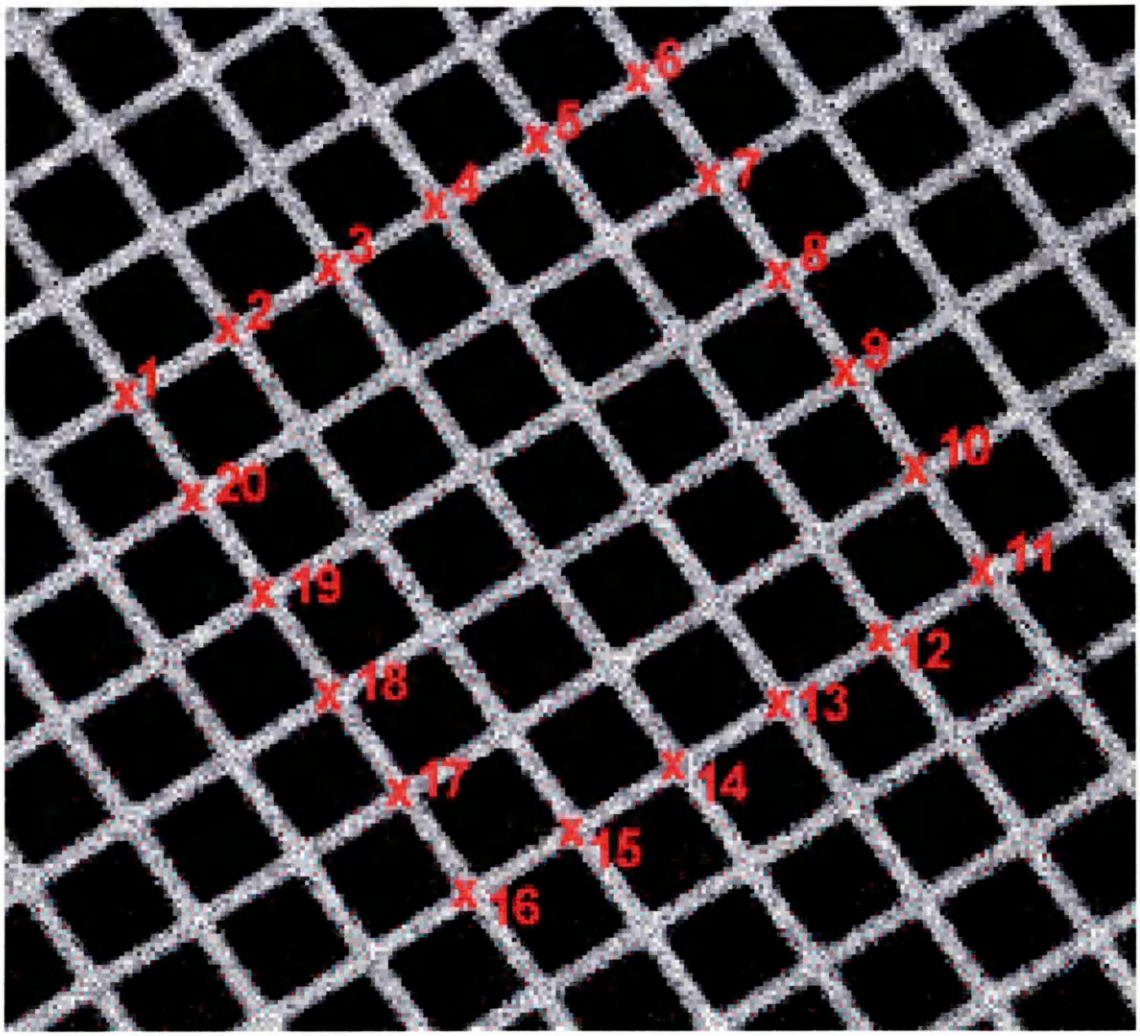

4.2.5 Results of Image Distortion Assessment.

The coefficients of the transformations between the images of the silicon grid acquired on the Hallam instrument are shown in Table 4.2.1.

Table 4.2.1 Coefficients for image transformations from Hallam instrument.

	Image Transformation.	
Coefficients.	10kV to 5kV	15kV to 5kV
a_0	0.694024	4.037447
a_1	0.994864	0.965953
a_2	0.003402	-0.000542
a_3	-0.000003	0.000055
a_4	0.000004	0.000006
a_5	-0.000024	-0.000005
b_0	0.260132	0.038761
b_1	-0.012126	-0.014675
b_2	0.994389	0.991082
b_3	0.000036	0.000060
b_4	-0.000006	-0.000011
b_5	0.000003	-0.000011

The coefficients of the transformations between the images of the silicon grid acquired on the Philips XL40 SEM instrument are shown in Table 4.2.2.

Table 4.2.2 Coefficients for image transformations from XL40

	Image Transformation.		
Coefficients.	5kV to 20kV	10kV to 20kV	15kV to 20kV
a_0	-0.551830	0.613785	1.535320
a_1	0.995317	0.994130	0.996105
a_2	0.015635	0.008075	0.003796
a_3	-0.000001	0.000000	-0.000001
a_4	-0.000001	0.000000	-0.000000
a_5	0.000001	0.000000	-0.000000
b_0	18.105101	13.274185	6.678392
b_1	-0.013008	-0.005041	-0.002636
b_2	0.995261	0.994846	0.994481
b_3	0.000000	-0.000001	0.000001
b_4	0.000002	0.000000	0.000002
b_5	-0.000000	-0.000000	-0.000001

For the transformations modelled the coefficients a3-a5, and b3-b5 only influence the final result if the value is greater than $\approx 1 \times 10^{-7}$ (as this causes a pixel shift of 0.1 pixels at the edge of the field of view). An examination of the coefficients shows a slight non- linearity for all transformations. Transformations between the middle 100 pixels of the images can be assumed to be affine as the non-linear coefficients have insignificant effect at this scale. This indicates increasing affinity between images as magnification is increased.

The coefficients a0, a2, b0 and b1 for the Philips XL40 SEM are plotted as a function of E_0 (transformation between E_0 and 20kV images), and are displayed as Figures 4.2.6, 4.2.7, 4.2.8 and 4.2.9. The coefficients a1 and b2 are not plotted as they remain relatively constant.

Figure 4.2.6.Coefficient a0 against beam energy.

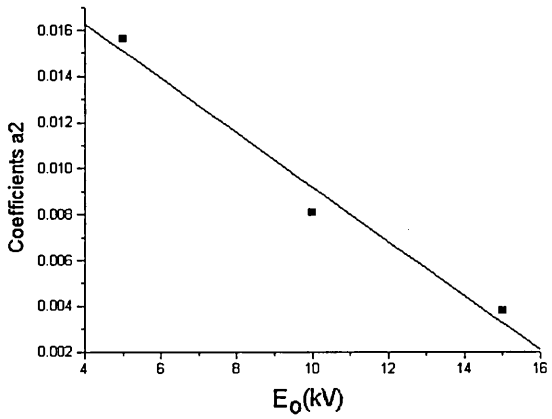

Figure 4.2.7.Coefficient a2 against beam energy.

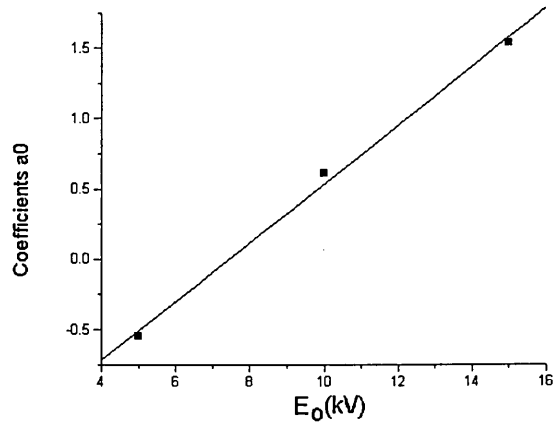

Figure 4.2.8.Coefficient b0 against beam energy.

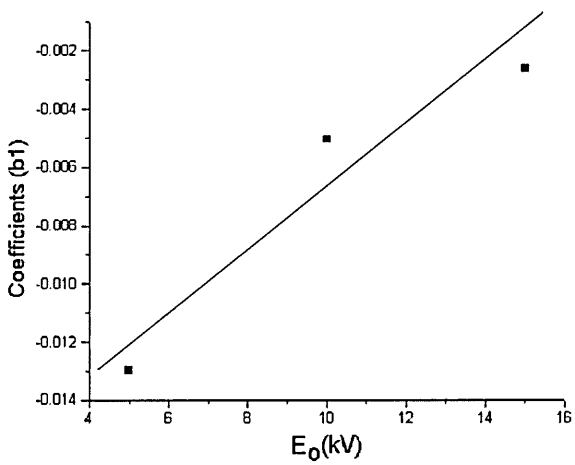

Figure 4.2.9.Coefficient b1 against beam energy.

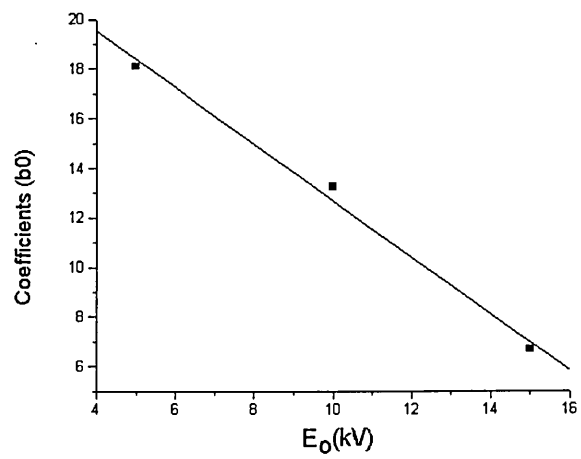

The coefficients a0, a1, a2, b0, b1, and b2 of the transformations between the images of the copper grid acquired on the Hallam instrument were plotted as a function of image beam energy relative to 5kV. If an obvious relationship were shown to exist between the coefficients and primary beam energy, it would be possible to apply the corrections as a function of beam energy, without having to manually determine the coefficients at each energy to be used. The plots are shown as Figures 4.2.10 to 4.2.15.

Figure 4.2.10 Coefficient a0 against beam energy.

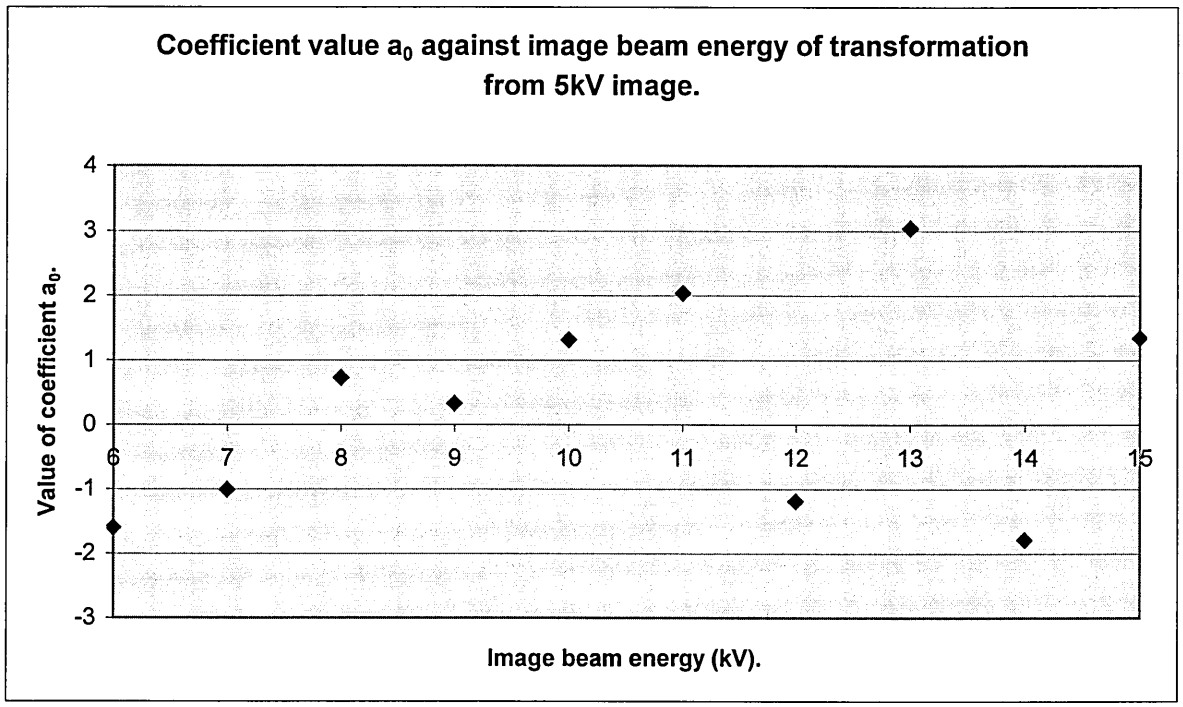

Figure 4.2.11 Coefficient a1 against beam energy.

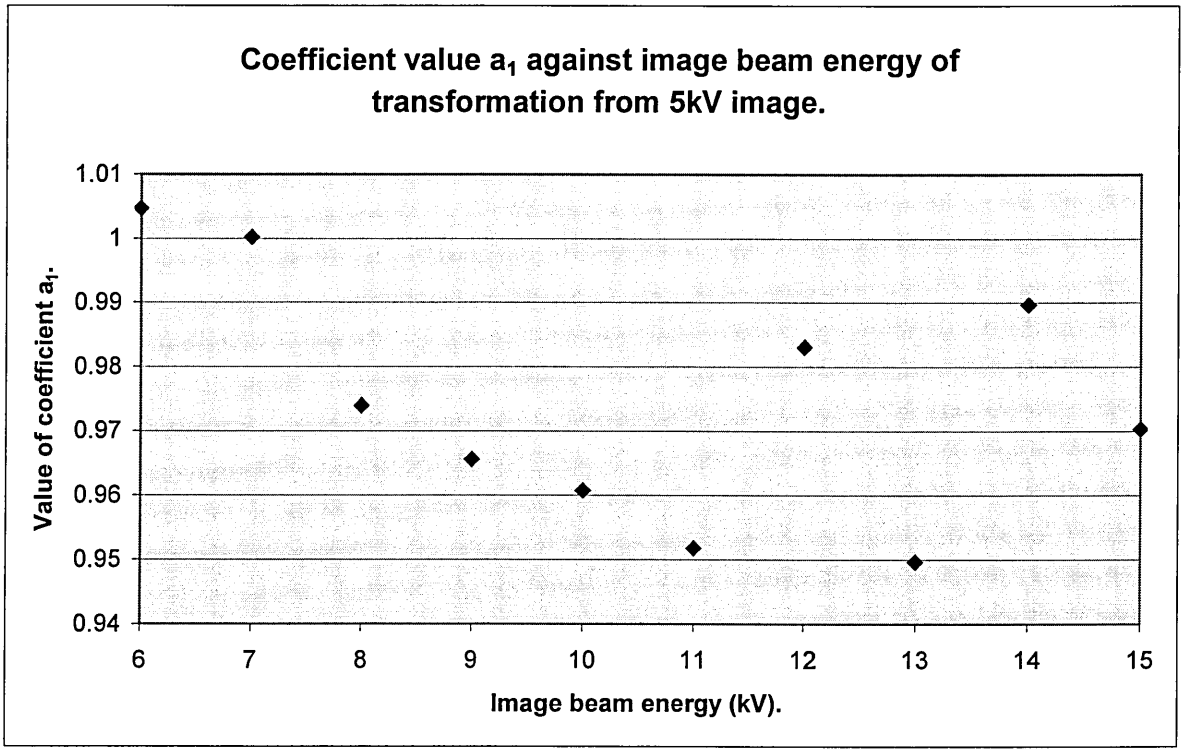

Figure 4.2.12 Coefficient a2 against beam energy.

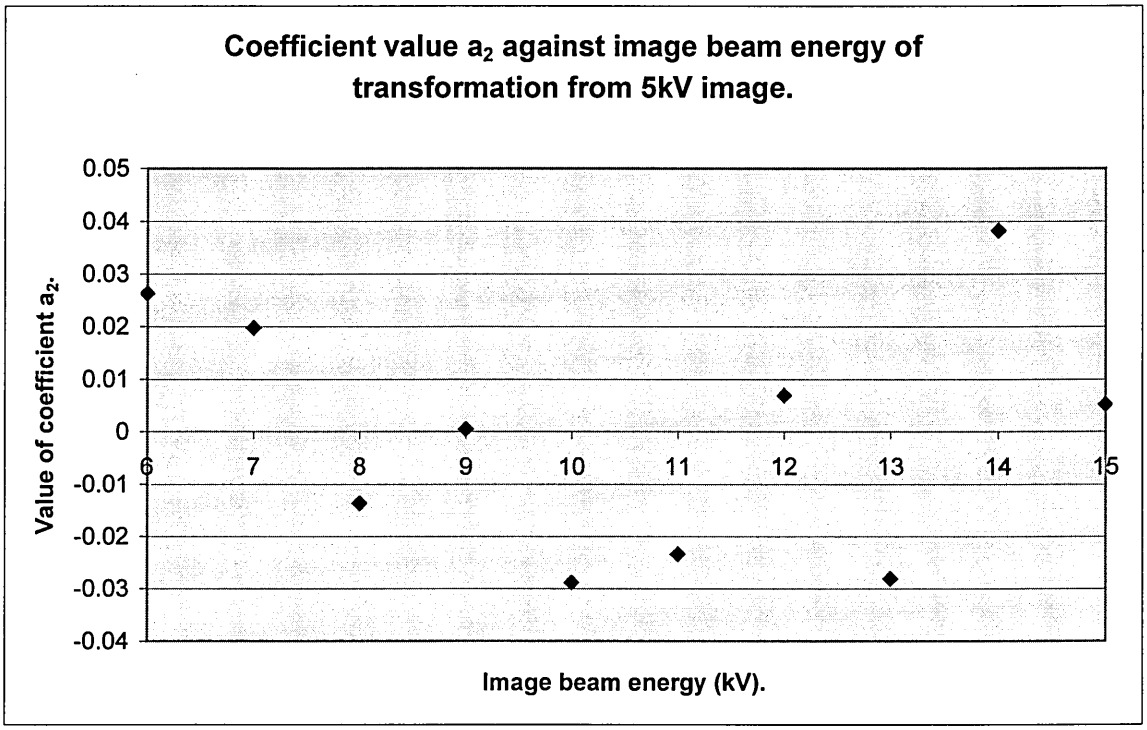

Figure 4.2.13 Coefficient b0 against beam energy.

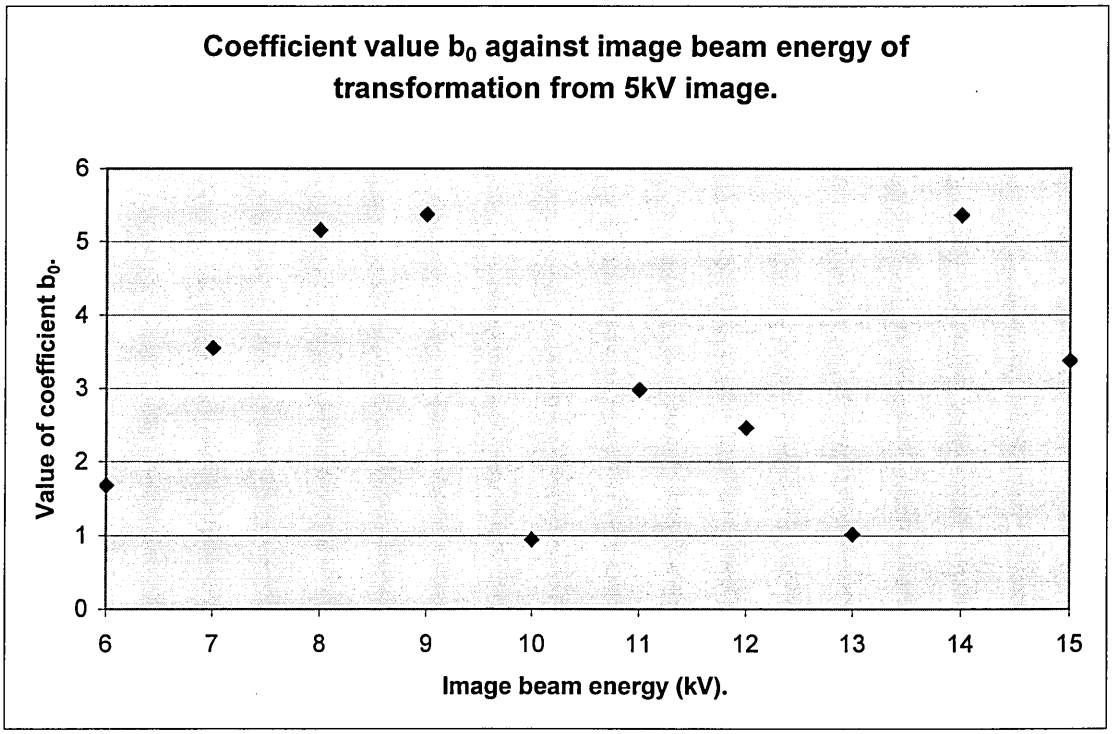

Figure 4.2.14 Coefficient b1 against beam energy.

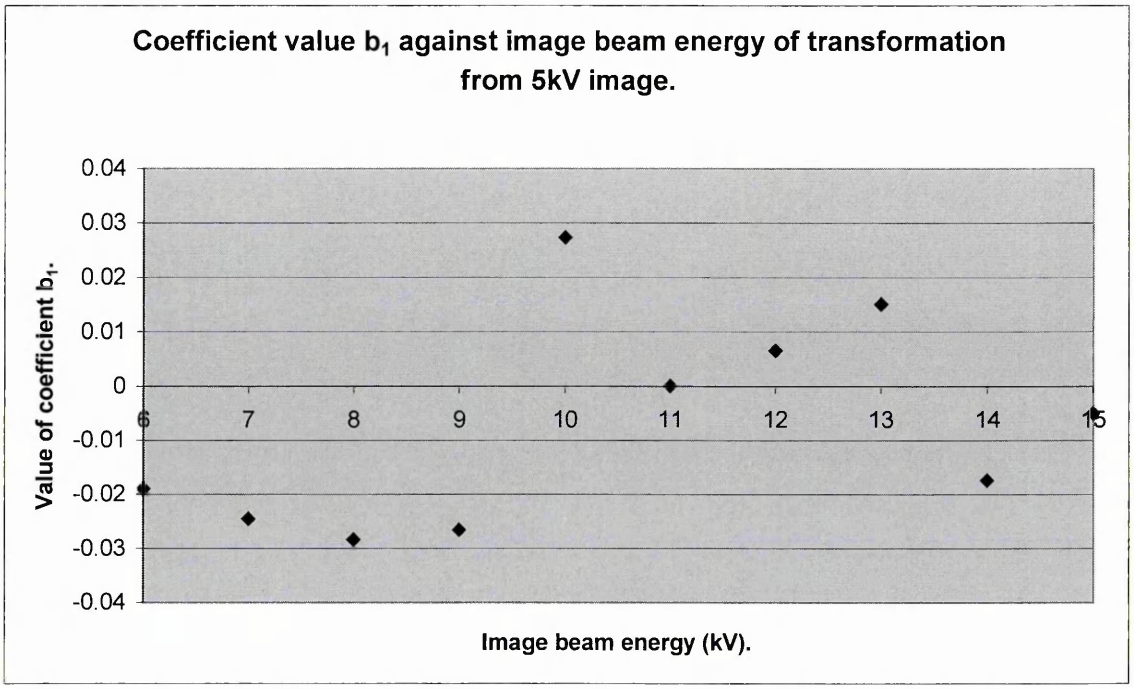

Figure 4.2.15 Coefficient b2 against beam energy.

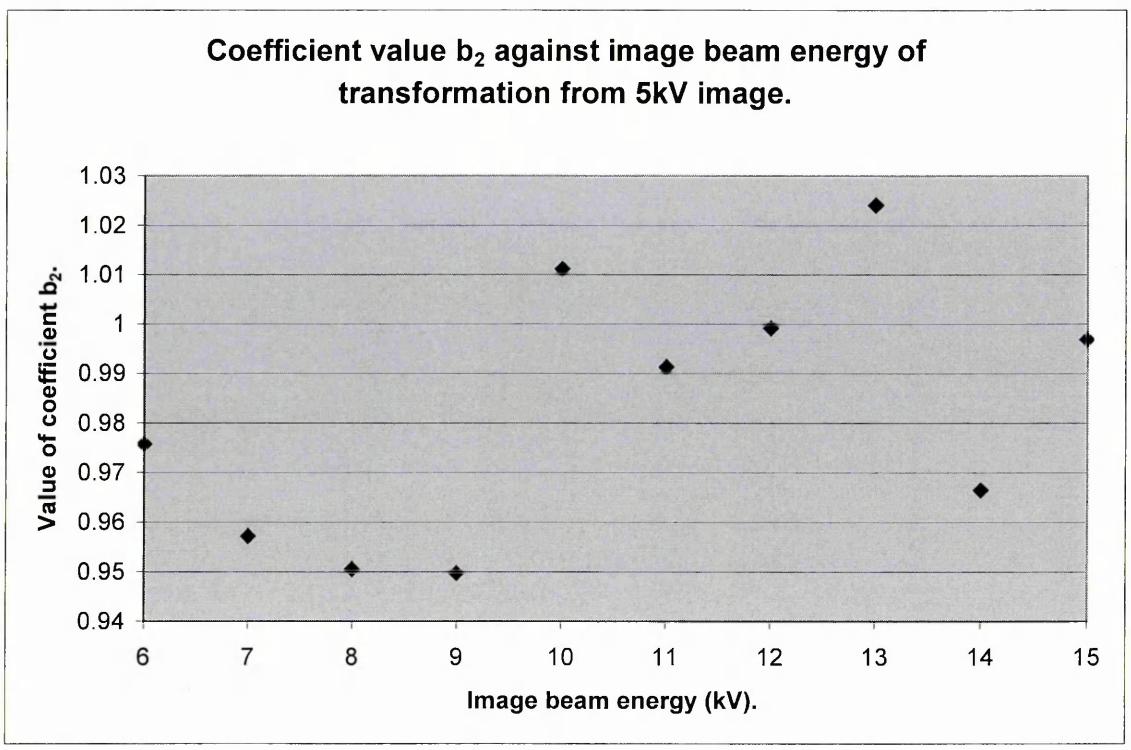

4.2.6. Discussion of transformations.

From the results of the silicon grid images acquired on the Hallam instrument displayed in Table 4.2.1, it is obvious that the terms a0, a1, a2, b0, b1, and b2 contribute to the transformed value of x' and y' significantly, characterising the obvious shift. The terms a3, a4, a5, b3, b4 and b5 have a small effect when applied to the actual co-ordinate values, but only at the extreme edges of the image.

For the results of the silicon grid images acquired on the XL40 displayed in Table 4.2.2., the terms a0, a1, a2, b0, b1, and b2 characterise the shift with the coefficients a3 –a5 and b3- b5 having minimal effect, The non-linear coefficients would cause a pixel shift of ≈ 1 at the edge of the image. Transformations between the middle 100 pixels of the images can be assumed to be affine as the coefficients have an insignificant effect at this scale, so on this instrument affinity between images appears to increase with magnification.

The non-linear coefficients for the transformations characterised on the Hallam instrument are about an order of magnitude higher than those of the XL40 image transformations. This is assumed to be caused by the defocusing and astigmatism of the beam on the Hallam instrument, which will affect the coefficients in two ways. The actual geometry of the image will be distorted as the shape of the beam is distorted, and the accuracy of the reference point co-ordinates defined manually will suffer as the image is of lower quality than the XL40.

The linear coefficients of the XL40 transformations were plotted in Figures 4.2.6 to 4.2.9 in order to ascertain if the coefficients vary as a simple function of E_0. The plots indicate that this may be the case.

The coefficients of the transformations between the images of the copper grid acquired on the Hallam instrument were plotted to further examine the variation in the transformation coefficients as a function of E_0. Some of the points of Figure 4.2.10 may lie on a straight line but other points (12kV,13kV,14kV) deviate dramatically from this. Similarly some points on Figure 4.2.11 may lie on a straight line, but again several points deviate strongly. No pattern can be observed in Figure 4.2.12 or Figure 4.2.13. In Figure 4.2.14 and 4.2.15 the points at beam energies 6kV, 7kV, 8kV and 9kV lie on a curve, but after this the points are scattered. We may conclude that the coefficients may not be characterised as a function of beam energy.

In the next section we shall consider how the coefficients may be used to align a series of images acquired at different beam energies. The ability to do this would enhance the thickness mapping capability of the instrument, as we could combine pixel intensity values from x-ray images acquired at different beam energies. If a value indicating thickness could be derived for each pixel, a thickness map could be generated.

4.3.0 Application of transformation coefficients to acquired images.

The aim of this work is to enable the comparison of images, which have been acquired at different beam energies. This may involve mathematical comparisons between images, which will require precise image registration. To realise this we must apply geometrical processes to one image, so that it will register with the other. Many image processing software packages provide this facility for geometrical manipulation of images, but there are two problems with this approach. Firstly, functions such as scaling, rotation and translation (affine operations) are available, but the application of these is difficult using the coefficients we have obtained. Also the spatial resolution to which these operations may be applied is limited. Secondly, the operation must be carried out on images stored in a conventional image file format (bitmap, tiff, jpeg etc.). This presents a problem as the values for pixel intensities in these file formats are stored as unsigned character integer types. This means the pixel values may only be expressed as integers between 0 and 255. This is sufficient for the display of an image but not when we need to store information with a higher numerical accuracy, which is the case when images are to be mathematically compared. It is necessary to store the image data in floating point format, then convert it to integer format for display.

These conditions require a program which will carry out a geometrical process on a file containing raw data, stored in floating point number format. The file would be classed as a raw image file as no header is present, only data representing pixel intensities. A raw image file stores the pixel value data sequentially from pixel (0,0) to (X_{max},Y_{max}) where X_{max} and Y_{max} are the image size. As the file has no header to store the image information, the file creator must have the image information stored elsewhere. The floating point data type may be between $3.4 \times 10^{\pm 38}$ with 7 digit resolution.

With geometrical processing one-to-one mapping of source to destination pixel is not possible. For example, with magnification changes one pixel in the source image may be mapped to many pixels in the destination image. Also, the mapping is further complicated because the mapping must be performed from the perspective of the destination image. This is called reverse mapping (Lindley 1991a) and is necessary to guarantee that every pixel in the destination image is assigned a value. Reverse mapping traverses the destination image space a pixel at a time and calculates, via the designated transformation, which pixel of the source image would be involved in producing the destination pixel. Reverse mapping also creates the need for approximation or interpolation. This occurs when the source image pixel that contributes to a destination pixel value is calculated. The lack of one to one pixel mapping results in the calculated source image pixel lying somewhere in the middle between four valid pixel locations in the source image. The fractional address of a source image pixel is shown in Figure 4.3.1.

Figure 4.3.1 Fractional address of a source image pixel (Lindley 1991b).

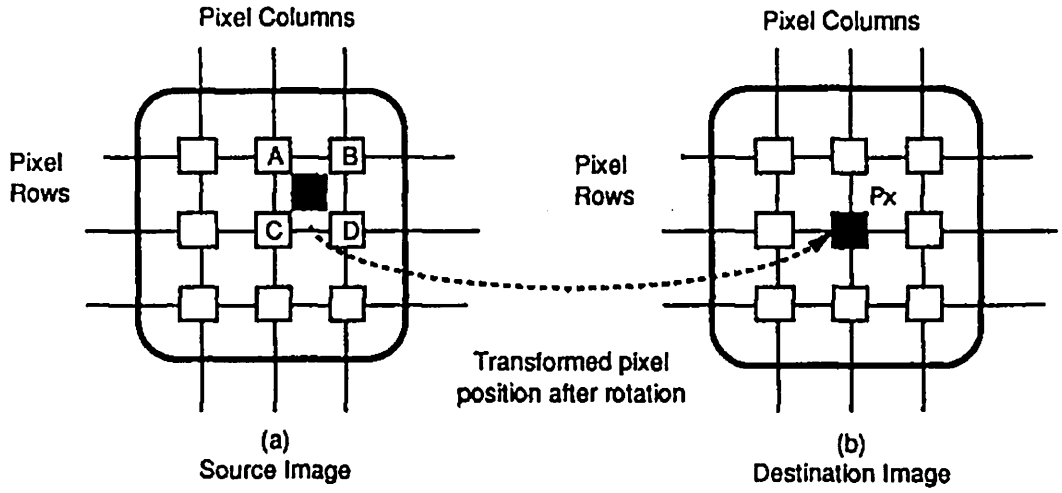

The simplest method of assigning a value to P_x would be the nearest neighbour approximation, where the fractional address of the black pixel in (a) would be truncated to the nearest integer pixel address (ie pixel A). This would produce a highly distorted image, so nearest neighbourhood approximation is not used here. In this work linear interpolation is used to calculate a new value for some point that is that is situated between other points of known value. Linear interpolation assumes that the contribution of a pixel in the neighbourhood (surrounding pixels) varies linearly with its distance from the point. To obtain an interpolated value for the pixel of interest in the destination image, three interpolations must actually be performed. They are the intensity contributions to the pixel of interest, P_x, from pixels A and B, the contribution from pixels C and D, and the contribution from AB and CD. Algebraically the operation can be expressed as (Lindley 1991b):-

Coldelta = Fractional Column Address of P_x – integer Column Address of Pixel A.

Rowdelta = Fractional Row Address of P_x – integer Row Address of Pixel A.

With these distances calculated, the three interpolations follow:

ContribAB =[Coldelta x (Pixel B intensity – Pixel A intensity)] + Pixel A intensity.

ContribCD =[Coldelta x (Pixel D intensity – Pixel C intensity)] + Pixel C intensity.

Therefore:

P_x = [Rowdelta*(ContribCD – ContribAB)] +ContribAB

4.3.1. Application of nearest neighbourhood approximation

The nearest neighbourhood interpolation method of geometrical transformation was integrated into a C program, which was written specifically for this project by the author. The source code of the program is shown in Appendix 1, and the functionality is shown as Figure 4.3.1.

The program requires three file names, that of the raw input image file, the name of the raw image output file and the name of the text file containing the transformation coefficients. The program reads the coefficients and for each destination pixel calculates the position of the source pixel. The value of the source pixel neighbourhood pixels are obtained, and the destination pixel value calculated. The program writes each destination pixel value to the output raw image file sequentially.

Precautions are taken to avoid spurious border effects which may occur when the program requests source pixels which are outside the border of the source image. In this case the pixel values are set to zero, so these regions should be apparent in the output images as black borders.

4.3.2 Implementation of transkV.exe and results.

The intended application of the program, transkV.exe, are EDX images, but to test the program the images whose transformation coefficients had been obtained were used. The images could be converted from tiff files to raw image files of floating point numbers using the image processing software Visilog supplied with the ISIS system. The output files of transkV.exe could also be displayed using this system and converted to conventional image formats.

The following image transformations were performed:-

Images of the silicon grid acquired on the Hallam instrument.
10kV image registered with 5kV image.
15kV image registered with 5kV image.

Images of the silicon grid acquired on the Phillips XL40 SEM.
5kV image registered with 20kV image.
10kV image registered with 20kV image.
15kV image registered with 20kV image.

Images of the copper grid acquired on the Hallam instrument.
10kV image registered with 5kV image.
15kV image registered with 5kV image.

The images are shown before and after transformation, along with the image it has been registered with.

Figure 4.3.1. The functionality of the program transkV.exe.

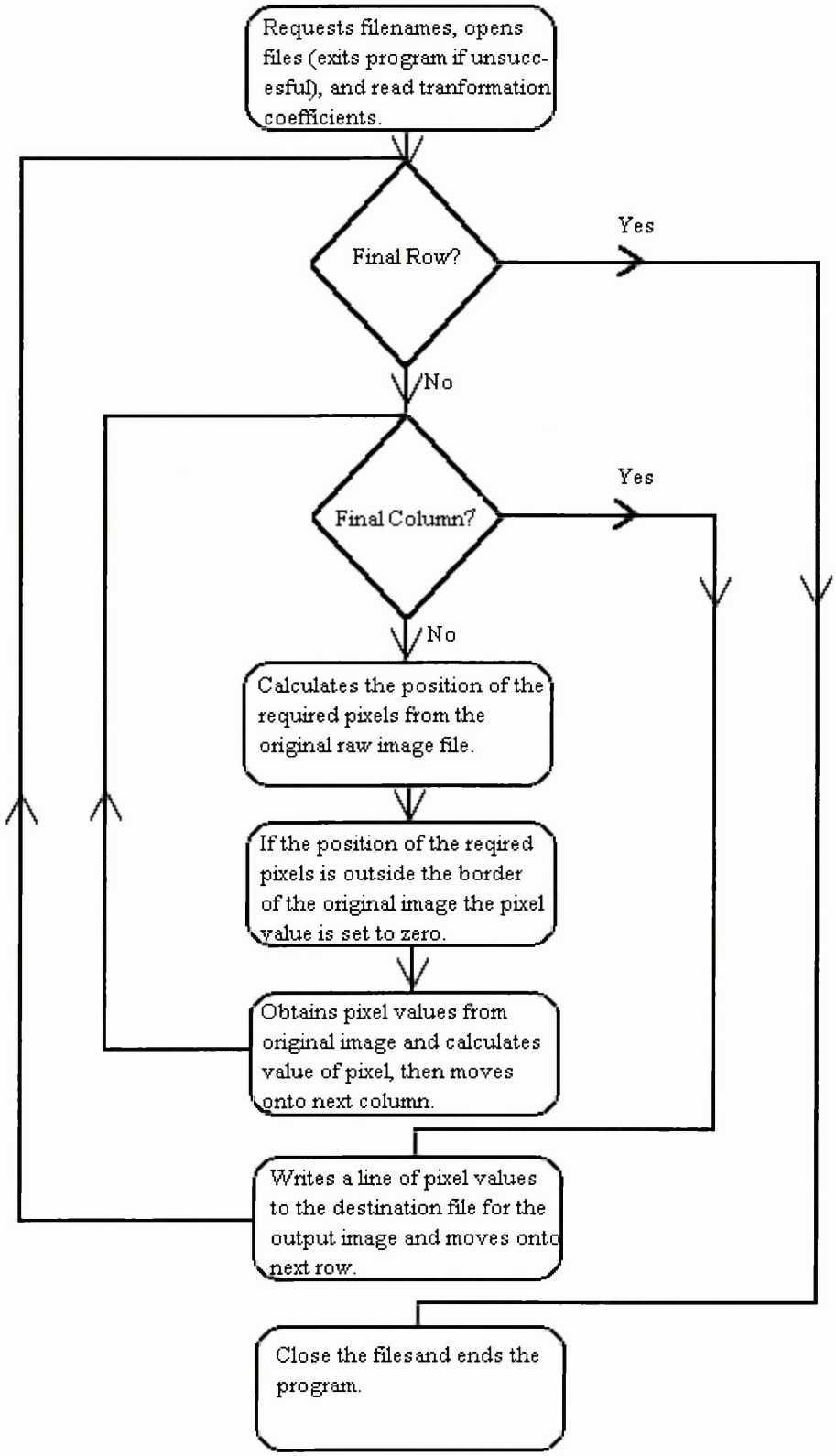

Figure 4.3.2. Original image of silicon grid acquired on the Hallam instrument at beam energy 5kV.

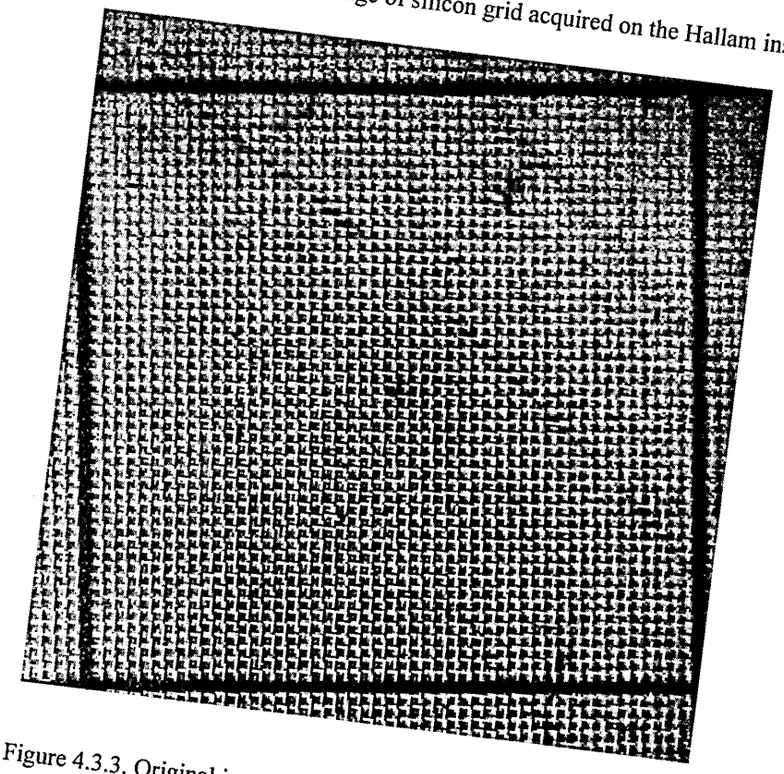

Figure 4.3.3. Original image of silicon grid acquired on the Hallam instrument at beam energy 10kV.

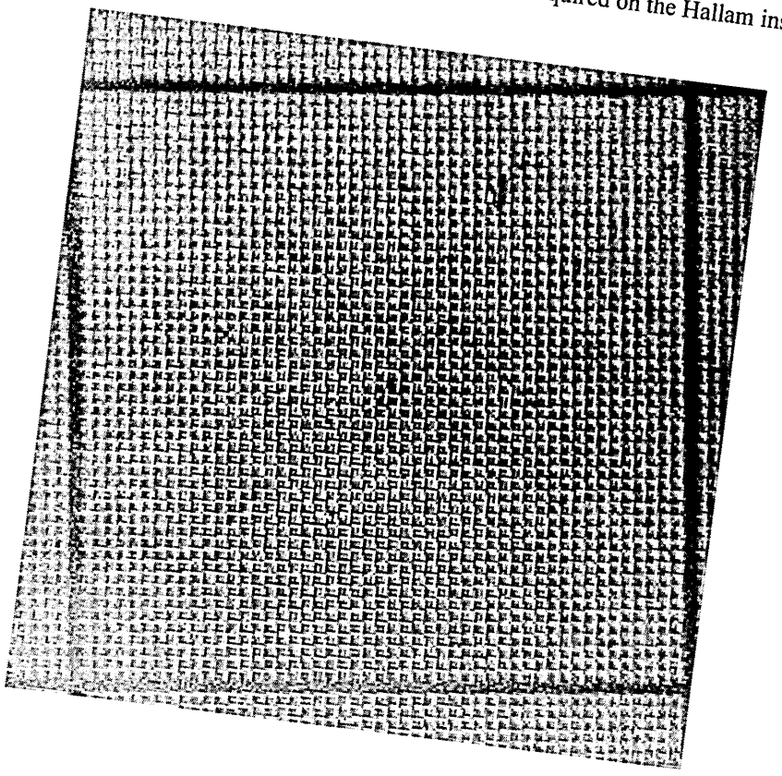

Figure 4.3.4. Modified image of silicon grid acquired at 10kV, registered with the 5kV image.

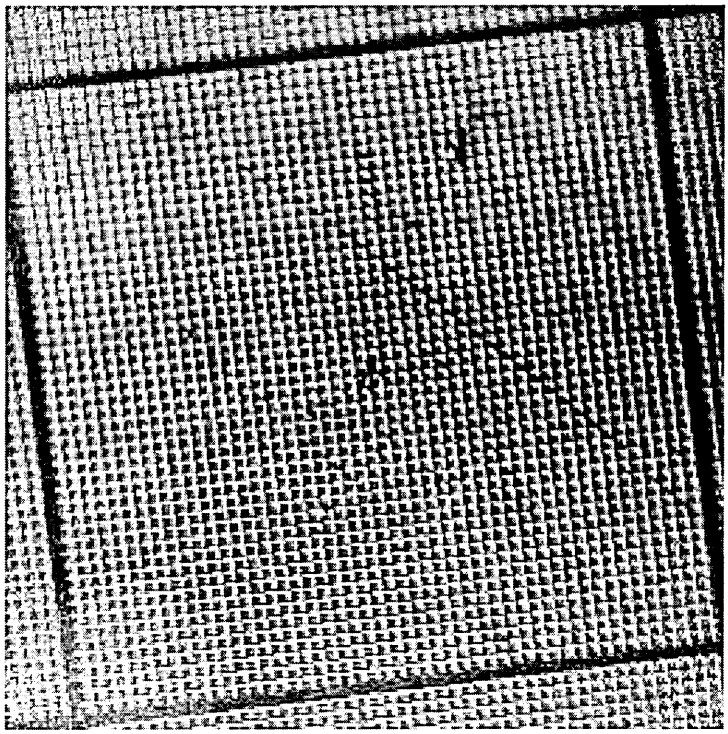

Figure 4.3.5. Original image of silicon grid acquired on the Hallam instrument at beam energy 15kV.

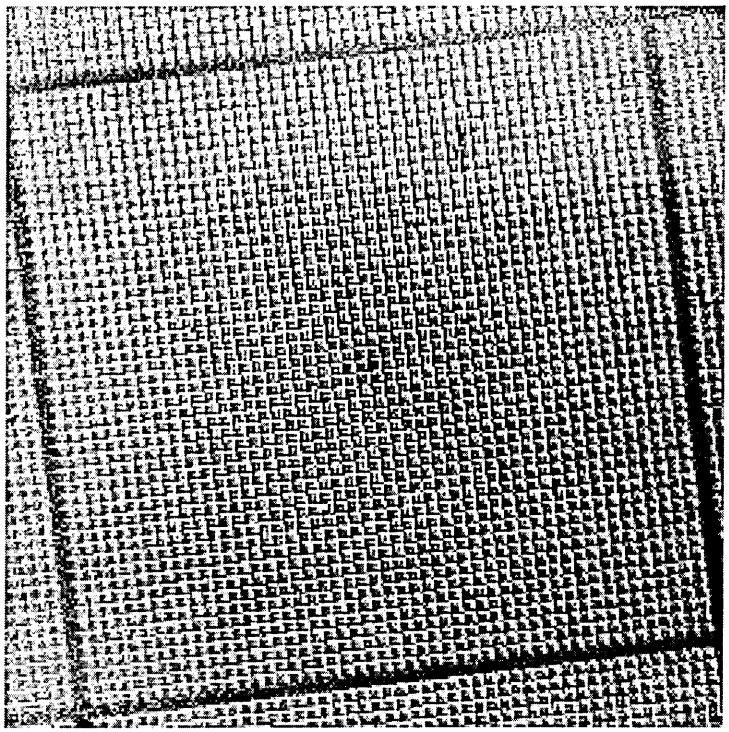

Figure 4.3.6. Modified image of silicon grid acquired at 15kV, registered with the 5kV image.

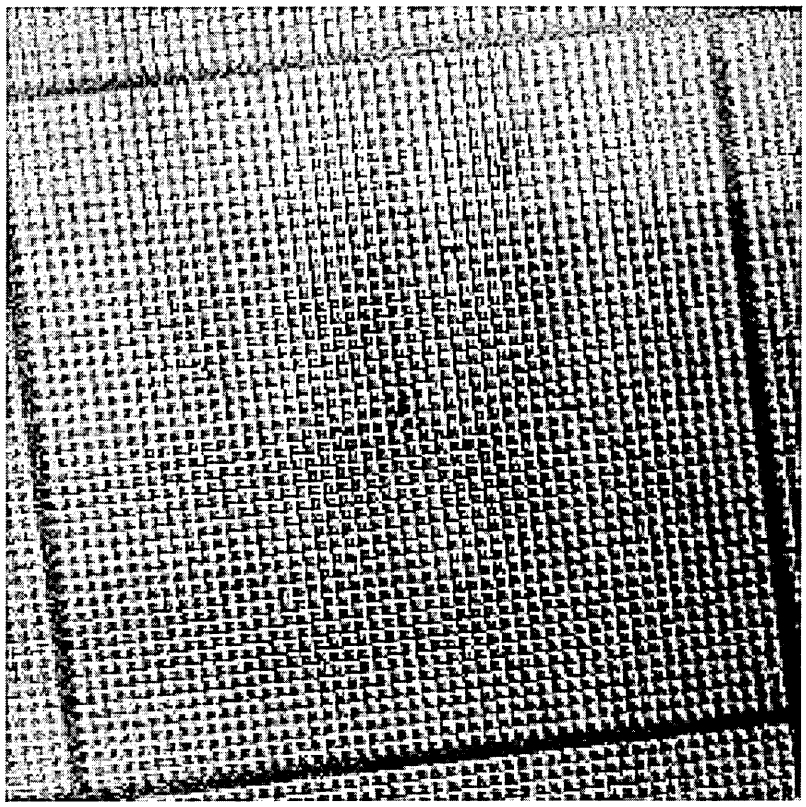

Figure 4.3.7. Original image of silicon grid acquired on the XL40 at beam energy 20kV.

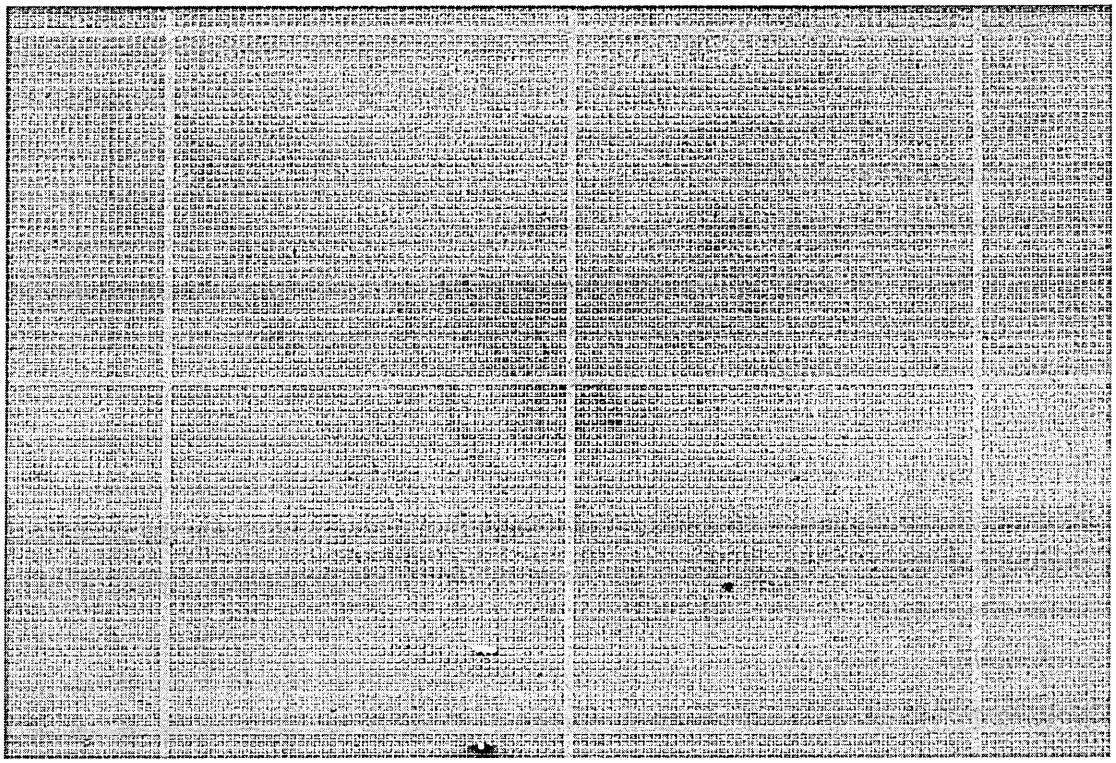

Figure 4.3.8. Original image of silicon grid acquired on the XL40 at beam energy 15kV.

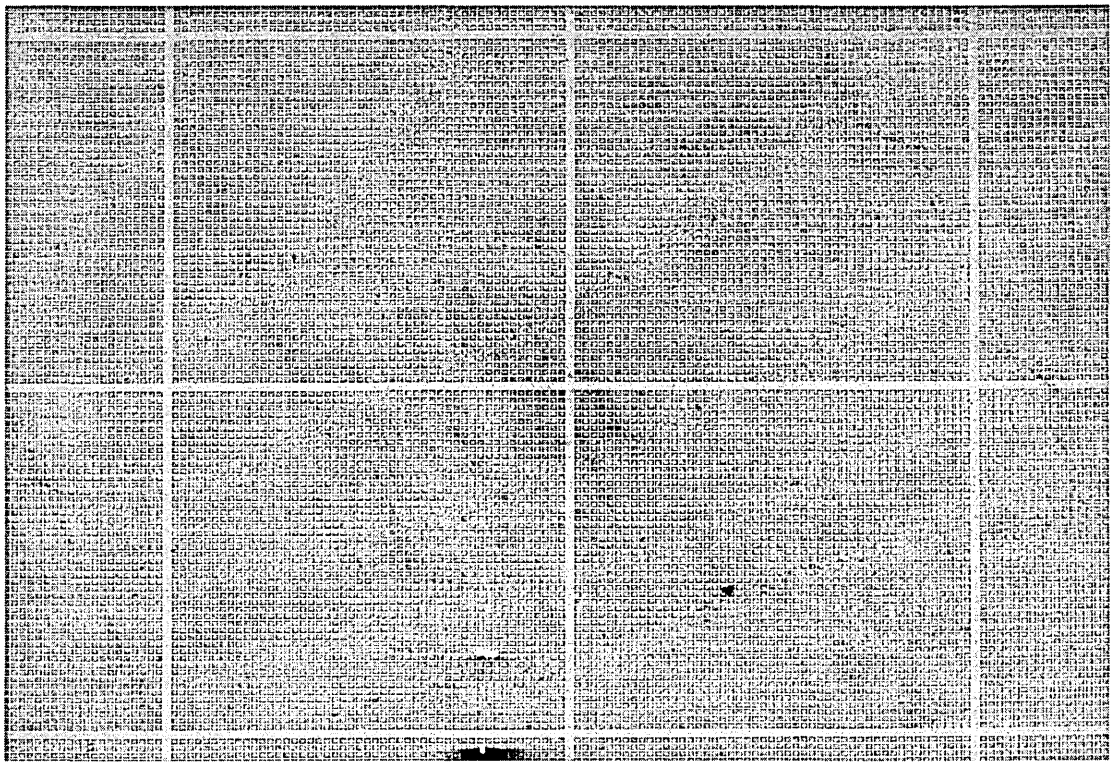

Figure 4.3.9. Modified image of silicon grid acquired at 15kV, registered with the 20kV image.

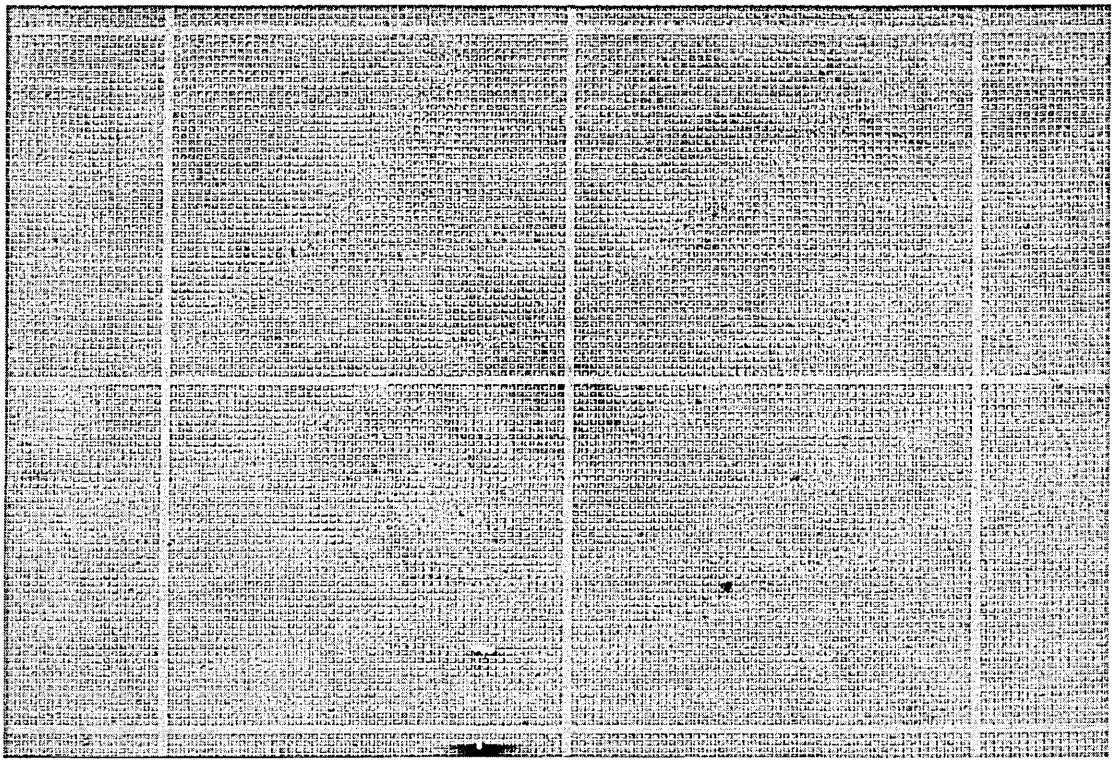

Figure 4.3.10. Original image of silicon grid acquired on the XL40 at beam energy 10kV.

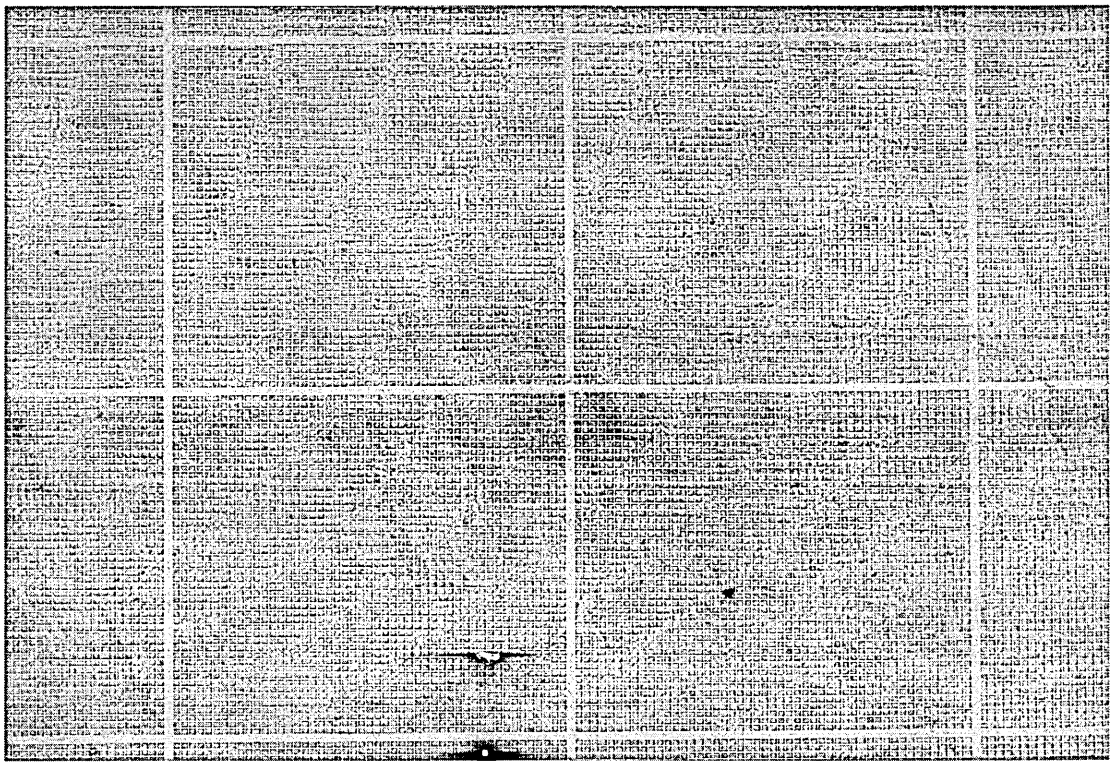

Figure 4.3.11. Modified image of silicon grid acquired at 10kV, registered with the 20kV image.

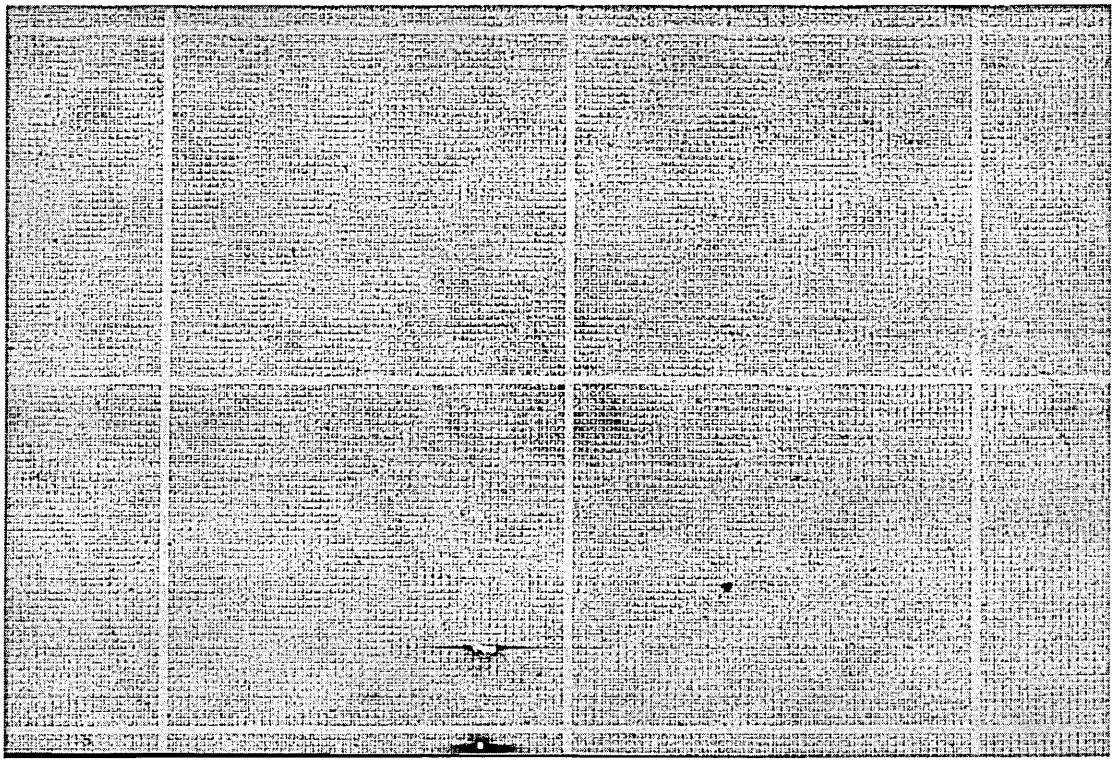

Figure 4.3.12. Original image of silicon grid acquired on the XL40 at beam energy 5kV.

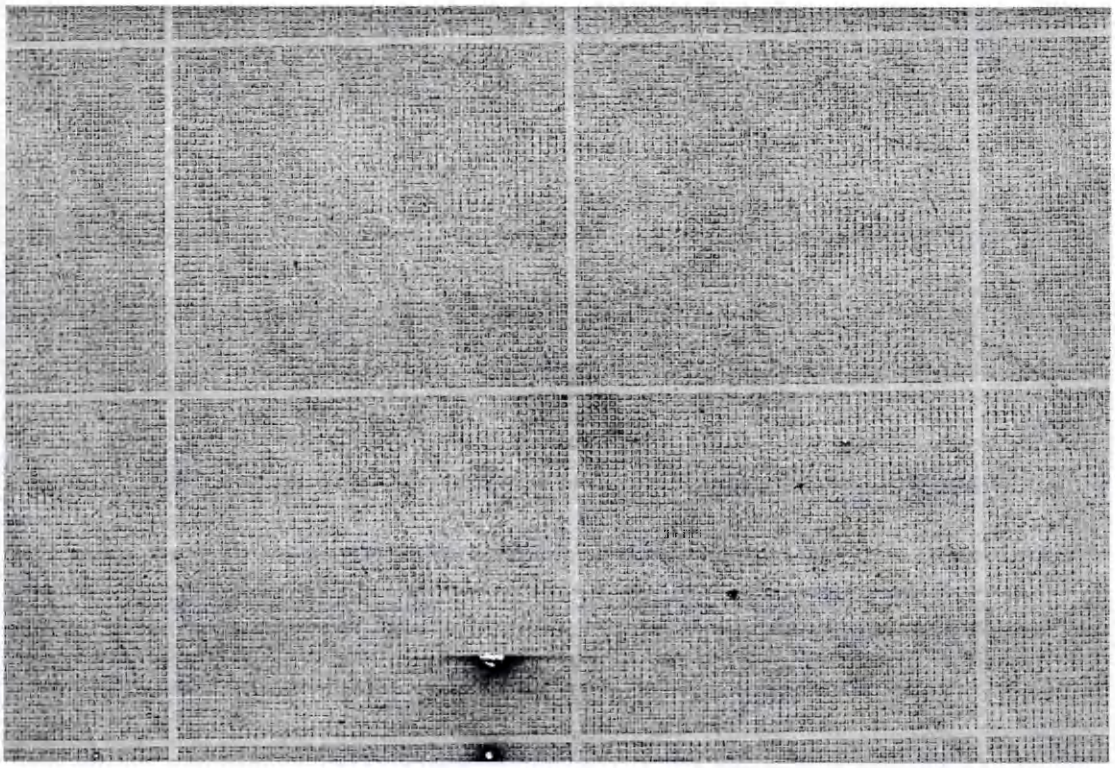

Figure 4.3.13. Modified image of silicon grid acquired at 5kV, registered with the 20kV image.

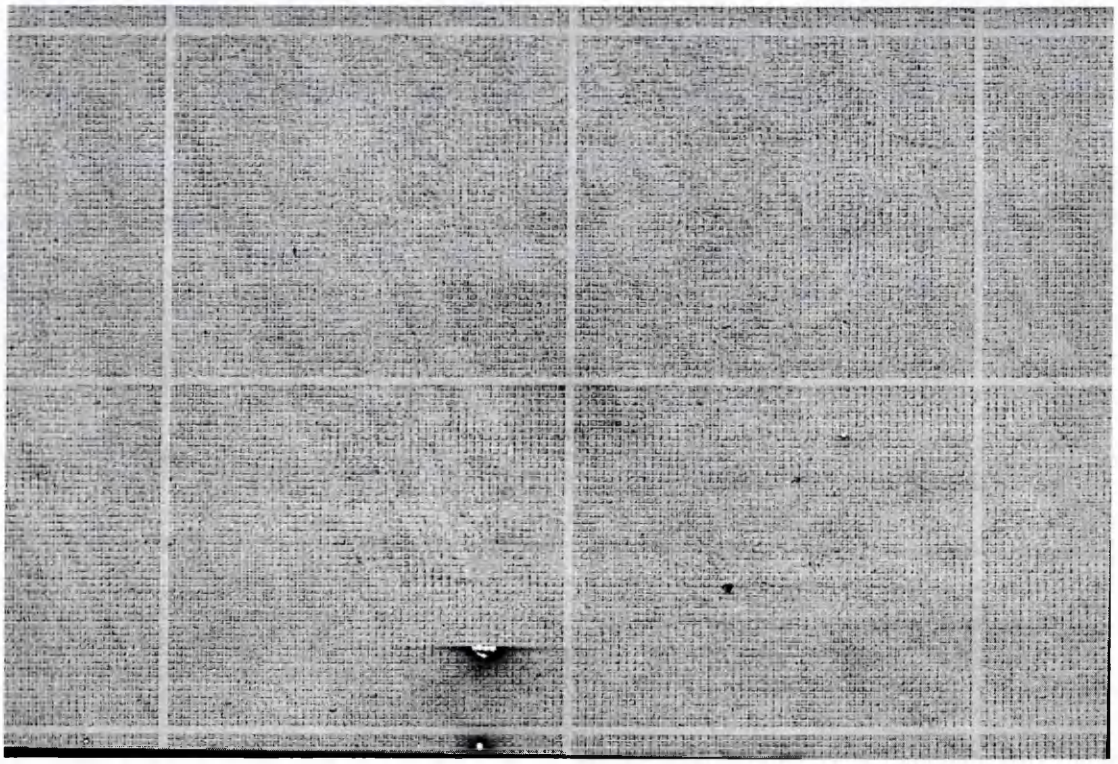

Figure 4.3.14. Original EDX map of copper grid acquired on the Hallam instrument at beam energy 5kV.

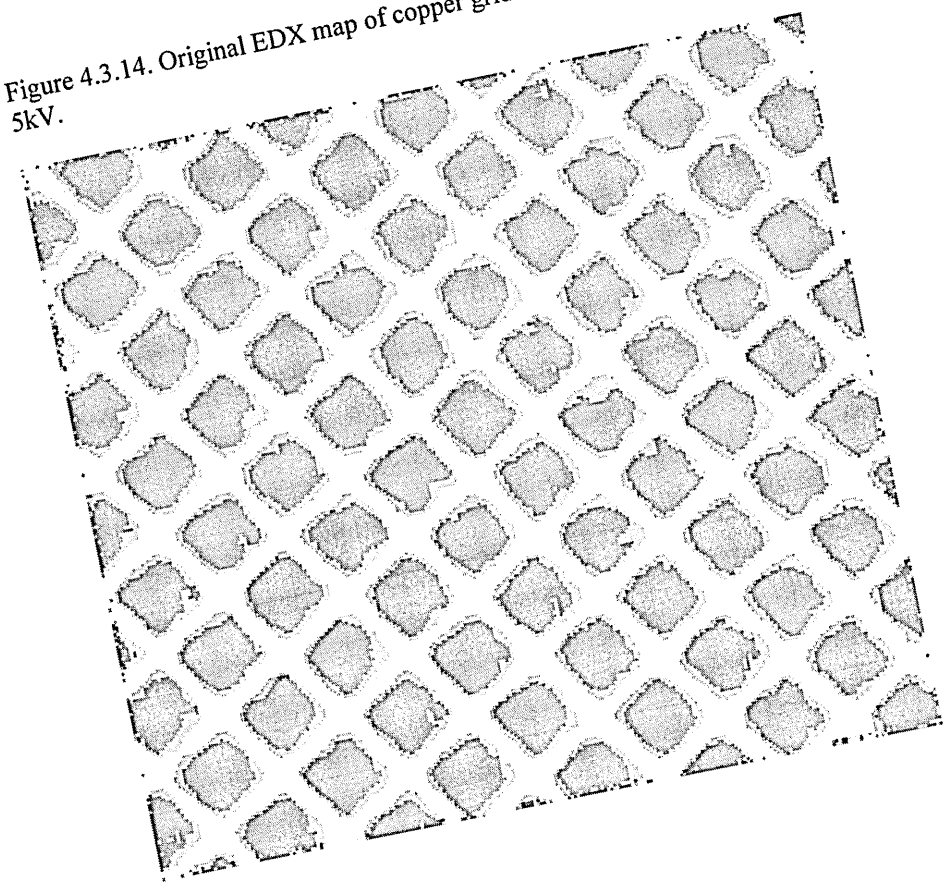

Figure 4.3.15. Original EDX map of copper grid acquired on the Hallam instrument at beam energy 10kV.

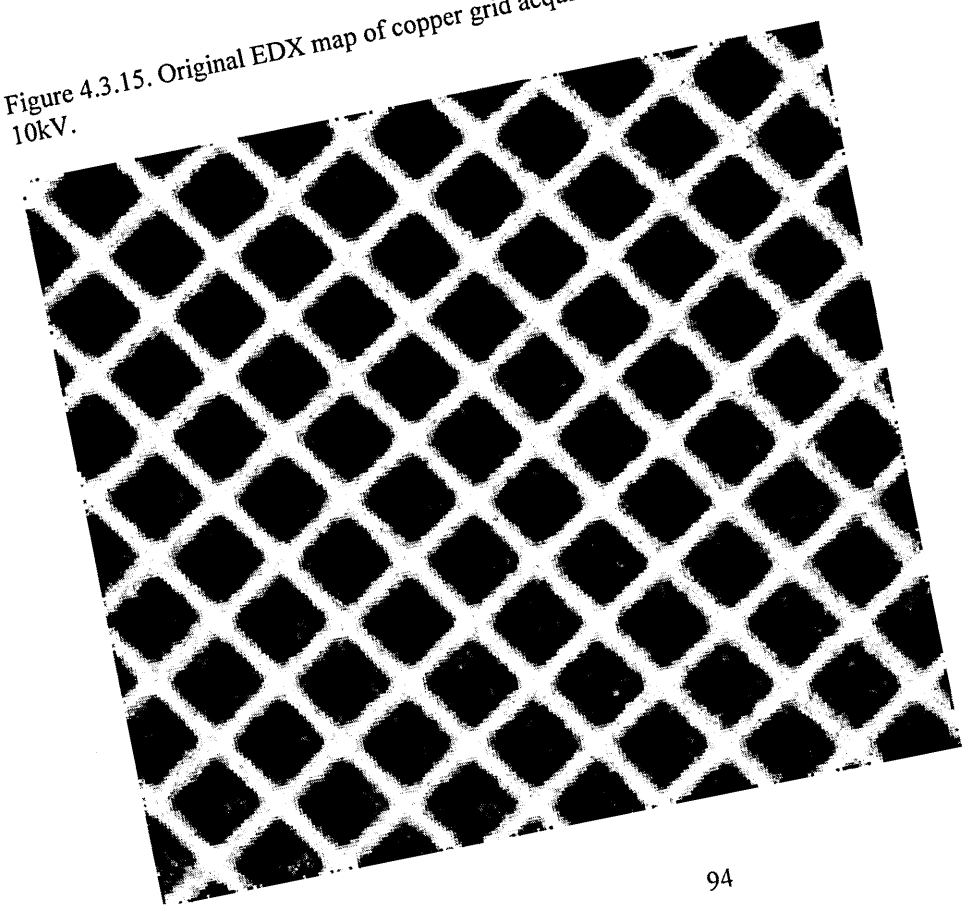

Figure 4.3.16. Modified EDX map of copper grid acquired at 10kV, registered with the 5kV image.

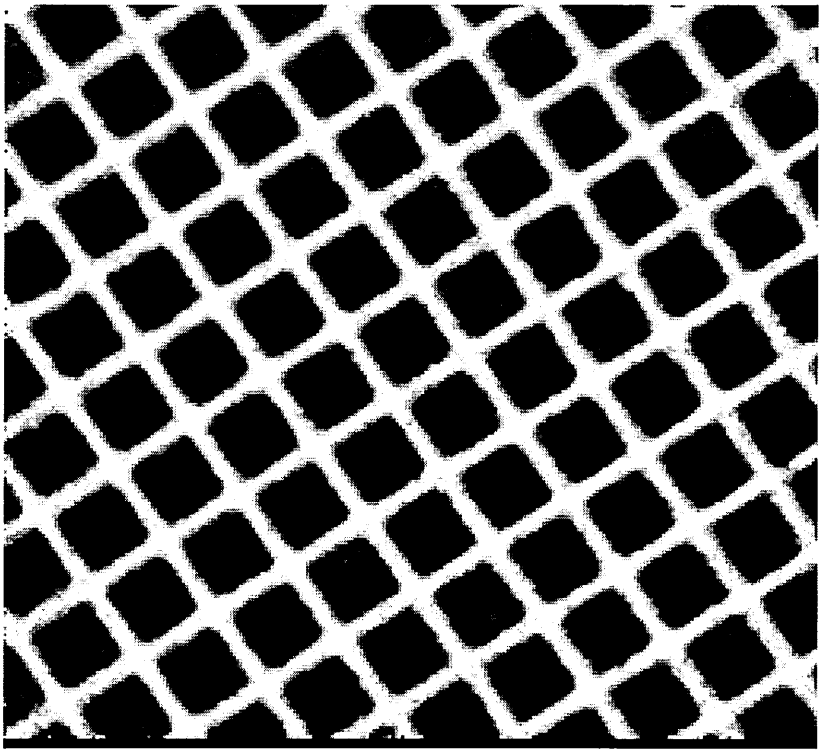

Figure 4.3.17 . Original EDX map of copper grid acquired on the Hallam instrument at beam energy 15kV.

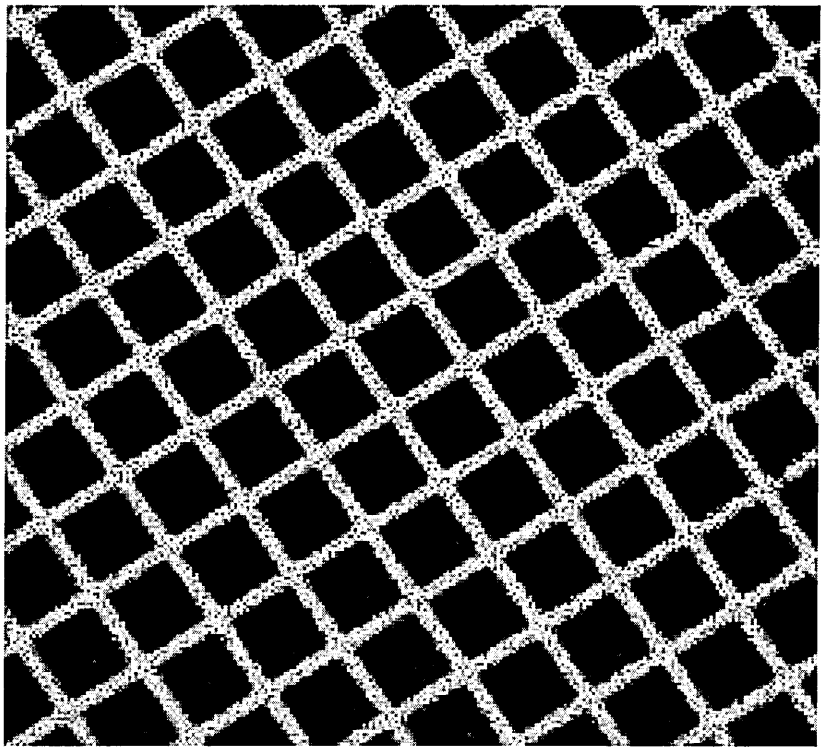

Figure 4.3.18. Modified EDX map of copper grid acquired at 15kV, registered with the 5kV image.

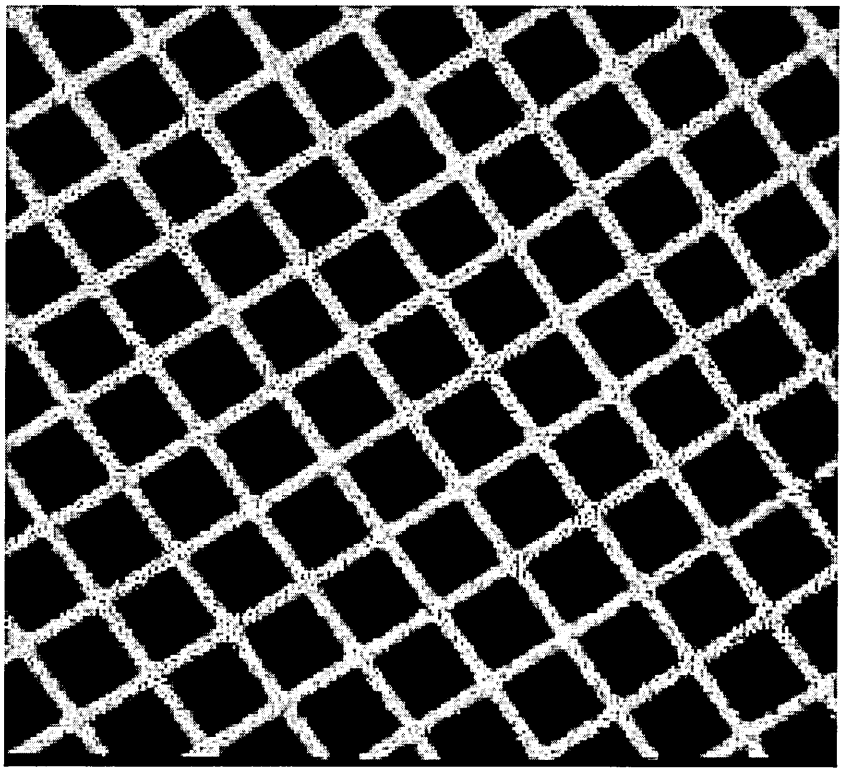

4.3.3. Discussion.

Examination of Figures 4.3.2 to 4.3.6 shows that transformations were effective for each image. If the corner of the square, which is formed by the main dark border is observed closely, small shifts can be seen between the original images (5kV to 10kV, 5kV to 15kV). It can be seen in the modified images that these shifts have been corrected.

Figures 4.3.7 to 4.3.13 also show the program to be effective . Examination of the black border created by void source pixel values reveal the increasing effect of rotation from 15kV to 5kV images. On a high resolution computer monitor the viewer can see a slight blurring effect between the original and the transformed image for this set of images. The images printed on paper are unable to display this. The images from the XL40 are acquired as rectangles. The program was designed to handle images where $x_{max} \neq y_{max}$, so the images were left with their original pixel dimensions.

Figure 4.3.14 shows an EDX image of the copper grid. As the Cu Lα x-ray peak is of low intensity with a 5kV primary beam energy, the initial image was of poor quality. The image shown was processed to enhance the grid lines and aid co-ordinate point measurements. Observations of Figures 4.3.15 to 4.3.18 reveal successful transformations. Comparison of Figures 4.3.15 to Figure 4.3.16 and Figure 4.3.17 to 4.3.18 reveal an obvious blurred effect between the original and transformed image. This is a consequence of the destination pixel being the average of four neighbouring source pixels, resulting in a degradation of image spatial resolution.

If this procedure was to be carried out for analytical purposes it would be necessary to acquire the original image with a pixel resolution twice that of the spatial resolution of the acquisition system. This would allow transformations to be carried out without reducing the spatial resolution of analytical information.

The offline correction system has proved that obtaining the transformation allows for distortions to be compensated. The original transformations coefficients could also be used to modify the acquisition scan signals. This would be an online correction of distortions, and be more effective than the offline procedure used here, as no image processing resulting in information loss would be necessary to register the images. As all modern microscope scan systems are driven through digital to analogue converters, this could be implemented into the acquisition software. Determination of the transformation coefficients, using a purpose made sample, would allow regular calibration of this system. The disadvantage of this system is that it must be implemented by the instrument manufacturer. For this to be done there must be commercial demand for compositional and thickness mapping by multi-kV analysis.

4.3.4 Conclusion.

The proposed technique for alignment of images acquired at different primary electron beam energies was shown to be successful. Presently, an algorithm has not been developed which can derive a thickness map from a series of maps acquired at different beam energies. As was pointed out in Chapter 2, this has been done for thickness measurements taken at points from a sample, so it should be possible to extend this to maps. This techniques of aligning maps may also produce a series of spatially aligned EDX maps which may be analysed using multivariate statistics (Prutton et al 1999, Bonnet 1997).

References for Chapter 4:

Bonnet N. (1997) Journal of Microscopy, 190, 2-18.

Forsythe G.E., Malcolm M.A. Moler C.B. (1977) Computer Methods For Mathematical Computations, Prentice Hall (New Jersey), Chapter 9.

Jian A.K. (1989) Fundementals of Digital Image Processing, Prentice Hall International (UK) pg 321.

Lindley C.A. (1991a) Practical Image Processing in C, John Wiley & Sons (UK) pg 418.

Lindley C.A. (1991b) Practical Image Processing in C, John Wiley & Sons (UK) pg 424.

Pratt W.K. (1991) Digital Image Processing 2nd Ed, John Wiley & Sons (UK) pg.430.

Press W.H., Teukolsky S.A., Vetterling W.T., Flannery B.P., (1992a) Numerical Recipes in C 2nd Ed. Cambridge University Press (UK) pg41.

Press W.H., Teukolsky S.A., Vetterling W.T., Flannery B.P., (1992b) Numerical Recipes in C 2nd Ed. Cambridge University Press (UK) pg43.

Press W.H., Teukolsky S.A., Vetterling W.T., Flannery B.P., (1992c) Numerical Recipes in C 2nd Ed. Cambridge University Press (UK) pg59.

Prutton M., Wilkinson D.K., Kenny P.G., Mountain D.L., (1999) Applied Surface Science, 144-145, 1-10.

Chapter 5 Characterisation and improvement of Scanning Small Area XPS System.

5.0 Introduction

This chapter deals with the characterisation and subsequent improvement of the scanning small area XPS system on the Hallam instrument. Although the instrument can operate in both magnetic and electrostatic magnification modes for spatially keyed spectroscopy, we shall limit this discussion to magnetic magnification as this provides the better spatial resolution.

It is essential for this study that the centre of the magnetic field generated by the immersion lens is aligned with the centre of the analyser field of view so this shall be examined and corrected if necessary. We can then proceed with the characterisation of the system. This involves the establishment of a method of spatial resolution measurement, and then an assessment of factors which may influence resolution. These include: photoelectron energy, sample height, scan deflection, and analyser acceptance angle (iris setting). The results of these investigations determine what measures need to be taken to improve the scanning small area XPS system.

5.1 Assessment of scanning system.

5.1.0 Alignment of magnetic field

It is obvious that to align the centre of the magnetic field with the centre of the analyser field of view, both positions must be identified. We shall assume that the centre of the analyser field of view is the sample region from where electrons enter the analyser through the area defining aperture when zero voltage is applied to the deflection plates. This is true if the lenses of the analyser transfer column, i.e. the retardation lens, deflection plates and aperture, are aligned correctly.

In order to identify the centre of the magnetic field generated by the immersion lens, the rotation of the image projected by the field shall be exploited. The rotation, which occurs as the lens current is changed, is around the centre of the field of view, so by monitoring the rotation we may determine the centre. As described in Chapter 2, the image is recorded by sequential pixel by pixel scanning of the image projected by the magnetic field. The deflection scans are modified so that the acquired image is corrected for rotation and the recorded image reflects the actual orientation of the sample relative to the axis of the instrument. For any particular photoelectron energy, as the coil currents or the sample height is adjusted the image will rotate, although obviously, the image focus will deteriorate accordingly. If the coil current is reversed by swapping the polarity of the input leads of the coil, but the current magnitude is kept constant, the image will remain in focus, but will be rotated. This is because the magnetic field generated will produce rotation in the opposite direction, but still project the image at

the same height.

This effect was used to centre the magnetic field. By imaging an interface and positioning it at the centre of the field of view , then reversing the current, the subsequent image of the edge allows the centre of the magnetic field to be located. Figure 5.1.1 illustrates this.

Figure 5.1.1. Identification of centre of rotation.

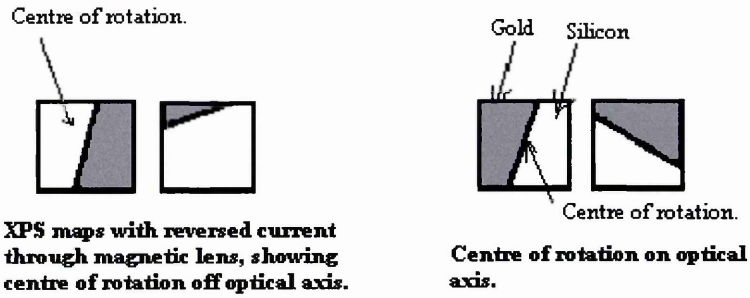

XPS maps with reversed current through magnetic lens, showing centre of rotation off optical axis.

Centre of rotation on optical axis.

The position of the magnetic lens could then be adjusted accordingly using the four adjustment screws, and the process repeated. Figure 5.1.2 shows two images of a gold grid, taken with the coil current in opposite directions. It demonstrates that the above procedure enabled alignment of the magnetic lens, as the centre of rotation is clearly at the centre of the field of view.

Figure 5.1.2 Maps of gold grid (100 lines/inch) acquired using Au 4f peak.

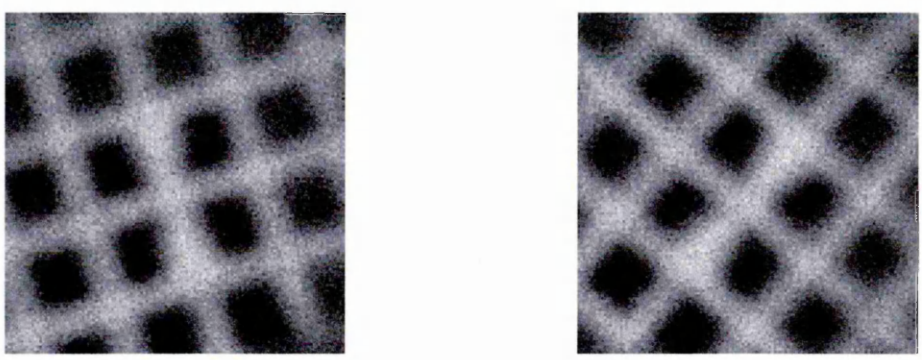

5.1.1 Experimental Edge Measurement

The spatial resolution attainable when using an analytical technique can be experimentally characterised by performing edge measurements on a sample. These measurements must be performed on a sample with an interface on the surface of the sample between two area of dissimilar elemental composition. The definition of an edge measurement is illustrated in Figure 5.1.3.

Figure 5.1.3. Definition of edge measurement.

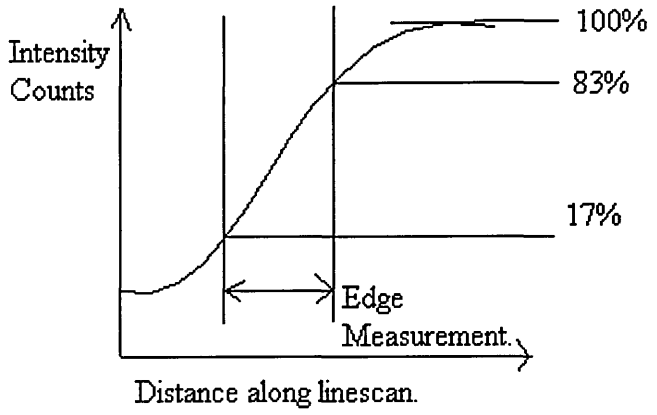

A linescan is performed across the interface. The total signal (100%) is that which is assumed to be originating from only the element present at the surface of the sample. The distance labelled as the 'edge measurement ' defines the resolution of the scanning system used. The values of 83% and 17% are standard for this type of measurement (Drummond 1997).

The first objective is to produce a clearly defined edge. This requires a sample with an interface region of width significantly less than the expected resolution of the system. With the 60μm aperture in place a maximum interface width of 6μm would ensure that the physical width of the interface would not degrade the measurement obtained using the XPS scanning system. This is based on the assumption that an interface width 10% the minimum spatial resolution would not interfere with the measurement. Silver was chosen to provide the signal as it is conducting and produces a strong 3p line at high kinetic energy (886eVfor Mg radiation and 1119eV for Al). This is advantageous in this case as the background to the peak is low. Silver also produces peaks at 681eV(Mg,3d), 915eV(Al,3d) and 336eV(Auger), allowing assessment of the resolution at lower kinetic energies. The silver was evaporated onto a 0.05mm silica substrate at a pressure of approximately 10^{-6} torr. To create the interface the silver was evaporated onto the substrate half masked by a razor blade. The sample was inspected with an optical microscope which confirmed an interface region less than 6μm.

When performing an edge measurement the interface is first mapped. The map can then be used to specify the two points on the sample between which the linescan shall be performed. All linescans presented were acquired using the following parameters.

Iris setting= 0.2

Channeltrons on= 5

X-ray emmission= 20mA at 15kV.

Aperture = 1mm (60micron diameter area defined in magnetic mode).

Magnification mode = Magnetic.

Figure 5.1.4 shows a map of the interface across which an edge measurement would be performed.

Figure 5.1.4. XPS Map of silver edge using the Ag 3d line.

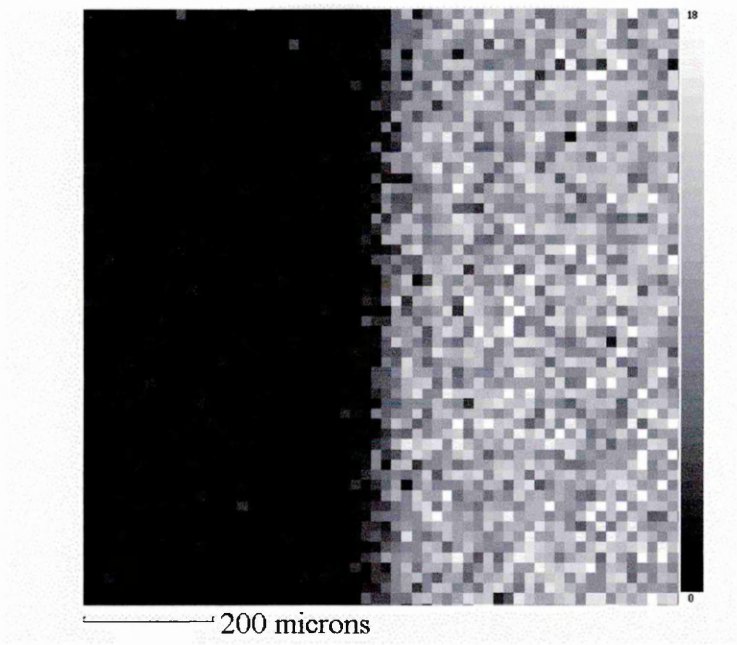

5.1.2 Spatial resolution as a function of position

In order to characterise the field of view, edge measurements were performed at various points, to asses the variation in resolution across the field of view. The measurements were taken along the x-axis from –1 to +1 mm, and the y-axis from –1mm to +1mm, both in increments of 0.01mm. The linescan performed at y=0, x=0 is shown as Figure 5.1.5. Before the edge width was calculated the raw data was smoothed using an algorithm provided with the Kratos analytical Vision software. The algorithm is based on the technique proposed by Savitsky and Golay (1964). The results of the smoothing are shown as Figure 5.1.6, for the x=0 y=0 scan. The diagrams also shows the edge resolution measurement which can be performed using the software. Using this procedure the edge measurement values were acquired and are shown as Figures 5.1.7 and 5.1.8, along the x-axis and y-axis respectively.

Figure 5.1.5 Linescan of the silver edge.

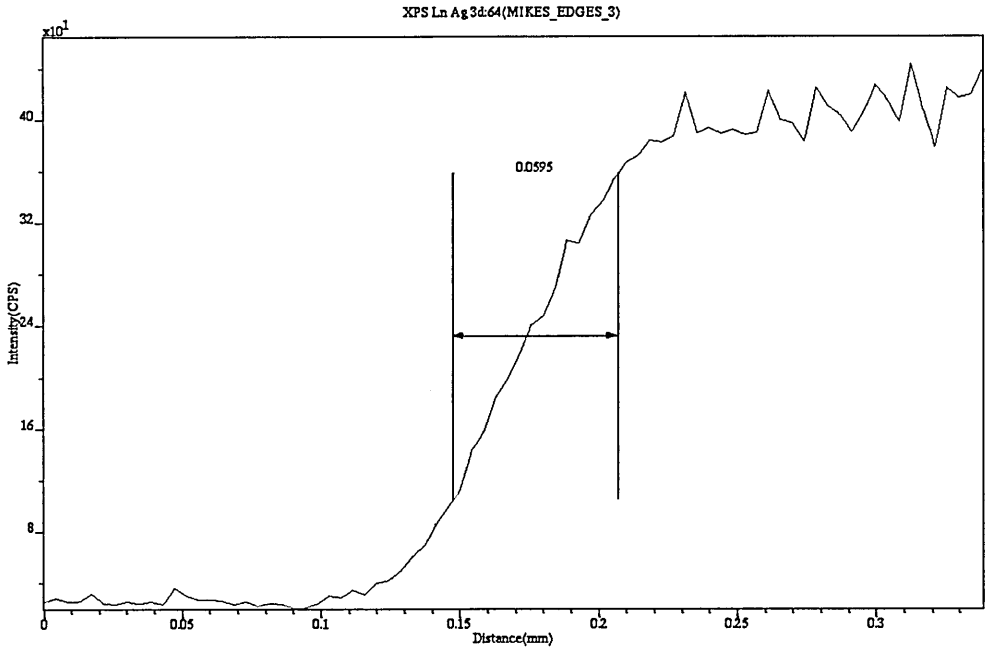

Figure 5.1.6 Smoothed linescan over silver edge.

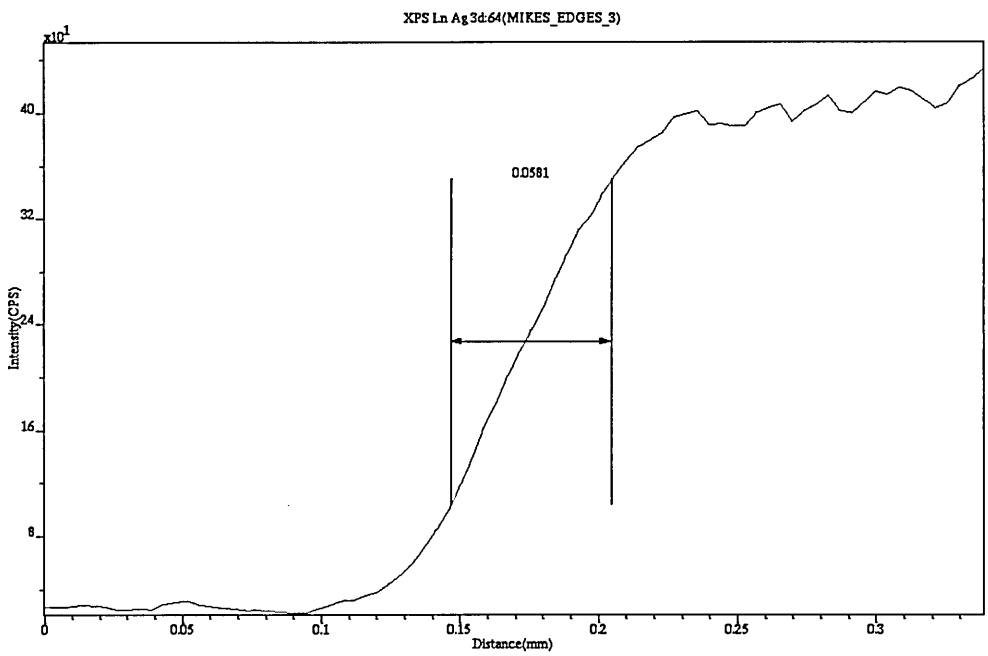

Figure 5.1.7. Edge measurements.

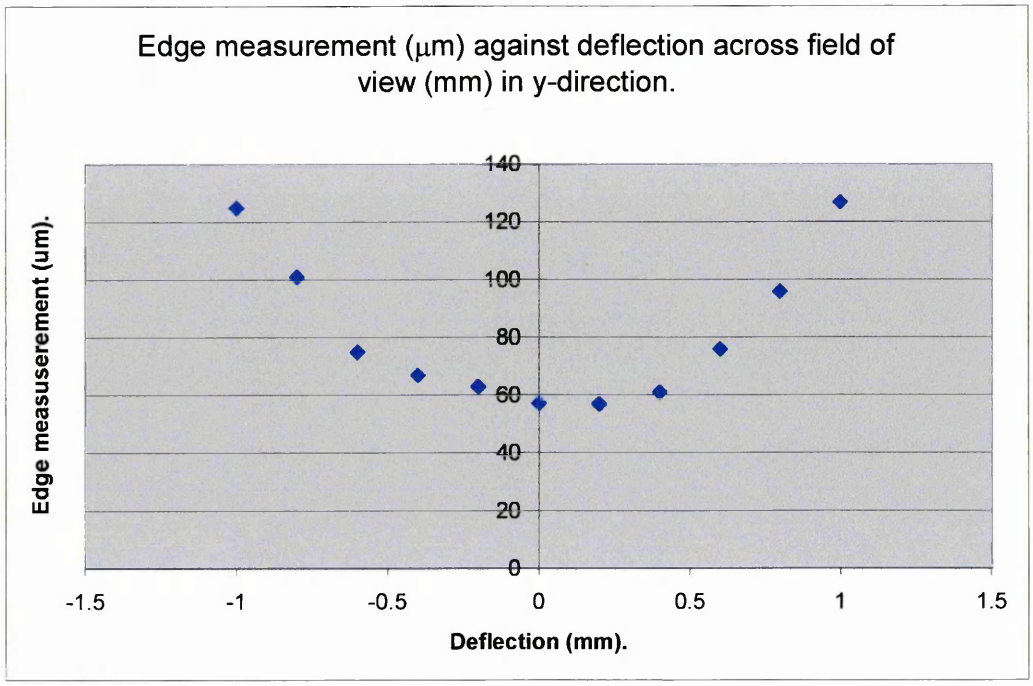

Figure 5.1.8. Edge measurements.

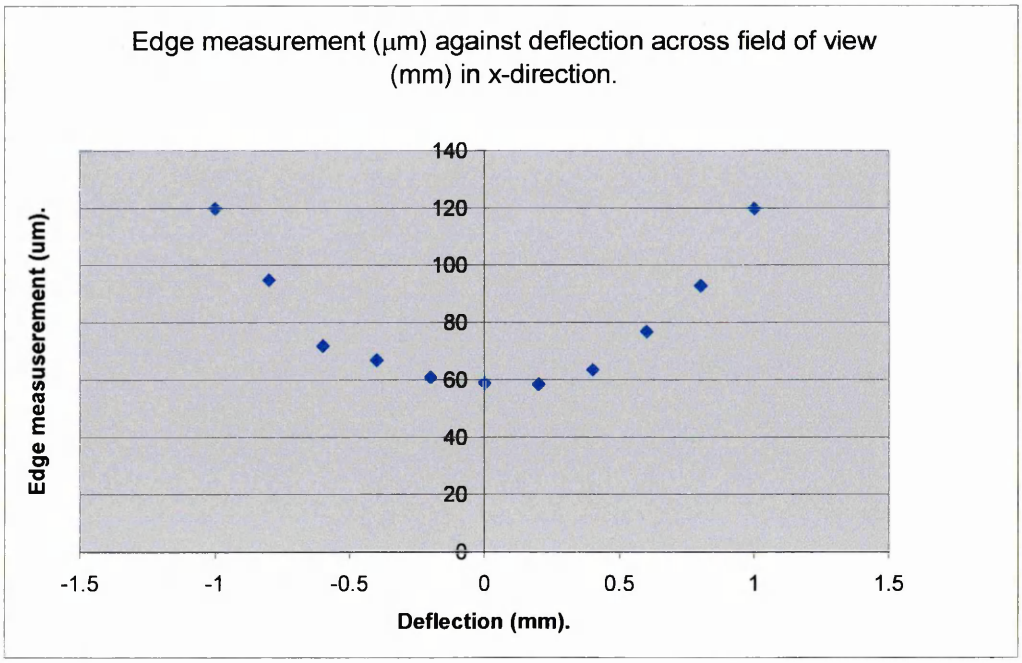

There is an obvious degradation in spatial resolution as we move away from the centre of the field of view. This appears symmetrically about the centre and affects both axes equally. As we would expect, the effect increases radially, so any correction to the system can be applied as a function of r, the distance from the centre.

5.1.3 Spatial resolution as a function of photoelectron energy.

Equation 2.3.7 states that the energy of the photoelectrons (E) should be proportional to the square root of the magnetic lens coil current (I) to maintain focus. The coil current was originally set for optimum focus using the silver 3d line excited by Mg radiation. It was observed that in order to get optimum focus for the 3d(Al) and 3p (Al and Mg) lines and the Auger line, slight deviation from the relationship in Equation 2.3.7 was necessary. The optimum focus was found at the centre of the field of view using the edge measurement procedure described in the preceding section. Figure 5.1.9 shows the deviation from the E α √I relationship and, for each energy, the corresponding edge measurement is displayed. The curve, which has been fitted to the points, is described by the function

$$E = 0.0015\sqrt{I} - 2\times10^{-7} I \qquad \text{Equation 5.1.1}$$

and demonstrates that the Eα√I relationship is inadequate over the energy range shown. The best spatial resolution is obtained at the highest kinetic energy. If we refer back to Equation 2.3.11, we see that chromatic aberration is inversely proportional to kinetic energy. Although it is stated in Section 2.3.4 that chromatic aberration is less significant that spherical aberration, the results show that it still has a measurable effect on the small area spot size.

Figure 5.1.9. Deviation from the Eα√I relationship.

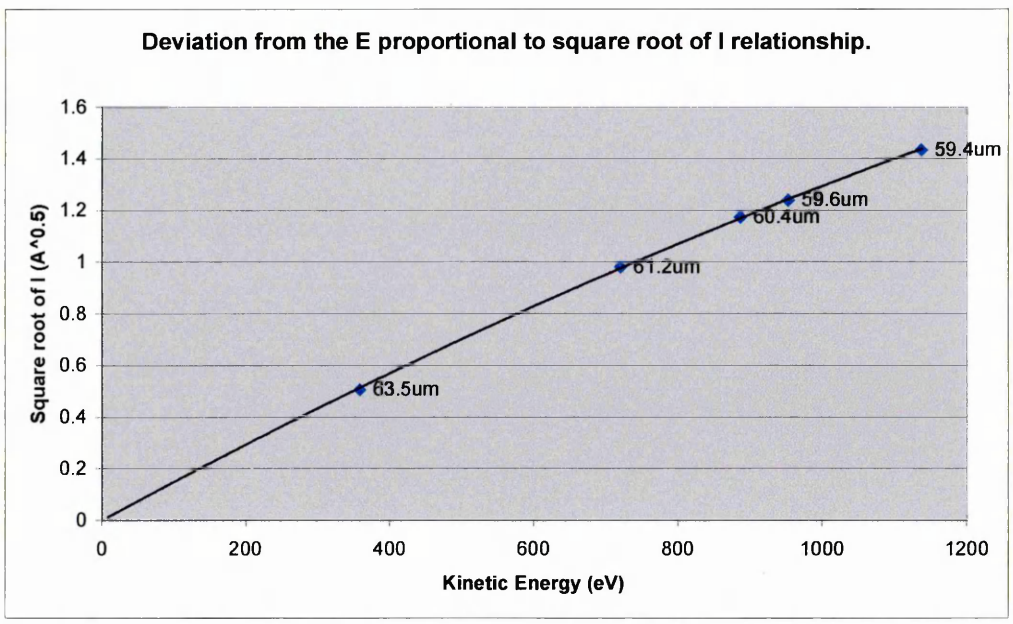

5.1.4 Spatial resolution as a function of iris setting.

The iris is used to set the acceptance angle of the analyser when operating in magnetic magnification mode. The diameter of the iris may be controlled using a linear drive inscribed with a scale (0 to 2, in 0.05 increments), so the iris position may be recorded. To investigate the effect of the iris position on spatial resolution and counts, edge measurements were performed at the centre of the field of view

using different iris positions. Figure 5.1.10 shows such measurements and Figure 5.1.11 shows the intensity from the silver as a function of iris position. The diameter of the iris at a given iris position may be obtained from the Kratos Axis 165 Operating Manual. These values were used to calculate the semi-collection angle at the iris settings, which are shown on the graphs.

Figure 5.1.10 Intensity against iris position.

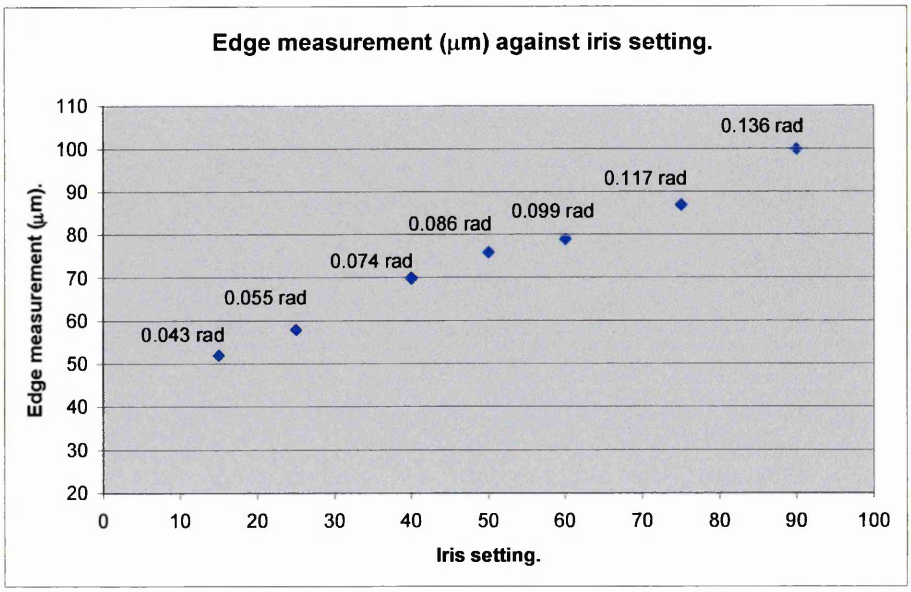

Figure 5.1.11 Intensity against iris setting.

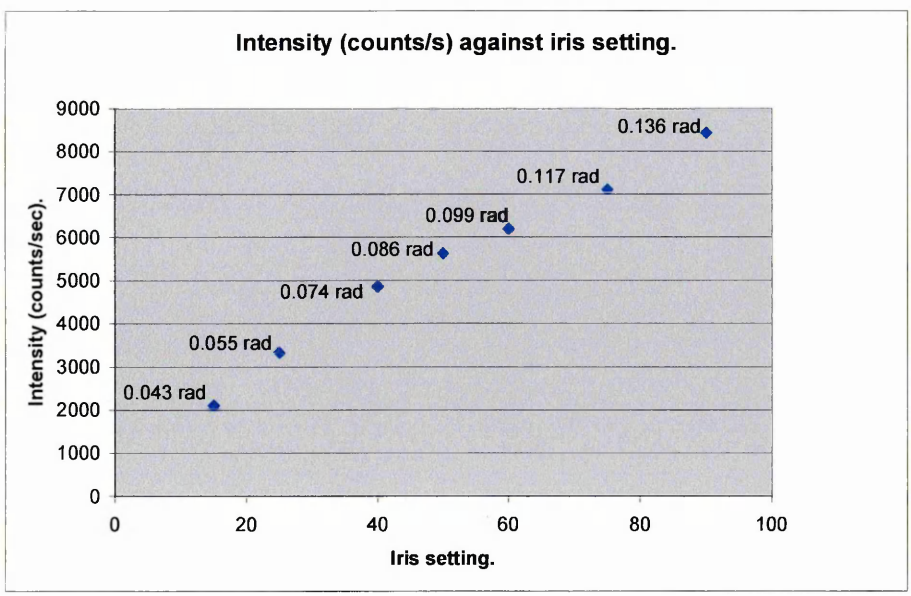

It is obvious that there is a trade off between spatial resolution and counts which depends on the iris position. As would be expected, signal is lost when the acceptance angle is reduced. Observation of Figures 5.1.10 and 5.1.11 reveals that as the edge resolution increases by a factor of 2, the intensity increases by a factor of 4. This indicates a relationship (spot size)$^2 \propto$ (intensity), which is consistent with the brightness formula given as Equation 2.3.14.

5.1.5 Spatial resolution as a function of coil current and sample height

The XPS image may be focused in two ways, either by adjusting the coil current or by adjusting the height of the sample. As the position of the sample is fixed by the necessity for images generated by electron excitation techniques and the XPS analysis area to overlap, the height must be fixed at a defined position. This position was set and the coil current versus photoelectron energy curve set for this position. Edge measurements were performed at the centre of the field of view at various heights to investigate the effect of sample position (Figure 5.1.12).

Figure 5.1.12 Edge measurement against sample height.

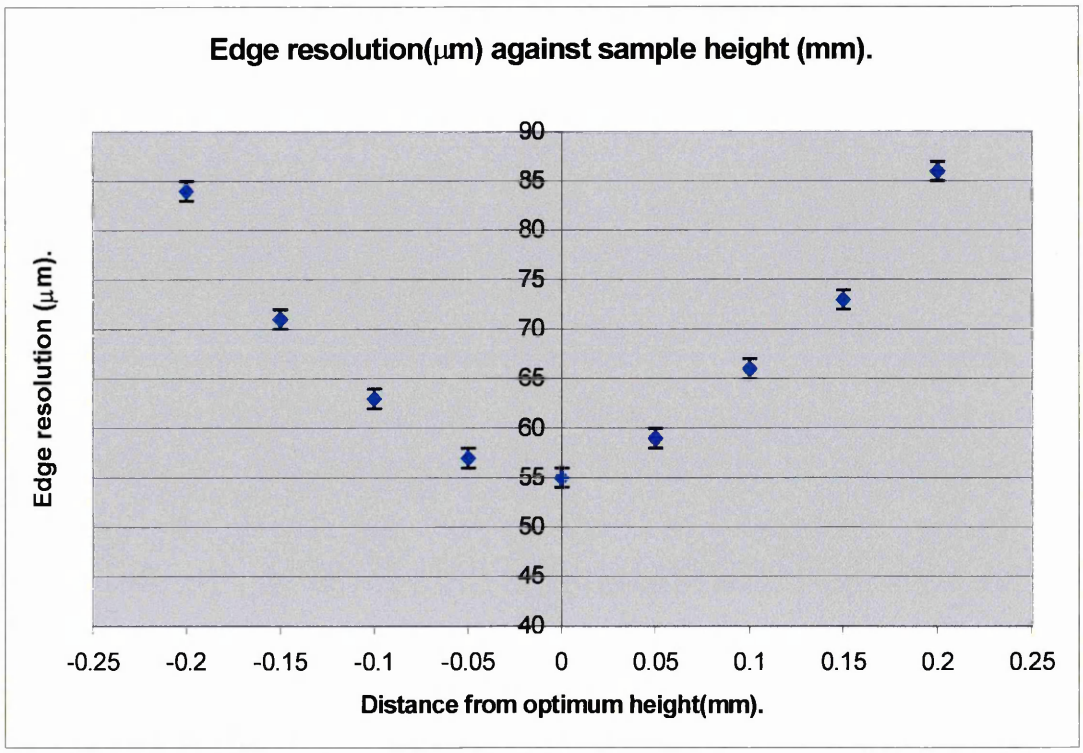

The effect of varying the coil current around the optimum position was also investigated. The edge measurements were recorded at various coil currents at x=0 y=0, and the procedure was repeated at x=0 y=0.5mm and x=0.5mm y=0mm. The 30μm area defining aperture was used for this experiment, so the resolution measurements shown in Figure 5.1.13 are better than those previously shown.

Figure 5.1.13 Edge measurement against coil current.

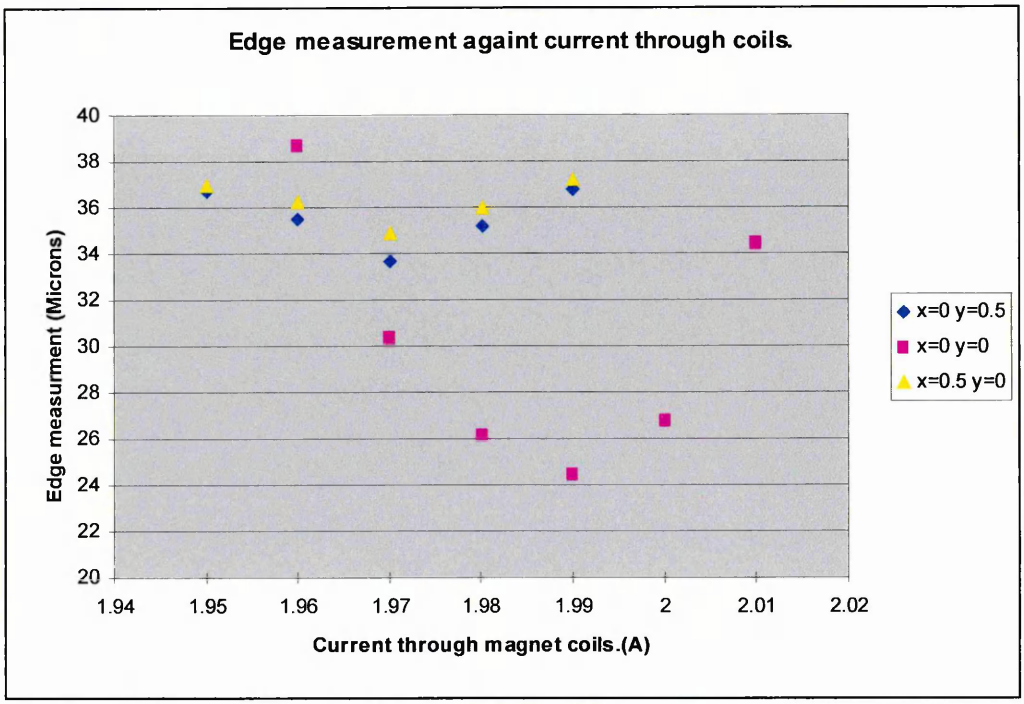

As we would expect, the resolution is optimised at a certain lens current value. It should be noted that the optimum lens current varies with the deflection across the field of view. It is desirable to have the optimum lens current for each point across the field of view.

5.1.6 Possible improvements to the SAXPS system

The limit of 30microns spatial resolution with the appropriate aperture in place is fixed by signal to noise considerations. Any further reduction in the diameter of the area defining aperture would render the signal prohibitively weak. Although the project would benefit from a higher spatial resolution it is clearly unattainable without drastic modifications to the basic Kratos system. The immediate problem which raises concern is the degradation of spatial resolution away from the centre of the field of view. In order to realise the objectives of the project improvement of this was deemed necessary. If EDX maps and XPS maps are to be compared, the varying resolution in the XPS maps is unacceptable.

The deterioration in resolution across the image can only be caused by two factors. The first is the projection of the image by the magnetic field. Figure 5.1.13 implies that different points of the image field of view focus at different coil currents. This leads to the fact that an image acquired at a fixed coil current will be defocused as we move away from the centre of the field of view. The effect is known as deflection astigmatism (Hawkes & Kasper, 1989) and is a consequence of the deflection plates scanning the flat surface of the projected image, as opposed to an ideal curved surface.

To correct the deflection defocus we need to vary the magnetic coil current as the deflection plates scan the projected image, thus applying dynamic focus. The dynamic focus would essentially alter the height of the projected image for each pixel position, retaining the optimum focus across the image. The acquisition system was modified by the instrument manufacturer to include a facility which allowed the coil current to be varied as a function of x and y deflection. The corrected coil current A_1 is set by

$$A_1 = A_0 + cr^2 \qquad \text{Equation 5.1.2.}$$

The adjustment is applied as a function of r, the distance from the centre of the field of view, as the effect is radially distributed. A_0 is the coil current for optimum focus at the centre of the field of view.

The second cause of image distortion could be the deflection of the photoelectrons through a wide angle by the quadropole electrostatic deflection plates. Around the centre of the electrostatic field generated by the plates the field lines will be straight, allowing a linear deflection of the electrons with applied voltage to the plates. As we move away from the centre a curvature of the field lines will occur which would cause a non linear defection with applied voltage, causing a distortion of the acquired image.

In order to investigate the deflection defocusing the acquired images must not be subject to further distortions caused by deflection field curvatures in the x-y direction. On this basis it was decided that the deflection of the electrons through a wide angle must first be investigated and optimised before dynamic defocusing could be implemented.

5.2 Improvements to scanning system.

5.2.0 Simulation of deflection system

The first step in assessing the distortions caused by the deflection system is to model the lens assembly. To achieve this we used the Simion 3d (Dhal 1994) computer program. The program allows a graphical model of the lens system to be drawn by the user. The user can then assign different voltages (or ampere turn values in the case of magnetic lenses) to the various lens electrodes drawn. Once the model is established the user may view the field lines generated, or simulate the effect of the field generated on a charged particle.

The actual dimensions of the octopole deflection lens are shown in Figure 5.2.1. When drawing the assembly for Simion the user must decide how many elements are to be used. The elements are effectively the pixels of the drawing. The greater the number of elements the closer the drawing is to the actual physical arrangement, thus the greater the accuracy of the final simulation. For this study an array of 1x240x240 elements was chosen. This generated a 2-d array of 57600 bytes, and gave sufficient accuracy, as we were interested in observing the field lines alone. The main reason for

choosing this number of points was to give a higher quality drawing for display.

Figure 5.2.1. Octopole lens operated as quadropole.

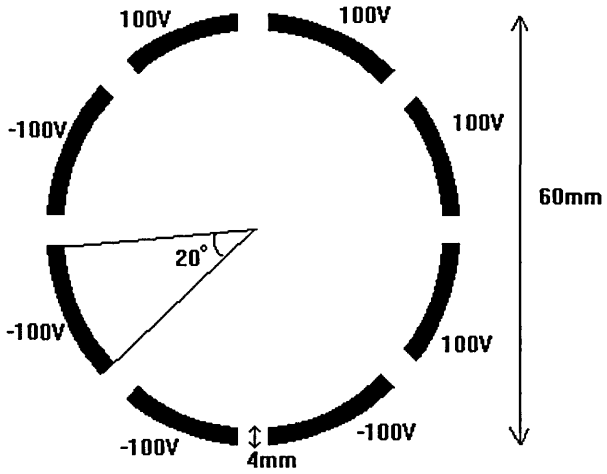

The octopole deflection lens assembly was drawn and a deflection voltage of V_x= 100V, V_y =100V was simulated. This meant applying the voltages shown in Figure 5.2.1 to the electrodes. As described in Section 3.4, the system consisted of eight electrodes with adjacent pairs connected (quadropole), so this is implemented in the model.

The simulation model is shown as Figure 5.2.2. The field lines show the direction along which the electrons will be deflected. The curvature of the field lines is evident, even in the central 50% of the assembly, which corresponds to the field of view. The field lines shown for this model mean that the linear relationship of applied voltage to deflection will not apply. This non-linearity accounts for some of the variation in image resolution as a function of position (Section 5.1).

We can now consider the case where each of the eight electrodes is controlled independently, and the system is operated as an octopole. This arrangement has been used previously to achieve wide angle deflection in an electron beam lithography column (Kelly et al, 1981). The octopole configuration is shown as Figure 5.2.3a, with the parameters V_x and V_y representing the voltages that would be used on a standard quadropole deflector. The value, a, is defined as $\sqrt{2}$-1, or 0.414, and the derivation of this is given by Kelly (1977). Figure 5.2.3b shows the voltages that needed to be applied to the Simion model to compare the octopole with quadropole system shown in Figure 5.2.2 and Figure 5.2.3. The previous Simion model was updated and is shown as Figure 5.2.4.

Figure 5.2.2. Simulation of quadroploe.

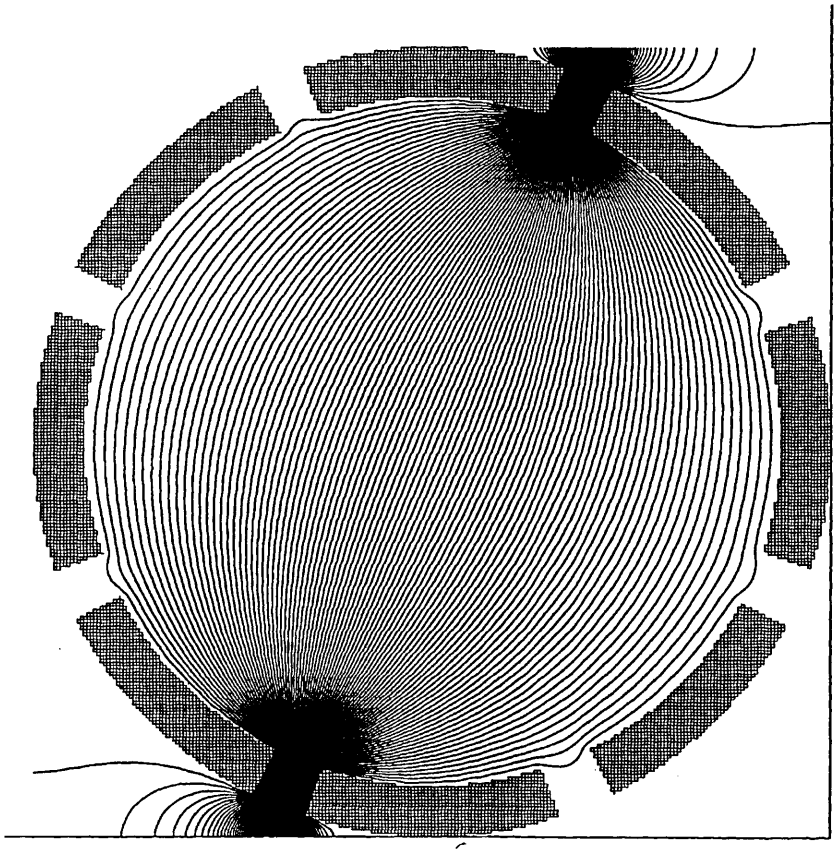

Figure 5.2.3a. Voltages applied to octopole deflector.

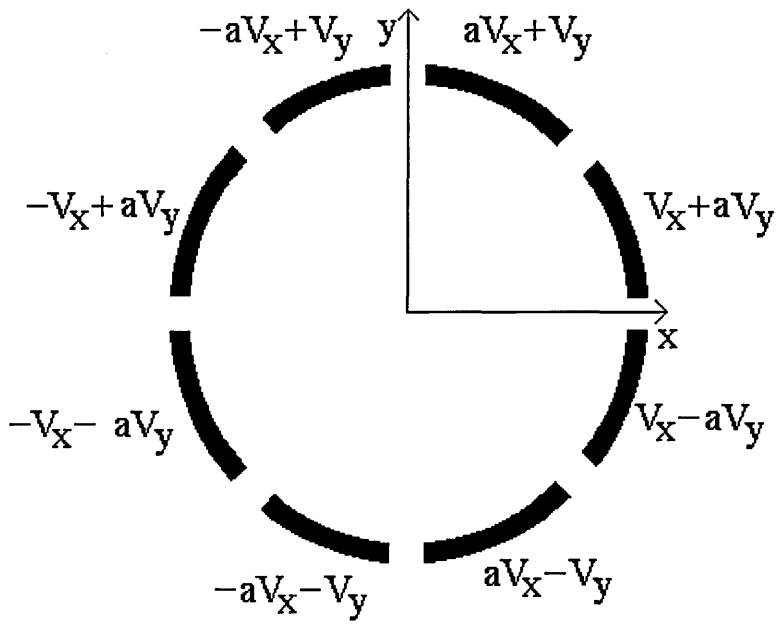

Figure 5.2.3b. Lens operated as octopole.

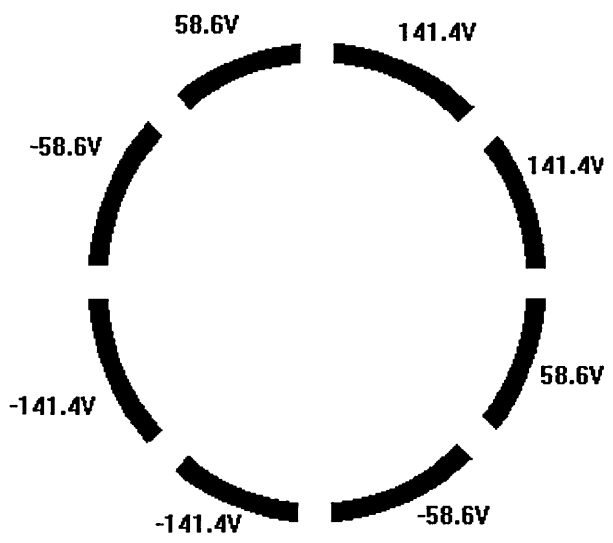

Figure 5.2.4. Octopole simulation.

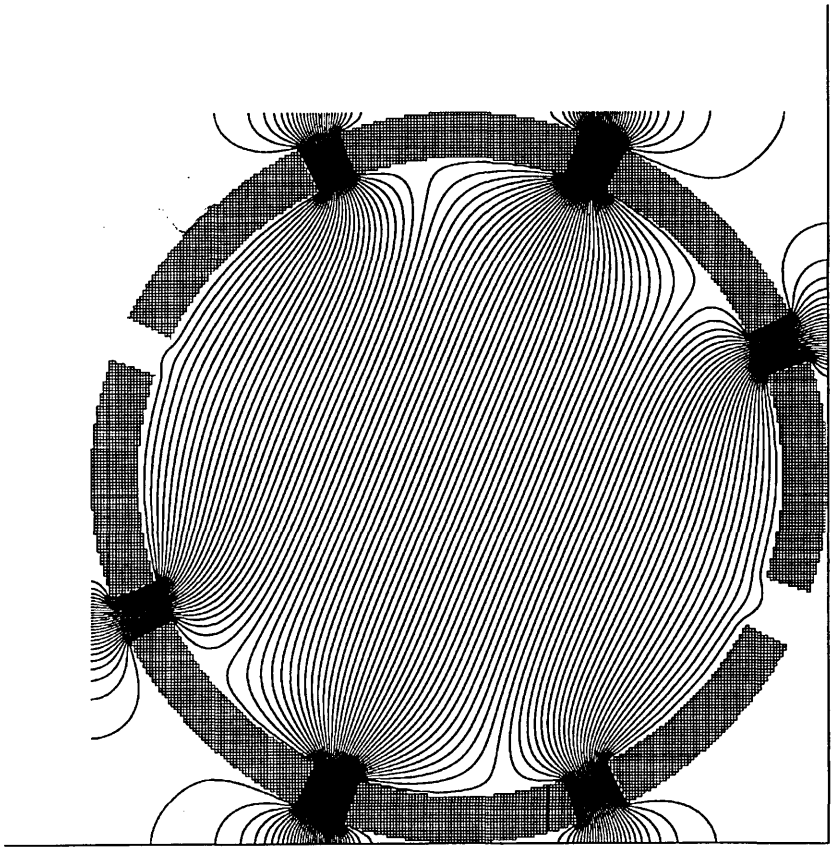

It is clear that the field lines are straight in the area of interest, giving linear deflection with applied voltage. On the evidence of this simulation study it was decided to modify the system to an octopole configuration.

5.2.1 Modification to an Octopole Scanning System

For an octoplole system it is necessary to have 8 individual power supplies to provide the required voltage to each electrode. The system was supplied with four power supplies so four more power supplies were needed. It was also necessary to modify the amplitude of the applied voltages to those required by an octopole configuration. The system used to drive the quadropole deflection plates is shown schematically as Figure 5.2.5.

Figure 5.2.5. Quadropole scanning system.

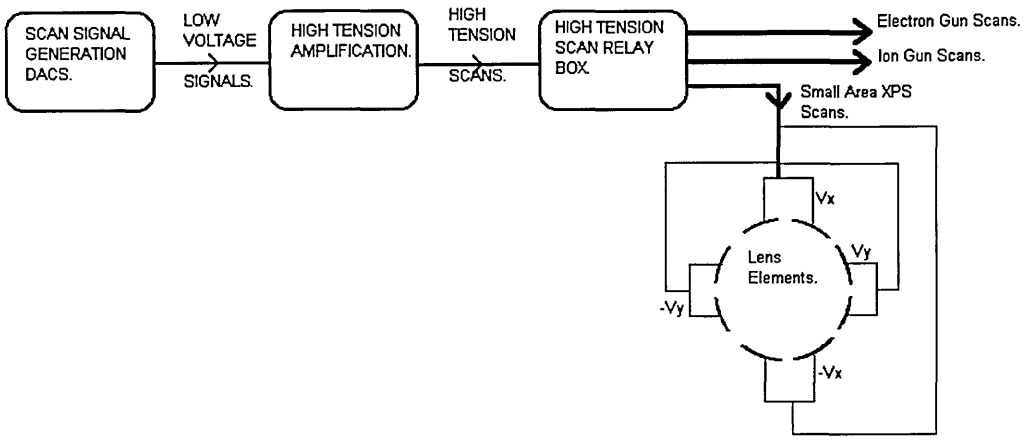

A low voltage signal is generated by the computer controlled digital to analogue converters. The reference signals v_x, and v_y, are amplified by the high voltage amplification circuits. As the Hallam instrument requires voltages of the order of ±500Vfor the ion gun and electron gun, which are not used simultaneously, the scans may be switched to different lens elements of the instrument using the high tension relay box. When the scans are used for scanning SAXPS the voltages $\pm V_X$ and $\pm V_Y$ are connected to the octopole lens system, with adjacent electrodes connected at the electrical feedthrough to the vacuum chamber.

A number of options were considered for the modification of the scanning voltages. These were:

1) To change the software so the generated reference voltages were modified.
2) To modify the reference voltage by analogue means.
3) To modify the high voltages by a passive resistor network.

For (1), if the software was altered, we would require two additional digital to analogue converters to provide the reference voltages required. This addition would also require a detailed knowledge of the digital circuitry and software architecture. For (3), to use a passive resistor network at the high voltage output would limit the field of view, as the derived voltages would have to be less than the actual output voltages. As the high voltage supplies are of low power, we would also be in danger of drawing too much current from the supplies with a resistor network.

On this basis it was decided to use (2), modify the reference voltages and provide four extra high voltage supplies. A schematic of this system is shown as Figure 5.2.6. The analogue computation would take the voltages v_x and v_y and produce reference voltages av_x+v_y, av_x-v_y, av_y+v_x, and av_y-v_x.

These reference voltages are amplified by the high tension supplies (the four existing supplies and four extra), each reference voltage amplified with a positive and negative gain.

Figure 5.2.6. Proposed octopole scanning system.

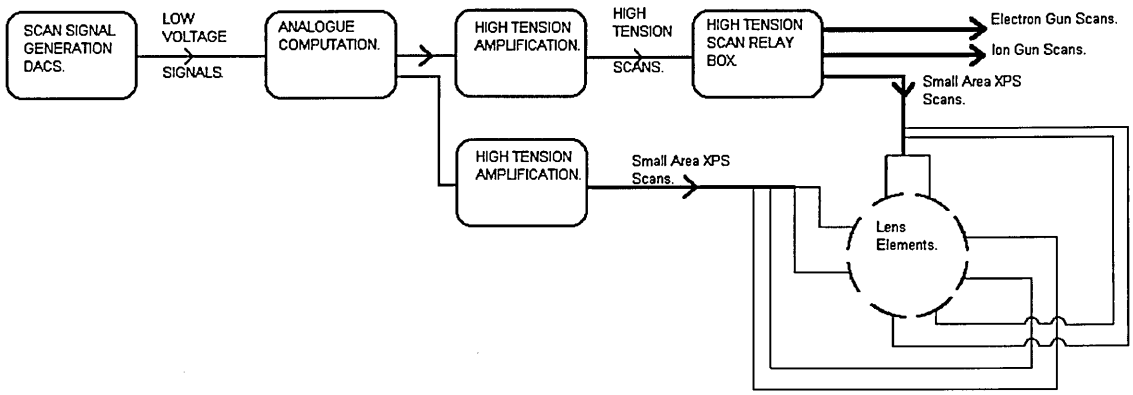

As there was a spare slot for a circuit board in the H.T. bus, the analogue computation and the high voltage supplies were built on the same board. The only connections required are between the Scan H.T. amplification unit (see Figure 3.10.1) and the new circuit, and between the output stage and the electrical feedthroughs connected to the electrodes. The following sections describe the circuit designed to enable an octopole scanning system.

Signal switching.

The electronics built on the new board must perform the additional functions shown in Figure 5.2.6, the first function being the low level switching. This was achieved using DJ402 cmos analogue switches. Each one of these 16 pin integrated circuits houses four single pole switches, and the position of the switch contact is controlled by a logic signal provided to the device. Two of these devices were used to direct reference signals appropriately. The function of the switches is shown in Figure 5.2.7.

Figure 5.2.7. Signal switching.

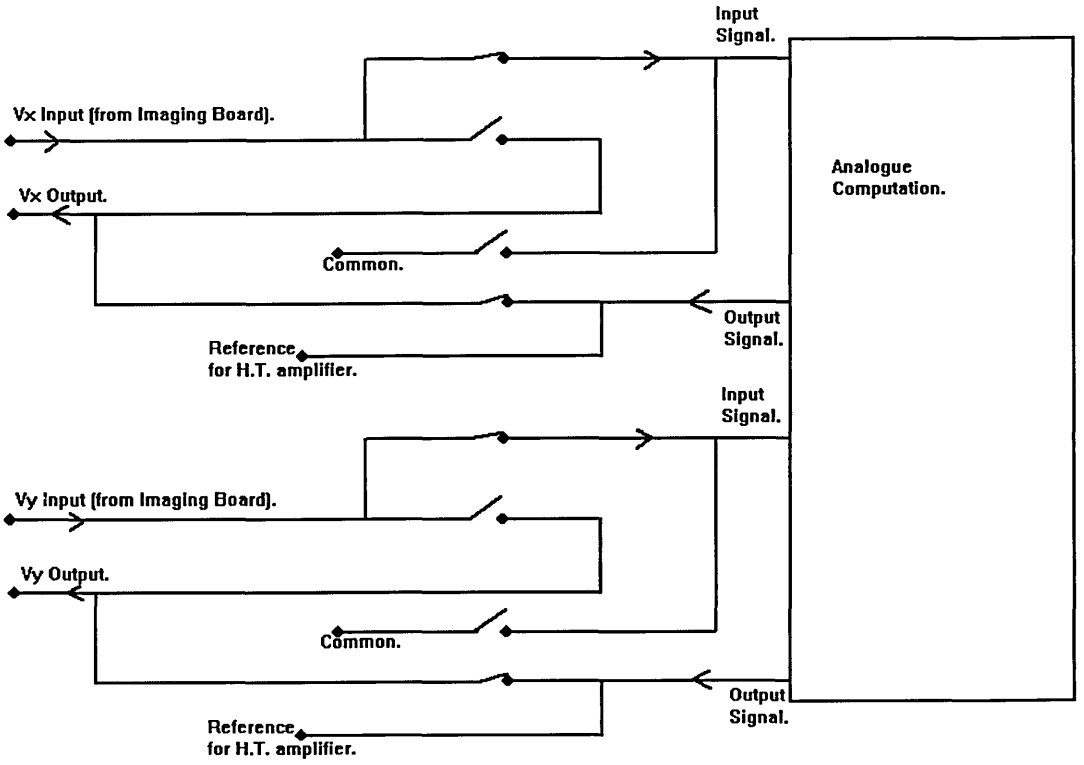

The arrangement is the same for the X channel input and Y channel input. The basic function of the arrangement is to maintain the multi-technique status of the instrument. When XPS mapping is required the switches will be in the position shown in Figure 5.2.7. When AES or electron microprobe analysis is required the switch positions will be reversed. In this position the scan reference voltages will remain unmodified and the input to the analogue computation will be grounded, so no extra signals will be generated. The position of the switches is set by a logic signal from the H.T. imaging board. The logic signal is inverted for the second integrated circuit, so its contacts are closed while the first integrated circuit contacts are open. When XPS is required the contacts are in the positions shown, so modified reference voltages are returned to the H.T. Imaging board, and extra reference voltages are generated for the on-board H.T. amplifiers.

Analogue computation.

The function of the analogue computation circuit was to derive the reference voltages required for the octople from the reference voltages used by the quadropole system. To achieve this, operational amplifiers are used, and configured to muliply voltages by the value 0.414 (the constant, a, shown in Figure 5.2.1) and to produce the summation of two input voltages. The schematic of this system is

shown as Figure 5.2.8. For the reader unfamiliar with electronics, a comprehensive introduction to operational amplifier behaviour is given by Jones (1985). The operational amplifiers used were 741's. These are general purpose op-amps ideal for a prototype board such as this.

Figure 5.2.8. Analogue Computation.

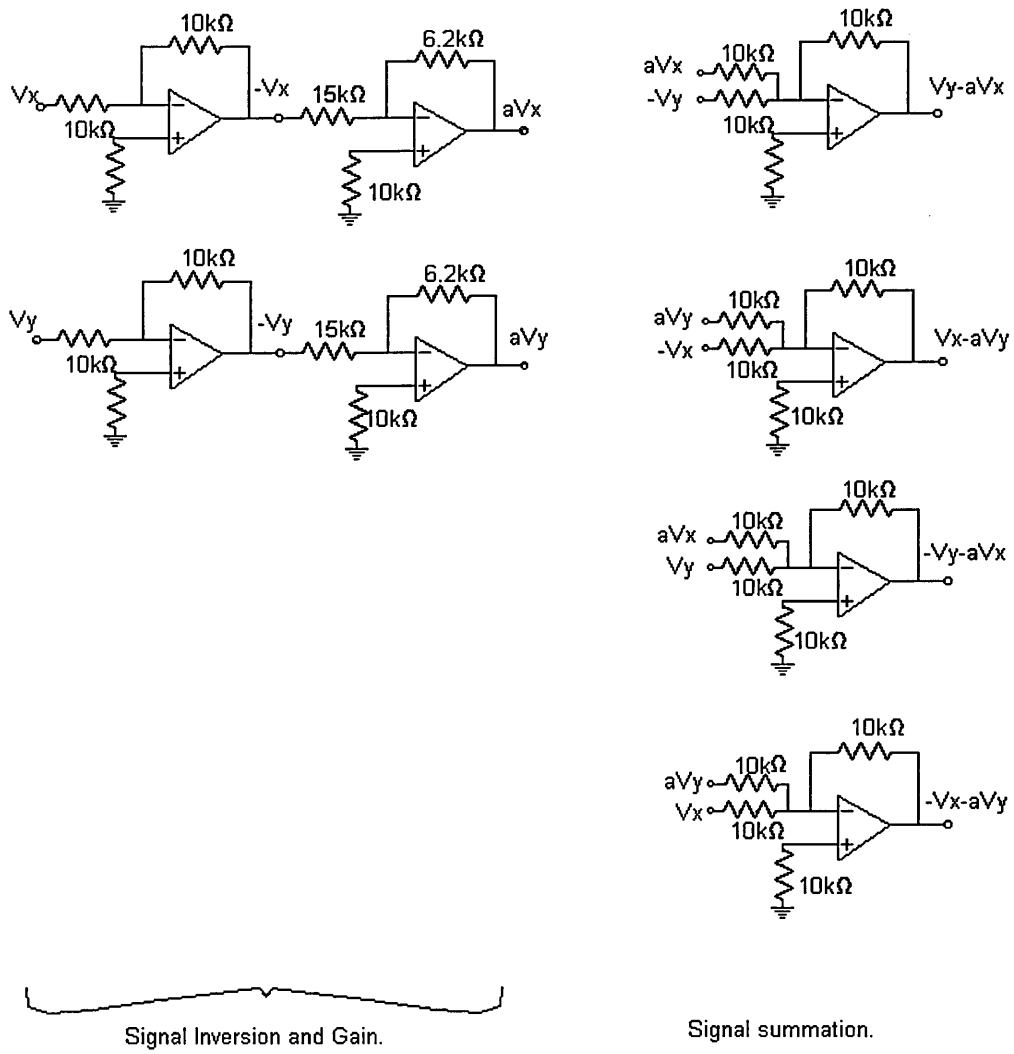

The output of the analogue computation are the four voltages aV_x-V_y, aV_y-V_x, V_x+aV_y and aV_x+Vy. Two of these voltages V_x+aV_y and aV_x+V_y are sent to the H.T. Imaging board, where the reference voltages are amplified to high voltages by a constant gain. The voltages aV_x-V_y and aV_y-V_x are used as reference voltages for the H.T. amplifiers on the new board.

H.T. Amplifiers.

The purpose of the H.T. amplifier is to amplify a voltage in the ±10V range by a gain of 50, producing a corresponding voltage in the range ±500V. A gain of 50 is required, as the field used to deflect the photoelectrons must be generated by lens voltages in the range –500V to +500V.

The schematic diagrams of the Kratos H.T. Imaging board amplifiers were available. The H.T. amplifiers were designed for use with D.C. and A.C. (up to 1kHz) reference voltages, so they could be used for small area XPS and scanning Auger/S.E.M. The circuits were however prone to failure, as the outputs were connected to electrodes positioned close to other high voltage electrodes, so breakdown could occur.

For the additional H.T. amplifiers a simple circuit described by Horowitz and Hill (1980) was used as the basis. The schematic of the circuit is shown as Figure 5.2.9. A full description of the circuit operation is given in the reference text. The use of the opto-isolator (Q_2) separated the high voltage components of the circuit from the low voltage control components, so the only electrical link is the high ohmic resistor R_4, and the circuit is well protected. The opto-isolator gives poor frequency response so, for an A.C. reference voltage the gain is not constant for different frequencies. However, the new amplifiers are used only for XPS mapping, where the scanning speed is slow and the reference voltage can oscillate at a maximum frequency of 50Hz, so poor frequency response is not a problem for the present application.

Figure 5.2.9 High voltage supply.

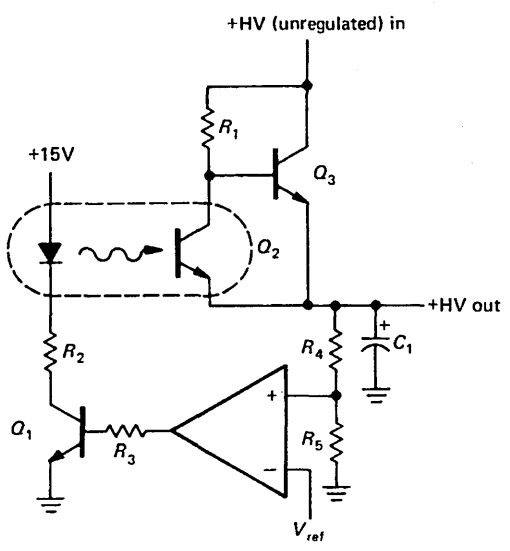

The circuit shown in Figure 5.2.9 is a unipolar amplifier but in this instance we require a bipolar amplifier.

Figure 5.2.10 shows a schematic for the design adopted for use on the new board. The main alteration is the inclusion of a negative high voltage. The mosfet shown in Figure 5.2.10 is used instead of a transistor because a voltage of 1000V can be present across the component, and the mosfet was the only device with such a rating. The other additional components are intended to provide protection from high voltage breakdown. The diodes between the input terminals of the operational amplifier absorb voltage differences between the terminal greater than ±0.6V.

Figure 5.2.10 High Voltage Supply.

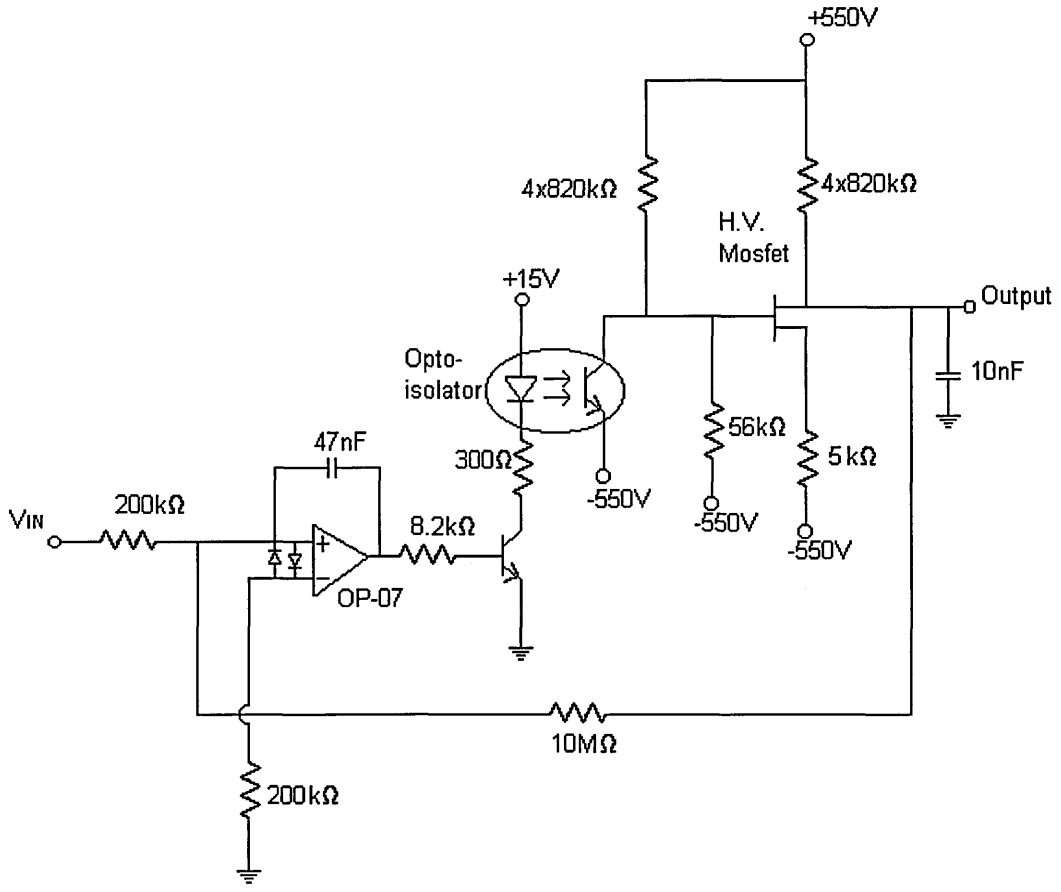

The voltages +550V and –550V are provided by Start Spellman Modular High Voltage power supplies. The 3 Watt supplies provide a voltage up to +750V or -750V at 4mA. The output voltage can be set using an external potentiometer. The power supply configuration is shown as Figure 5.2.11.

Figure 5.2.11 High Voltage Power Supply Units.

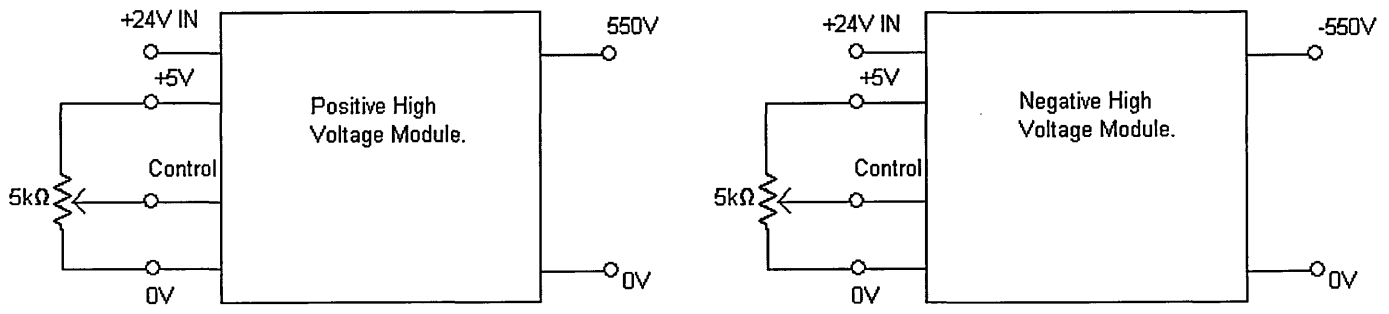

The Complete board.

The electronics were constructed on eurocard and a simplified diagram of the complete board is shown as Figure 5.2.12. All connections were manually wired on the underside of the board as production of a printed circuit board would have been both time consuming and expensive.

Figure 5.2.12 New Octopole Board.

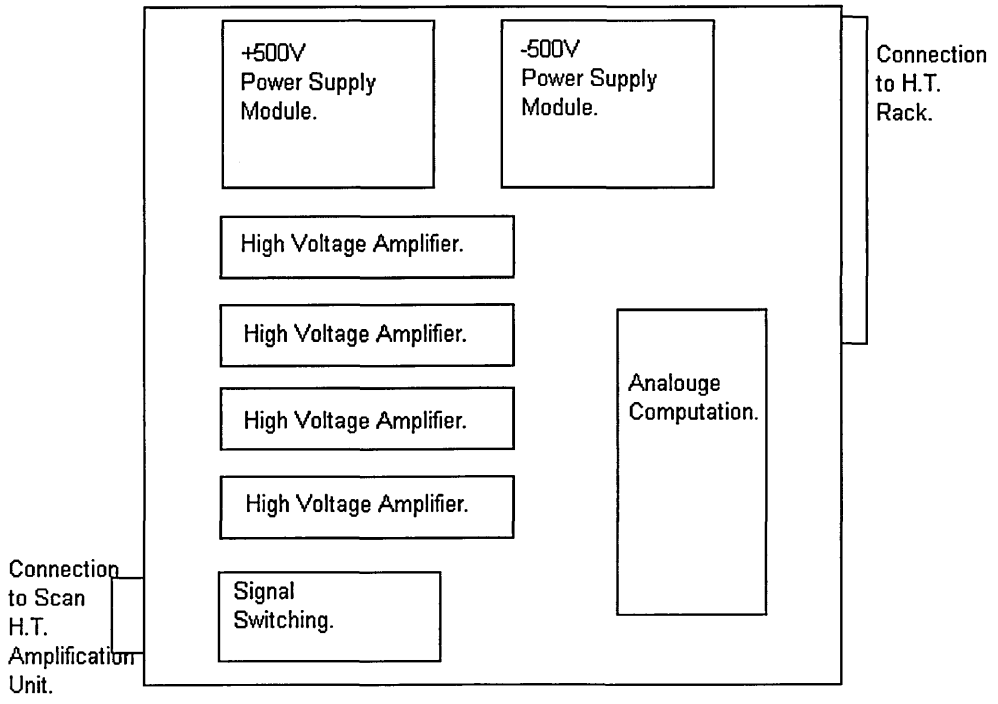

The board was tested by supplying all the required power voltages through the 32 pin socket and by generating the reference voltages using a signal generator. Table 5.2.1 shows the reference voltages and the output voltages produced for each electrode.

Table 5.2.1 Output voltages for each channel of the Octopole system.

Input Reference Voltages.(V)		Output Voltages (V) (Channels 1 to 4 are the outputs from the Scan H.T. amplification unit, and channels 5 to 8 are those from the new board.)							
X	Y	1 Measured aVx+Vy	Ideal aVx+Vy	2 Measured -aVx-Vy	Ideal -aVx-Vy	3 Measured aVx-Vy	Ideal aVx-Vy	4 Measured -aVx+Vy	Ideal -aVx+Vy
0	0	0.5	0	0.7	0	0.8	0	0.8	0
0	6	300.5	300	-299.7	-300	-300.7	-300	300.3	300
6	0	124.5	124.2	-124.0	-124.2	124.5	124.2	-124.7	-124.2
3	3	212.5	212.1	-211.5	-212.1	-88.2	-87.9	88.1	87.9
3	6	362.3	362.1	-361.8	-362.1	-237.9	-237.9	238.1	237.9
6	3	274.8	274.2	-274.0	-274.2	-26.2	-25.8	26.4	25.8
6	6	424.8	424.4	-424.1	-424.4	-176.5	-176.2	176.5	176.2
		5 Measured aVy+Vx	Ideal aVy+Vx	6 Measured -aVy-Vx	Ideal -aVy-Vx	7 Measured aVy-Vx	Ideal aVy-Vx	8 Measured -aVy+Vx	Ideal -aVy+Vx
0	0	0.3	0	0.2	0	0.3	0	0.3	0
0	6	124.5	124.2	-124.4	-124.2	124.5	124.2	-124.7	-124.2
6	0	300.6	300	-300.2	-300	-300.7	-300	300.8	300
3	3	212.5	212.1	-212.6	-212.1	-88.1	-87.9	88.1	87.9
3	6	274.7	274.2	-274.4	-274.2	-26.0	-25.8	26.1	25.8
6	3	362.4	362.1	-362.4	-362.1	-238.2	-237.9	238.1	237.9
6	6	424.9	424.2	-424.5	-424.2	-176.0	-176.2	176.0	176.2

The largest discrepancy between the measured and ideal signal is 0.8V, which appears on channels 3 and 4 at zero reference volts. This error in deflection voltage corresponds to an XPS image displacement of approximately 3μm. This is well below the expected minimum spatial resolution of 30μm. For each channel the deviation from the ideal voltage value for each set of reference voltages is below 0.8V. This means that the accuracy and linearity is sufficient for high resolution XPS mapping.

5.2.2 Effect of improvements to scanning system.

In order to asses the improvement of the XPS scanning system a direct comparison of images was used. Linescans were a useful diagnostic tool but repetition of the experiment after each adjustment was prohibitively time consuming. A silver grid surface was prepared by evaporating silver onto a 200lines/inch copper grid. The grid bars were approximatley 50μm in width over a 3mm diameter mesh, providing an adequate test of the spatial resolution over the field of view.

To show the effect of the octopole system, maps of the silver grid were acquired with the 60μm area defining aperture in place. It was found that this area selection setting provided adequate spatial resolution to show the improvement of the circuit modifications without compromising the signal to noise ratio unnecessarily. A map was acquired with the quadropole scanning system using the silver 3p

peak, the spectrum of which is shown as Figure 5.2.13. The map resolution was 160 by 160 pixels with a pixel dwell time of 100ms, the final image consisting of 5 aggregated map scans. The magnesium x-ray source was used operating at 20mA. The octopole board was fitted and connected accordingly, and a second map was acquired under the same conditions. The two maps are displayed in Figure 5.2.14.

Figure 5.2.13. Spectrum of Ag 3p peak with 60μm area defining aperture in place.

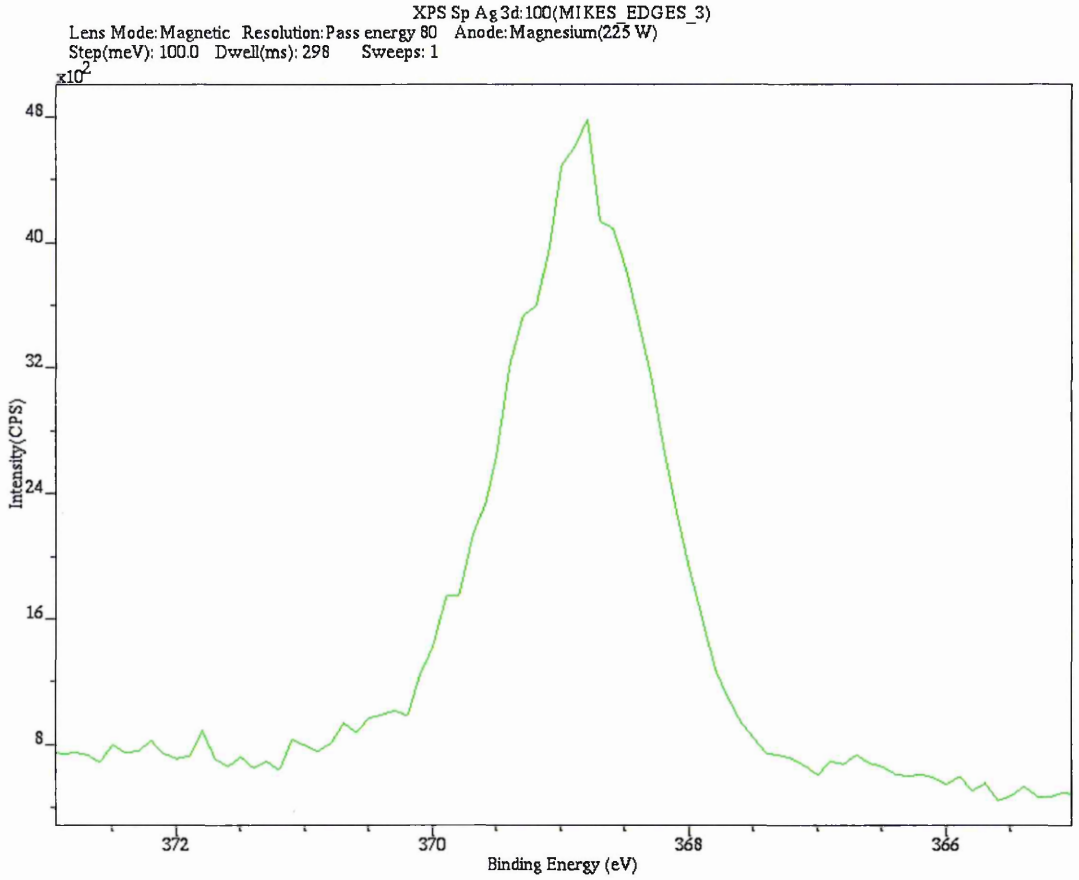

Figure 5.2.14. Before and after the implementation of the octopole scanning system.

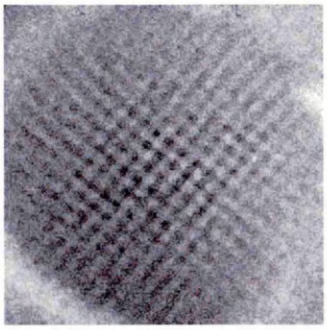

Before

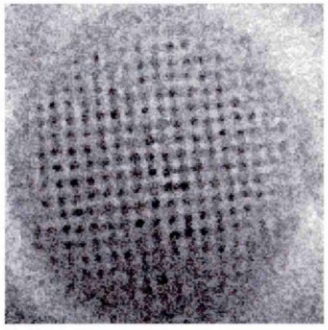

After

The image acquired using the quadropole system shows a curvature in the grid pattern, coupled with a loss in spatial resolution, with increasing distance from the centre. Although the image acquired using the octople system still shows image degradation as a function of deflection, the distortion of the grid pattern is not present.

Once the improvement in distortion had been achieved, implementation of the dynamic focussing proceeded. To asses the performance of this it was necessary to use the high spatial resolution attainable with the 30μm area defining aperture. The silver grid was argon ion etched in the analysis position, to remove any carbon overlayer and increase the silver peak intensity. This is necessary when using the 30μm aperture as the signal is very weak. The 3p spectrum is shown in Figure 5.2.15. With the aperture in place a count rate of approximately 0.01% that of the count rate without an aperture in place is obtained. Maps were acquired under the same conditions as the previous experiments but 10 map scans were performed for each image to improve signal to noise ratio. A series of images were obtained with the value c of Equation 5.1.1 set to 0.02, 0.04, 0.06, 0.08, 0.1 and 0.12. An obvious improvement in image was observed with c set to 0.08. The image acquired at this value is compared to one acquired without dynamic focus in Figure 5.2.16.

Figure 5.2.13. Spectrum of 3p peak with 30μm area defining aperture in place.

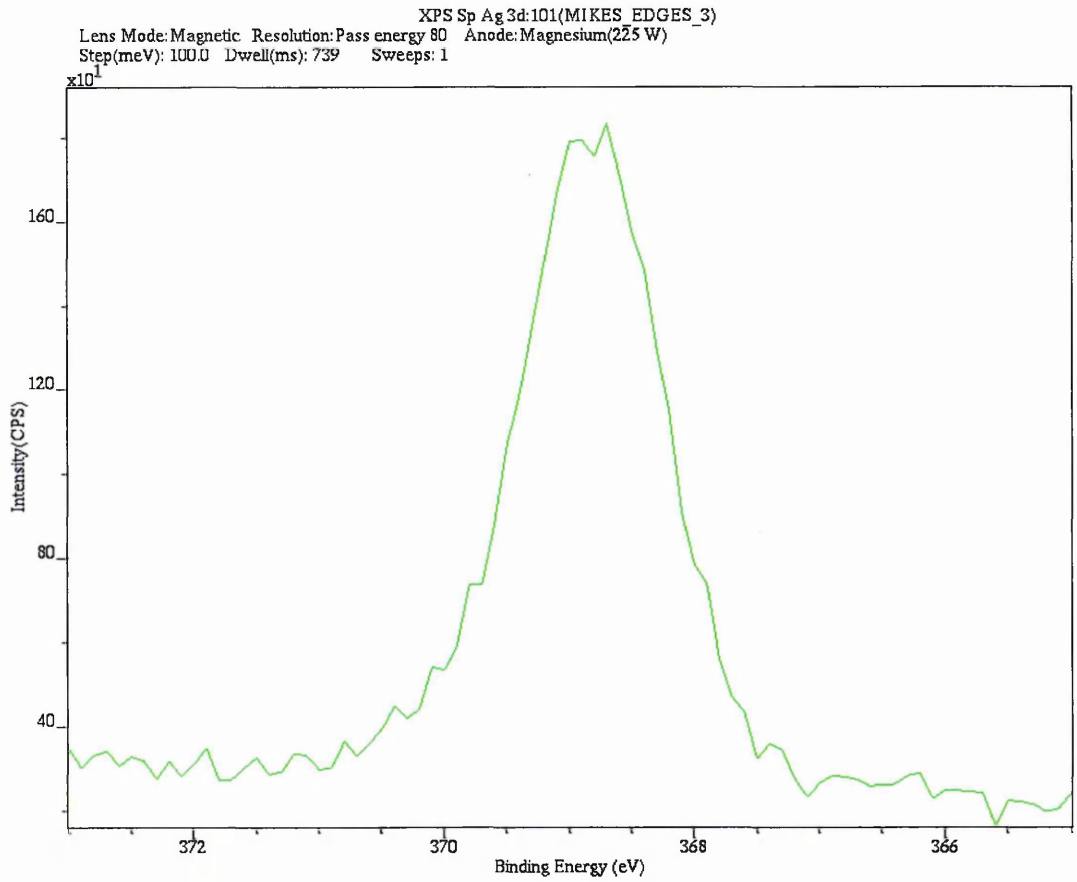

Figure 5.2.16. Before and after the implementation of dynamic focus.

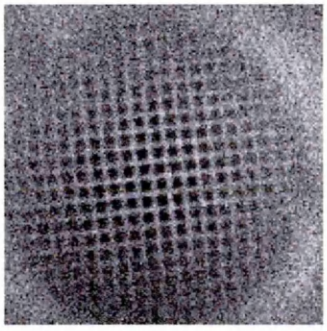

Before

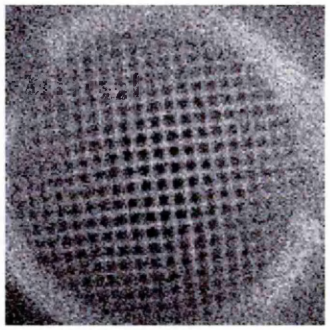

After

The higher spatial resolution of these images is obvious in the centre of the images compared to those acquired using the 60μm aperture, but the images appear noisier. The effect of the dynamic focus is most noticeable when observing the border of the grid mesh, but can also be seen when observing the grid pattern itself. The image acquired using dynamic focus shows a barrel effect, which is due to a small variation in magnification as the magnetic lens current is varied.

5.3 Application of improved Scanning Small Area XPS and alignment with electron beam techniques.

In this section the use of scanning small area XPS on a real sample shall be demonstrated. This also gives an opportunity to show the alignment of the XPS images with the electron beam induced images, in this case EDX images. For this demonstration a 100nm TiAlN film on stainless steel was used. The sample had been subjected to argon ion bombardment in a VG surface analysis instrument based at British Steel's Swindon Technology Centre. This was carried out by Dr Tim English. The ion beam had been rastered to create a wedge depth profile. A depth gradient across the sample is created by carrying out more ion beam scans for successive lines across the raster area. By examining this sample with SAXPS it was possible to see the film composition as a function of depth represented spatially in the X-Y plane. An SEM image of the wedge is shown as Figure 5.3.1. The unsputtered region is easily identifiable, and the wedge area can be visually divided into three areas.

Figure 5.3.1 SEM image of wedge.

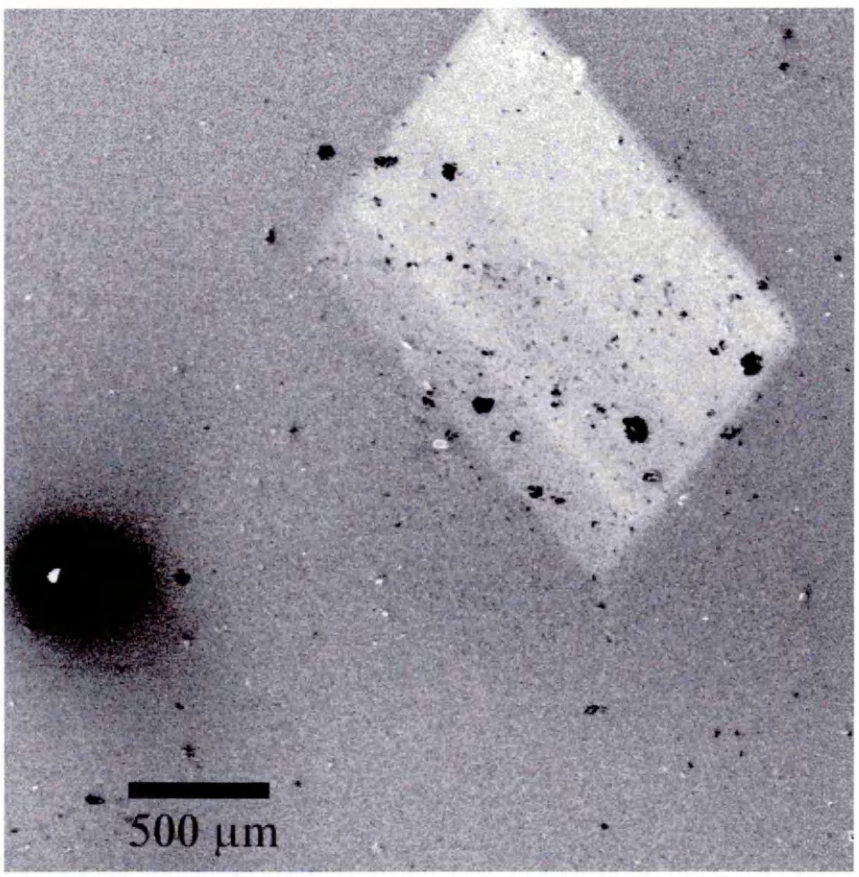

A wide XPS spectrum of the coating is shown as Figure 5.3.2. The wedge area was scanned using small area XPS. The strong Titanium and Oxygen present in the wide spectrum were used to generate maps. An XPS map using the Iron peak was also obtained to show were the coating had been sputtered

away complety. The maps are show as Figure 5.3.3. The EDX maps for titanium and iron are shown as Figure 5.3.4.

Figure 5.3.2. Wide spectrum of PVD coating.

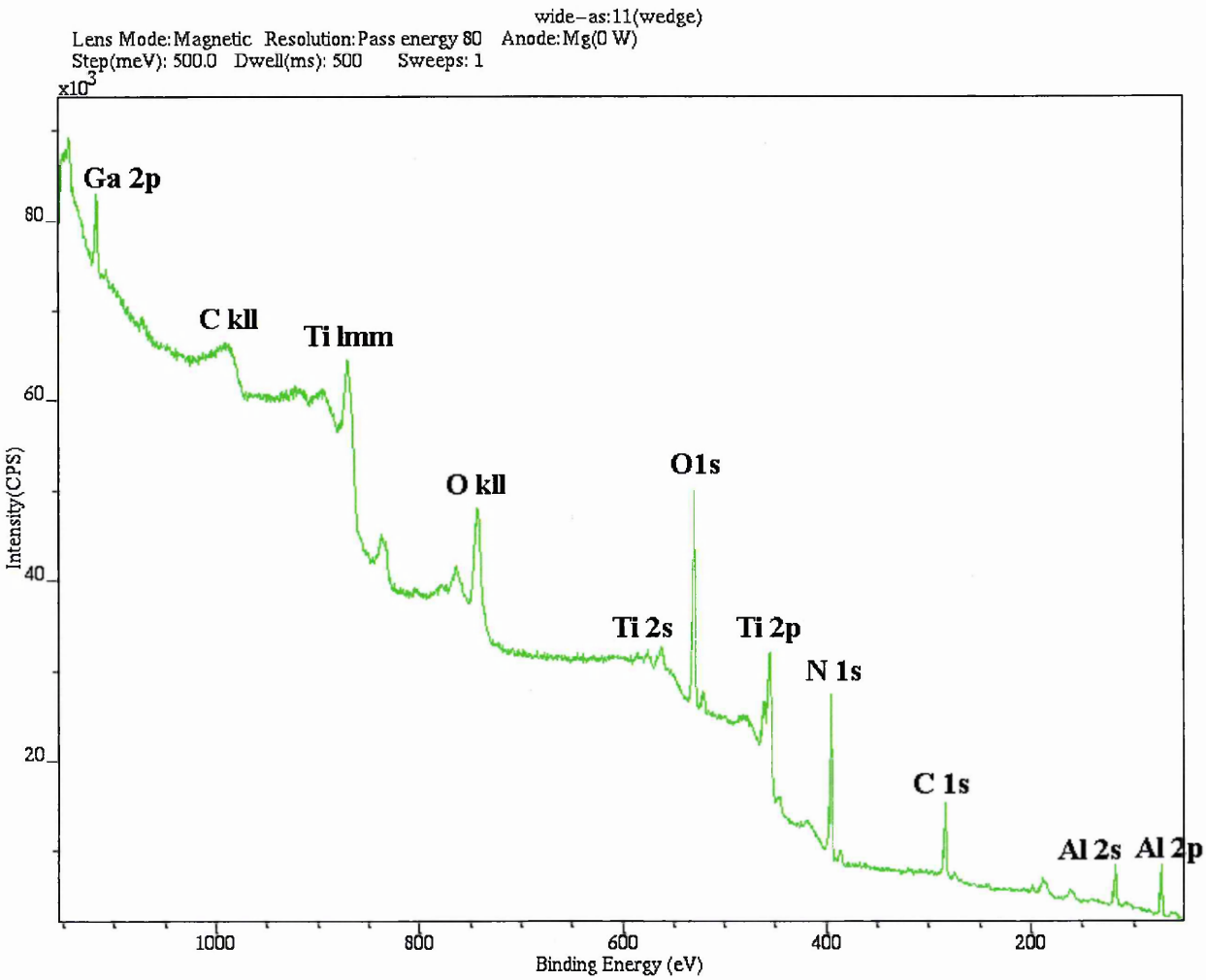

Figure 5.3.3 XPS Maps of coating.

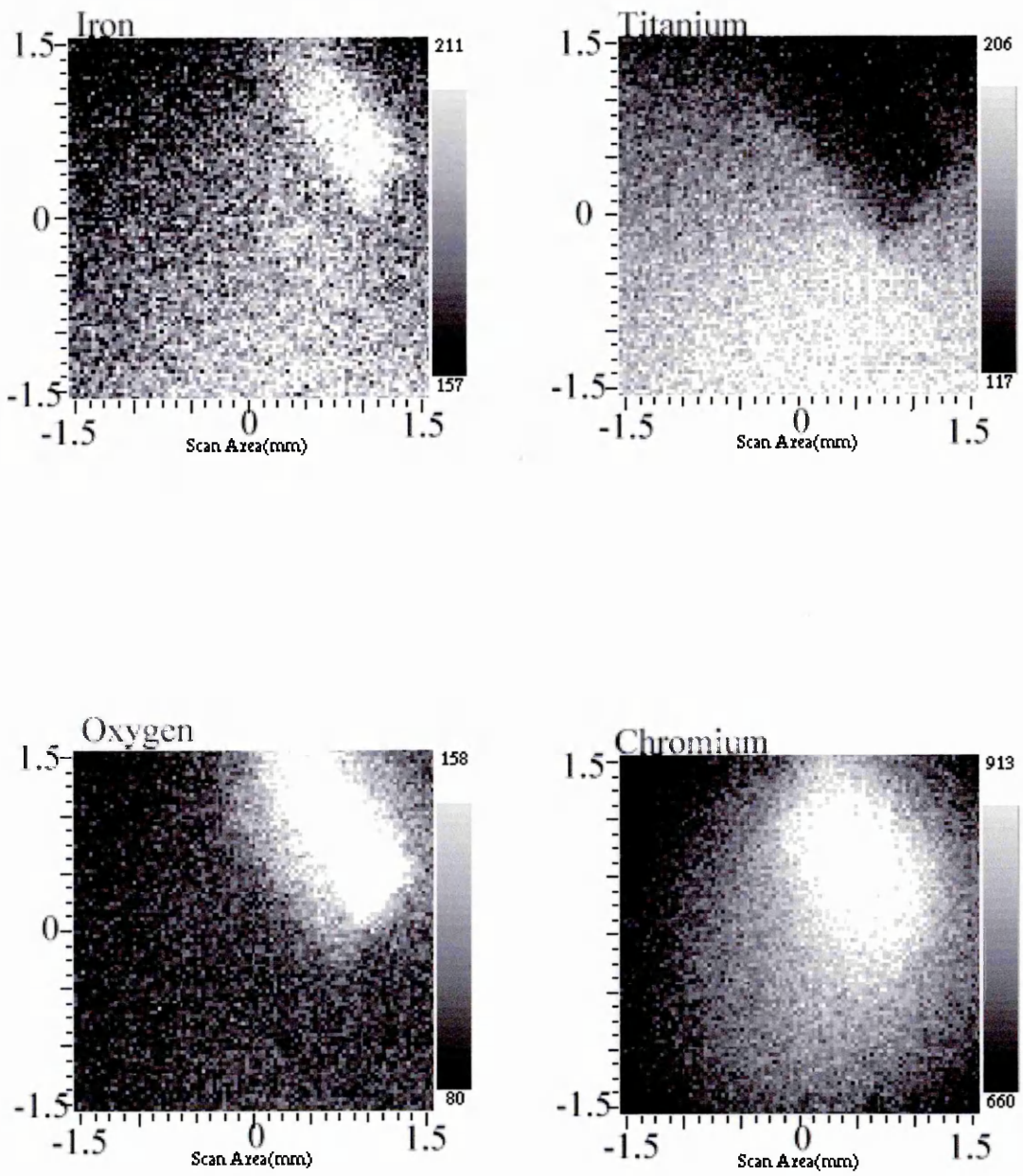

Figure 5.3.4 Edx maps of titanium and iron.

Titanium

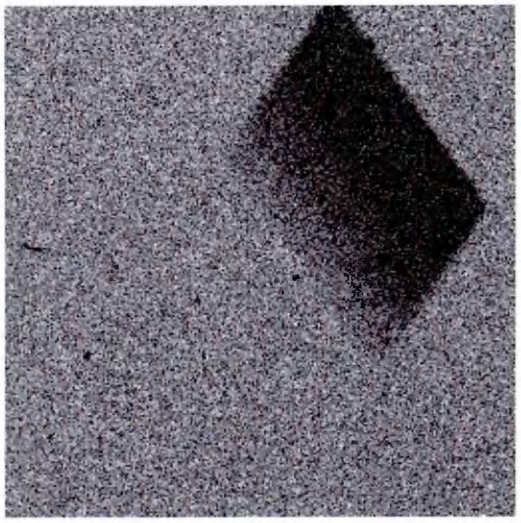

Iron.

5.4. Conclusion

The successful alignment of the centre of the magnetic field generated by the snorkel lens, with the centre of the analyser field of view, enabled us to consider distortions around the centre of the field of view radially. The spatial resolution measurements along the x and y axis showed a major deterioration in resolution as a function of distance from the centre of the field of view. The spatial resolution was measured as a function of other parameters, such as photoelectron energy, iris setting and sample height, in order to understand how to obtain the optimum resolution. The measurement of optimum coil current as a function of position (Figure 5.1.13) demonstrated the need for dynamic focus of the snorkel lens during scanning.

The simulation studies revealed that with the quadropole deflection system, distortion of the field of view was occurring. The octopole deflection system was simulated, which demonstrated that within the analysis area, the distortion would not be apparent. This was sufficient evidence to proceed with the modification of the deflection system to an octopole configuration.

After careful consideration, it was decided that the most appropriate method of modifying the deflection system, was to modify the reference voltages, and generate four extra H.T. voltages for the electrodes. The electronics to do this was built, tested and installed on the system.

The dynamic focus was implemented onto the system, and the parameters associated with this were optimised. The improvement to the images was demonstrated by generating a map of a silver grid, before and after the modification.

Finally, a qualitative example of corresponding EDX and XPS maps was presented. In conlusion, the scanning aspect of the small area XPS capability has been improved, enabling comparison of XPS maps with maps derived from other techniques.

References for Chapter 5:-

Hawkes P.W. & Kasper E, (1989) Principles of Electron Optics Vol. 1, pg504, Academic Press, London.

Horowitz P. & Hill W., (1980) The Art of Electronics, pg 209, Cambridge University Press, Cambridge.

Kelly J. (1977), Electronics and Electron Physiscs, 43, 43.

KellyJ., Groves T., Kuo H.P.(1981) Journal of Vacuum Science and Technology, 19, 936-940.

Dahl D.A. (1994) Simion Version 6.0, Idaho National Laboratory.

Savitsky A. and Golay M. (1964) Analytical Chemistry, 36, 1627.

Chapter 6 Calibration of instrument transmission as a function of energy.

6.0 Introduction

In this section the quantitative calibration of the instrument for XPS is described. The two methods used are both described in Chapter 2, the first of which is the method based on the dependence of signal intensity with instrument pass energy E_p, proposed by Carrazza and Leon (1991). The second method was that of applying a bias voltage to the sample, proposed by Zommer (1995). The results are compared using peak area measurements of gold, silver and copper, to assess how effective is each technique.

6.1.1. Application of method proposed by and Leon using peak area measurements.

The sample used to obtain the signal intensities can be any target which produces a constant flux of electrons with time. In the literature reports, signal intensity measurements were taken from both peak area intensities and background measurements. Measurements taken from peak areas constrain the values of E_k at which the measurements can be taken, but produce a strong signal, thus increasing the signal to noise ratio. In order to cover a wide range of values of E_k the following elements were chosen to produce the peaks to be used for area measurement : Cu, Fe, Ag, Au. The elements are shown in Table 6.1 with the corresponding peak energies to be used (Wagner et al 1979).

Table 6.1.1 XPS signals used for the area measurement in the determination of the instrumental transmission function and their kinetic energy after excitation with Mg and Al x-ray sources.

	Kinetic Energy E_k	
XPS Signal	Mg Source (eV)	Al source (eV)
Cu 2p	320	553
Fe 2p	544	777
Ag 3p	886	1119
Ag 3d	720	953
Au 4f	1169	1402

All samples were in the form of foils and were polished and solvent-cleaned prior to measurement. Samples were cut to a 1cm^2 area. Once introduced to the analysis chamber the samples were sputter cleaned to reduce the carbon overlayer, increasing the signal intensity from the peak. Foil thickness was measured before mounting on the stub and, once loaded in the analysis chamber, sample stub heights

were adjusted to ensure that the surface of different samples was at a constant height with respect to the analyser. For each sample experimental parameters were kept constant. These parameters are listed below in Table 6.1.2.

Table 6.1.2. Experimental parameters.

Iris setting .	1.5
Channeltrons on.	1,2,3,4,5,6,7,8.
X-ray emission.	20mA at 15Kv.
Magnification mode.	Magnetic.
Aperture.	Slot mode.

A step size of 0.1eV and dwell time of 1s was used to scan the region of each peak. The main peak areas were measured after subtraction of the Shirley background (Shirley, 1972). The pass energies at which the areas were measured were 20eV, 40eV, 80eV and 160eV. Although the instrument can operate at pass energies 5eV and 10eV, measurements at these values would be of no benefit. It was found that, below 20eV pass energy, the line width produced by the flood source was the dominant factor contributing to the signal intensity, so below pass energy 20eV, the log I vs. log E_p relationship deviated from that of a straight line.

6.1.2. Results of peak area measurements.

For each kinetic energy point log I was plotted against log E_p. Figure 6.1.1 shows the plots at 320eV (Cu 2p) and 886eV(Ag 3p) respectively.

Figure 6.1.1. Log(I) against log(E_p) for kinetic energies 320eV and 886eV.

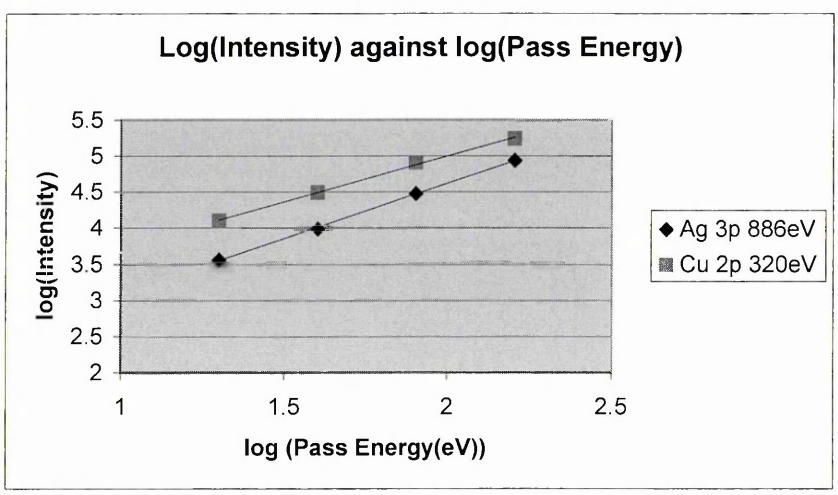

A straight line was fitted to the plots using a function of the Microsoft Excel spreadsheet program and the gradient of the straight line was obtained. The gradient is equal to $n(E_k)-1$, so using these values a plot of the function $n(E_k)$ was generated and is shown as Figure 6.1.2.

Figure 6.1.2. Plot of $n(E_k)$.

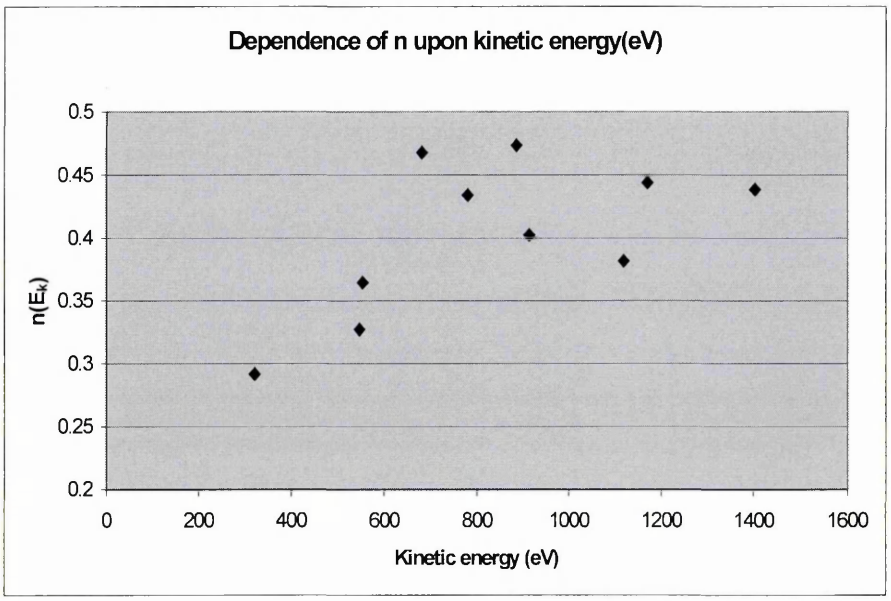

At this stage it is necessary to apply a polynomial fit to the data shown in Figure 6.1.2. It is obvious from inspection of the graph that it would be difficult to fit a polynomial curve to this data. The literature (Carrazza and Leon, 1991) indicates that the function should be smooth, in which case the best function could be found for all points, but the uncertainties would be large. It was concluded that a suitable $n(E_K)$ curve could not be derived from this data so the alternative method using background measurements was applied.

6.1.3. Application of method proposed by Carrazza and Leon (1991) using Background Measurements.

Using the background to obtain signal measurements allows a large number of intensity measurements to be taken from one sample. To obtain a background measurement the average intensity at 5 points 0.1eV about a given E_k was taken. A polished gold foil sample was used, producing high background counts across the energy scale. Signal intensity was measured at increments of 100eV, from 100eV to 1200eV for the Mg source. The multitude of points available using background measurements dispensed with the need to combine Al and Mg anode measurements. The characteristic peaks were avoided so flat regions of the spectrum could be used, in which case E_k deviates from the 100eV increment. The experimental parameters were the same as those used for peak area elemental

measurements listed in Table 6.1.2. The magnification was changed to electrostatic mode and the experiment repeated while all other conditions remained the same.

6.1.4. Results of background measurements.

The background measurements were again plotted as log I against log E_p at each energy. The plots at 300eV and 800eV are shown as Figures 6.1.3 for the magnetic magnification mode and Figures 6.1.4 for the electrostatic magnification mode.

Figure 6.1.3 Plot of log (I) against log (Ep (eV)) at 300eV and 800eV.

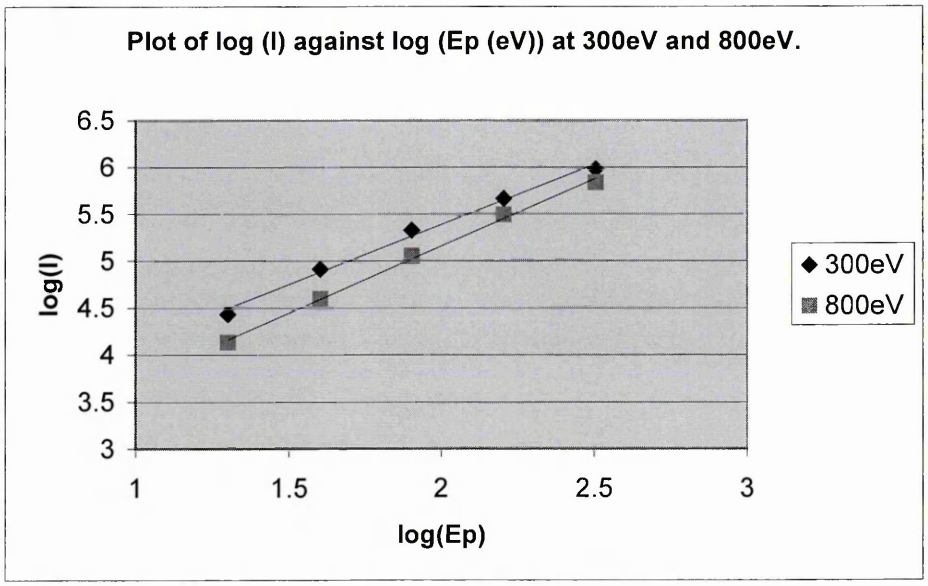

Figure 6.1.4 Plot of log (I) against log (Ep (eV)) at 300eV and 800eV.

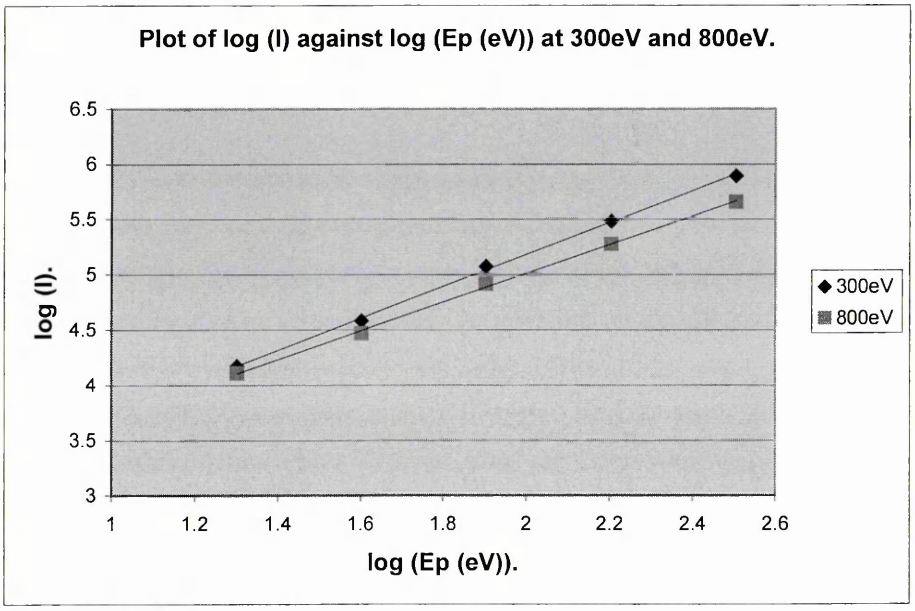

The values of $n(E_k)$ were derived for each energy point and are plotted as Figures 6.1.5 and 6.1.6 for magnetic and electrostatic modes respectively.

Figure 6.1.5. Plot of n(Ek) for Magnetic mode.

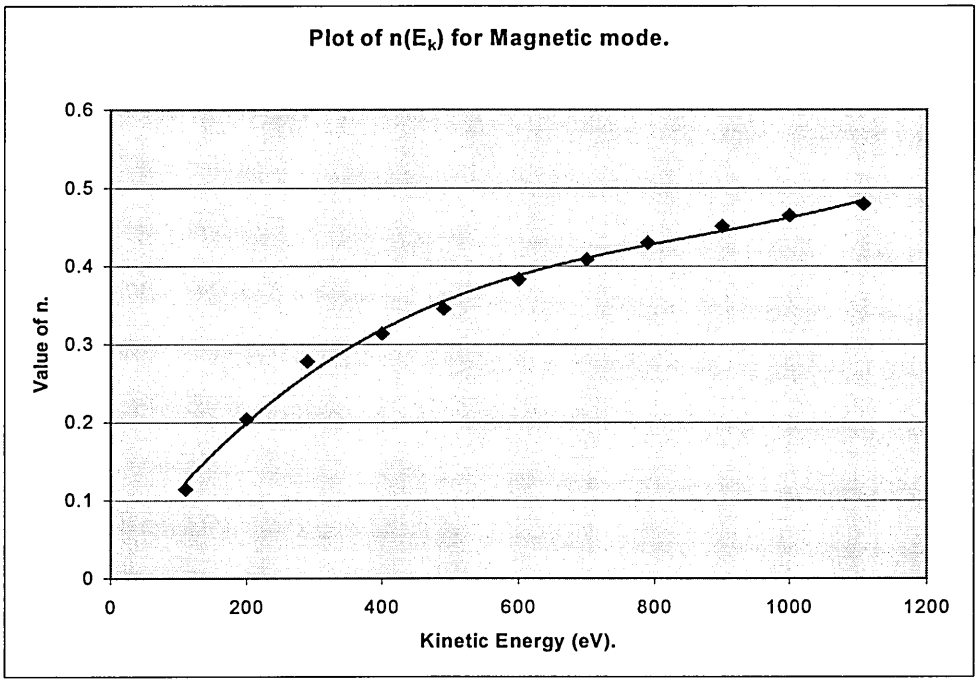

Figure 6.1.6. Plot of n(Ek) for Electrostatic mode.

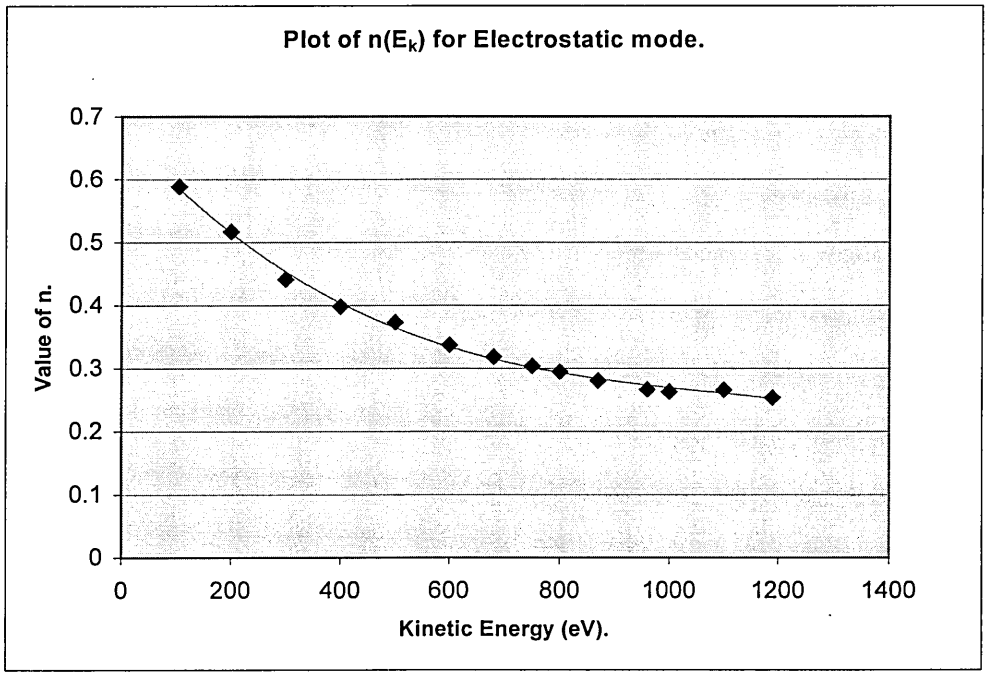

It is clear from the graphs that in both cases the function $n(E_k)$ could be represented by a polynomial, established for each curve using the Excel software polynomial fit function. It was found that a fourth order polynomial provided an acceptable fit without the need to introduce further coefficients. The polynomial for magnetic and electrostatic magnification modes are shown as Equations 6.1.1 and 6.1.2.

$$y = 4.5063E\text{-}10x^3 - 1.1709E\text{-}06x^2 + 1.1750E\text{-}03x + 1.0074E\text{+}00 \qquad \text{Equation 6.1.1.}$$

$$y = -2.5041E\text{-}10x^3 + 8.1490E\text{-}07x^2 - 9.7354E\text{-}04x + 6.7846E\text{-}01 \qquad \text{Equation 6.1.2.}$$

If we refer back to Section 2.2.2, Equation 2.2.17 states that

$$I = kE_k^{-n(E_k)} E_p^{n(E_k)+1} \qquad \text{Equation 2.2.17}$$

If we substitute the polynomials Equations 6.1.0 and 6.1.1 into Equation 2.2.17, and the intensity I is normalised at 100eV, we get the transmission function for the instrument at different pass energies. Figures 6.1.7 to 6.1.11 show the transmission functions for pass energies 20, 40, 80, 160 and 320eV, respectively, in magnetic magnification mode and Figures 6.1.12 to 6.1.16 show the transmission functions for pass energies 20, 40, 80, 160 and 320eV, respectively, in electrostatic magnification mode.

Figure 6.1.7 Transmission Function at Pass Energy 20eV (Magnetic mode).

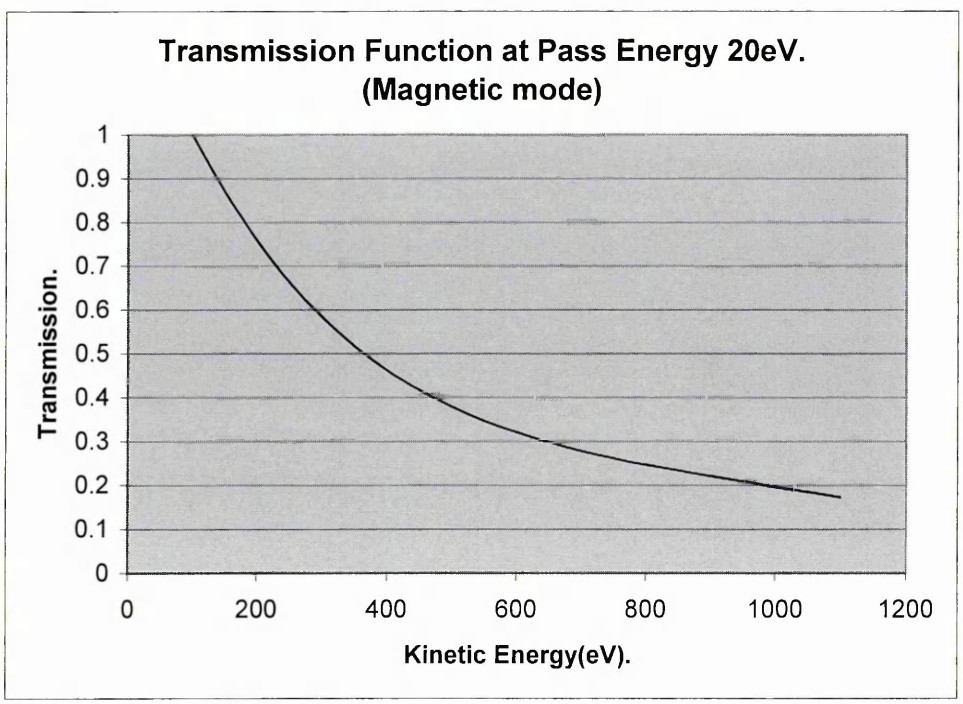

Figure 6.1.8 Transmission Function at Pass Energy 40eV (Magnetic mode).

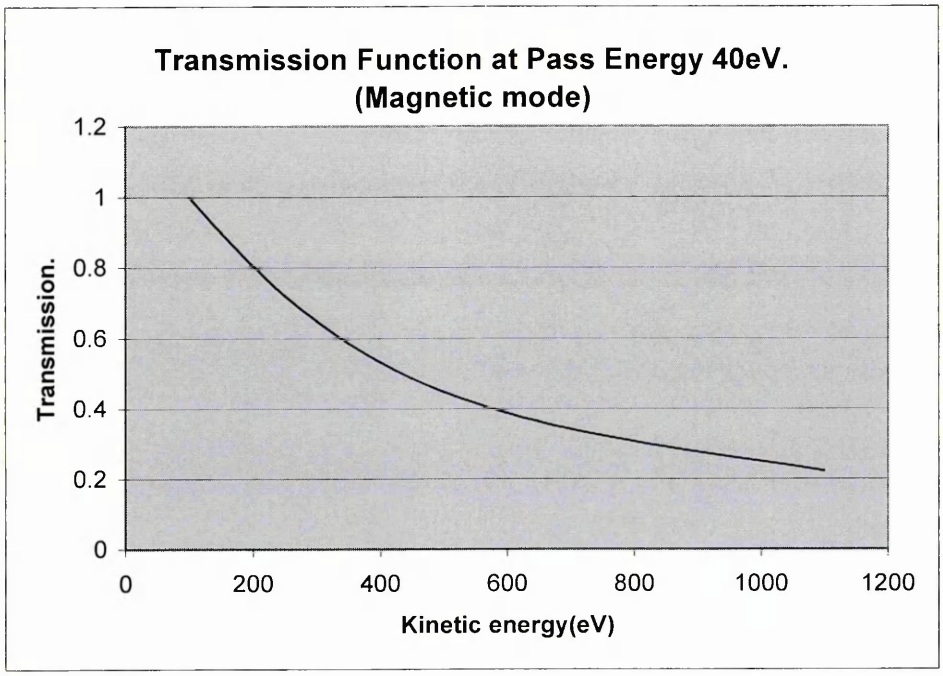

Figure 6.1.9 Transmission Function at Pass Energy 80eV (Magnetic mode).

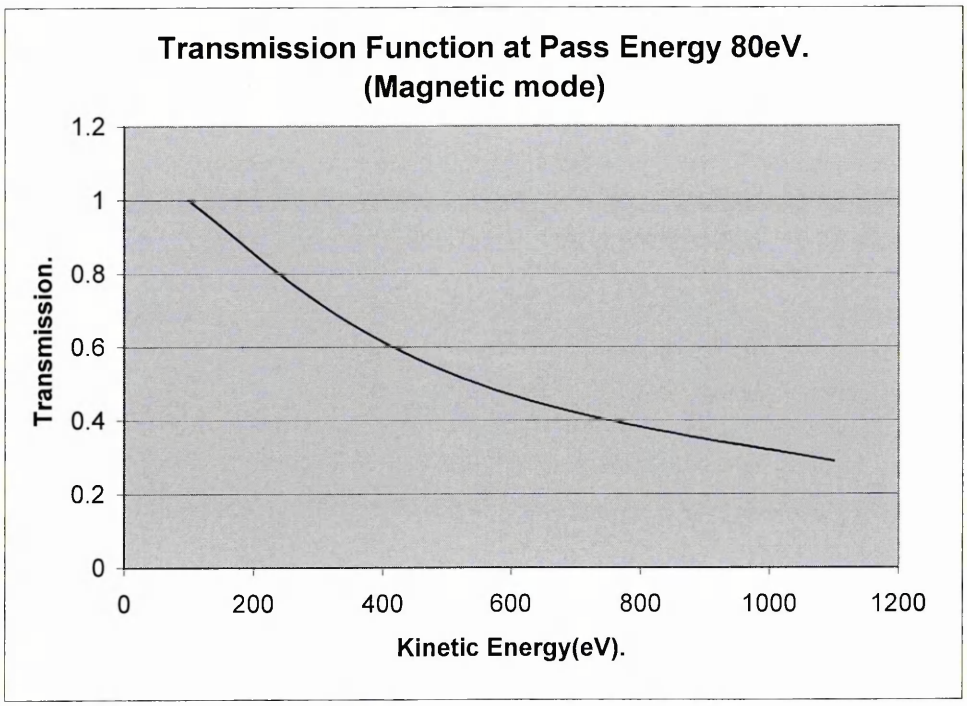

Figure 6.1.10 Transmission Function at Pass Energy 160eV (Magnetic mode).

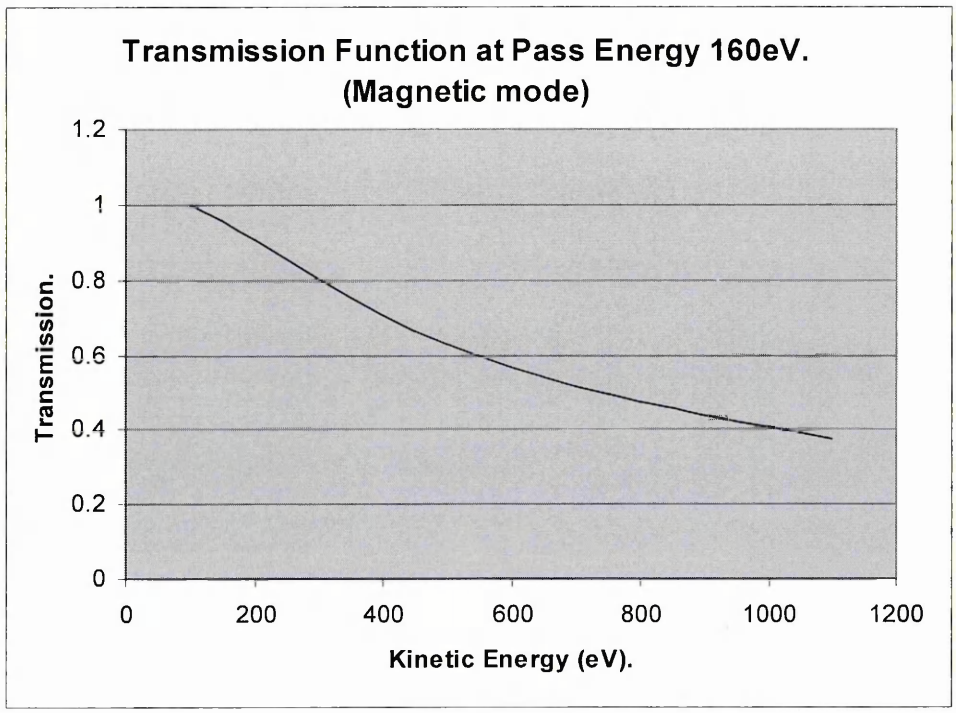

Figure 6.1.11 Transmission Function at Pass Energy 320eV (Magnetic mode).

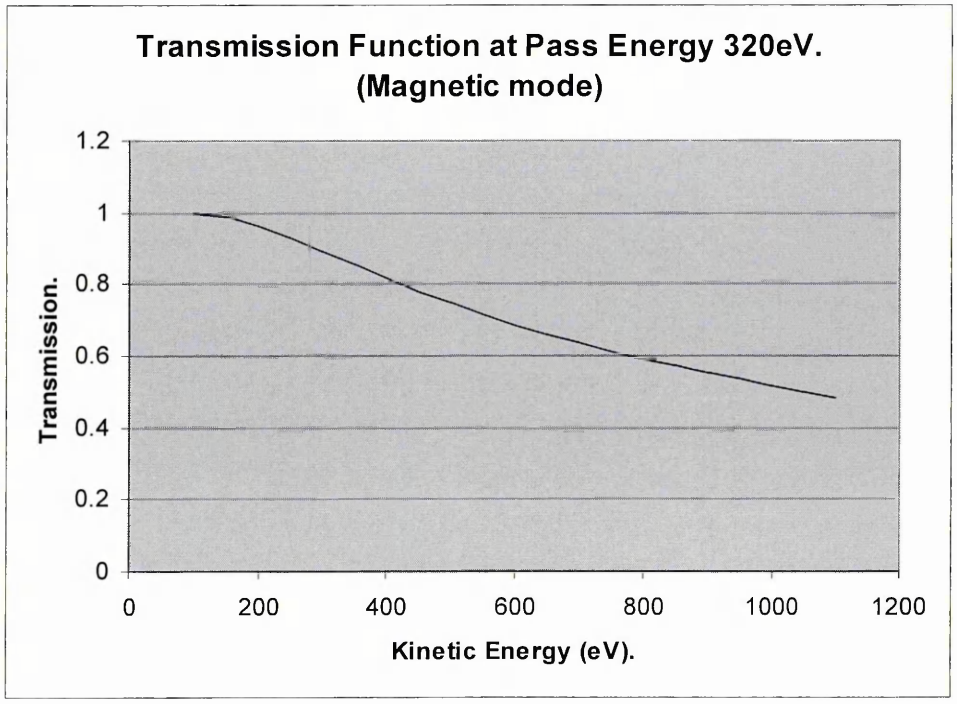

Figure 6.1.12 Transmission function at Pass Energy 20eV (Electrostatic mode).

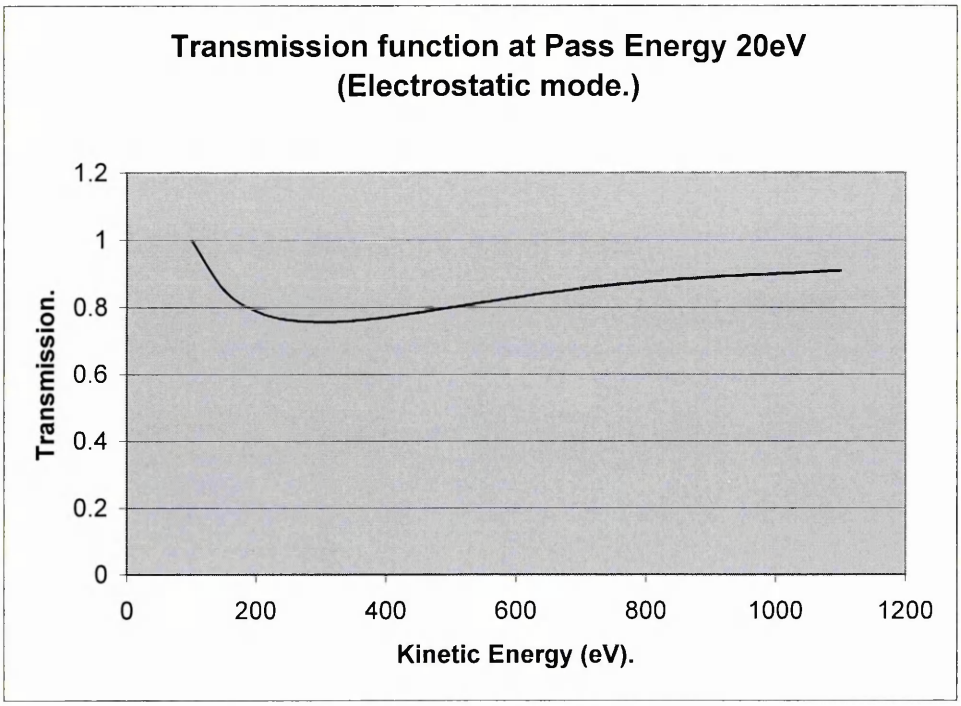

Figure 6.1.13 Transmission function at Pass Energy 40eV (Electrostatic mode).

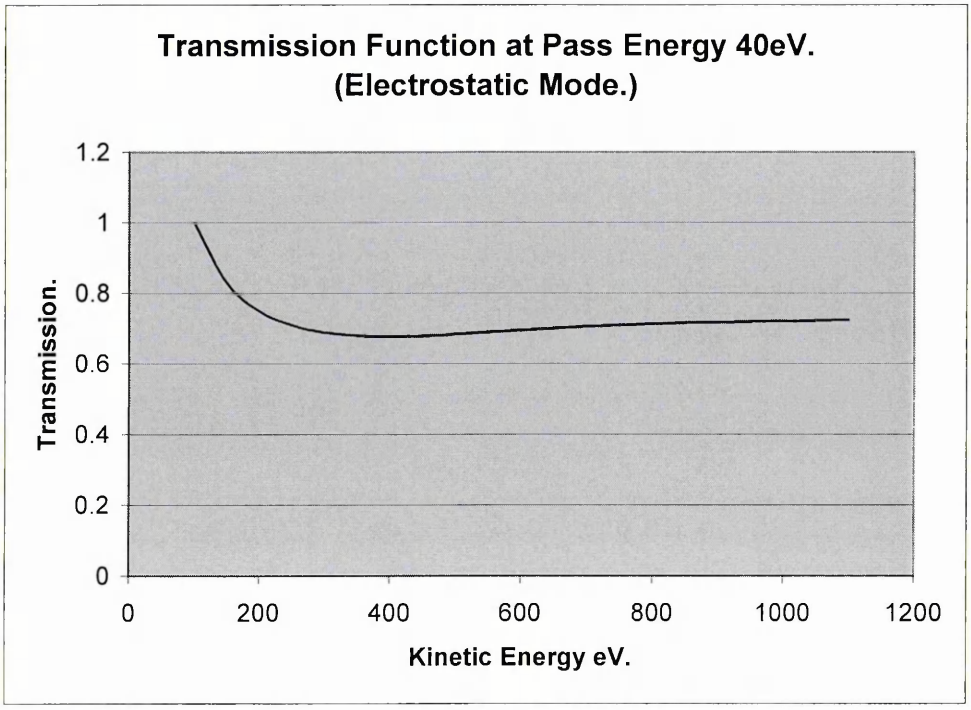

Figure 6.1.14 Transmission function at Pass Energy 80eV (Electrostatic mode).

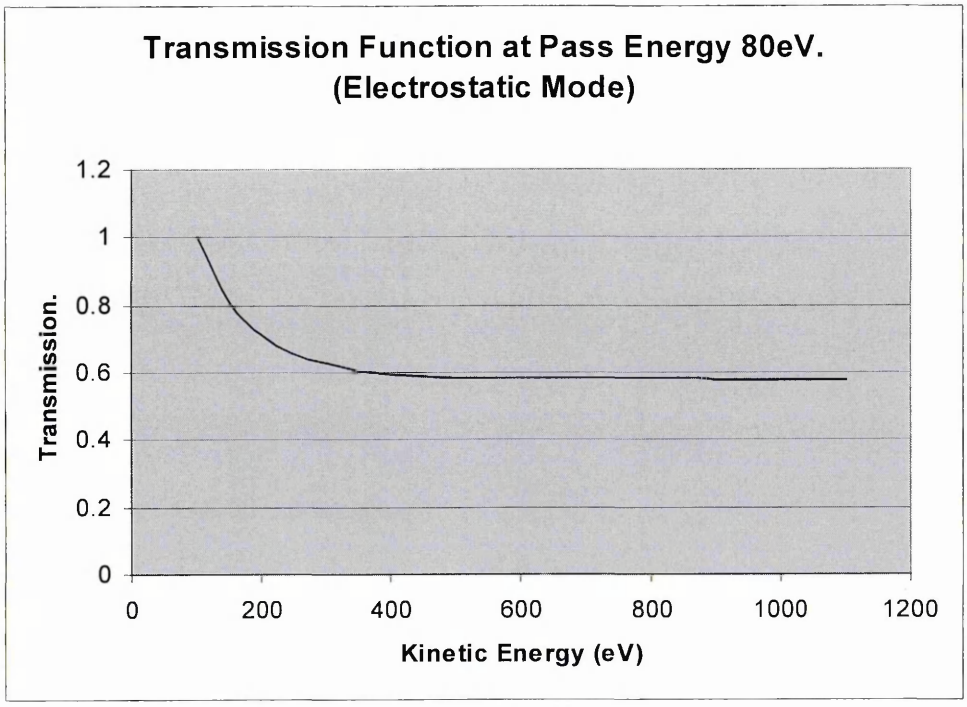

Figure 6.1.15 Transmission function at Pass Energy 160eV (Electrostatic mode).

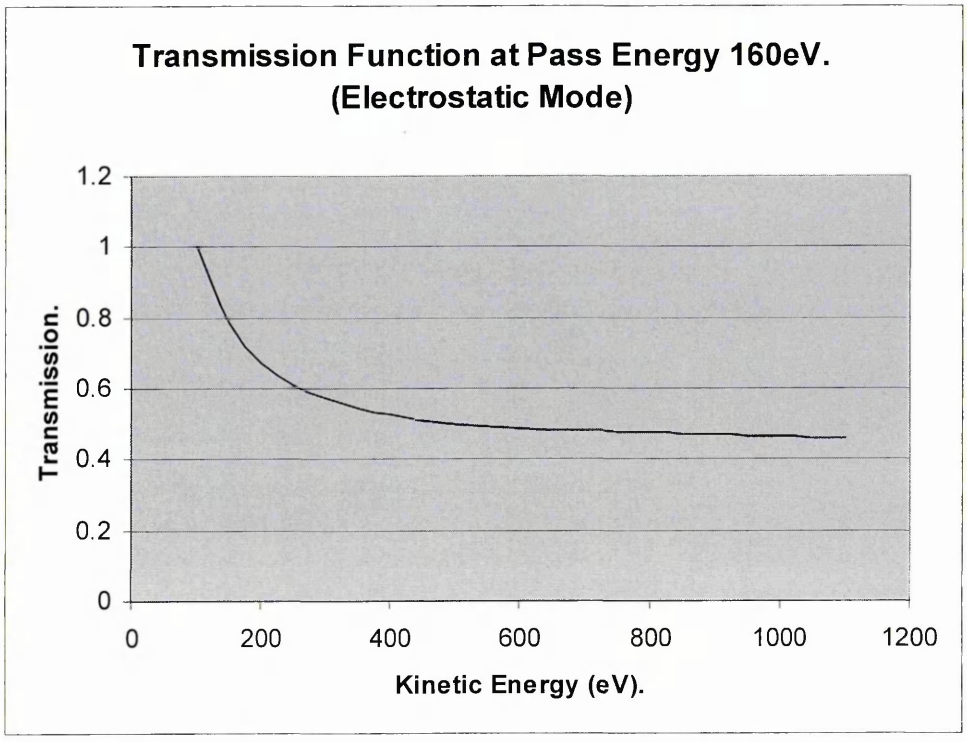

Figure 6.1.16 Transmission function at Pass Energy 320eV (Electrostatic mode).

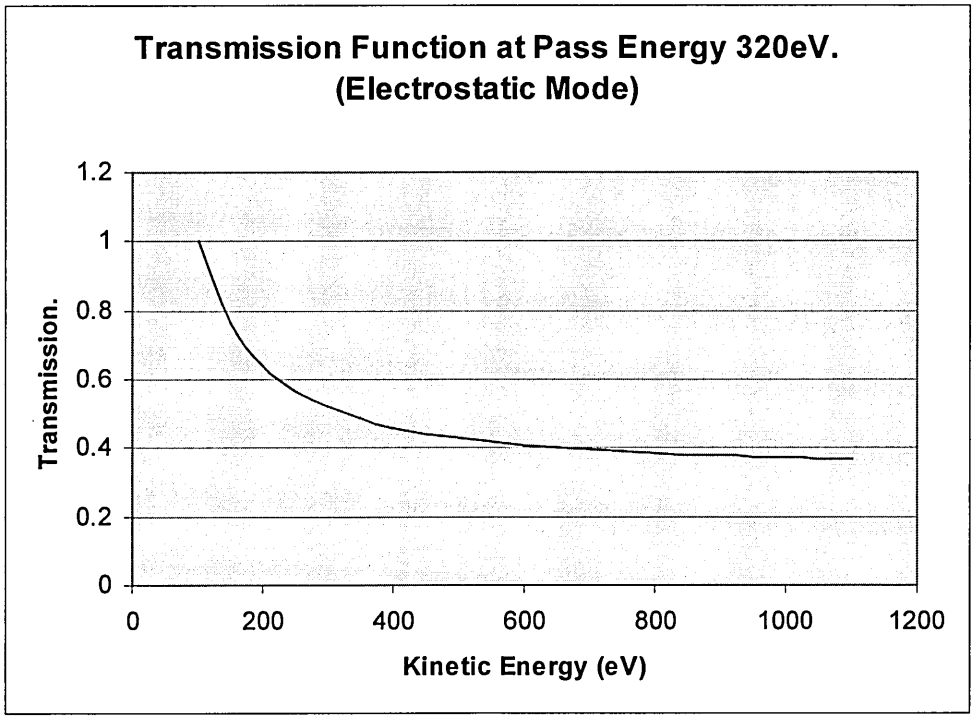

The calculated intensity values as a function of pass energy are plotted for electrostatic and magnetic modes and are shown as Figures 6.1.17 and 6.1.18 respectively.

Figure 6.1.17 Transmission as a Function of Pass Energy at Kinetic Energy 300eV. (Electrostatic mode)

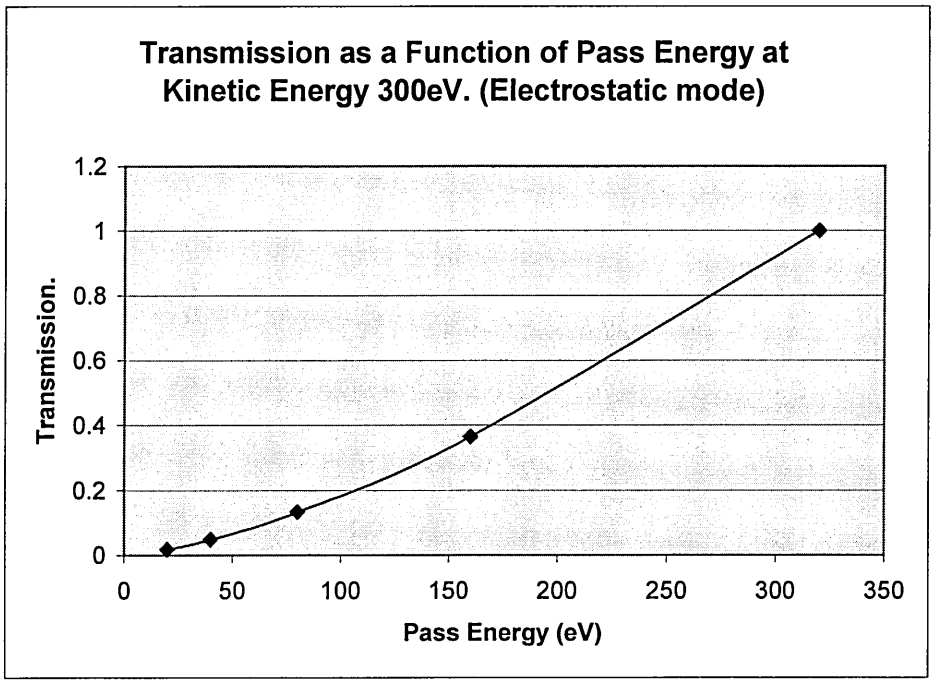

Figure 6.1.18 Transmission as a Function of Pass Energy at Kinetic Energy 300eV. (Magnetic mode)

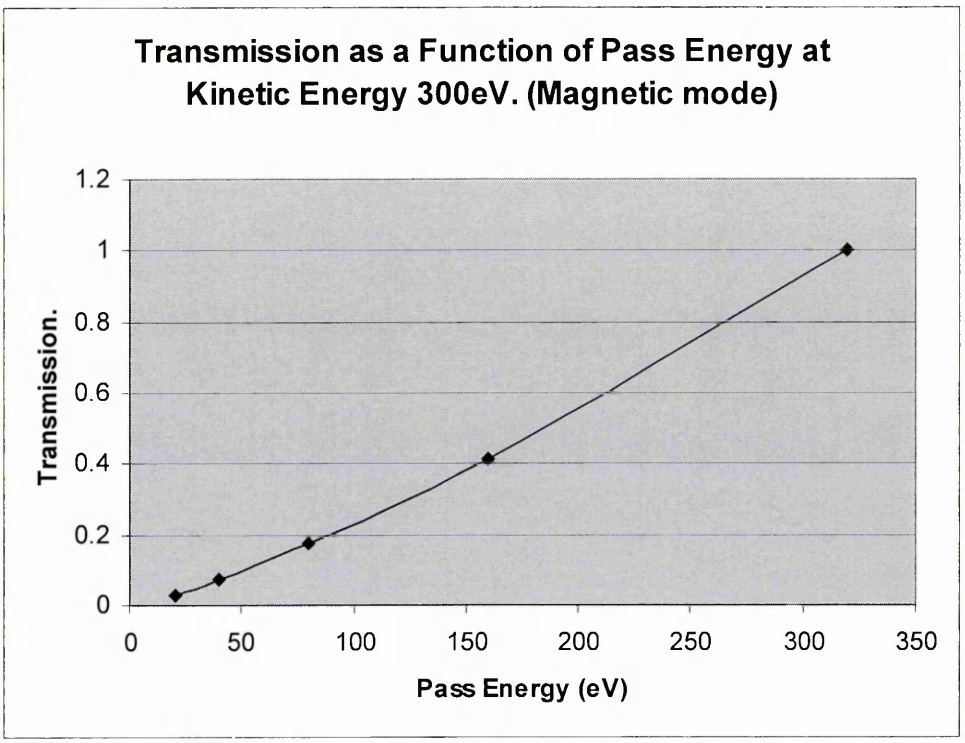

The background measurement experiment was repeated six months after the first experiment in order to determine any change in transmission function with time. All conditions were the same as the previous experiment. Again, gold was used as the sample, and sputter cleaned to remove contaminants, and increase signal intensity. The wide spectra were acquired and the background intensity measurements obtained. The log I against log E_p plots were generated and the straight line gradients obtained. The $n(E_k)$ curves for both magnetic and electrostatic magnification modes were plotted and are shown as Figures 6.1.19 and 6.1.20 respectively.

The polynomial fits for these curves are shown as Equations 6.1.2 and 6.1.3.

$$y = 4.2565E\text{-}10x^3 - 1.1494E\text{-}06x^2 + 1.1146E\text{-}03x + 5.7391E\text{-}02 \qquad \text{Equation 6.1.3.}$$

$$y = -1.7127E\text{-}10x^3 + 6.6329E\text{-}07x^2 - 8.9316E\text{-}04x + 7.0116E\text{-}01 \qquad \text{Equation 6.1.4.}$$

Figures 6.1.19 Second Plot of n(Ek) for Magnetic mode.

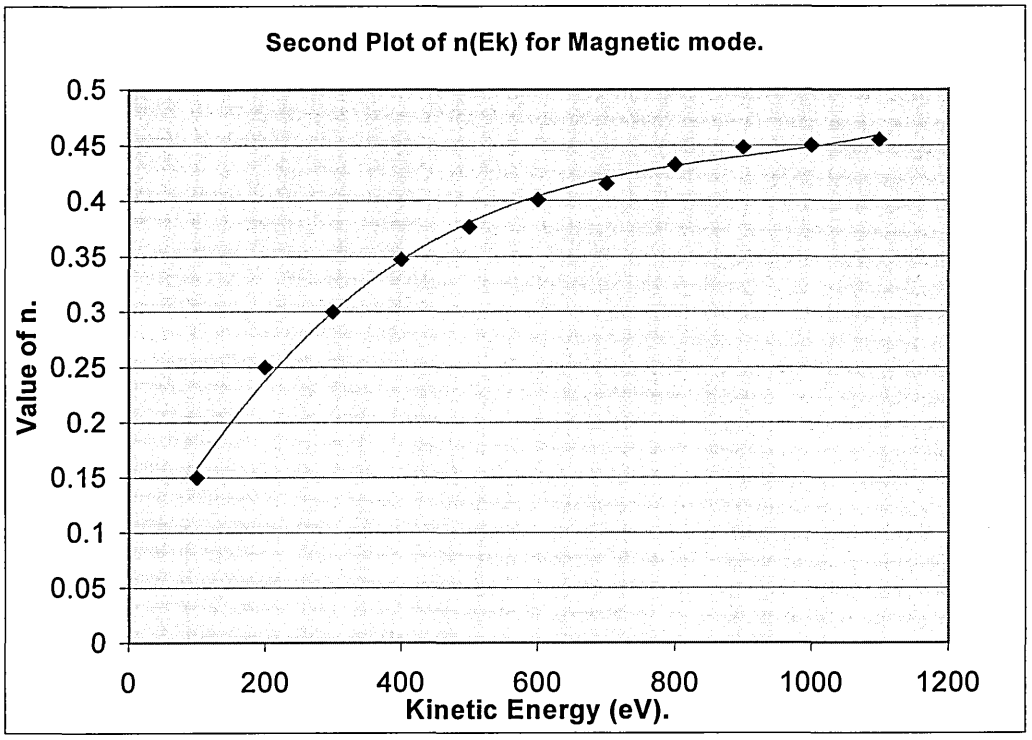

Figures 6.1.20 Second Plot of n(Ek) for Magnetic mode.

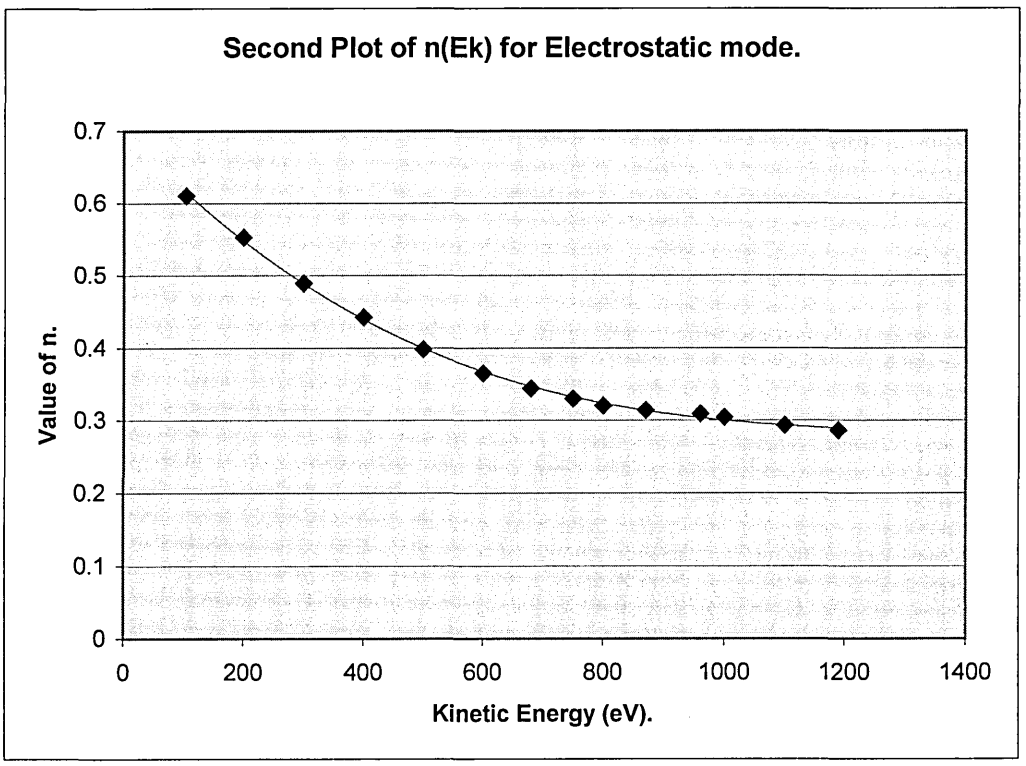

The transmission functions were evaluated and are compared in Figures 6.1.21 and 6.1.22 for pass energy 80eV with the transmission functions previously evaluated.

Figures 6.1.21 Transmission function at 80eV derived from first and second experiment. (Magnetic mode.)

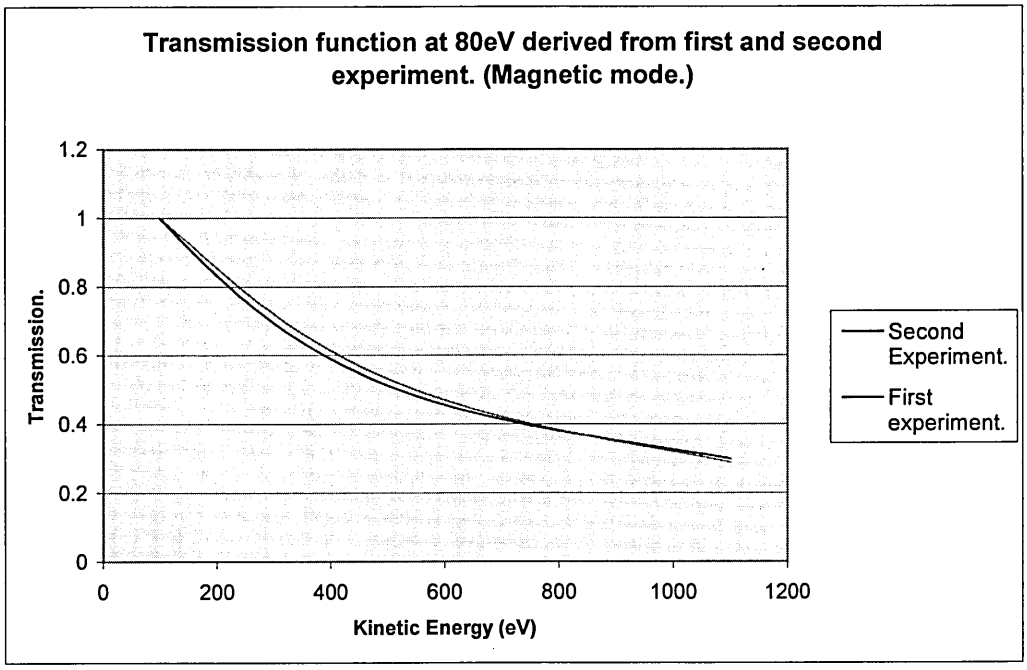

Figures 6.1.22 Transmission function at 80eV derived from first and second experiment. (Electrostatic mode.)

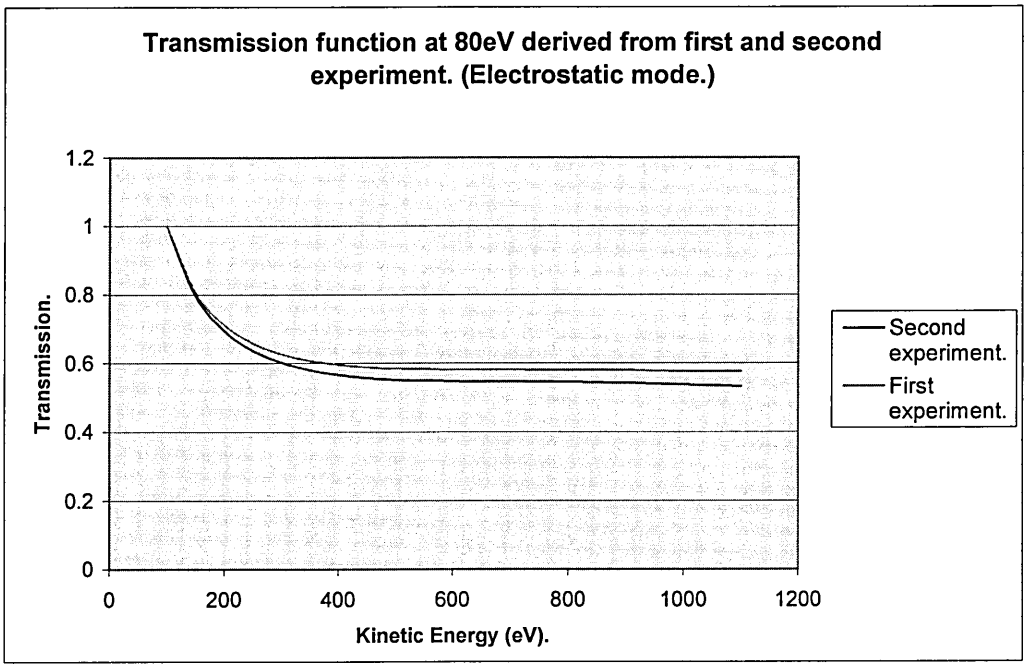

6.1.5 Extension of this technique for regular calibration.

The previous experiment was carried out before the PC and the work station were linked. The data acquisition was carried out on the workstation but the processing of the data for this experiment was carried out on the PC. Once the spectral data could be transferred to the PC in the form of a text file, online, rapid determination of the $n(E_k)$ curve was possible.

To reduce the duration of the procedure wide scans of the sample were performed using a step size of 10eV. The data for a wide scan were exported from the Vision software in the form of a text file (counts written sequentially, line by line, in 6 character format) and this file was then transferred directly to the PC. This procedure was carried out for wide scans performed under identical conditions for a gold sample but with pass energies 20, 40, 80, 160 and 320eV. Each text file was imported into the spreadsheet Excel, and placed into adjacent columns. The first five rows of such a spreadsheet are shown as Table 6.1.3.

Table 6.1.3. Spreadsheet layout for calibration procedure.

Kinetic Energy (eV)		Pass Energy(eV)				
		20	40	80	160	320
100		65864	228575	660215	1342476	2851093
110		65864	228575	660215	1342476	2851093
120		56797	197739	660215	1342476	2851093
130		52837	178319	660215	1342476	2851093
140		49515	161580	660215	1318186	2851093

Conversion of the data to logarithms could can be performed automatically. For each row (corresponding to a kinetic energy point) evaluation of $n(E_k)$-1 could be performed simultaneously using an Excel function, this generating the $n(E_k)$ curve rapidly. The curve would consist of more points than previously (130 for a 100 to 1400eV wide scan), so the degree of scatter from the polynomial fit would be evident.

The above procedure was applied to wide scans using both magnetic and electrostatic magnification, under Mg radiation. The $n(E_k)$ curves are shown in Figure 6.1.23 and the normalised transmission functions are shown in Figure 6.1.24.

Figure 6.1.23 Dependence of the value n upon the kinetic energy of the incident electrons.

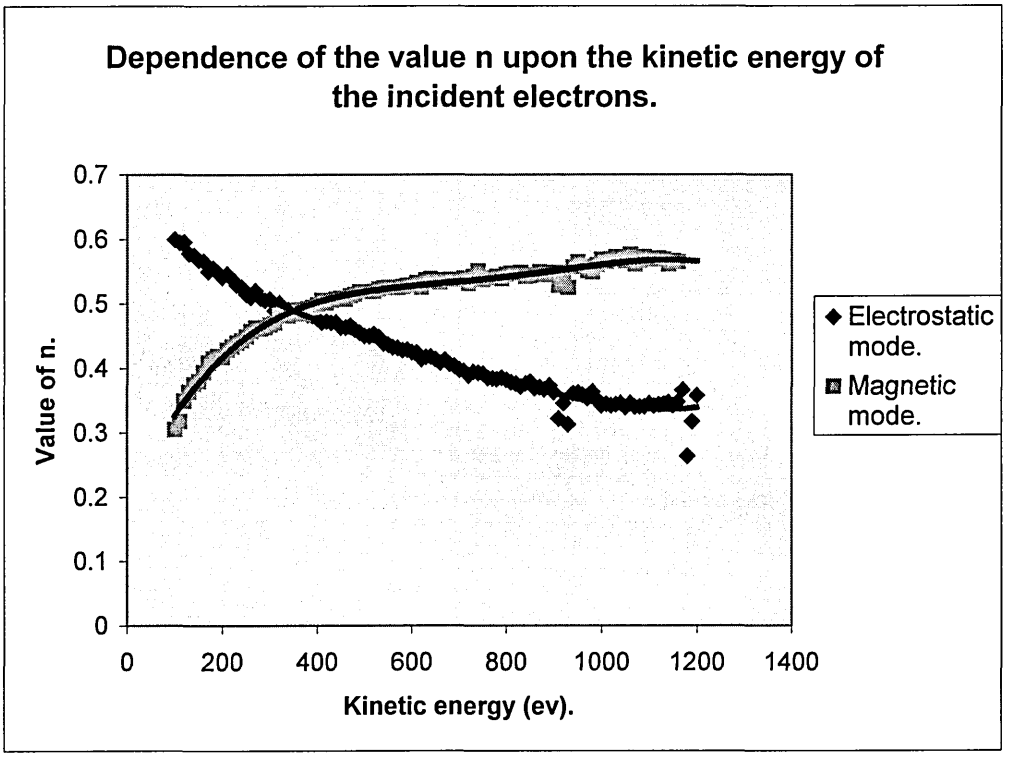

Figure 6.1.24 Transmission function of at FAT 80eV.

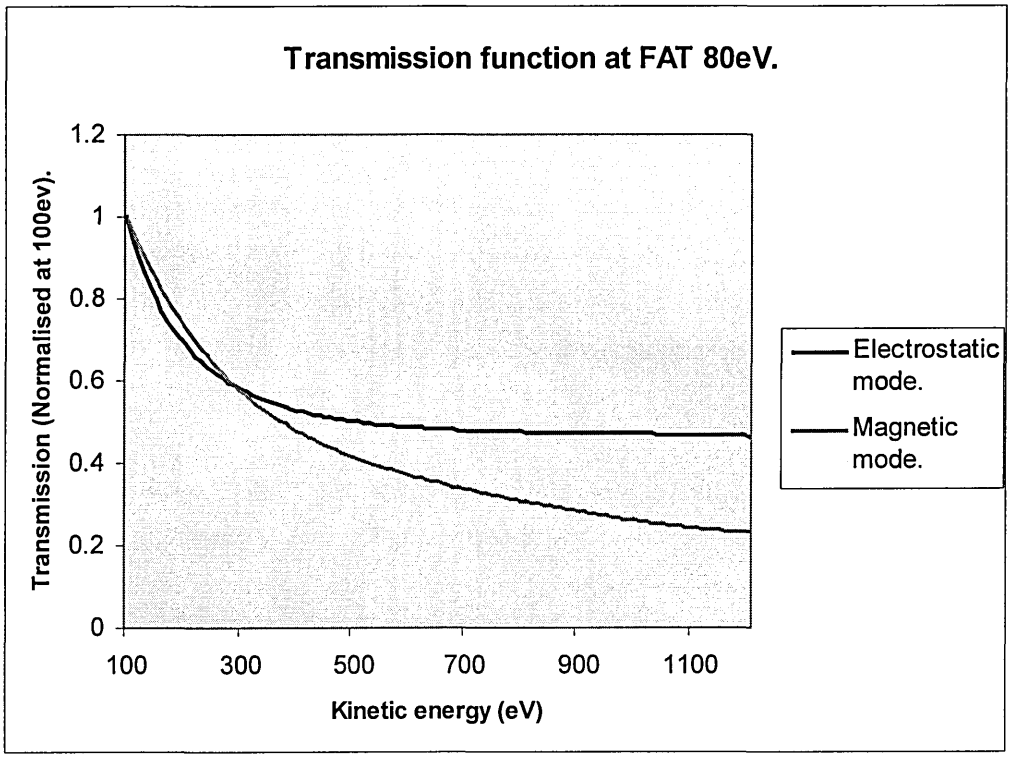

As this approach appeared to be successful, it was applied to the calibration of the analyser with the 120μm area defining aperture in place. The $n(E_k)$ curve obtained is shown as Figure 6.1.25.

Figure 6.1.25 Plot of n(Ek) for magnetic mode with 120um aperture in place.

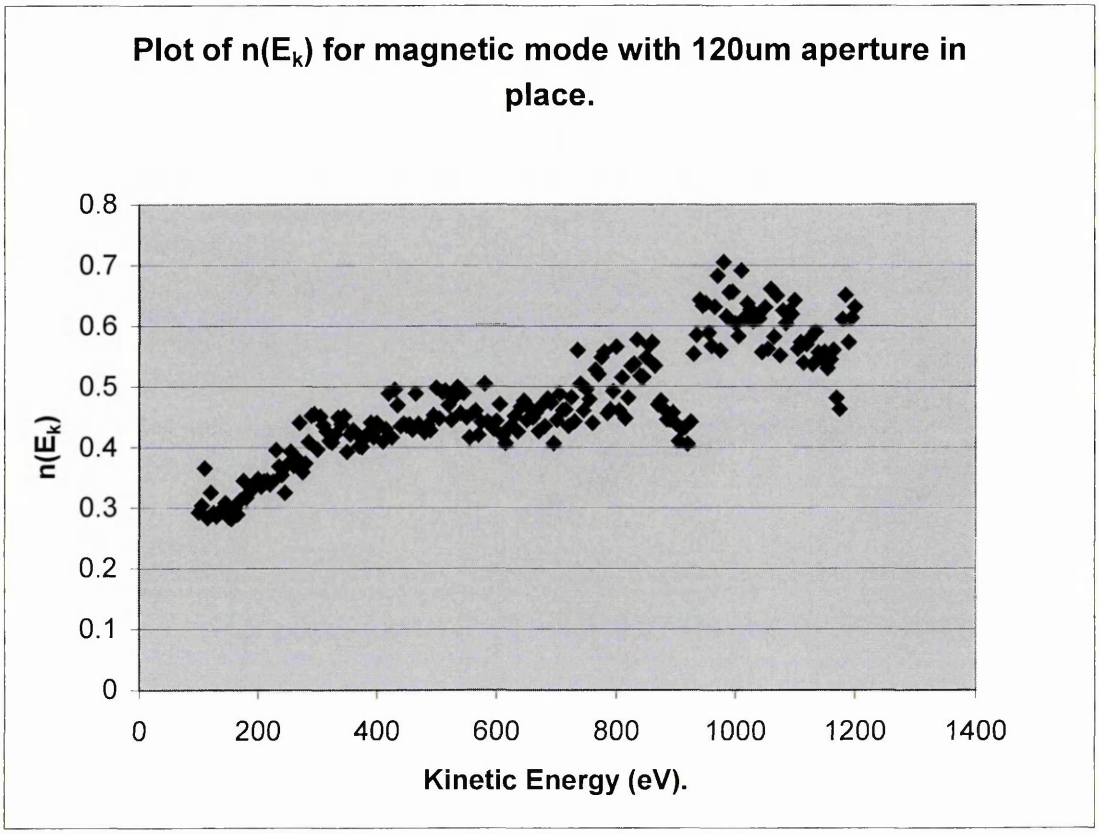

The scatter in the plot was deemed too high, so the data was not used for further calibration work.

6.1.5. Comparison of transmission function with elemental measurements.

In order to evaluate the measured transmission functions, it is necessary to compare sensitivity values derived from the transmission functions, with sensitivity values derived from elemental measurements. If we consider Equation 2.2.11

$$S = \sigma_A(h\nu)T(E_A)\lambda(E_A) \qquad \text{Equation 2.2.11.}$$

then, by substituting values for σ and λ and using the calculated transmission functions, the sensitivity factors for elements on the Hallam instrument may be calculated. These can be compared with sensitivity factors derived from peak area measurements of pure elements on the instrument. The published values of σ were available (Schofield, 1976) and the values of λ could be calculated using Equation 2.2.12

$$\lambda = E^m \qquad \text{Eqaution 2.2.12.}$$

using Wager's value of m=0.66 (Wagner et al 1981).

To measure relative elemental sensitivity factors it is necessary to use pure elemental standards. The pure elements chosen were gold, silver and copper. Earlier investigation using foils purchased commercially yielded unexpected results. Measured sensitivity factors showed large deviations from theoretical sensitivity factors (60% for copper). As the foils had a slightly different thickness and displayed different finishes (polished to varying degrees), it was decide that further attempts were necessary to standardise the sample.

To obtain a common finish the three metal samples were prepared by evaporating the metals onto glass microscope slides. This was done using an Edwards carbon/metal coating unit. The glass slides were solvent-cleaned and the pressure in the coating chamber was less than 5 x 10^{-5}Torr for all three elements. Chippings were cut from the metallic foils and were used as the evaporation sources. Each slide was coated with approximately 2μm of metal by evaporating the appropriate mass of metal according to the equation

$$t = m / \rho 4\pi r^2 \qquad \text{Equation 6.1.5}$$

where t is the thickness of the coating, m is the mass of metal evaporated in kg, ρ is the density of the metal in kg/m^3, and r is the distance from source (metal clippings in tungsten basket) to sample (glass slide) in m. The thickness of 2μm was chosen as this would provide enough material to sputter clean without completely removing the metal. The samples exhibited a common mirror like finish. The area of the glass substrate was 2cm^2, ensuring that the elemental metal completely covered the field of view in both electrostatic and magnetic modes. The gold, silver and copper samples were mounted on the same stub with each coating surface electrically linked to the stub with a track of silver paint to prevent charging effects.

The samples were placed in the analysis chamber and ion sputtered using 5kV argon ions to remove all traces of oxygen and carbon. The carbon and oxygen content was monitored by running wide scans after each sputtering period. The wide scans for the clean samples are shown as Figure 6.1.26. The peaks are labelled for each element (photoelectron and Auger), and the oxygen (O1s) and carbon (C1s) peak positions are shown on each spectrum.

Figure 6.1.26. Wide Spectra from Cleaned Samples.

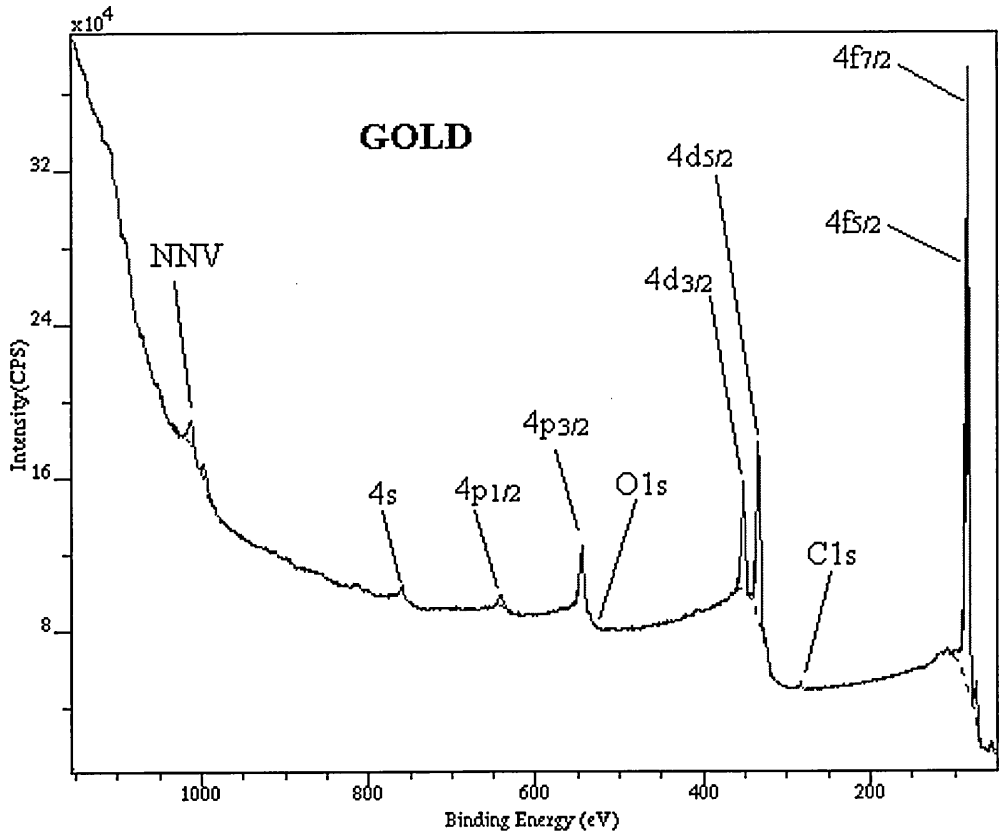

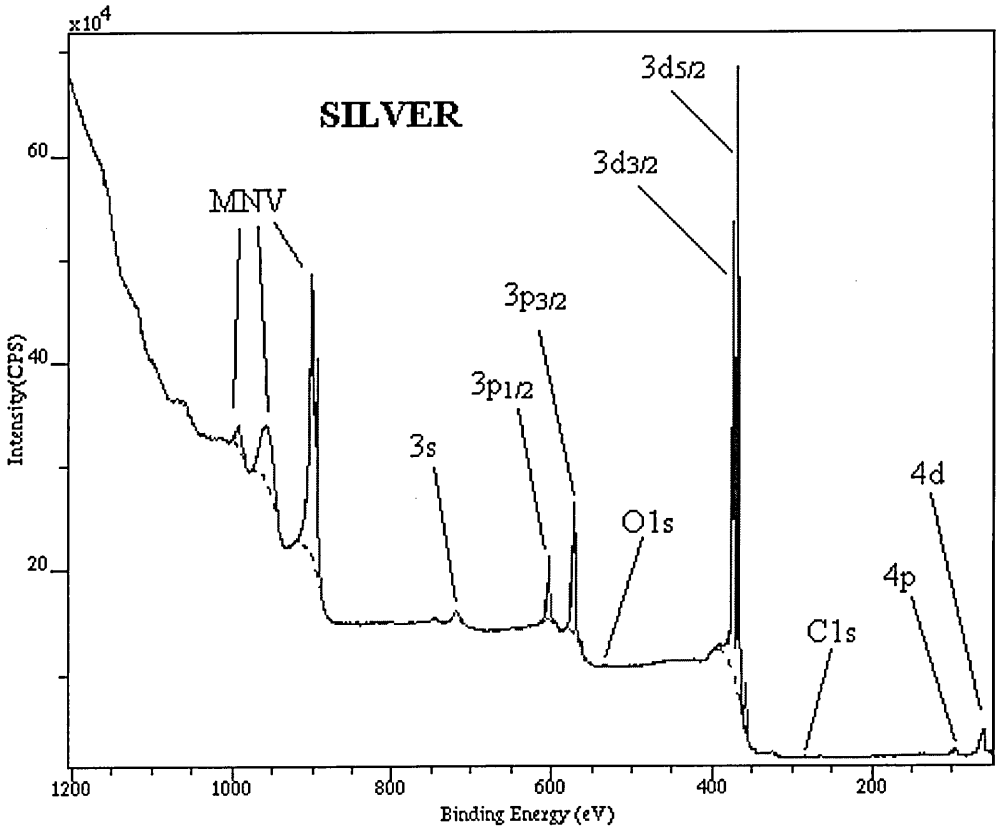

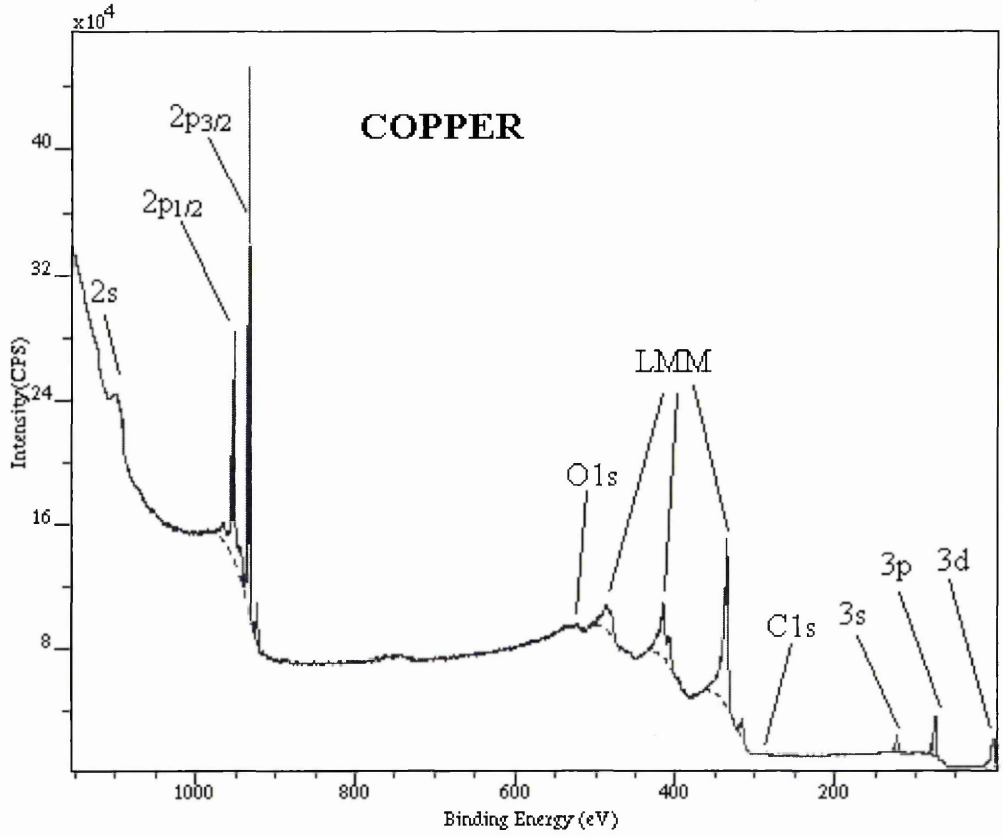

The strongest line of each element was scanned using the standard experimental parameters, with both electrostatic and magnetic magnification. This was carried out at pass energies 20,40,80 and 160eV. The spectra for magnetic magnification scans are shown as Figures 6.1.27 to 6.1.30 for pass energies 20, 40, 80 and 160eV respectively. The spectra for electrostatic magnification scans are shown as Figures 6.1.31 to 6.1.34 for pass energies 20, 40, 80 and 160eV respectively. Peak area measurements of the spectra were taken by fitting a Gaussian function to the spectra. This method was chosen rather that direct measurement of the area under the peak, as it allowed a peak to be generated which was not distorted by neighbouring peaks. Background subtraction was carried out automatically using the Shirley method (Shirley, 1972). Using Equation 2.2.11 relative sensitivity values were calculated for gold, silver and copper (sensitivity normalised for Cu 2p peak) and compared to those derived from measurements. Tables 6.1.4 and 6.1.5 show results for peak area measurements taken using the electrostatic and magnetic modes, respectively. Table 6.1.6 shows the percentage error as calculated by: error=100(calculated value – measured value)/measured value.

Figure 6.1.27 Spectra for magnetic mode pass energy 20eV.

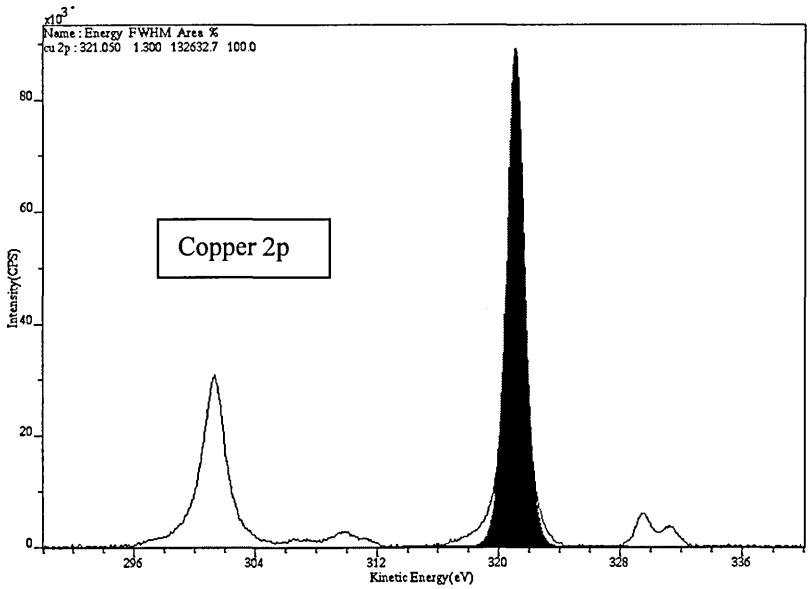

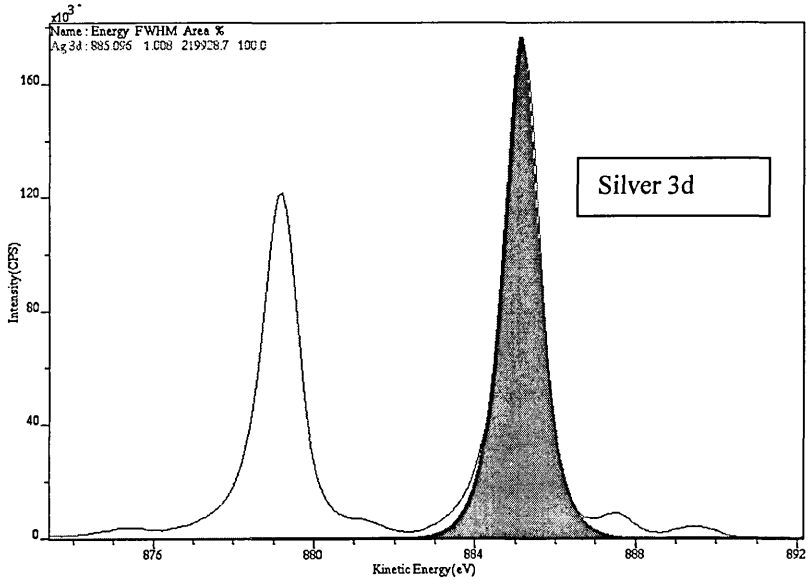

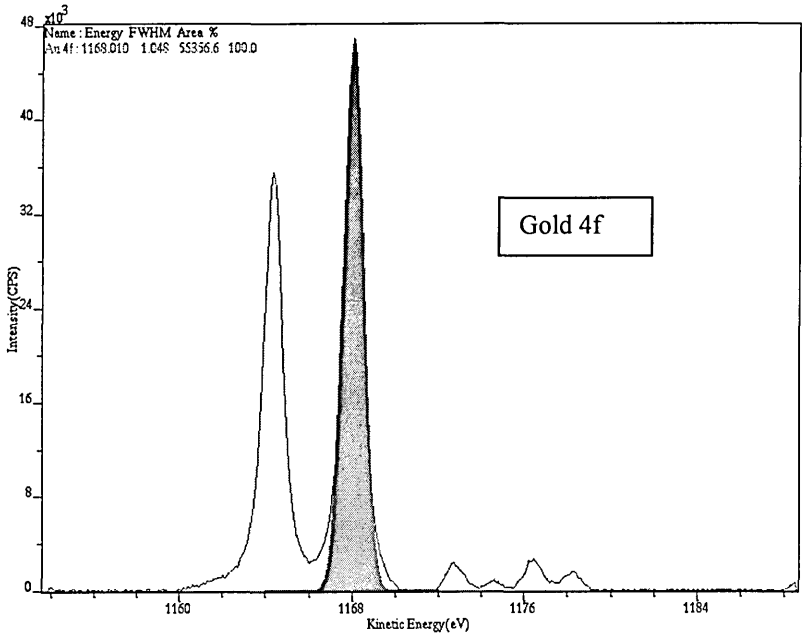

Figure 6.1.28 Spectra for magnetic mode pass energy 40eV.

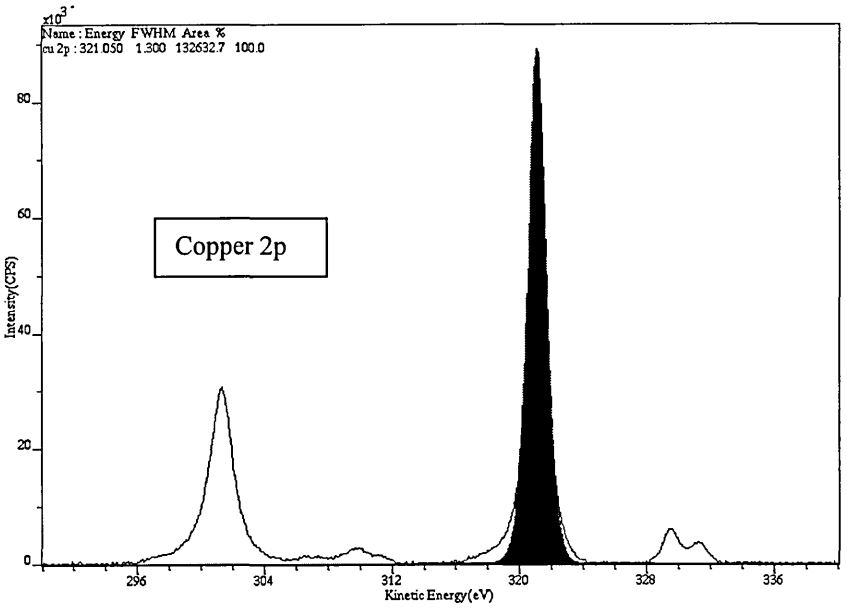

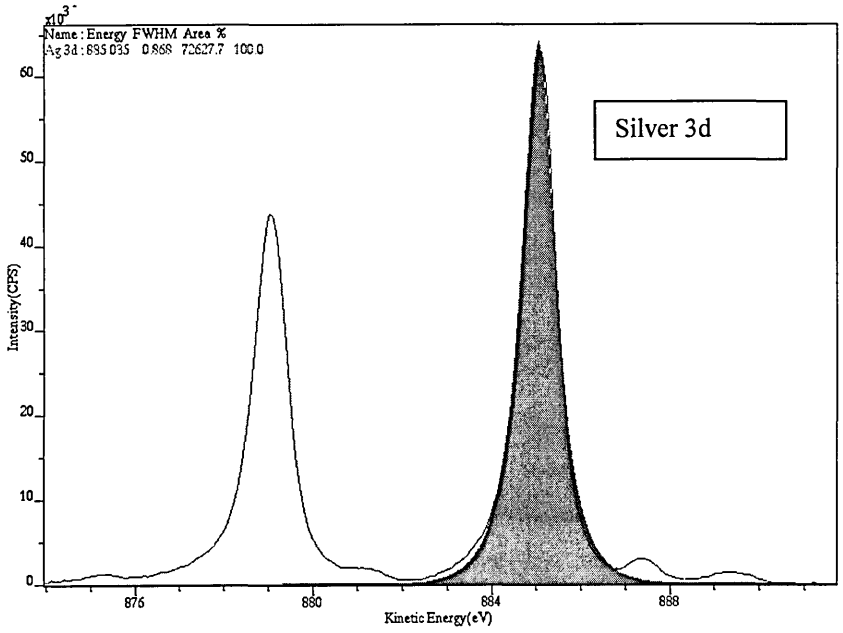

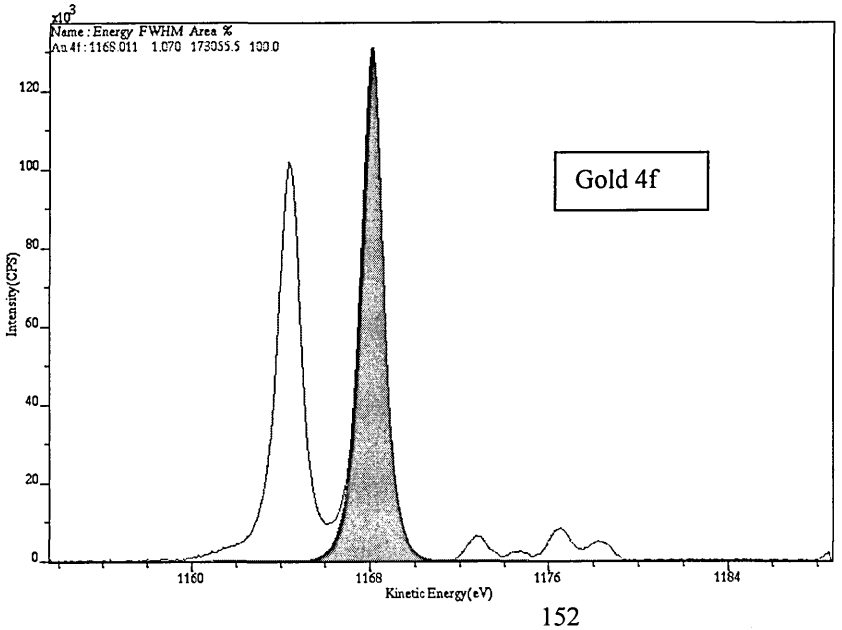

Figure 6.1.29 Spectra for magnetic mode pass energy 80eV.

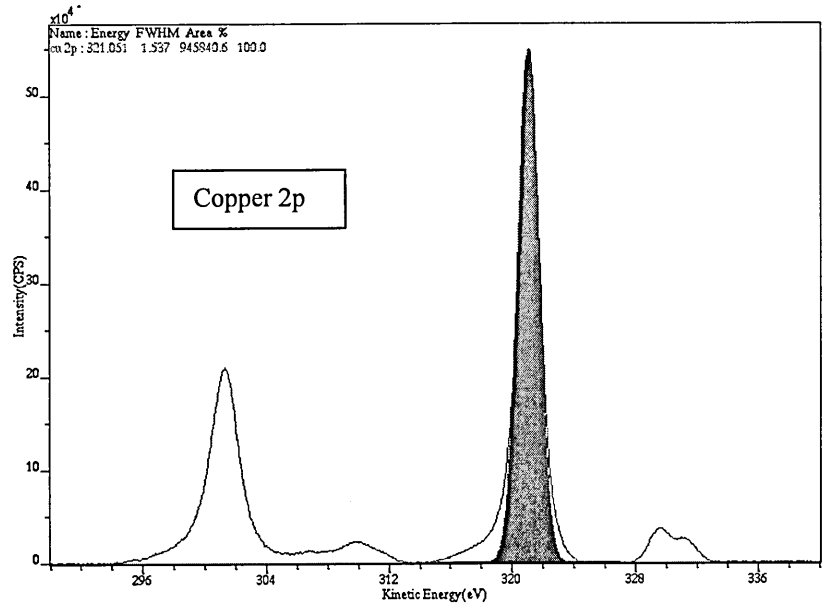

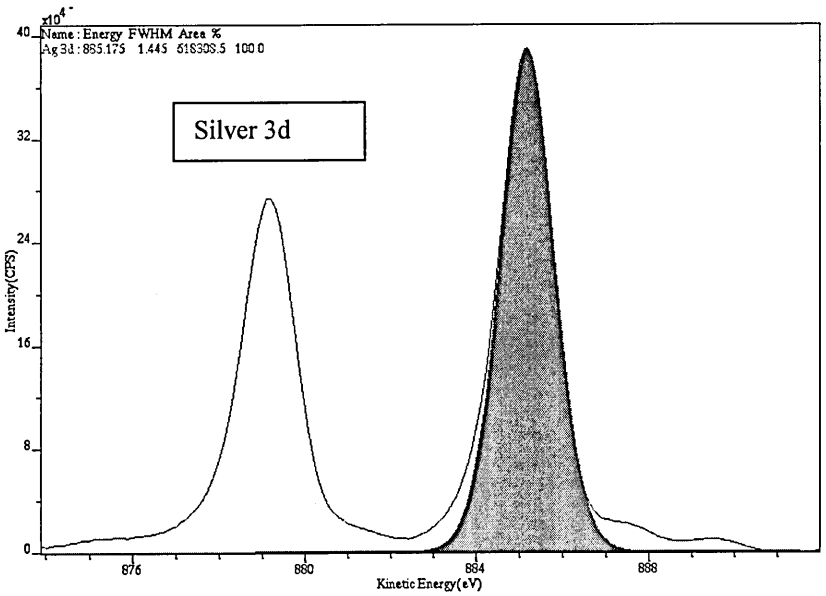

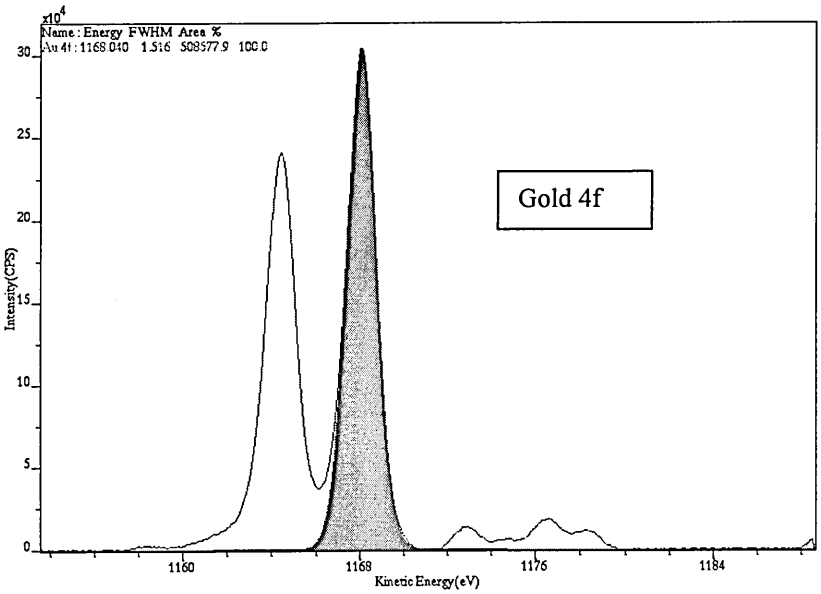

Figure 6.1.30 Spectra for magnetic mode pass energy 160eV.

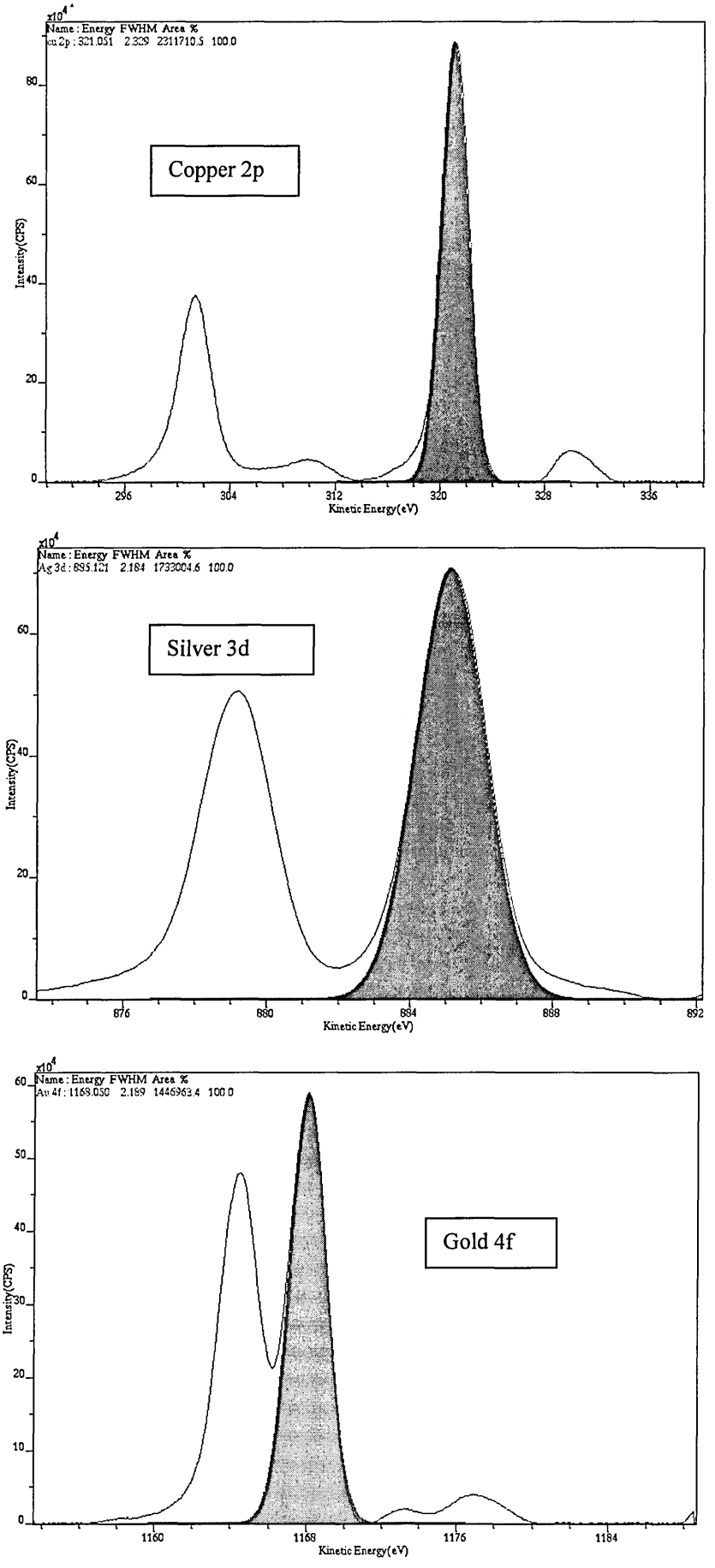

Figure 6.1.31 Spectra for electrostatic mode pass energy 20eV.

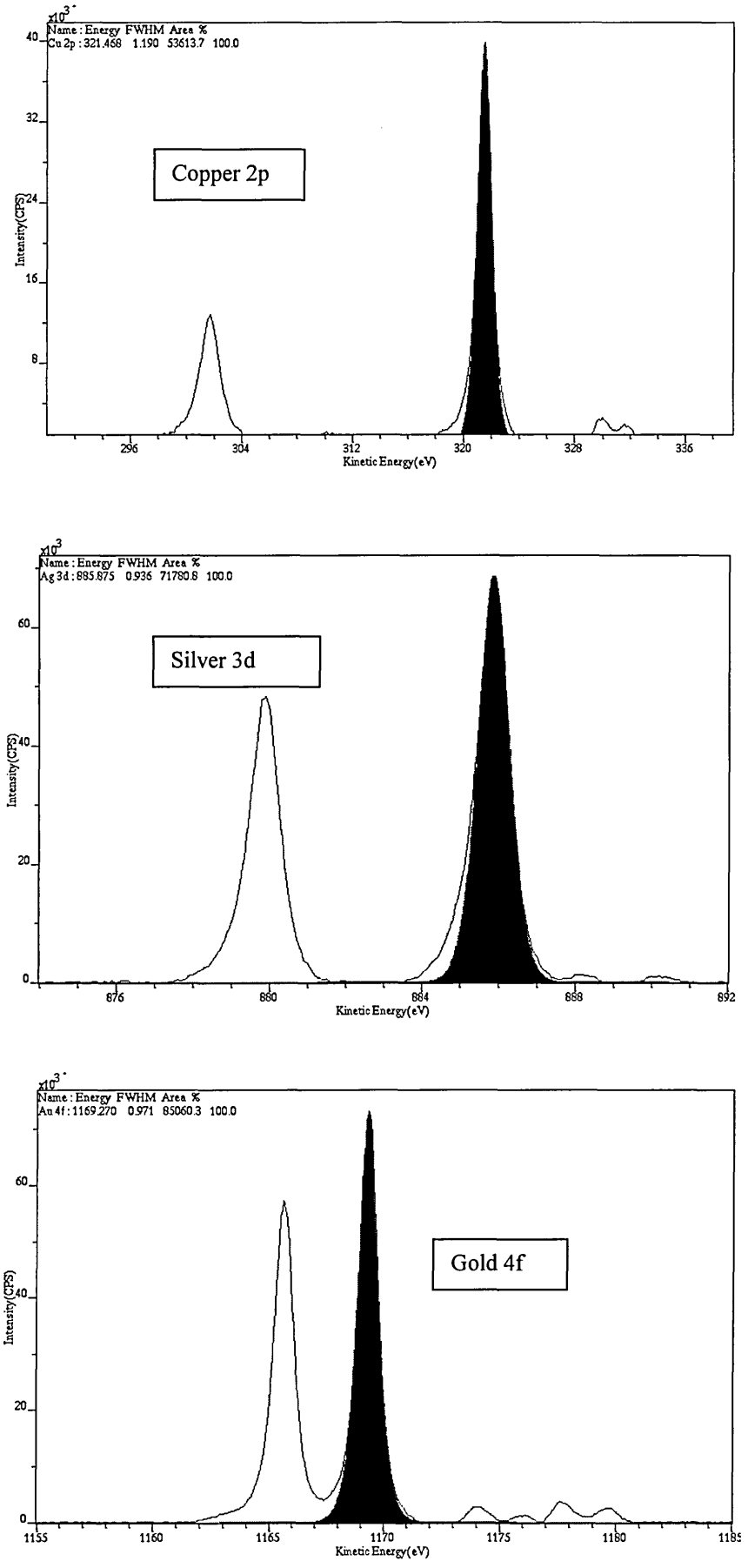

Figure 6.1.32 Spectra for electrostatic mode pass energy 40eV.

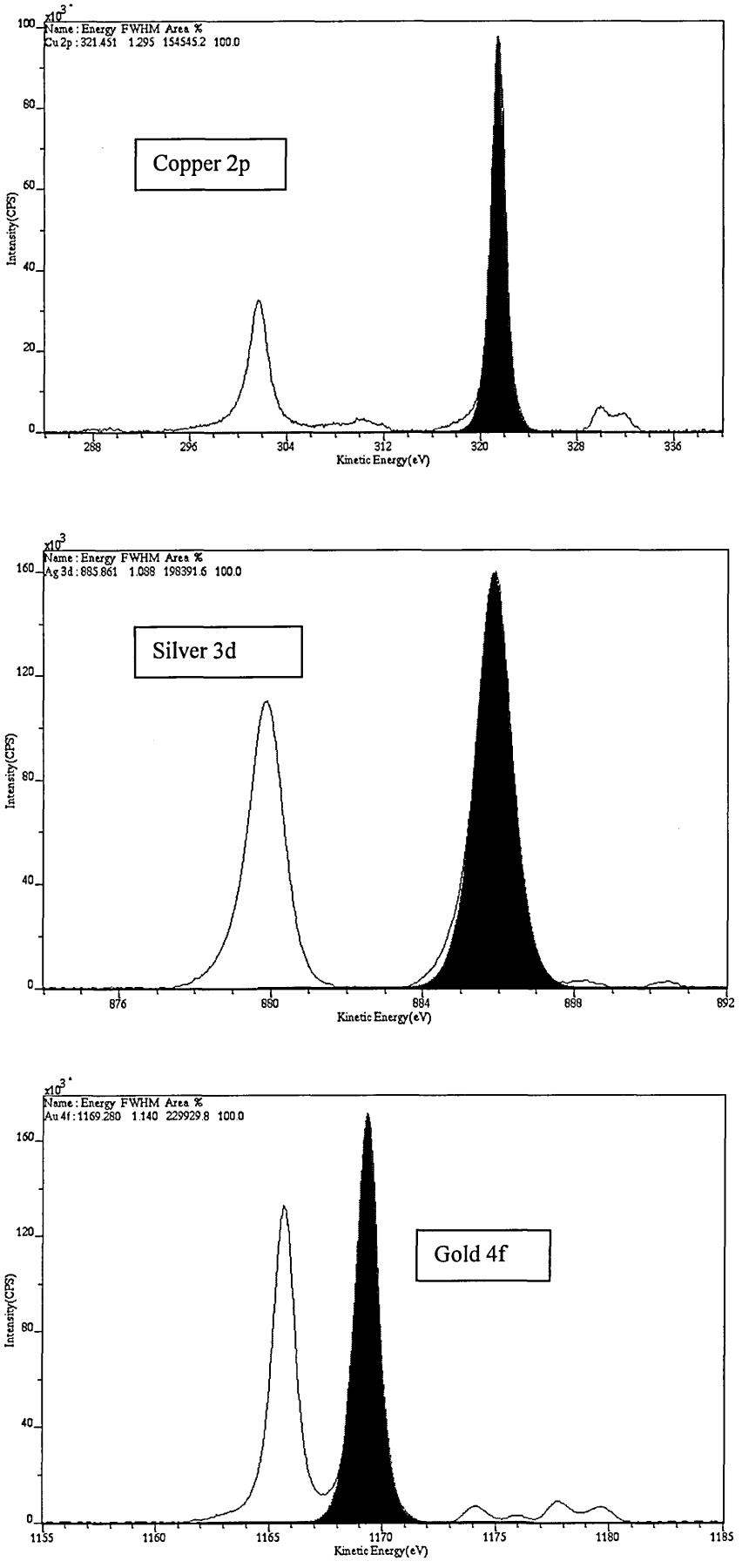

Figure 6.1.33 Spectra for electrostatic mode pass energy 80eV.

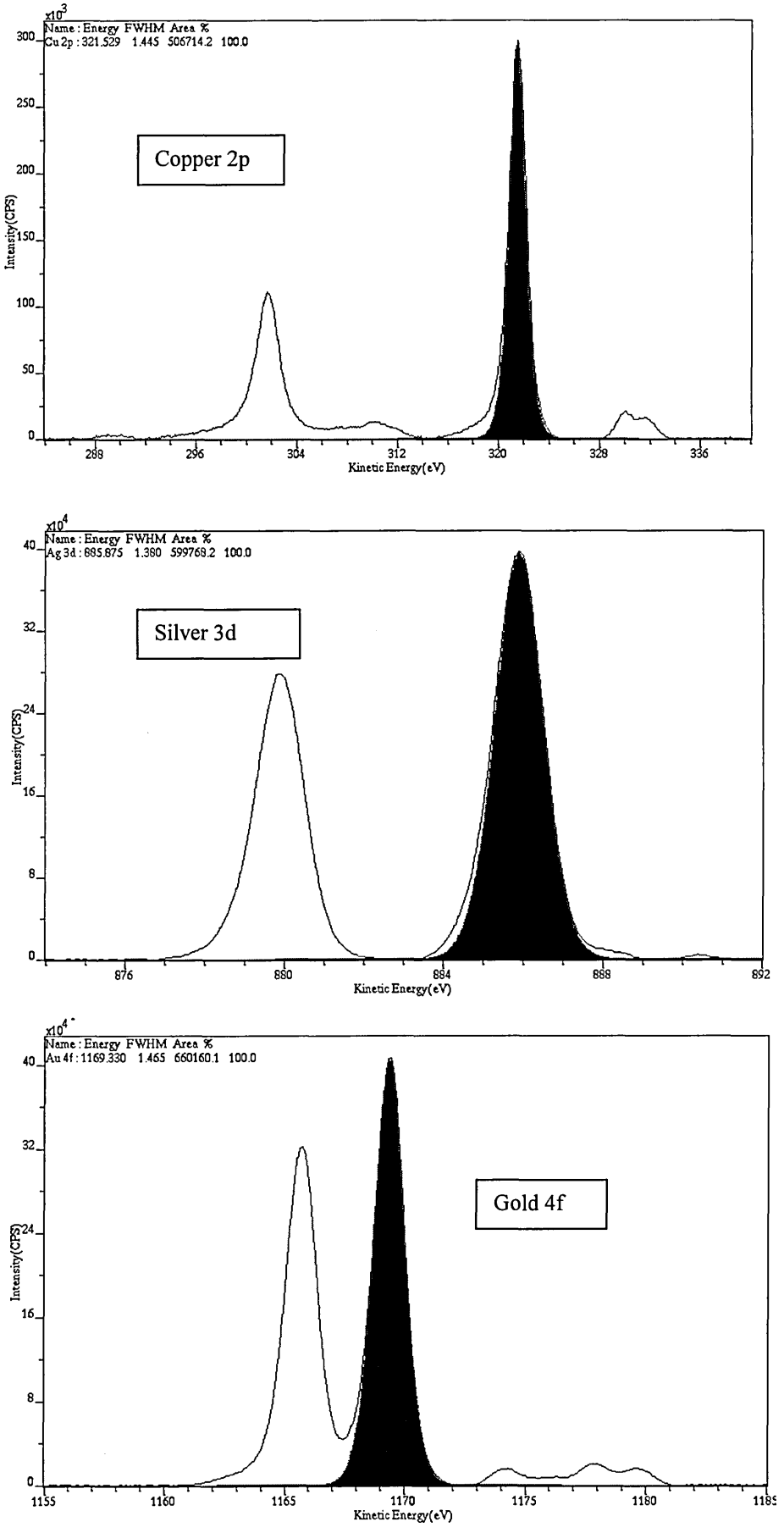

Figure 6.1.34 Spectra for electrostatic mode pass energy 160eV.

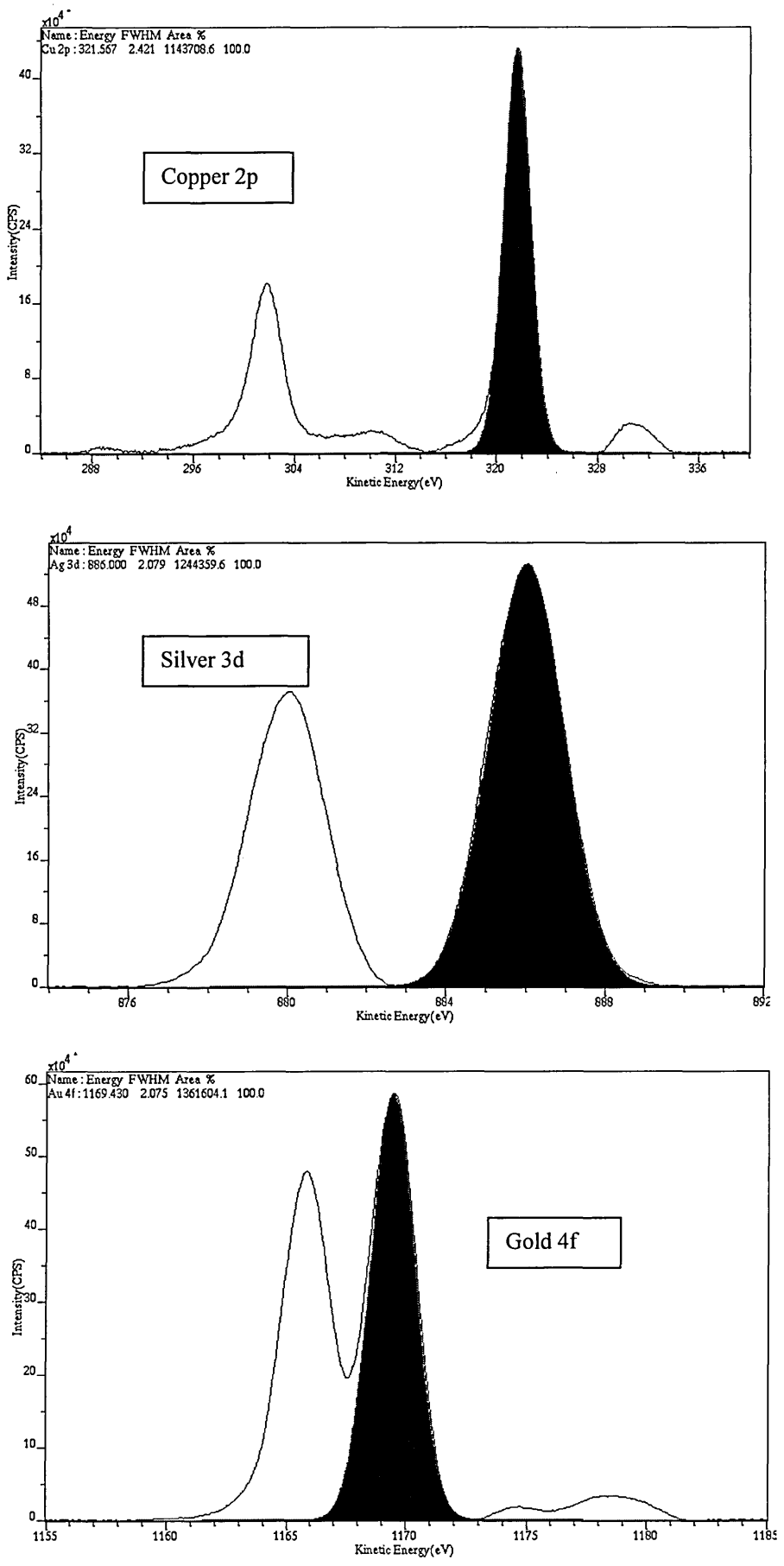

Table 6.1.4. Ratios calculated using sensitivity factors and measured ratios for electrostatic magnification.

Pass Energy (eV)	Ag 3d /Cu 2p		Au 4f/ Cu 2p		Ag 3d /Au 4f	
	Measured.	Calculated.	Measured.	Calculated.	Measured.	Calculated.
20	1.35	1.52	1.58	1.67	0.85	0.90
40	1.30	1.35	1.48	1.47	0.88	0.92
80	1.20	1.21	1.32	1.29	0.91	0.93
160	1.07	1.07	1.17	1.13	0.92	0.95

Table 6.1.5. Ratios calculated using sensitivity factors and measured ratios for magnetic magnification..

Pass Energy (eV)	Ag 3d /Cu 2p		Au 4f/ Cu 2p		Ag 3d /Au 4f	
	Measured.	Calculated.	Measured.	Calculated.	Measured.	Calculated.
20	0.54	0.53	0.41	0.41	1.31	1.30
40	0.58	0.59	0.47	0.48	1.23	1.25
80	0.66	0.67	0.54	0.56	1.22	1.20
160	0.73	0.75	0.61	0.65	1.18	1.15

Table 6.1.6. Percentage error between measured and calculated values.

Pass Energy (eV)	Percentage Error. (Electrostatic.)			Percentage Error. (Magnetic.)		
	Ag 3d /Cu 2p	Au 4f/ Cu 2p	Ag 3d /Au 4f	Ag 3d /Cu 2p	Au 4f/ Cu 2p	Ag 3d /Au 4f
20	-13%	-6.1%	-6.5%	1.7%	0.50%	1.3%
40	-4.3%	0.4%	-4.7%	-2.8%	-1.3%	-1.5%
80	-0.7%	2.1%	-2.8%	-1.0%	-2.7%	1.6%
160	-0.3%	3.6%	-3.4%	-2.6%	-5.0%	2.3%

6.2.0. Application of bias method proposed by Zommer (1995).

For this experiment (see section 2.3.4) gold was chosen as the sample. As this method relies on the comparison of signals from the same emitted photoelectron energy the choice of sample is not important as long as it is conducting, so the bias voltage may be applied to it. The socket of port B (see Figure 3.2.2), which is normally used to measure sample current, was used to apply the bias voltage to the sample, by connection to a 0-60V, 0-3A power supply. The power supply ripple was mesured with an oscilloscope and was found to be under 50mV.

The signal at each point was measured by scanning the kinetic energy E_k over 0.5eV with a step size of 0.1eV, so the scan range was from E_k-0.25eV to E_k+0.25V. The scan was performed five times for each E_k point. This was carried out for each bias voltage E_b. To scan the same E_k value when a bias voltage is applied, the input value for the scan range must be equal to E_k-E_b. At each value of E_k, the bias voltage was varied from -10V to +20V in steps of 5V. The value of E_k at which measurements were taken, was varied from 100eV to 1200eV in steps of 100eV.

6.2.1 Results

For a given value of E_k the intensity for a particular value of $E_b$was taken as the average of the five points in the scan. The data was stored in a spreadsheet so for each value of E_k, the intensity was plotted against the bias voltage. Figures 6.2.0 and 6.2.1 show these plots for E_k=300eV and E_k=800eV.

Figure 6.2.0 Plot of Intensity against Bias Voltage at E_k=300eV.

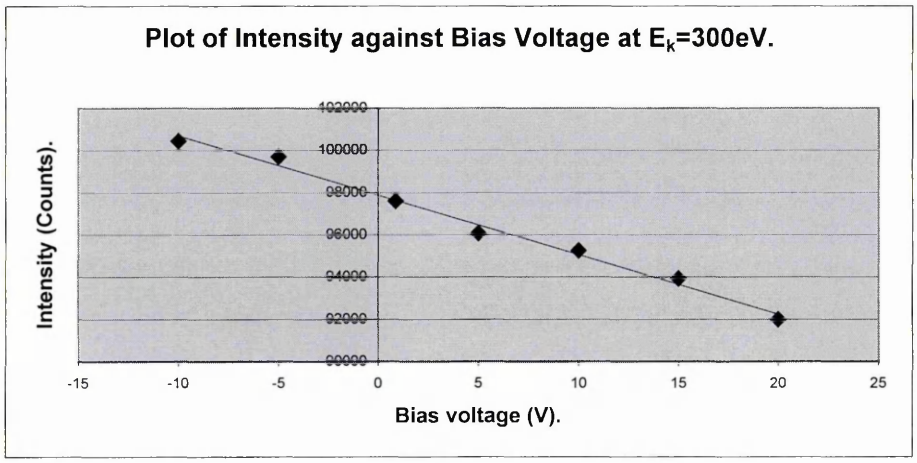

Figure 6.2.1 Plot of Intensity against Bias Voltage at E_k=800eV.

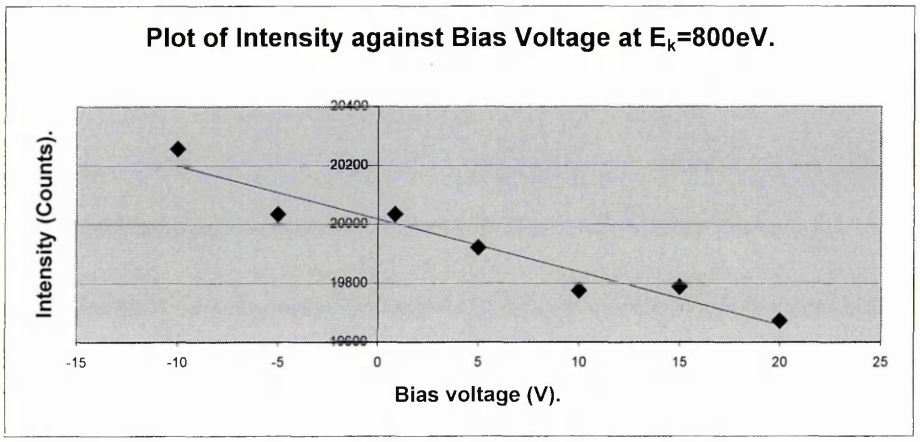

From these plots the gradient could be obtained using the line of best fit function of the Excel software. The gradient, dI/dE_b was obtained for each value of E_k. This was multiplied by $1/I(E_k)$ and gave the value $p(E_k)$ of Equation 2.2.21 where

$$p(E) = \frac{1}{I(E_k)} \frac{dI}{dE_b} \qquad \text{Equation 2.2.21}$$

Figure 6.2.2 shows the values of p against E_k.

Figure 6.2.2 Plot of $p(E_k)$.

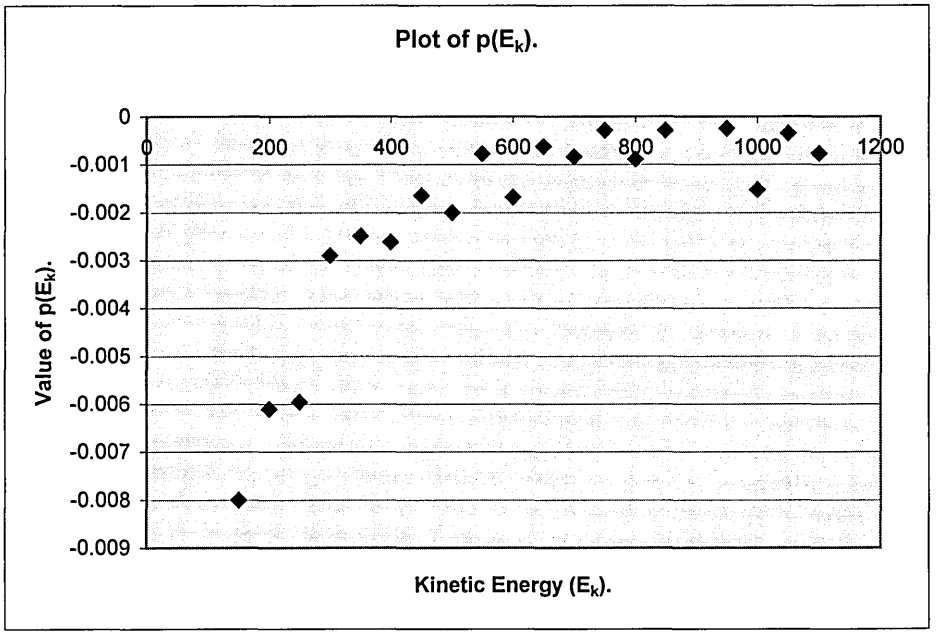

It is necessary to fit a polynomial to this function, which, if we recall Equation 2.2.21 must be integrated. Inspection of the function shows that there would be large uncertainty in fitting a smooth function to this plot. A many ordered polynomial, however would be cumbersome to integrate and the literature indicates a smooth fit (Zommer, 1995).

6.2.2 Further investigation of method.

The uncertainty when fitting the polynomial to the points of Figure 6.2.2 is of obvious concern. Further attempts were made to improve statistics by using longer dwell times and increasing the number of scans but no significant improvement was achieved. To investigate the degree of scatter the connection between the PC and workstation was utilised to assist the analysis of large amounts of data. By using many data points to plot the p(E) curve of Equation 2.2.21 the scatter around a smooth curve would be evident.

A silver sample was used to provide the intensity for this experiment. Wide scans were acquired using the standard experimental conditions.

The scans were acquired with varying bias voltages applied from -10V to +10V in increments of 5V. Thus 5 wide scans were obtained. The files were exported from Vision as text files and imported into the spreadsheet Excel over the Ethernet connection. Scan counts were placed into adjacent columns in order of bias voltage. The data in each column after the -10V column was moved down 10 rows to compensate for the bias voltage, so that the actual photoelectron energy registered for each column. This could be verified by checking that, at peak intensity positions, the intensity in adjacent columns of the same row all peaked.

At each of the 2350 rows, the Excel function LINEST() was applied to the 5 columns to obtain the parameter dI/dE_b. This was converted to $1/I(E_k)dI/dE_b$, and placed in another column, so the function $p(E_k)$ of Equation 2.2.21 could be plotted for all 2350 points. This plot is shown as Figure 6.2.3.

Figure 6.2.3 Plot of $p(E_k)$

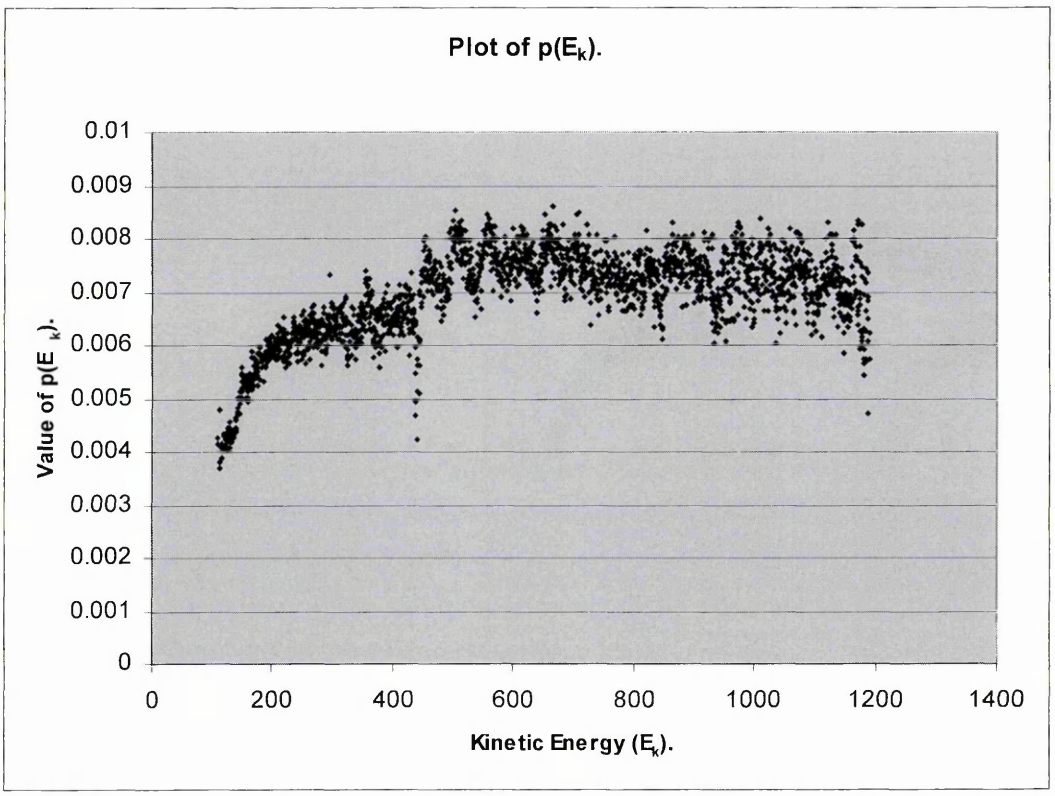

It is obvious that a large amount of scatter exists and proves that a polynomial could not be fitted to the data without a great degree of uncertainty. There seems to be an oscillation in the data, which must be investigated further if the technique is to be used on an instrument of this type.

6.3 Discussion.

The background measurements of section 6.1.3 produced $n(E_k)$ plots to which a polynomial could be applied. It is of concern that the peak area measurements of section 6.1.1 were not suitable. The value of n at a given value of E_k should not change just because a peak is used to obtain the intensity measurement. If this were true then the technique would not be applicable to calibration for quantification using peak area measurements. The experiments performed by Carrazza and Leon (1991) also show differing results between background measurements and peak area measurements. A smooth $n(E_k)$ curve can be seen for the background measurements, while the peak area measurements are scattered. Weng et al (1992) used only peak area measurements when they attempted to asses this method, and examination of their results reveals large scatter when $n(E_k)$ is plotted. We can conclude that the problem with the peak area measurements is not isolated the Hallam instrument, and consider only background measurements to be appropriate for the calibration.

Inspection of Figures 6.1.21 and 6.1.22 show a slight difference in the transmission function derived at a six month interval. This could be due to experimental errors, or a change in the transmission function with time. A possible reason for the large change in the electrostatic transmission function may be residual magnetism. From this evidence it seems prudent to carry out calibrations at given time intervals. If this is to be the case then a procedure for regular calibration such as the one described in section 6.1.4 is recommended. For both the magnetic and electrostatic modes a polynomial could be fitted which described $n(E_k)$ with confidence. This was not so for Figure 6.1.25, where calibration was attempted with the 120μm area-defining-aperture in place. We can conclude that with the apertures in place the signal is too weak to obtain data applicable to instrument transmission function derivation. Small area spectra may be used semi-quantitatively to compare peak area measurements with spectra from spatial point to point, but absolute quantification is not possible.

The form of the $n(E_k)$ curves obtained on the Hallam instrument differed from that obtained by Carrazza and Leon (1991). The curve obtained from the LHS-11 analyser had a minima of n=0.4 at E_k=420eV, with n=0.65 at E_k=150eV and n=0.55 at E_k=1200eV. All forms of the $n(E_k)$ curve result in a $T(E_k)$ curve where the transmission falls with increasing photoelectron energy.

From Table 6.1.6 we can see that the calibration appears to be more accurate for the magnetic mode. The largest error for the electrostatic mode is –13% compared to –5% for magnetic mode. It is obvious that the transmission function should be derived from magnetic mode only, and this mode be used for quantification. If an accuracy greater than 5% is desired, then a more tedious method (direct comparison of data with pure elemental spectra) should be used. The errors may be due to the area measurement of the elemental peaks, the derived transmission functions $T(E_k)$, or the values of σ and λ obtained from the literature.

The data obtained using the technique proposed by Zommer (1995) were unsuitable for calibration purposes. The experiment was repeated on numerous occasions using longer collection times to improve statistics but the results shown in section 6.2.1 were typical. The results presented by Zommer show a smooth curve to which a polynomial may easily be applied, but this paper is the only example of this method. It is the view of the author that this technique is not suitable for calibrating the type of lens spectrometer system on the Hallam instrument.

6.4 Conclusion.

The optimum method for rapid determination of transmission function and calibration of instrument for quantification has been identified. It was found that the best method was that proposed by Carrazza and Leon (1991) for the instrument operating in magnetic magnification mode. We can conclude that the method proposed by Zommer (1995) is unsuitable for use with the Hallam instrument.

References for Chapter 6:-

Carrazza J., Leon V., (1991) Surface and Interface Analysis, Vol. 17, 225-229.

Schofield J.H., (1976) Journal of Electron Spectroscopy and Related Phenomena , Vol. 8, 129-137.

Shirley D.A., (1992) Phys Rev. B,5,4709.

Zommer L., (1995) Vacuum, Vol. 46, 617-620.

Wagner C. D., Riggs W. M, Davis L. E., Moulder J. F., (1981) In Handbook of X-ray Photoelectron Spectroscopy (G. E. Muilenberg, editor), Perkin-Elmer Corporation (Physical Electronics).

Weng L.T., Vereecke G., Genet M.J., Bertrand P., Stone W.E.E., (1993) Surface and Interface Analysis, Vol. 20, 179-192.

Chapter 7 Conclusion.

The work detailed in this thesis was carried out in order to facilitate the aims of the DTI project 'Simultaneous Quantitative Thickness Mapping and Chemical Analysis of Thin Films'. The literature study presented in Chapter 2 provided important information to all participants of the DTI project. In particular, the literature review gave an indication of the limitations of each technique e.g. thin film thickness mapping and small area XPS, both on the Hallam instrument and on other electron microscopes and surface analysis instruments. The demonstration of thickness mapping given in Chapter 3 proves that this capability has been successfully implemented on the Hallam instrument.

The work detailed in Chapter 4 was at the request of Oxford instruments. The ability to align EDX maps acquired at different beam energies would enhance the thickness mapping capability provided by their software. This work began with an investigation of beam movement as a function of beam energy on the Hallam instrument, where stray electrical fields were found to cause the beam shift. The more general distortions, between images acquired at different beam energies, were then considered. Polynomial equations were used to describe the transformations between images as a function of x and y. The program 'distcof' was written to determine these coefficients, and applied to images acquired on the Hallam instrument, and on a Phillips XL40 electron microscope. From the coefficients we were able to conclude that the image transformations were affine for both instruments. An offline method of image alignment was developed in the form of the program 'transkv', which was applied to images acquired on the Hallam instrument and the XL40. The realignment of the images by this method caused a small amount of blurring but proved that the coefficients had been correctly determined.

The aim of the work detailed in Chapter 5 was to improve the small area XPS spatial resolution across the field of view. The first task was to characterise the small area XPS scanning system. It was found that the spatial resolution deteriorated away from the centre of the field of view. Through experiment and simulation of the deflection system we were able to determine what could be done to improve this. The octopole deflection system was implemented by the addition of analogue electronics. The effect of the octopole deflection was demonstrated by presented images before and after it was installed. The dynamic focus of the magnetic lens was then implemented, and the effect of this was also demonstrated by presenting images acquired before and after implementation.

The final experimental chapter of this thesis covered the work concerned with XPS quantification. The purpose was to determine a method of calibrating the instrument and quantifying spectra acquired on it. We found that the method proposed by Carrazza and Leon (1991) could be used to determine the instrument transmission function. Spectra acquired from pure elements were used to establish how successful this procedure had beeen. Using magnetic magnification mode we found

that an accuracy of 5% was achieved. I attempted to determine the transmission function using the method proposed by Zommer (1995), but found it unsuitable for use with the Hallam instrument.

The work carried out in this thesis contributed substantially to the DTI project (Wirth 1998). We may now consider how the instruments unique configuration may be exploited. The spatial resolution of Small Area XPS is not sufficient to allow pixel point to point comparison with EDX images, as is possible with AES and EDX maps were the data is generated at the same point by the primary electron beam. The techniques could, however, be combined to investigate films of varying composition with depth. XPS mapping can be used to find a homogeneous area of a sample to apply quantitative XPS (wide area), thus establishing the composition at the surface. If the sample is depth profiled in many stages by ion bombardment, then XPS may be carried out at intervals between the sputtering. At each interval, a thickness map of the film using x-ray analysis could be acquired. This would give an indication of how far into the film the depth profile was at that stage. At the end of the depth profile we would have a surface composition at each stage, which could be used to correct the thickness measurement from errors caused by varying composition with depth. This type of procedure, however, must be approached with caution, as there may be a disturbing influence of sputtering on surface composition. This possible modification of composition by sputter depth profiling, highlights the importance of non-destructive depth profiling techniques such as EDX.

References:-

Carrazza J., Leon V., (1991) Surface and Interface Analysis, Vol. 17, 225-229.

Wirth A (1998) DTI/ESPRC Link Nano-technology Final Report, Project Ref No. MOT 8/12/041.

Zommer L., (1995) Vacuum, Vol. 46, 617-620.

Appendix 1

This section shows the source code relating to the software described in Chapter 4. The comments within the /*.. */ markers are not part of the code but serve to describe what the code is doing.

C code for the main program coeff.exe.

```
#include <math.h>                                        /*Includes header file.*/
#include "nrutil.h"
#include <stdio.h>
#define SWAP(a,b) {temp=(a);(a)=(b);(b)=temp;}
#define points 14

main()                                                   /*Start of the main program.*/
{float xres[7],float yb[points],float yres[7]);          /*Variable definitions.*/
float c[points][7],cor[points][7];
float xrig[points],yrig[points],ysol[7],xsol[7];
int p,i,q;
void svdcmp(float a[points][7],int m,int n,float xb[points],
FILE *fptr;
char name[15];

printf( "Please type name of text file(including path).\n");
scanf( "%15s",name);
if ((fptr = fopen(name,"r"))!=NULL)                      /*Opens text file to read coordinates from.*/

for (p=1;p<=13;p++)                                      /*Reads coordinated.*/
{
fscanf(fptr,"%f,%f,%f,%f",&cor[p][1],&cor[p][2],&cor[p][3],&cor[p][4]);
}

for (p=1;p<=13;p++)                                      /*Assigns values to the input arrays.*/
{
c[p][1]=1.0;c[p][2]=cor[p][1];c[p][3]=cor[p][2];
c[p][4]=cor[p][1]*cor[p][1];c[p][5]=cor[p][2]*cor[p][2];c[p][6]=cor[p][1]*cor[p][2];
xrig[p]=cor[p][3];yrig[p]=cor[p][4];
}

svdcmp(c,13,6,xrig,xsol,yrig,ysol);                      /*Calls the function svdcmp().*/

if ((fptr = fopen(name,"a"))!=NULL)

for (p=1;p<=6;p++)
fprintf(fptr,"a%d= %f  \n",p-1,xsol[p]);                 /*Prints the output values to the text file.*/

for (p=1;p<=6;p++)
fprintf(fptr,"b%d= %f  \n",p-1,ysol[p]);

fclose(fptr);                                            /*Closes the text file.*/
exit(0);                                                 /*Exits the program.*/
}
```

C code for main program of transkV.exe.

```
#include <stdio.h>
#include <math.h>

main()
{float line[1536],xcof[6],ycof[6],nx,ny,fx,fy,neigh[4],contrib1_2,contrib3_4;  /*Decleration of variables.*/
char inname[15],outname[15],cofname[15];
unsigned  i,j,y,x,xpix,ypix;
unsigned long pos1,pos2;
FILE *inp;
FILE *outp;
FILE *cofp;

printf( "Please type name of input binary file(including path).\n");        /*Request flienames for the input*/
scanf( "%15s",inname);                                                      /*raw image file, text file containing*/
printf( "Please type number of pixels (x,y).\n");                           /*coefficients, and output raw image*/
scanf("%d,%d",&xpix,&ypix);                                                 /*file.*/
printf( "Please type name of output binary file (including path).\n");
scanf( "%15s",outname);
printf( "Please type name of text file containing\n");
printf( "tranformation coefficients.\n");
scanf( "%15s",cofname);

if ((cofp=fopen(cofname,"rt"))==NULL)                                       /*Opens the files.*/
return 0;
for (i=0;i<6;i++)
fscanf(cofp,"%f\n",&xcof[i]);
for (j=0;j<6;j++)
fscanf(cofp,"%f\n",&ycof[j]);
fclose(cofp);
for (i=0;i<6;i++)
printf("%f\n",xcof[i]);
for (j=0;j<6;j++)
printf("%f\n",ycof[j]);
if ((inp=fopen(inname,"rb"))==NULL)
return 0;
if ((outp=fopen(outname,"wb"))==NULL)
return 0;

for (y=0;y<ypix;y++)                                                        /*Start of main loop*/
{
for (x=0;x<xpix;x++)
{
nx=xcof[0]+(xcof[1]*x)+(xcof[2]*y)+(xcof[3]*x*x)+(xcof[4]*y*y)+(xcof[5]*x*y);        /*Calculates the position of the*/
ny=ycof[0]+(ycof[1]*x)+(ycof[2]*y)+(ycof[3]*x*x)+(ycof[4]*y*y)+(ycof[5]*x*y);        /*required pixel positions.*/

if (((unsigned)nx<0) || ((unsigned)nx>(xpix)) || ((unsigned)ny<0) || ((unsigned)ny>(ypix)))
{line[x]=0;}                    /*If required pixel is outside image border the destination pixel is assigned a zero*/
                                /*value.*/
else
{pos1=0;                                /*The required pixels values are obtained and the destination pixel*/
fx=nx-(unsigned)nx;                     /*values are calculated*/
fy=ny-(unsigned)ny;
pos1=(((unsigned long)xpix*(unsigned long)ny)+(unsigned long)nx)*4;
pos2=(((unsigned long)xpix*(unsigned long)ny)+(unsigned long)nx+(unsigned long)xpix)*4;
fseek(inp,pos1,SEEK_SET);
fread(&neigh[0],4,2,inp);
fseek(inp,pos2,SEEK_SET);
fread(&neigh[2],4,2,inp);
contrib1_2=(fx*(neigh[1]-neigh[0]))+neigh[0];   /*Calculation*/
contrib3_4=(fx*(neigh[3]-neigh[2]))+neigh[2];
line[x]=(fy*(contrib3_4-contrib1_2))+contrib1_2;
}

}
fwrite(line,4,xpix,outp);               /*The destination pixel values are written to the raw image output file.*/
}
fclose(inp);
fclose(outp);
}
```